AN ABSTRACT OF THE DISSERTATION OF

Jason Kelley for the degree of Doctor of Philosophy in Water Resource Engineering presented on September 1, 2016.

Title: Addressing Data Resolution in Precision Agriculture

Abstract approved: _____
Chad W. Higgins

Irrigated agriculture constitutes the greatest consumptive water use globally, so that irrigation efficiency measures are an important part of global efforts to best utilize this limited resource. However, greater irrigation efficiency must be achieved while simultaneously maintaining or increasing crop yields and farming profitability. Incremental water use decisions are made at the local level by farmers under many real world constraints; consequently they face significant risks in operating large and complex irrigation systems. These decisions should be supported by reliable information upon which to base operational plans and irrigation scheduling. Implementing precision irrigation effectively depends upon highly resolved estimates of crop water demand so that application rates match demand precisely both in location and timing. A fundamental challenge in mapping the irrigation requirement is addressing the heterogeneity of soil, biophysical, and atmospheric processes which mediate water demand. However, existing methods to determine the irrigation requirement assume that field conditions are homogeneous. Precision irrigation systems may enable more specific water distribution than traditional irrigation equipment, but allocating the correct amount of water requires crop water estimates that accurately reflect the variability of the irrigation requirement and consider the scale and timing at which irrigation can be delivered.

This dissertation synthesizes the results from field studies which analyzed spatial patterns of

irrigation performance and crop water demand under real field conditions. The first experiment quantified the performance of a precision irrigation system and determined the data resolution required for effective utilization of the system's capability (Chapter 2). Field trials were conducted with a variable rate center pivot sprinkler (VRI) under normal farming conditions to determine this spatial resolution. The result was the definition of a performance coefficient and characteristic length scale associated with the irrigation system. The characteristic length scale describes the highest resolution prescription possible with VRI. Following on these findings, a second study compares an electromagnetic (EM) soil mapping method using extensive laboratory soil characterization as a basis for comparison (Chapter 3). The motivation of the study was to validate the EM method's capability to detect small scale variations in soil water holding capacity, and to determine under which conditions the EM method can obtain reliable and robust soil maps. The findings reinforce earlier work on the importance of instrument calibration, and also show that specific soil characteristics may preclude using EM methods to map soil in some regions.

Following the soil mapping study, further studies investigated methods to measure crop evapotranspiration (ET). A literature review was conducted to establish a catalog of contemporary methods to monitor ET, focusing on those commonly used in agriculture (Chapter 4). From this review, the surface renewal method (SR) emerged as potentially able to map ET feasibly and cost-effectively. Four field experiments were conducted over two years under a range of field conditions to establish a robust protocol for the determination of surface fluxes with SR (Chapter 5). Three of these experiments specifically investigated the potential for SR to be implemented from a moving sensor platform, such as an unmanned aerial vehicle. Experiments showed SR could estimate sensible heat flux as accurately as eddy covariance during moving trials. However, analysis of the minimum flux averaging period demonstrated that SR cannot resolve fluxes at the requisite spatial scales for precision irrigation. Nonetheless, SR remains

promising for other practical applications in measuring surface fluxes. Future research questions and potential applications are explored in Chapters 5 and 6.

The methods described here are directly relevant to water managers at the levels of farms and irrigation districts. Efficient irrigation planning depends on timely, reliable, and site-specific information in order to anticipate crop water demand, irrigate adequately to prevent drought stress, and maximize yield from the available resource. Growers and irrigation specialists currently have many resources at their disposal, including regional and satellite based ET estimates, state and local soil mapping, and scientific irrigation planning software. However, these methods do not provide site-specific and real time measurements of actual crop water demand, and farmers do not have any reliable means by which to validate the accuracy and precision of these estimates. For this information to be directly useful in irrigation planning, it should be validated by on site measurements. Reliable, local, and real time information is required to realize the full potential of precision agriculture.

Addressing Data Resolution in Precision Agriculture

by
Jason Kelley

A DISSERTATION

submitted to

Oregon State University

in partial fulfillment of
the requirements for the
degree of
Doctor of Philosophy

Presented September 1, 2016
Commencement June 2017

Doctor of Philosophy Dissertation of Jason Kelley presented on September 1, 2016.

APPROVED:

Major Professor, representing Water Resource Engineering

Director of the Water Resources Graduate Program

Dean of the Graduate School

I understand that my dissertation will become part of the permanent collection of Oregon State University libraries. My signature below authorizes release of my dissertation to any reader upon request.

Jason Kelley, Author

ACKNOWLEDGEMENTS

My teachers at Oregon State made a huge difference for this "older than average" student, and were instrumental in expanding my skills and lending perspective. Jack Istok's lectures gave me my first glimpse into the behavior of fluids, and my first glimpse of engineering problem solving. Desirée Tullos brings humanity to teaching and engineering, and was a great friend and occasional foil - she was largely responsible for the direction of my studies. I was particularly lucky to take some of the last courses offered by Stan Gregory, who teaches with dignity, style and wit, and also demonstrates how to lead a meaningful life. Richard Cuenca reminded me of the importance of our agricultural heritage, teaching with deep knowledge of both the *agris* and the *cultura*. After waiting over a decade to meet Jay Noller, I felt fortunate to take his classes, and he also generously made time to work with me individually. Jay's insights into human knowledge and his vision of the landscape continues to inspire my work.

Chad Higgins showed me that it is possible to capture flashes of ingenuity, and how these moments should always end up as a great plot. His brilliance, limitless positive outlook, selfless hard work, and patience make possible a lot of opportunities that I would've otherwise missed. The science gods were kind in giving Chad to me.

Colleen Barr is a trusted friend and a brilliant colleague- any quality in this work reflects her contributions. Charles Hillyer laid the foundation for my work in agriculture and supported my first forays into ag research. Robert Predosa (Preducky) deserves thanks for questioning my pontification.

The students are often the only reason I show up to work. Payse Smith started the original project which became the SR experiment. In addition to all those who sat through my lame coursework, Missy Buntin, Sonja Michelson, Austin Anderson, Thomas Hart, Anna Leitschuh, Nicole Fairley, and Natalie McDonald all put in a lot of extra time listening to my rambling.

Xan Augerot, Shane Harvey, Scott Bailey, Adam Stebbins, and most of all Andrew Niemi all trusted me with design work and opportunities to practice science and engineering in the "real world". Rick Valley, Bear Pitts, Steve Wisnovsky, Steve Trask, Sarah Wyland, Rashel Gonzales, Pat Welle all contributed to my understanding and patiently allowed me to develop my own professional practice.

Huge thanks are owed to the farmers who extend their hospitality and let us set up a bunch of half-baked ideas on their fields: Larry Magill, Jason Bradford, Jake Madison, Steve Berg, Frank Morton, Don Horneck, and several members of my family. Funding from several agencies made

possible the research described in this dissertation- the Northwest Energy Efficiency Alliance funding two summers of research on variable rate irrigation and soil mapping. The US Bureau of Reclamation supported field deployments in the upper Colorado River Basin. The USDA provided funding for one season of my research.

Many were friends and opened up new opportunities for me at OSU: Tonatiuh Rodriguez-Nikl, Paul Montagne, Cindy Olson, Jen Cohen, Frank Chaplen, Ganti Murthy, John Bolte, Marshall English, Milo Clausen, Mike Olsen, Chris Thomas, Julia Jones, Cara Walter, John Selker, Rebecca Hochreutener, Kellie Vaché, Yutaka Hagimoto, Chadi Sadye, Ziru Liu, Steve Drake, Heather Holmes, Walt Mahaffee.

Paul Malloy, Aparna Shrivastava, Becca Miller, Jesse Narog, Pat Haluska, Gaby Coughlin, Andrew Kearney, Kendra Brown, Marco Keiluweit, Sus Theis, Jordan Beamer, Haley Ohms, Kusra Kapular, Brieanne Lee-Tharp, Roslyn Odum, Myles Gray, Brian Doherty, and June Marion are friends and comrades- their support and contributions can't be appreciated enough. Rick Valley; Dave and Sharon Thormahlen; Jenny Swanson and Gary Wheeler; Robert Batten; Peter Guillozet; John, Ole, Sol, and Arame; and Cheryl Barclay, all who haven't heard from me in a while, but are part of this nonetheless.

My extended family has supported my work over the last seven years enthusiastically and selflessly. I am fond of saying that my grandfather Homer Stevens was the first to teach me about irrigation- he definitely taught me how to drive a tractor. I was also fortunate to know Mary and Gene Machado, and Sally Bush: they all had a part in who I am. Bob and Estelle Kelley always encourage me. Shona and John Trumbly and Wanda Montgomery told me that I could and better do it. Diane Kelley wouldn't let my head get too big, Meghan Leddy keeps it real, Jeannette Washington works harder than I can imagine. Jayden, who will be an engineer one day, helped with the SR experiments. Jill Golden is always there for me; Peter Eschwey and I sneak off when we can; James Condino reminds me what is really important; Star Heutmaker inspires me to be a better person; I call Reese Prouty when the students cry; Jesse Berdine is often the only one keeping me sane. The love and encouragement of Allegra Carlson makes it all worth it, and she is a brilliant reader too. Most of all, none of this would be possible without the support, thoughtfulness, and friendship of my parents John and Melanie Kelley.

I am truly blessed with an abundance of teachers, friends, and family.

It is certain that I have forgotten some who have helped me along the way, even with this long list. You know who you are, and I can only humbly beg your forgiveness- I have been typing for a long time.

TABLE OF CONTENTS

LIST OF FIGURES

LIST OF FIGURES, continued

DEDICATION

In memory of a few people who had a profound influence on me and others; fostering curiosity, scholarship, and personal commitment to service. They each contributed directly to my professional life, but more importantly they each taught me something about how to live a good life. Their lives were dedicated in service to their communities and the world.

Katharine Shone Stevens (1911 - 1971)

Lauralie May Stevens (1941 - 2014)

Ande Grahn (1951 - 2010)

Don Horneck (1958 - 2014)

1. Improving Agricultural Water Use Efficiency Requires Higher Resolution Data

Irrigation withdrawals constitute the largest consumptive use of water globally. Improving water use efficiency can significantly reduce energy and water consumption, with concomitant enhancement of crop productivity and economic returns. Precision irrigation methods are widely seen as a pathway to increase efficiency and yield, and to improve profitability. Proponents of precision agriculture have emphasized the potential to optimize water allocation and thereby reduce consumptive water use. However, there are not yet clear and objective measures of the real benefits, efficiency, and cost-effectiveness of these techniques and products. To achieve the potential benefits of precision application, irrigation planning requires site-specific, real time estimates of crop water demand. In practice, allocation decisions require information about the crop water requirement that is much more detailed than are available using standard methods such as the Penman Monteith equation. While significant progress has been made in providing this data, challenges remain to provide a level of detail that matches the information needs of precision agriculture.

Irrigation facilitates more than 40% of global food production on less than 20% of agricultural land, and requires more than 80% of global consumptive water use (Siebert and Döll, 2010). Efficient irrigation planning depends on reliable and site-specific information to anticipate crop water demand, to assure that irrigation is adequate to prevent drought stress, and to maximize yields from the water that is available. Growers and irrigation specialists can access many sources of water use information including historical irrigation records, regional weather networks, and remotely-sensed estimates of weather and water demand (Perry et al., 2009). However, appropriately local and real-time estimates of crop water requirements are either unaffordable or not available. Further progress in predicting crop water demand depends on new measurement technology and methods. For this information to be useful to producers, it must be

affordable, accessible, and feasible to act upon with existing irrigation systems (SARE, 2015). For this information to be useful to producers, it must be affordable, readily accessible, and updated regularly (Clary, 2015).

Advances in precision irrigation can potentially reduce water use while maintaining yields, but these systems are similarly constrained by an absence of local real time data at the field scale (Evans and Sadler, 2008). In practice, implementation of science based irrigation strategies, such as deficit irrigation, site specific irrigation, or variable rate irrigation requires reliable data about crop water demand. In the case of incremental water use reductions, the risks of under-watering often outweigh the costs of over-watering (English and Raja, 1996). Without local and real time data, science based estimates of crop water demand are too coarse to make incremental water decisions within the framework of a farm's overall water planning (Berne et al., 2015).

Extensive work at the state and regional level has been put into developing publicly accessible irrigation information (Farahani et al., 2007). Most notably, state and regional weather networks include automated calculation of reference evapotranspiration (ET_o) using the Penman-Monteith equation. Reference ET can be used with calibrated crop coefficients to estimate a crop specific ET. In the Pacific Northwest, US Bureau of Reclamation operates the Agrimet network with 70 standardized agricultural meteorological stations transmitting hourly weather and ET_o data (*www.usbr.gov/pn/agrimet*). California's Dept. of Water Resources operates the CIMIS network of 145 weather stations, including spatial mapping of 18 statewide zones for ET_o (*www.cimis.water.ca.gov*). Washington State operates AgWeatherNet with 172 automated stations (*weather.wsu.edu*). Yet despite the significant investment that has gone into developing these networks, reference ET estimates don't account for local variability in crop development, microclimate, or for new crop varieties (Allen et al., 2011).

Because environmental parameters can vary widely between sites, regional ET is not easily

interpolated to site-specific, real-time estimates. Consequently the information available to irrigators is often inadequate for optimizing on-site water allocation. Because various methods used to estimate ET employ different physical measurements, the resulting estimates do not always agree. Crop variability, patchy soil types, and microclimates can confound accurate ET estimates. Comparing estimates from multiple methods is often done in research, but there is no objective and transparent way to compare methods for the average user. Consequently, irrigators are left without a clear idea of which estimate is best. Farmers are pragmatic and risk-averse; ET estimates must be reliable and cost effective if they are to be adopted into existing farming systems. Regional drought, shifts to global commodity markets, and climate change have all been factors in the growing attention given to water use efficiency and the sustainable use of water. Improving the availability and quality of ET estimates contributes directly to risk reduction and increases productivity and sustainability of agricultural systems.

As growers attempt to conserve water and to maximize the use of limited water allocations, there is a greater risk of plant stress. Under drought stress, plants transpire less than potential evapotranspiration, thereby limiting photosynthetic productivity and ultimately crop yield. From the perspective of irrigators, irrigation scheduling is ideally allocating available water to meet crop water demand which is largely determined by weather and crop development. In actuality, allocation is also constrained by water availability and sourcing, mechanical limitations, and a desire to reduce power costs. Usually, water use efficiency is not a major consideration, both because of the enormity of other considerations and because the cost of water is overshadowed by fixed costs and the significant risks posed by under-irrigation (Knox et al., 2012). While scientific methods to establish site specific irrigation demand are available, farmers often base irrigation planning on regional weather data, reference ET estimates, and the farmer's personal knowledge (Molden et al., 2010).

Verification of the actual benefits achieved with precision irrigation has lagged behind development and implementation. Attempts to characterize precision systems have largely relied on pre-existing engineering guidelines in which performance was characterized by uniformity of application ("coefficients of uniformity"). Pressurized irrigation systems expanded agriculture to areas previously too difficult to irrigate due to topography, aridity, or distance from a viable water source. Pressurized systems offered many advantages over flood and furrow irrigation: they reduce water lost to deep infiltration and tailwater; sprinklers allow more control over the irrigation timing and depth; automated systems reducing labor costs. Improved irrigation and other farming modernization has been matched with a doubling in grain production rates over the last half century (Tilman et al., 2002). Irrigated grains account for the largest water use globally; approximately 3000 km^3 is used annually to grow rice, wheat, and corn (Siebert and Döll, 2010).

Engineering analysis of pressurized irrigation systems were focused on uniformity of application as the best measure of system efficiency. Implicit in the idea of uniform application is the assumption that field conditions are homogeneous. In the real world, field conditions are not homogeneous. Crop water demand is not uniform; soil characteristics are variable at both small and large scales; growth rates and crop yield varies with soil nutrition, water availability, and other factors. Precision irrigation, in contrast, has the potential to improve efficiency precisely by applying water non-uniformly, instead prescribing irrigation matched to crop water demand on small spatial scales. Site specific application doesn't fit standard performance test which are based on uniform application rates. **Chapter 2 discusses an experiment which quantifies the spatial resolution that can be achieved by a precision irrigation system under actual field conditions**. It is shown that while the system that was tested can be programmed to deliver water to areas 10 meters across, the physical constraints imposed on a sprinkler only allow water application to be resolved to areas with dimensions over 20 meters in scale length. By

determining the smallest area in which a specified amount of water can be reliably delivered, this study establishes the resolution which is relevant to irrigation planning.

Once the spatial resolution of a precision system is established, a method is required to map crop water demand at this scale. One way to determine crop water demand is to track how much water is stored in the soil. Plants access water stored in the soil, but this is mediated by soil texture and the plants' ability to extract the water. Because soil texture is a major determinant of water holding capacity, a map of soil texture can be used to predict irrigation demand. Soils that hold more water can be irrigated less often and at greater rates. Conversely, fine textured soils can hold water strongly, decreasing the fraction of water available to plants. Because of this, soil texture and water holding capacity are used to schedule irrigation and set the rate of application. Soil texture and depth can vary greatly over short distances, or may not vary at all at field scales. Soil texture and water holding capacity can also change seasonally and annually. In practice, irrigation scheduling can be managed by measuring and tracking the plant available water in the soil, and applying irrigation prior to the onset of drought stress in the crops. To improve irrigation efficiency via spatial variability of soil properties, very high resolution soil maps must be available upon which to base those application rates. **Chapter 3 describes a soil mapping experiment that was conducted to verify the utility of measuring electrical conductivity as a proxy for soil texture.** Previous attempts to utilize this method for precision irrigation systems had sometimes worked, and sometimes failed without clear reasons. A wide array of physical and chemical tests were utilized to determine the cause of the intermittent success of the method. The study confirmed previous findings regarding the importance of data quality control, and suggests post-processing techniques to improve raw field measurements. More importantly the study also shows that some common soil characteristics prevent reliable soil texture determinations from electrical conductivity measurements. A few simple, low cost tests can

determine the presence of specific soil characteristics which are confounding factors, thereby indicating if electrical conductivity is an appropriate method to generate soil maps in a specific location. Electrical conductivity mapping is an inexpensive, repeatable, and non-destructive method to map soil, and while not universally applicable, it is an important tool in mapping irrigation demand.

Soil moisture measurement helps determine how much water that is available to crops. Another way to determine how much irrigation is required is to directly measure the rate of crop water use. The amount of water required by crops is linked to the rate of evapotranspiration (ET). For photosynthesis to occur, carbon dioxide is absorbed from the air and water is simultaneously lost through leaf stomata. Water plays many biophysical roles in vascular plants, including photosynthesis and respiration, pressure required to maintain plant turgor, and vascular transport of nutrients. Consequently, water stress immediately and directly reduces crop metabolism and yields. But the largest consumptive use of water is stomatal loss, from which water vapor is ultimately transported away to the upper atmosphere.

ET is controlled by solar radiation, water availability, crop physiology, and other environmental factors. Understanding and measuring the transport of water vapor is critical to improving irrigation efficiency. **Chapter 4 reviews the most important methods for measuring ET in agriculture**, categorizing four types of measurement method: water balance, energy balance, biophysical phenomenology, and atmospheric turbulence. Chapter 4 briefly covers some remote sensing methods, including satellite mapping of ET. For mapping ET at sub-field scales, field methods are emphasized. In this review, the surface renewal (SR) method is identified at having particular promise for mapping ET at field scales. **Chapter 5 describes a series of field experiments that determine the minimum measurement time required for the surface renewal flux method, and validate the application of SR theory for a measurement**

taken while moving. The experiment showed that SR does work as well moving as it does for stationary systems, but that it was not practical for mapping as proposed due to a 3-5 minute minimum time to measure flux. New applications that may feasibly map ET are suggested based on the experiments conclusions. **Chapter 6 concludes by suggesting new directions for research in ET estimation,** and briefly surveys potential applications to support precision irrigation systems.

Advances in computing, sensors, and manufacturing will be leveraged in coming decades to transform agriculture. Globally, growing demand for food and other agricultural products will motivate the development of these new methods to increase production efficiency. Uncertainty about climate change and the availability of ground and surface water resources will only exacerbate the need for reliable and robust methods to measure water usage. The research presented here contributes to the current and future data required, which will help guide precision agriculture to meet the future's demands.

2. Catch Can Experiments of Variable Rate Irrigation System Performance

Variable rate irrigation (VRI) can improve the precision of water distribution by applying at a variable irrigation rate (depth of water). A variable prescription can increase the system efficiency by matching the irrigation rate to the actual crop water demand, which may vary within a field due to patchy field conditions such as crop health, soil texture, and microclimate. Under ideal operation, VRI can irrigate small ($\geq$100 m^2) discrete management areas independently at different rates. Under actual field conditions, achieving the ideal prescription for water application is hampered by confounding effects such as mechanical limitations of the irrigation equipment, surface redistribution, and wind drift. A series of field trials were conducted to test the capability of a VRI system to deliver water according to a prescription covering the full design characteristics in terms of spatial resolution and application rates. The test used a two-dimensional array of 440 catch-cans measuring application from a multi-scale irrigation prescription, expanding on the standard ASCE center pivot uniformity protocol for testing sprinkler irrigation performance. To quantify the effectiveness of the VRI system, a new performance coefficient is proposed, based on the Heermann-Hein uniformity coefficient. The analysis shows that the most significant disparity between the prescribed and measured irrigation application occur near transitions in the prescription (for example, on the bounds between areas prescribed to receive 60% and 80% of full application). By analogy to dispersion, a characteristic length scale σ is identified to describe the transitions that occurred between areas with different application rates. Analysis shows that σ is independent of the application depth, and is independent of orientation of the transitions (radial or tangential) or direction of the pivot travel. This indicates that a traditional, single line catch-can test can provide sufficient information for the determination of the length scale. The length scale can be used to determine the size of the smallest independent management zone, and the minimum management zone size was

determined to be 23 m for the pivot under investigation.

2.1 Background

Land surface variability is linked to the spatial variability in crop water demand, nutrient requirement and yields (Sadler et al., 2002). Changes in soil texture, nutrient variability, infiltration rates, holding capacity and rooting depth create a spatially variable water demand across the landscape. Irrigating uniformly across irregular field conditions leads to some areas being under-irrigated, resulting in yield reductions. Simultaneously, other parts of the field will be over-irrigated, waste irrigation water potentially leading to erosion and other secondary inefficiencies. To mediate these problems, conventional practice is to uniformly irrigate to the average of the lowest quartile of irrigation demand (Burt et al., 1997; Kruse, 1978). This uniform irrigation application rate assures that no more than 1/8th of the field is under-irrigated; however, the result of this is that 7/8ths of the field is potentially over-irrigated. To improve water use efficiency, precision irrigation systems should be able to distribute water to adequately meet irrigation demand without under or over-allocation.

The ideal solution would be to match the distribution of irrigation water with crop water demand everywhere in the field, and eliminate areas of over-application. Such techniques are called site-specific or variable rate irrigation (VRI) (Bronson et al., 2006; Gossel et al., 2013; Hamer, 1980; Plant, 2001). VRI systems employ computer controlled valves that can apply water in a spatial pattern (referred to as a prescription. Such a system can 'allow growers to maximize their irrigation efficiency while simultaneously minimizing negative effects' (Kim et al., 2009). Various studies have shown water conservation, fertilizer application reduction, and potential economic benefits using VRI. (Hedley and Yule, 2009) showed that 9%-19% water savings can be achieved with VRI. (Koch et al., 2004) demonstrated that up to 46% less nitrogen fertilizer was applied through the use of VRI, resulting in a net return of \$18.21 to \$29.57 ha^{-1}. Modeling

studies have analyzed VRI technology and reported varying degrees of conservation. (Feinerman and Voet, 2000) performed a model economic analysis based on the management zone size, the degree of uniformity and soil properties, concluding that net savings in water and fertilizer are possible in all cases. In a more conservative perspective, (Evans and King, 2012) performed an extensive review of published model studies for VRI, finding that water savings between 0%-26% have been reported.

Technical reviews of the hardware used to achieve site-specific irrigation and some applications of the technology can be found in (Chávez et al., 2010a, 2010b; Kim and Evans, 2009; Perry et al., 2003). Site-specific resource management is accomplished by dividing the field into discrete management zones where the water and fertilizer demands can be managed independently. Differing irrigation levels within each management zone are achieved through an actuated ON/OFF duty cycle of the sprinkler nozzles with the application depth specified as a percentage of full irrigation (determined by flow rate and speed of pivot travel). The effect on uniformity of duty cycle and application depth were tested in a series of systematic catch-can tests (Dukes and Perry, 2006; King et al., 2005; Perry et al., 2004). In each of these studies, it was determined that while lower application depths (relative to the full application rate) led to slightly lower uniformity, this effect was not significant. More recently, (O'Shaughnessy et al., 2013) found similarly good uniformity testing a VRI system under windy conditions; however the authors also indicate that uniformity can be sensitive to the width of management zones. Several studies have investigated the fidelity between the prescribed and actual applied water as a result of VRI. (Sui and Fisher, 2015) tested a commercial VRI system and measured an overall application depth 5% greater than the desired depth. (Perry et al., 2003) performed a catch-can test along a single radial line and found that there was a detectable under-application of water, while the pattern of applied water followed the prescribed pattern in a qualitative manner. (King et al., 2009) performed a catch can test along a single radial line and tested both uniform and

variable applications. They found a correlation coefficient of 0.9 between prescribed and measured quantities of both water and a surrogate fertilizer. (O'Shaughnessy et al., 2011) performed a catch-can test along radial transects and along arcs of constant radius. They found that the coefficient of uniformity within management zones was acceptable (up to 0.88) for zones when application rates were 50% or greater. They also observed areas of overshoot, where the observed application depth was significantly greater than expected after a prescribed step change in application depth. Finally, a series of catch-can tests were performed as a validation of an automated VRI approach in which the prescribed water depth was adjusted in real time with data inputs (Kim and Evans, 2009; Kim et al., 2009; King et al., 1999). In these studies, the correlations between the prescribed and measured water applications were from 0.96-0.98.

In this study, several objectives were identified to quantify VRI performance and efficiency. First, the study design and irrigation prescription attempted to identify the smallest achievable size of management zones. This is facilitated by the identifying a characteristic length scale for each transition as derived from the dispersion equation. Second, the study design maximized the number of transitions of different magnitudes (between prescribed irrigation depths) to address the effect of application depth on performance. A third objective addressed anisotropy between transitions in radial and angular directions. Performance of VRI systems with regard to these parameters begins to inform design criteria for these systems. To address spatial variability, a performance coefficient was described, which expands the concept of the uniformity coefficient. The overarching goal is to determine the spatial scale at which a VRI system can reliably deliver an irrigation prescription.

2.2 Field Methods

The test was performed using a 9-span Valley 8000 Series Center Pivot (Valmont Inc., Valley, NE, USA) with a design flow rate of 3539 l min^{-1}. In the fall of 2012 the pivot was

retrofitted with a Valley Variable Rate Irrigation (Valmont Inc., Valley, NE, USA) package with 30 management zones. This VRI system uses hydraulic solenoid valves to actuate the flow for groups of sprinklers. The number of nozzles per management zone (a single group of sprinklers actuated simultaneously) varied from 7, at the center, to 3, at the pivot end. The VRI system was installed with the maximum number of management zones possible with this manufacturer's VRI system. The hydraulic solenoids operated on the manufacturer's default duty cycle of 20s. Along the pivot (in the radial direction), management zones were 12 m in length. In the direction of

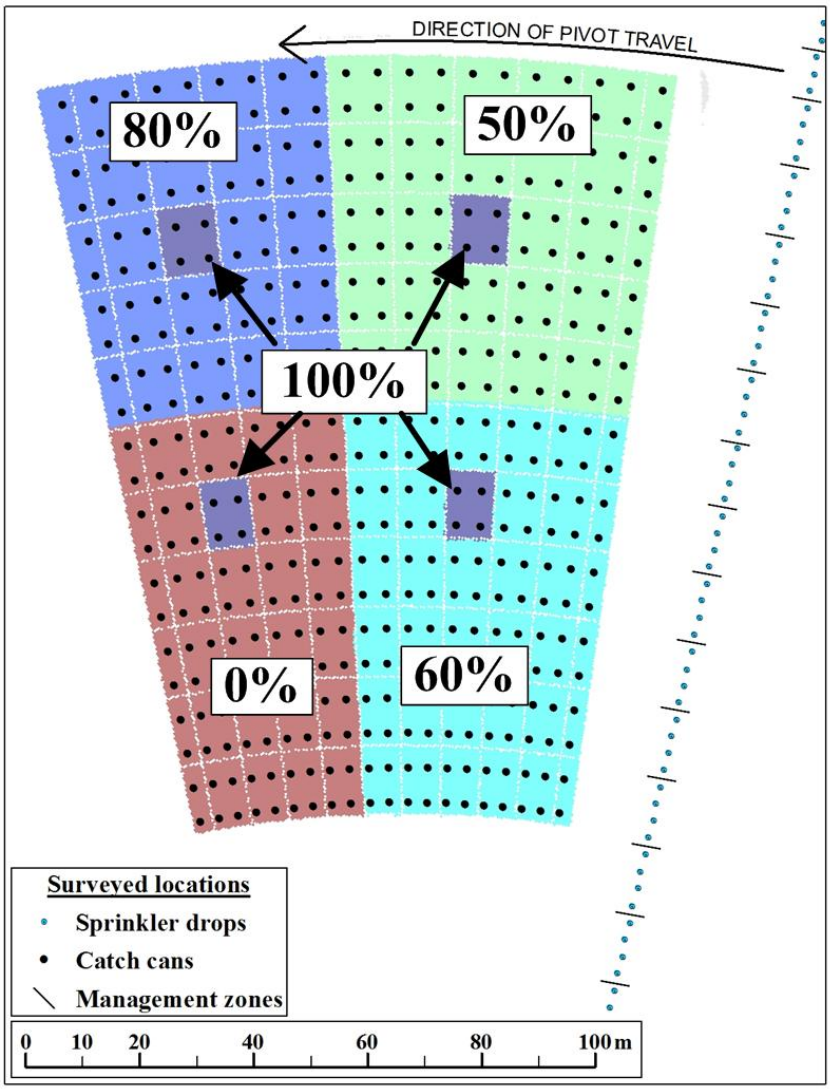

Figure 2-1: Catch can experimental design.
Surveyed location of catch cans, pivot management zones and drop tubes (sprinklers). The color coding of the prescription indicates the percentage of full application. in each quadrant of the prescription.

pivot travel (concentric arcs), management zones covered 2 degree increments, ranging in arc lengths from 6.7 m (at innermost part of study area) to 11.5 m (at outermost extent of study area) (Figure 2-1). The pivot was equipped with Nelson R3000 sprinklers (Nelson Irrigation, Walla Walla, WA, USA) (brown plate) with nominal flow of 29.9 to 44.7 l min^{-1} under the tested area. The sprinklers were attached to weighted drop tubes with sprinklers at 1.8 m height above the ground. The manufacturer reports the sprinkler throw diameter to be approximately 18.9 m at this height and at the pivot's working pressure and flow rate. Each sprinkler had a Nelson Uni-Flo pressure regulator (Nelson Irrigation, Walla Walla, WA, USA) which limited the nozzle pressure to 103.4 kPa.

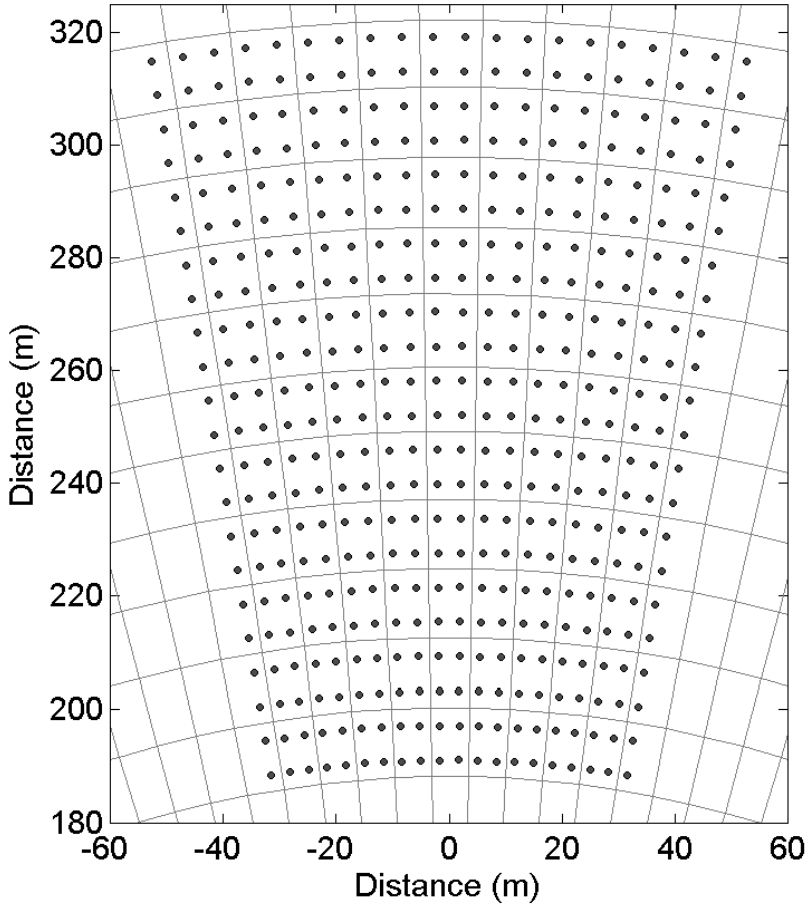

Figure 2-2: Surveyed locations of catch cans and management zone boundaries.
The actual locations of the catch-cans (indicated by circles) and the management zones (bounded by lines) as determined with the GPS RTK site survey.

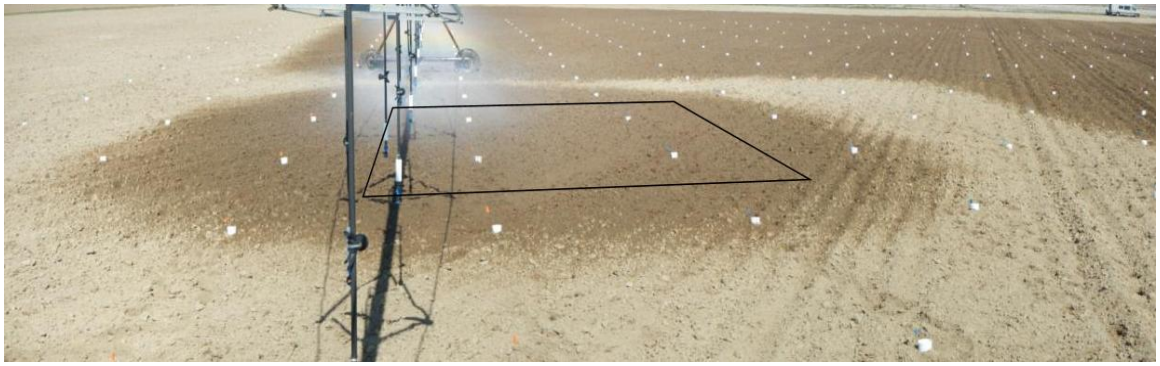

Figure 2-3: Single Management zone during trial

The area within the black square is set to full irrigation depth (100%) while the area immediately surrounding this box is prescribed to receive no water (0%). Radial lines of catch cans (white) proceed from foreground to background. Arcs of catch cans are oriented across the field of view

The study was conducted in an agricultural field in Benton County, Washington, USA. The field was plowed, disked and harrowed prior to the experiment, leaving a smooth surface free of vegetation. Elevation within the test area ranged between 224.1 to 226.8 m above sea level. Weather conditions were generally cold and humid with wind speeds ranging between 0.0 and 4.5 m s^{-1} (mean 1.7 m s^{-1}), temperature ranged between 2^{o}C to 13^{o}C and relative humidity ranged from 30%-70%. Using a regular gridded sample design (Figure 2-2), 440 containers were used to sample the irrigation application depth (2.1 liter polypropylene, 15 cm tall and 15 cm in diameter). These catch cans were placed under the 5th, 6th and 7th spans of the pivot (towards the outer part of the total pivot length) to obtain consistent spacing in both the tangential and radial directions- i.e radial spacing becomes narrow closer to the center. The management zones had three nozzles per management zone in the area where the containers were located. Containers were spaced 6.1 m apart in the radial direction and 1^{o} apart in the angular direction (equating to a range from 5m to 8m in the tangential direction) with the entire array covering approximately 1 ha of the field. The containers were located with a survey grade differential GPS (Topcon HiPer II GNSS receiver, Livermore, CA, USA). Using real-time kinematic (RTK) staking, the sample design was uploaded to the survey, and stakes were placed within 10 cm of their nominal position. Catch cans were then placed and secured with stakes to prevent movement during the

trials. It should be noted that this number of sampling collectors exceeds by at least fourfold all other experiments of which the author is aware. This extensive measurement array was required to capture the 2 dimensional distributions and transitions in the experimental design.

Two tests were performed using identical prescriptions for irrigation depth (Figure 2-4). with color corresponding to the prescribed depth of application (delineated in percentage of full application). During both tests, the pivot was run at 10% of maximum speed with an expected 100% application depth of 33 mm. Between the first and second test, the pivot was walked back to its original position so that it traveled in the same counterclockwise direction for both tests. For both tests the pivot was positioned so that when movement began, the pivot was located more

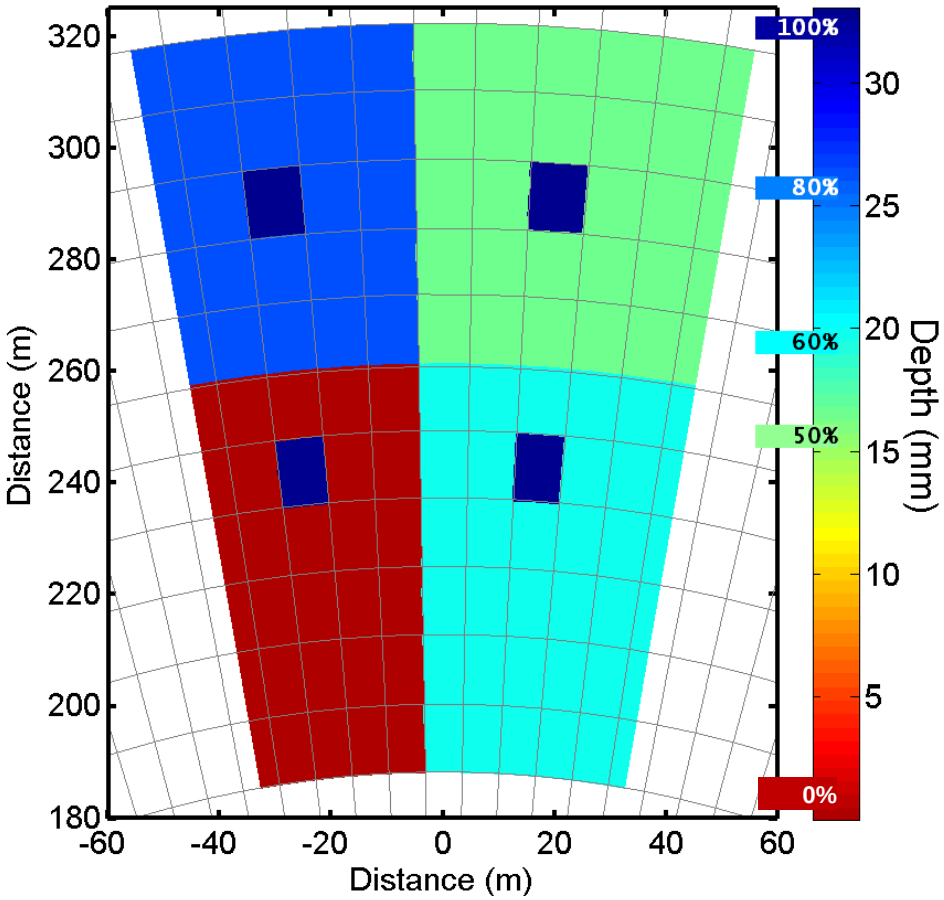

Figure 2-4: Irrigation prescription used for experimental design.
Prescription for the percentage of full application rate to be applied in each management unit. The prescription is divided into four quadrants: red 0% (dry), green 50%, turquoise 60% and med. blue 80%. Within each quadrant an isolated management zone is set to full (100% - dark blue) irrigation, which is a depth of 33 mm.

than twice the distance of the sprinklers' design throw radius away from the first container. The pivot was run until the observed sprinkler throw had travelled beyond the last line of catch cans. Application depths were determined by weighing each container (using an Ohaus CL Series scale with 1 g resolution). Prior to the experiment, each bucket was numbered and the tare weight was recorded. Prior to each trial, the buckets were cleaned of debris and insects, placed in vertical orientation and staked in place. Buckets were lidded once they were observed to be outside the visible sprinkler throw. After the experiment, the applied depth was calculated using the measured mass, density of water, and diameter of the container's opening.

The prescription was designed to address three study objectives. A broad range of step changes in application depth were incorporated into the prescription, so that adjacent zones receive applications rates differing by 10, 20, 30, 40, 50, 60, 80 and 100%. Step changes in application depth occurred in both the radial direction and in the direction of pivot travel. The prescription included an experimental control (areas prescribed to receive 0% application rate) and a range of spatial scales of application from 6 by 5 management zones down to a single management zone. The smallest scale is represented by a single management zone of 100% application located in each quadrant. The resulting wetting from irrigation in a single management zone (of 100% application rate, located within the 0% control quadrant) is visible in the site photograph taken during trials (Figure 2-2 and 2-3).

2.3 Results and Discussion

The measured application depths from trials 1 and 2 reflect the prescribed depths for the large areas, but diffuse transitions obscure smaller areas in each quadrant (Figure 2-5). Data points without color indicate missing data. Missing points and outliers accounted for less than 1% of the data in trial 1 and 2% in trial 2. Overall, the pattern of applied water tracks the pattern of the prescription (Figure 2-4). In trial 1, there appears to be a secondary transition in the 80% section

(upper left quadrant). This may be a relic of factors related to the pivot line pressure, or to the water main pressure or flow rate. Another possible explanation may be a switch between operational modes of the pivot controller. When all management zones are set to the same level (such as 100%, 80%, etc.), the pivot regulates water delivery by pivot speed, rather than by cycling valves open and closed. However, the cause of this anomaly is unknown and was not apparent in the second trial.

Overall, the measured water depth is less than the prescribed water depth in most areas. In particular, the prescribed 100% management zone within the area of 0% application is substantially under-applied. On a global average, the applied water is ~7% less than the prescribed amount (statistically significant $p<0.05$ using a 2 tailed t-test). When the data are conditionally sampled on prescribed water depth, all areas (except the control area of 0% application) were statistically different from the prescription at the $p<0.05$ level due to the under-application of water. Similar under-application for VRI systems was also found by (Perry et al., 2003).

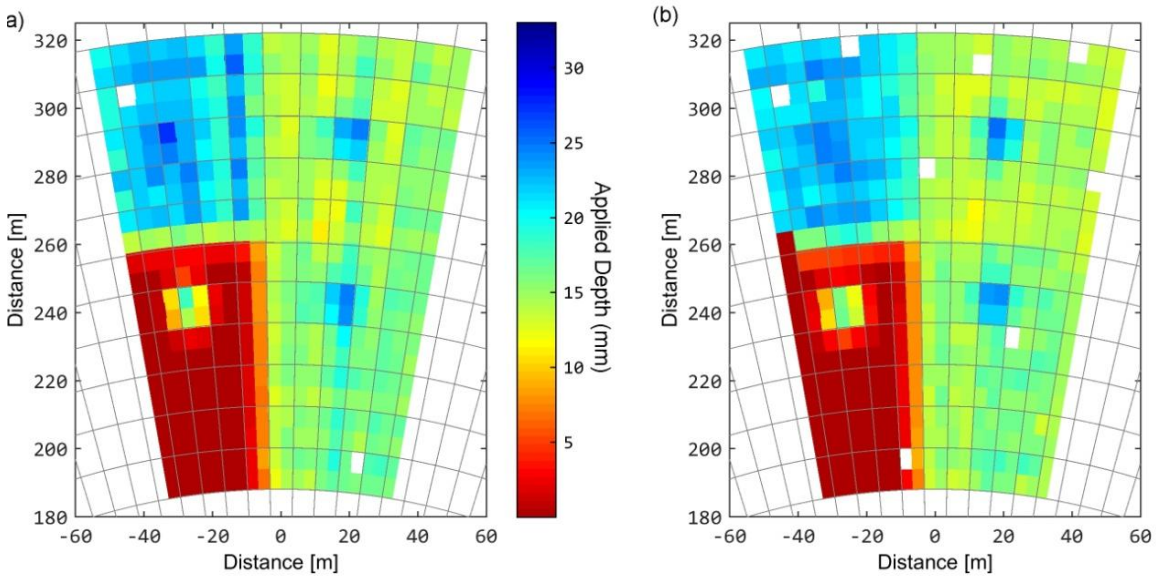

Figure 2-5: Applied irrigation depth measured by the catch can array.
Color indicates measured application depth for trial 1 (a) and trial 2 (b).

Further statistical analysis was performed on the data to verify that the measured depths are significantly different in the different prescription areas. All permutations comparing regions of different depths (100%, 80%, 60%, 50% and 0%) were checked to verify that VRI delivered statistically different water depths across the experimental area as expected. All measured zones were statistically different at the $p<0.05$ level. Thus, the pivot was capable of providing statistically different water depths at 10% increments.

The difference between the measured and prescribed irrigation depth is positive with over-application, and negative where under application occurred (Figure 2-6). The samples locations with the greatest difference between the measured and prescribed depths occur near the transitions between zones with different application rates. Further, the magnitude of the difference appears to be a function of total step change in prescribed water depth. This is most apparent at the boundary between the 60% and 0% regions, and at the boundary between the 100% and 0% regions (figure 2-1). Relative to the prescribed water depth, the former transition represents the greatest over-application; while the latter represents the largest under-application of water.

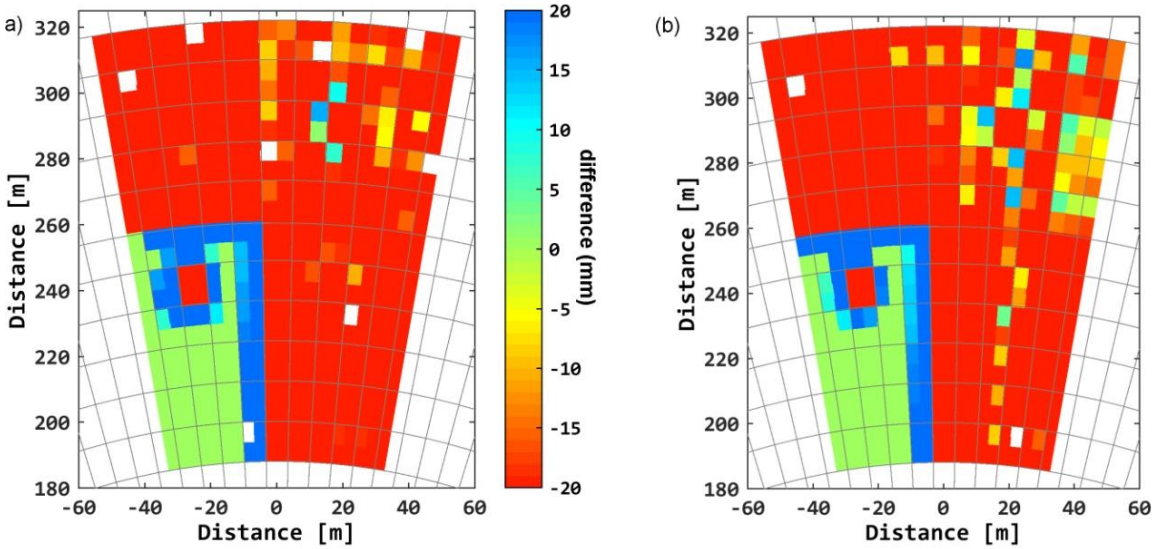

Figure 2-6: Difference between measured and prescribed application depth.
Negative values (red) indicate under-application, positive (blue) is over-applied. Trial 1 (a) and trial 2 (b).

To evaluate the performance of the pivot in quantitative terms, a new 'performance coefficient' is derived following the approach of (Heermann and Hein, 1968) who demonstrated the coefficient of uniformity for center pivot systems. By following their approach, and replacing the measured average depth with the prescribed water as the comparator, a new coefficient is defined as

$$C_p = 1 - \frac{\sum_i \left| r_i D_i - r_i P_i \right|}{\sum_i r_i D_i}, \qquad \text{Eq. 2-1}$$

where r_i is the distance along the boom associated with each sampling location (catch-can), P_i is the prescribed water depth at each catch-can and D_i is the measured water depth at each catch-can, with *i* the summation index (for each catch can). Here it is assumed that the catch-cans are equally spaced in the radial direction. This assumption was relaxed following the approach of (Marjang et al., 2012). The performance coefficient can be evaluated along lines of catch-cans arranged in the radial direction, or along arcs of catch-cans arranged at a constant distance from the pivot center. In this study, both radial lines and arcs were employed for a two-dimensional analysis.

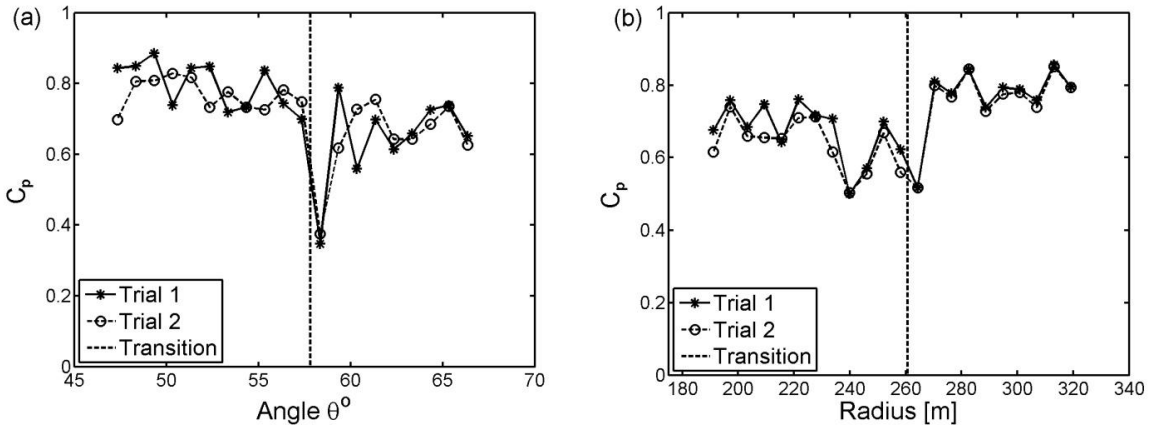

Figure 2-7: Performance coefficient and position across prescribed transitions
Performance coefficient as a function of pivot angle (a) and radius (b) shows a strong degradation in performance near transitions between differently prescribed water levels (denoted by the vertical dashed line).

The performance coefficient can be calculated for each position (radial distance from the pivot center and angular displacement from arbitrary “north”), showing that diffusion causes diffuse boundaries between the prescribed depths (Figure 2-7). It is apparent that the locations at significant transitions in prescribed water depths have the largest deviation from the prescribed depth. This is consistent with the previous observations (Figure 2-6). This is expected, as field conditions prevent the perfect reproduction of the prescribed sharp transitions - sprinkler throw, wind dispersal, and the random nature of dispersion all create “fuzzy” edges. In mathematical terms, smoothing of an expected depth at the prescribed sharp transitions can better describe these boundary areas. The fuzzy boundary is a result of diffusive transport from the sprinklers; diffusion generates a characteristic distribution (in time or space) described by Fick’s law. Following standard dimensional analysis, a characteristic length scale is used here to determining the minimum management scale of the VRI pivot (derivation shown in Appendix A). The distribution of the measured irrigation depth across these boundaries is used here to estimate the minimum feasible size for a management zone.

Measured water depths near the transitions in the prescribed water depth (both in the radial and angular directions) were isolated and analyzed (Figure 2-8). Samples located within 10 m of more than one transition, such as those at the very center of the measurement array, were excluded from this analysis. In each case, the data tend to a smooth profile from one application depth to another. This behavior suggests that a redistribution process similar to dispersion may be an underlying mechanism at transitions. Just as the throw diameter of a nozzle defines an area receiving an acceptably uniform application depth, the solution to the diffusion equation (Eq. 2-2) describes the pattern of dispersal observed in the transitions.

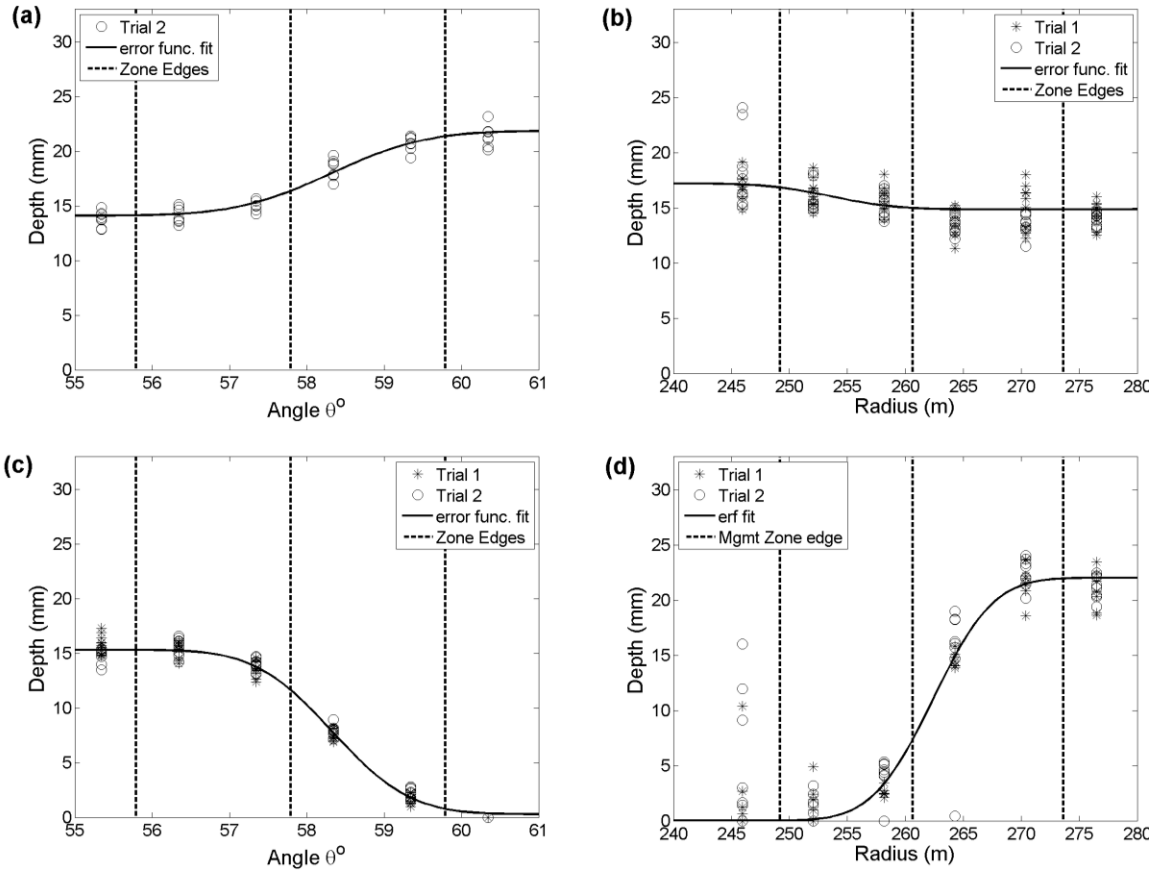

Figure 2-8: Measured application depths near the points of transition
(a) transition from 50% to 80% (b) transition from 60% to 50%
(c) transition from 60% to 0% (d) transition from 0% to 80%.
The solid black lines are the empirical fits (using non-linear least squares optimization). Dashed lines are the boundaries between management zones.

A transition in a single dimension that is driven by a dispersive process is described by

$$\frac{D(x)-D_{min}}{D_{max}-D_{min}}=\frac{1}{2}\left(-\text{erf}\left(\frac{x-a}{\sqrt{2\sigma^2}}\right)\right) \qquad \text{Eq. 2-2}$$

where D(x) is the application depth as a function of position (x), D_{max} is the maximum application depth across the transition, D_{min} is the minimum application depth across the transition, *a* is the position at which the transition occurs, and σ is a "characteristic length" of the transition (see Appendix A). This is a characteristic length in the same sense that the standard deviation describes the half height, half width of a Gaussian distribution. By defining the wetted area in terms of a characteristic length, a spatial distribution of applied water (with a known confidence

interval) can be determined from samples of measured depth. Note that advection (wind drift in this case) is neglected in Eq. 2-2. If wind drift is significant, it can be included in Eq. 2-2 with a variable transform following(Fischer et al., 1979). Non-linear least squares optimization (Matlab function 'nlinfit') was used to find the optimal value of σ for each one-dimensional transition (Table 2-1) and the resulting fitted function for each case are plotted with the actual data point in Figure 2-8.

The average of these length scales is 4.15 m. From this analysis, there is no discernible dependence on the magnitude of the transition. The dispersion profile has been reduced to a non-dimensional form, strengthening the case for independence (Eq. 2-2). The results suggest that there may be a dependence of the transition length scale on the radial position. When the transition length scale for each arc is computed independently, no pattern emerges to suggest that the length scale depends on radial position (results not shown).

Transition	Orientation	Length scale, σ
60% → 50%	Radial	4.4 m
60% → 80%	Angular	5.0 m
50% → 0%	Angular	3.1 m
0% → 80%	Radial	4.1 m

Table 2- 1: Length scales for transitions in applied depth of irrigation.
The values of the transition length scale is determined by fitting Eq. 2 to the data. Plots of the data and function fits are shown in Figure 8

The 100% application island (Figure 2-4) in the lower left shows 100% application cannot be achieved given the measured characteristic length scale of the pivot. In effect, dispersion transports water out of this zone, resulting in local under-application. This is due to the small area relative to the proximity of transition, i.e. the small unit has a small ratio of area to boundary length. Consequently, the best achievable application depth in a single management zone of this size is less than the initial prescription. The local under-application of water in this zone occurs

because the 100% management zone is not independent of neighboring management zones. A single management zone of this size (approximately 12m by 12m) is too small to prescribe a set water level.

To determine the minimum size of a management zone that can be independently managed, prescriptions were generated that mimicked the case of an isolated area that was different from all surrounding neighbors. Then this prescription was convolved with Eq. 3. The resulting function describes the best possible application depth at the center of the management zone. By defining the best achievable depth in terms of a management unit size, and defining an acceptable degree of uniformity, the smallest unit size can be found. Figure 2-9 shows the results of varying the relative difference in application depth between the isolated management zone and its surroundings, the absolute magnitude of application depth, and the characteristic length scale. The performance asymptotically approaches unity as the management zone size increases (Figure 2-9). Δh_{max} is the difference between the maximum depth at the center of the isolated management to the depth in surrounding zones (far from the transition). The change in prescribed depth across the transition is $\Delta h_{prescribed}$, and the ratio of these two differences is used here as a proxy for local performance. L is the length of the edge of a square management zone, and σ is the characteristic length scale. When a management zone is perfectly independent of its neighbors, the ratio $\Delta h_{max}/\Delta h_{prescribed}$ is equal to 1. A ratio $\Delta h_{max}/\Delta h_{prescribed} = 0.99$ reflects an acceptable level of performance and uniformity within each management zone, although Figure 2-9 can be used to determine minimum management zone sizes reflecting any depth ratio. Corresponding to a value for $\Delta h_{max}/\Delta h_{prescribed}$ of 0.99, $L/\sigma = 5.6$. Taking $L/\sigma = 5.6$, and $\sigma = 4.15$, the smallest management zone achievable for the pivot under investigation is 23 m. Note that the minimum management scale is about 20% larger than the manufacturer's specified throw diameter (~19 m) of the Nelson R3000 brown plate sprinklers.

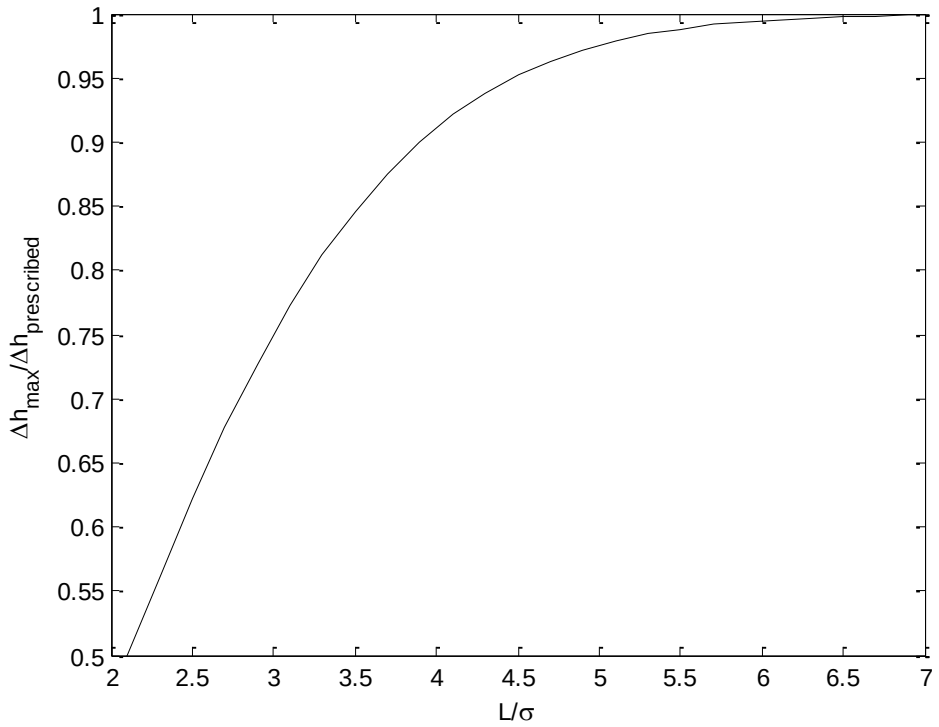

Figure 2-9: Characteristic length scale, L/σ, of the VRI system

The ratio of best achievable application depth change to prescribed depth change, $\Delta h_{max}/\Delta h_{prescribed}$, is a function of the management zone size and the characteristic length scale, L/σ, of the pivot. This plot is used to determine the smallest independent management zone that is effectively isolated from its neighbors.

The measured minimum management zone size is specific to this pivot with the current set of nozzles, but the approach outlined above is general to any sprinkler based precision irrigation system. Since the characteristic length scale does not depend on position, direction or change in prescribed depth, it need only be measured in one direction across a single transition. A standard catch can test with a single line of catch-cans is sufficient as long as there is a single, detectable transition along this line. Eq. 2 can then be used to fit the sample data and determine the characteristic length scale. Given an acceptable cutoff ratio of $\Delta h_{max}/\Delta h_{prescribed}$ the measured characteristic length scale can then be used in conjunction with Figure 2-9 to determine the minimum management zone size to be used in VRI system design or when optimizing a variable rate prescription.

2.4 Conclusions

Two trials of a catch-can test were performed measuring the performance of a VRI enabled center pivot. The pattern of applied water generally followed the prescribed pattern, however there was a bias toward under-application by about 7% (statistically significant at $p<0.05$). The effectiveness of VRI was described with a new performance coefficient. Performance of the VRI system was diminished near step changes in the prescribed water application. Further investigation revealed that the applied water followed a dispersion profile with an average characteristic length scale of 4.15 m. The resulting minimum management zone size was determined to be 23 m for the system under investigation.

The approach outlined above can be conducted to find the characteristic length scale of a VRI system with a traditional catch-can test. A single ray of catch-cans combined with a prescription that contains one transition in applied water depth is sufficient. Once the characteristic length scale is known, the minimum management zone size can be found using Figure 2-9, or calculated as $5.6\ \sigma$ with a performance coefficient approaching 0.99.

The identification of the 23 meter minimum management scale defines the data resolution required for effective precision irrigation systems. Information about the spatial variability of crop water demand needs to be resolved to this scale if precision irrigation is to achieve the potential efficiency improvements suggested in the literature. Furthermore, resolving crop water demand data to scales finer than this minimum scale is not useful, at least with existing VRI systems.

3. Accuracy of an Extensive, High Resolution Soil Mapping Method

Many technical solutions are offered to farmers that can theoretically increase water use efficiency, economize material inputs, and improve yields. In practice, it is difficult for farmers to accurately evaluate the utility and cost effectiveness of these technologies. Information technology is one type of technical solution, and includes management software, sensor systems, and communication technology. When implemented successfully, all of these can aid farmers in making better management decisions. However, this class of technology can be the most difficult for farmers to utilize in real time decisions because it is difficult to independently validate the reliability and accuracy of the methods. High resolution soil mapping is one example of information technology, and can guide improved irrigation, fertilization, and other management decisions. Very high resolution (<10m) soil mapping is now a service offered by several vendors, and is used to measure the spatial distribution of a wide variety of parameters, including nitrate and micronutrients, soil pH, texture, and water holding capacity. While farm managers may have a very good general sense of soil properties in the field, spatially explicit determinations, especially of those parameters which change over time, are usually addressed by over-application of water, fertilizer, or other inputs, to prevent loss of yield in the most depleted areas of the field. To use soil maps to reduce inputs, farmers need confidence that soil maps accurately reflect field conditions. Mapping by measuring the soil's apparent electromagnetic conductivity (EC_a) allows generation of high resolution maps, but requires establishing a field specific relationship between the EC_a and soil properties of interest. In this study, high resolution maps of EC_a were compared to co-located physical samples. To evaluate that confounding effects from soil properties were not responsible for spurious correlation, correlation and principal component analysis were used to describe variability in both the EC_a measurements and soil samples. A conditional sampling approach was used to find possible factors in high and low correlation. All field methods and data used in this study were commercially available and comparable to methods generally

available to farmers. We demonstrate that soil chemical properties in these three fields strongly influence the accuracy of soil EC_a mapping in predicting soil texture. The analysis shows that soil properties may confound the use of EC_a to determine soil texture. A few simple qualifiers are identified that can help farmers determine if EC_a mapping is reliable under their specific field conditions. The analysis also shows that quality control can identify problematic measurements and potentially improve data in post-processing. In summary, the study shows that soil mapping by EC_a can be a useful tool for describing within field variability in practical applications, but that a number of conditions and checks must be applied to ensure validity.

3.1: Background

Maps of water demand variability (within an irrigated field) are an essential component in a precision irrigation system. VRI systems are capable of applying spatially variable amounts of water to areas as small as 0.1 ha. To utilize this capability requires information of a similar resolution (~30m), so that appropriate water application prescriptions can be generated that deliver adequate irrigation without over application . Differences in soil properties such as texture, organic matter, and water holding capacity are factors in water demand variability. Because of this, maps of soil properties are a key input for irrigation decision support systems. Verifying the accuracy of soil information and maps is a necessary step towards successful implementation of precision irrigation management.

Characterization and mapping of soil characteristics are intrinsically difficult due to variability in soil, which exists at many spatial scales, both in horizontal distribution and vertical profiles (Miller, 2012). Traditional sampling and mapping techniques are often labor intensive, requiring excavation of physical samples and soil profile pits, and depend on trained soil scientists. Alternately electromagnetic properties of soils can be measured non-destructively and repeated EM measurements can be obtained at relatively low cost (Doolittle and Brevik, 2014). First used in mining survey (Smith, 2014), measurement of EM properties is part of several

standardized soil methods (Anderson-Cook et al., 2002; Johnson et al., 2003; Toushmalani, 2010). The electromagnetic induction method uses a pair of coils to measure the apparent electrical conductivity (EC_a) of the soil. Using a powered transmitting coil, a magnetic field induces electrical current through the soil profile. The secondary magnetic field generated from these currents is measured by a receiver coil. The soil EC_a is then determined by the relationship between the difference in field strength between the primary and secondary coils (Davis et al., 1997).

Soil EC_a value is strongly influenced by soil properties such as soil texture, water content, temperature, and salinity (Corwin and Lesch, 2005). Other soil properties such as cation exchange capacity (Triantafilis et al., 2009), organic matter (Martinez et al., 2009), pH (Dunn and Beecher, 2007), bulk density (Brevik and Fenton, 2004), ionic composition (McBride et al., 1990), CaCO3 content (Vitharana et al., 2008), salt concentration (Halvorson and Rhoades, 1974; Kaffka et al., 2005), and top soil depth (Rhoades and Corwin, 1981) have also been studied as factors influencing conductivity. Soil EC_a has been used as a surrogate for many the above properties in agricultural practice to guide seeding, fertilization, and irrigation. Several of these studies cited above highlight the challenge in correlating a single physical variables of interest with soil EC_a, and that confounding factors may affect EC_a measurements in those soils where multiple soil characteristics (Heil and Schmidhalter, 2012). Interaction of soil properties can generate a combined effect on the measured EC_a, leading to inconsistent correlations with targeted soil properties (Corwin and Lesch, 2005).

Nonetheless, EC_a mapping has proved to be effective for several applications: refining NRCS soil maps (Doolittle et al., 2008); verifying crop yield maps (Anderson-Cook et al., 2002); mapping soil water content (Brevik et al., 2006); coordinating direct soil sampling (Shaner et al., 2008); exploring scaling in soil heterogeneity (Heil and Schmidhalter, 2012; Saey et al., 2013). In soil with absence of salinity or with low solubility salts, it has been shown that EC_a can be

used to capture soil texture and soil moisture content information (Brevik et al., 2003). However, there has been fewer reviews of EC_a mapping as applied in precision irrigation. For precision agriculture applications, end users require robust verification to assure proper allocation of expensive or limited material inputs such as fertilizer and irrigation. To ensure that the EC_a method can produce high quality, accurate soil maps in complex soils, simple correlative relationships must be checked for confounding effects from non-target parameters.

In previous studies that examined the quality of EC_a maps, soil core samples taken after mapping were used to establish correlation between EC_a and target soil properties such as clay content, organic carbon, water holding capacity, and crop yield. A sufficient number of samples must be taken to characterize the full range of soil variability, although this is typically cost prohibitive in commercial applications. To remain cost effective, a typical sampling strategy collects ~30 samples for a 50+ ha field. Ideally, the soil samples themselves should include the full spectrum of variables that can influence the EC_a map, and represent the range of variability of each parameter within the field. For instance, clays with a higher cation exchange capacity such as montmorillonite, illite, or vermiculite result in higher EC_a values as they have a stronger ability to hold cations. However, a limited number of samples cannot fully represent the spatial variability of the soil, and correlation is typically based on a relatively small number of subsets, rated on a three point scale of high, medium, and low values of EC_a.

In this study, soil EC_a maps of three irrigated fields were evaluated to verify their suitability for informing precision irrigation decisions.. These fields all contained areas with some type of calcic soil. In each of the three fields, 126-137 samples were collected concurrently with EC_a mapping, and 31 soil physical and chemical properties were examined to identify factors that affected the accuracy of the EC_a mapping. The accuracy and repeatability of EC_a mapping is also explored through the development of a self-consistency protocol. This procedure can be also be used to post-process the EC_a data, removing and interpolating between problematic

measurements. The result of this study predicts the likelihood of mapping robustness and reliability under certain soil conditions. More generally, this approach should be employed before directly incorporating mapping information into precision agriculture applications.

3.2: Project Context

Validation of soil maps generated from electromagnetic resistivity data was part of an ongoing research project on precision irrigation coordinated by the Northwest Energy Efficiency Alliance (NEEA). The soil mapping experiment was conducted on three large irrigated fields (>50 ha) in arid regions of Oregon and Washington. In addition to soil characterization, the overall study includes long term monitoring and demonstrations of variable rate irrigation (VRI) systems (Chapter 2), measurement of electricity and water use, yield mapping, and economic feasibility assessment. The overarching goal of the project is to evaluate methods to improve water use efficiency and reduce power consumption. Maps of plant available water (PAW) are a critical piece of information used to implement irrigation scheduling (Figure 3-1), but these maps do not convey certainty or explicitly state uncertainty about the method used to derive PAW. In practice, PAW is derived from soil textural properties- percent sand, silt, clay, and organic matter (Saxton and Rawls 2006). Ideally, maps are resolved at the scale of tens of meters, corresponding to the scale of VRI management units. Soil maps available from the National Resource Conservation Service are only guaranteed to be accurate at much coarser scales[1]. PAW provides the basis for timing and depth of irrigation, and mapping the water holding capacity of the soil at smaller scales improves efficiency by allowing redistribution of irrigation from over-applied to under-applied areas. Previous EM maps of soil texture contracted by NEEA had proved to be accurate in some fields, but for unknown reasons, had been unreliable or completely inaccurate in other fields.

[1] Soil Survey Staff, NRCS/USDA. Web Soil Survey. http://websoilsurvey.nrcs.usda.gov/.

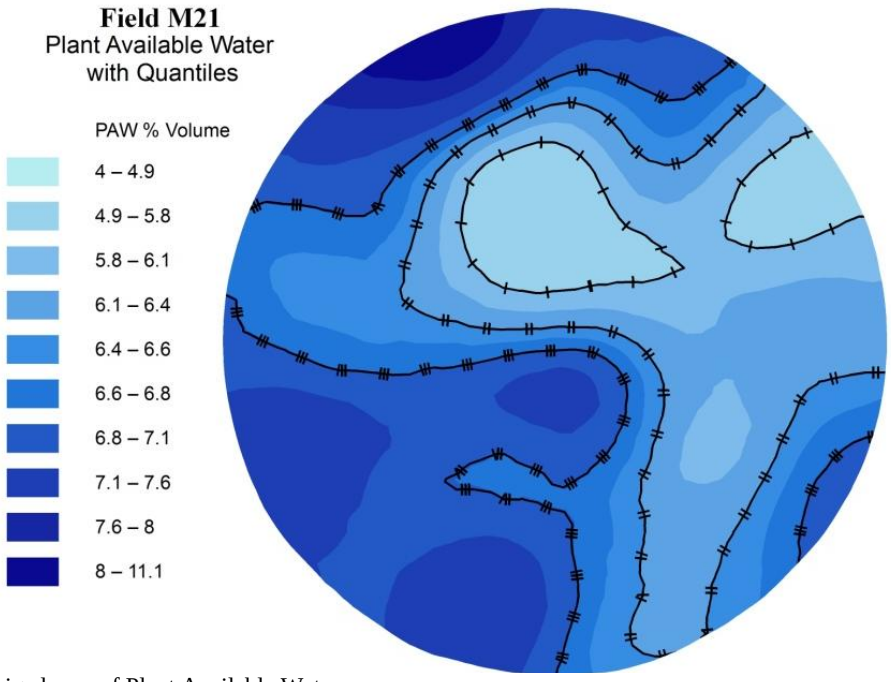

Figure 3-1: Kriged map of Plant Available Water
PAW value was determined from sampled soil texture, using method of Saxton and Rawls 2006.

3.2.1 Description of field sites

The three fields under investigation are located on the Columbia River plateau. Field B207 is located in Benton County, Washington; M54 and M21 are located in Umatilla County, Oregon. Mapped soil types in the three fields are loamy fine sand or sandy loams, and approximately half of B207 is mapped as silt loam. All are well drained, unconsolidated soils that are primarily alluvial, with eolian inclusions. Profiles are mostly deeper than 1m, although soil can be shallow along terraces. Slopes vary from 0-30%. All profiles have a calcic horizon starting at a depth of 40-120cm, and all soils are slightly to strongly alkaline. Duripan is present in some profiles coincident with calcic horizons, and a plow pan is found throughout the fields. Soil series by field are: field M21 (Figure 3-2), Quincy loamy fine sand (majority), Adkins fine sandy loam, and Taunton fine sandy loam; field M54, equal areas of Quincy fine sand and Burbank fine sand; field B207, Warden silt loam (majority), Warden very fine sandy loam (NRCS, 2014). All fields have been irrigated for at least twenty years, and were previously cultivated for dryland crops for several decades prior to the installation of pressurized irrigation systems.

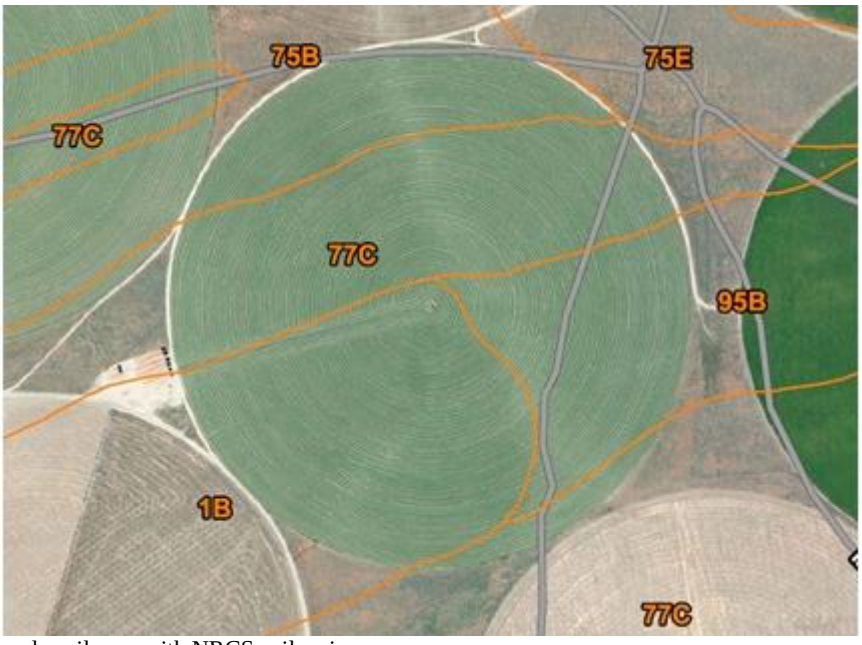

Figure 3-2: Example soil map with NRCS soil series.
An aerial photograph of M21 is superimposed with the SSURGO map of soil type. Soil series shown are 75B & 77C : Quincy; 1b Adkins; 95B Taunton. Aerial Imagery Source NAIP (2011)

3.2.2 Field Data Collection

This study evaluated reliability of soil maps generated under normal field conditions using commercial mapping products in the format and quality as normally available to farmers. Physical soil samples were collected by a farm consultant and characterized by a local agricultural soil testing laboratory. EC_a data was collected by two different vendors. Data deliveries included some additional information not generally included with products that are available to farmers, and additional correspondence with the soil lab and contractors helped verify reported values. However, the maps used in this study are essentially in the same format and of the same quality as those available to end users.

Both vendors used the EM38 (Geonics, Canada) to collect EC_a data. The EM38 is a non-contact instrument in a nonconductive housing that is drawn over the field in a series of parallel transects. In fields M21 and B207, these transects were spaced 10m apart; in field M54, transects were spaced 20 m apart. The instrument uses a double dipole configuration which yields

Figure 3-3: Geonics EM38 and towing assembly
The EM38 is dragged over the entire field in parallel transects, measuring EC_a at regular intervals.

measurements of EC_a averaged over 50 cm and 1 m depths independently. The speed of travel is variable but results in a measurement resolution of 5-10m along the transects. The moving instrument platform also includes a GPS which records the location of each measurement. The final result is a map of EC_a resolved to ~10m at 2 depths. EC_a data was delivered by contractors in shapefile format, with EC_a measurements for subsoil and topsoil. Data for field M54 included records of speed, heading and other supporting metadata.

Figure 3-4: Typical sampling plan for lab test soil samples.
Regular (hexagonal) grid spacing 60-70 m, with red dots indicating sample locations.

Sample data from standard physical and chemical tests were used as the basis for comparison with EC_a data. A regular sampling pattern (Figure 3-4) was designed to maximize areal extent for the given number of laboratory tests (126 samples each from M21 and M54, 137 samples from B207), and without making any assumptions about the spatial scale of variability in the soil. Small scale variability (<50m) could not be captured with this sample design while maintaining this extent. However, irrigation and cultivation management operates on a scale approximately the same order of magnitude as the sample spacing; it is impractical to address finer scale variability with VRI and current farming practices. Coordinates of sample locations were generated in the GIS software, and located with a handheld GPS to within 5 meters of the designated locations during sampling acquisition.

Core samples were collected from 15 to 46 cm (6 inches to 18 inches) depth, and each sample was composited from all depths. Laboratory tests reported the following parameters: base ions (Mg, K, P, Ca, Na), total base ions, base saturation, cation exchange capacity, texture (sand, silt and clay content), organic matter, nitrate and ammonium, pH, salinity, micronutrients (B, Zn, Fe, Cu, Mn, S), wet and dry sample weight, moisture content and dry matter. Analyses were conducted by AgSource Laboratories[2], following the Soil, Plant and Water Reference Methods for the Western Region (Gavlak et al., 2003). Soil parameters reported by the lab were joined to sample locations in a geodatabase using GIS software.

Project coordination, data management, and spatial analysis was conducted using ArcMap version 10.1, using coordinate geometry (COGO) tools, Spatial Analyst and Geostatistical Analyst toolboxes (ESRI 2011. ArcGIS Desktop: Release 10. Redlands, CA: Environmental Systems Research Institute). After initial visual inspection for transcription errors, all data was stored in the GIS database, and locations were re-projected to a common coordinate system (NAD83/UTM zone 11N). For the analysis, subsets of EC_a points in each field were identified in

[2] AgSource, 323 6th St., Umatilla OR 97882. *www.agsource.com*

which measurements were repeated in close proximity (<10m). EC_a measurements were also interpolated using kriging (universal model in ArcMap toolbox *spatial statistics*) to allow comparison between co-located physical soil samples and EC_a values.

3.3 Spatial Analysis Method and Results: Self-consistency of EC_a

The first step in evaluating the validity of the method was to establish repeatability and stability of direct EC_a measurements. Within each field, calibration of the EM38 instrument was only performed once. This calibration is required to adjust for a number of physical parameters, particularly temperature of the instrument, air, and soil. Physical construction of the instrument is designed to minimize other confounding factors, but some do remain. (Sudduth et al., 2001) evaluated sensitivity of EC_a measurements from a mobile platform, including sensitivity to speed, acceleration, and drift over the measurement period, and suggested a number of quality control measures to assure consistency. Data used in this study included quality control (QC) checks that were performed in post processing, although QC methods were not explicitly stated in the data reports received by the authors. To determine the degree of self-consistency within each field, the distribution of measurements of were evaluated for drift and, where possible, for covariance with other meta-data (such as speed of the moving platform).

When EC_a data is viewed in a map, there is an apparent bias towards higher values at places where the instrument has changed heading or speed (Figure 3-5). To check the repeatability and internal consistency of EC_a measurements and to identify any bias, co-located EC_a points (places where measurements were repeated) were evaluated on the basis of available metadata, including location, point ordering, and when provided, speed and heading.

3.3.1 Outliers- factors related to a moving platform

Data collected for field M54 included additional supporting metadata, including

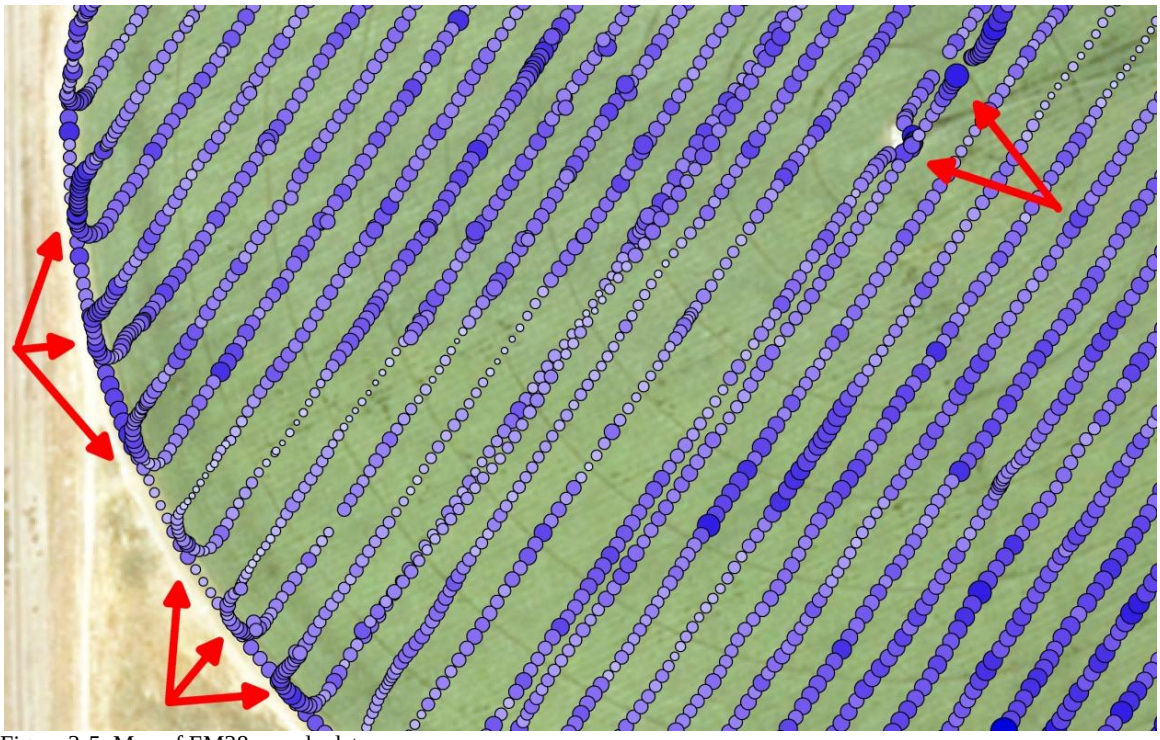

Figure 3-5: Map of EM38 sample data.
EM point measurements have been scaled and colored by value. Red arrows indicate anomalous increases, hypothesized to be associated with change of speed or change of direction of the EM38.

instantaneous heading and speed measurements derived from GPS. In data from this field, there were anomalous spikes up to 500% of surrounding EC_a values, assumed to result from instrument error. To identify potential outliers on the basis of EC_a value alone, these were binned and plotted on a log vertical scale (Figure 3-6). The log scale isolates single outlier values, and it is straightforward to identify a reasonable cutoff for possible outliers (in this case , values above 20 for Dipole 1, and above 24 for Dipole 2 were flagged).

Plotting EC_a values directly against speed or heading did not clarify a likely relationship – scatter among the points was too great to distinguish any pattern among outliers (not shown). To detect any patterns, EC_a, speed, and heading data was treated as a continuous signal, and changes were detected as fluctuations in this signal, ie $EC_a' = EC_a(x) - \overline{EC_a}$, in which an overbar is the local mean value (x) is the measurement at one location, and the prime (x′) indicates a fluctuation from the mean. A local (running) mean and fluctuations were calculated for

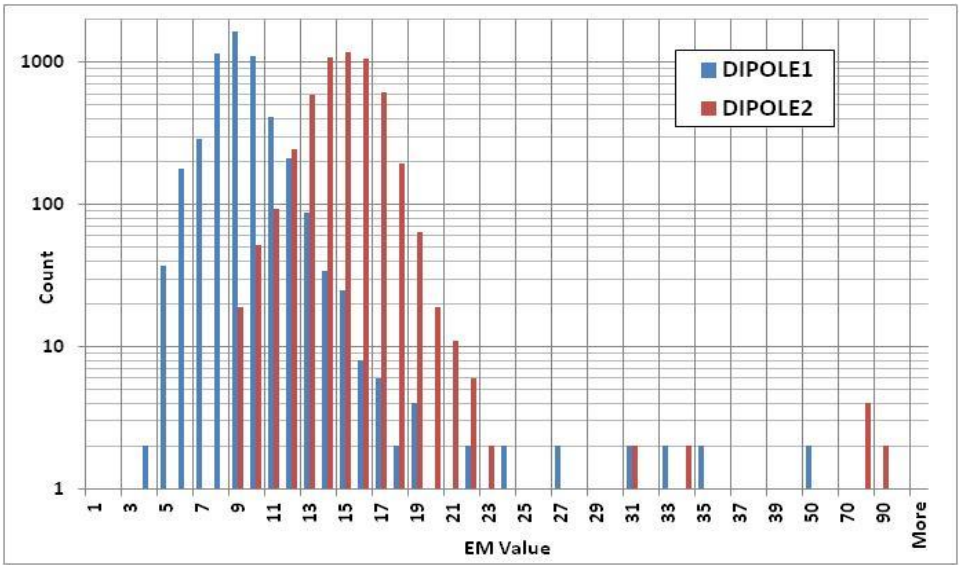

Figure 3-6: Histogram of EM value from field M54,
Outliers for Dipole 1 (deep) and 2 (shallow) were identified as being <20 and <23, respectively. Note that vertical scale is logarithmic.

averaging periods ranging in length from 10 to 150 counts. For brevity, only plots from averaging 150 measurements are shown.

Figures 3-7 and 3-8 show EC_a fluctuations for field M54, plotted against speed (actual value) and against fluctuations in heading (indicating a change in direction of travel). Outliers identified by EC_a value in the log scaled histogram are circled. In both cases, outliers are clustered. In Figure 7, the majority of outliers occurred at one speed (5.4-6.3 m/s, 12-14 mph). Although this may indicate that measurements taken at high speed may be problematic, this is not the highest speed, and a clear relationship is not evident. In contrast, figure 8 shows outliers clustering strongly at the most extreme changes in heading. This indicates that measurements taken while turning the platform may be problematic, and confirms the observed patterns in the scaled data map (Figure 3-5). The histogram of EC_a readings in field M54 indicates outliers that are corroborated by physical measurements taken while the instrument is moving. Similar outliers were not apparent in the distributions of EC_a readings in field M21 and B207. Whether this is related to difference in operator technique or because outliers were removed in post-processing, the removal of outliers from field M54 was a simple method to improve data quality.

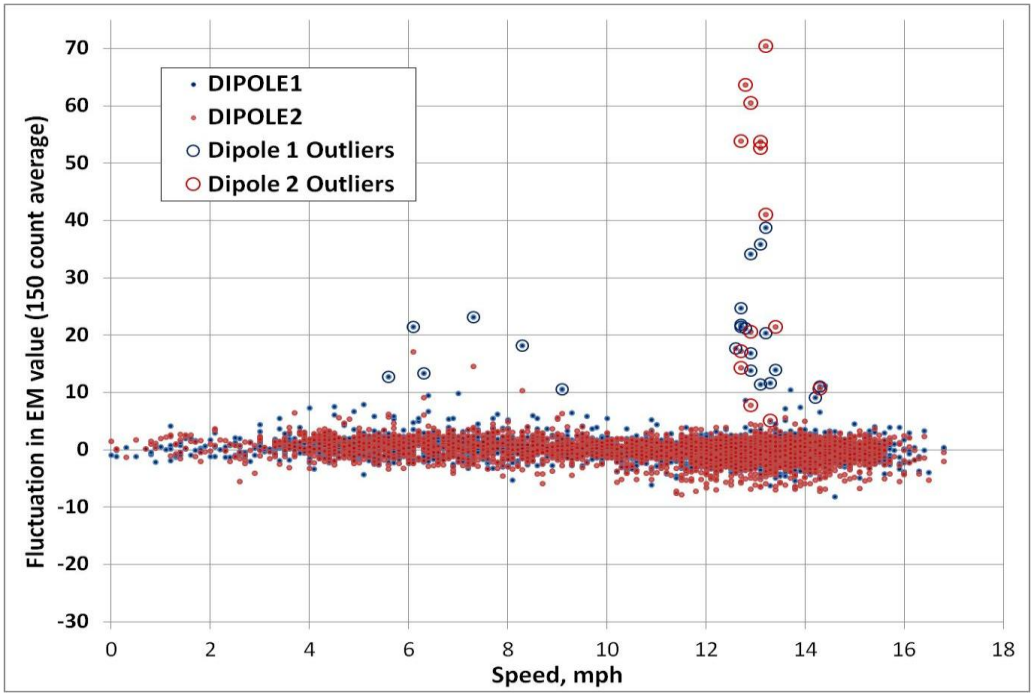

Figure 3-7: Fluctuations of EM measurements ranked by velocity

Fluctuation of EM from a running mean of 150 measurements. Most outliers identified in Figure 6 (circled) occur at a narrow range of speed; no specific cause is attributed to these anomalous observations.

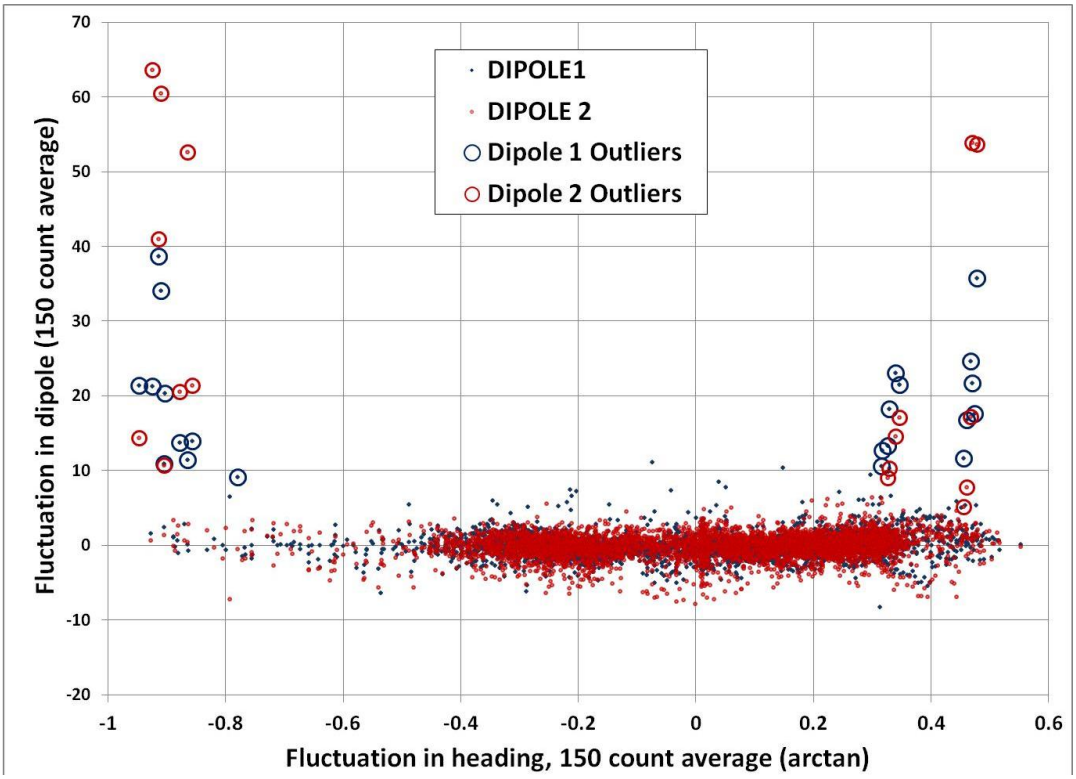

Figure 3-8: Fluctuations of EM measurements ranked by heading

EM fluctuations are plotted against fluctuation in heading (both averaged over 150 measurements). Outliers are located at extremes changes, indicating that bad measurements are associated with turning the instrument.

3.3.2 Measurement drift

Even with the rapid rate at which EC_a measurements are collected, mapping large fields takes multiple hours, which can introduce systematic error and causing instrument readings to drift. Drift may be due to change in temperature of the topsoil or the instrument, internal instrument calibration, or other variables that are not measured. To evaluate measurement drift in data from each field, co-located measurements were identified and exported from the GIS database (using the Python script "Near"). In each case, the operator completed the coverage with one complete circumference of the field edge, providing a contiguous record of points which were used as a control (Figure 3-9). The control EC_a values were compared to nearby EC_a points recorded at different times (at the end of each pass across the field), thus generating a wide range of time separation between control and test points. To check for small scale variability, the difference in control and test EC_a values were plotted against spatial distance between points, with no significant difference for comparisons within the 10m buffer.

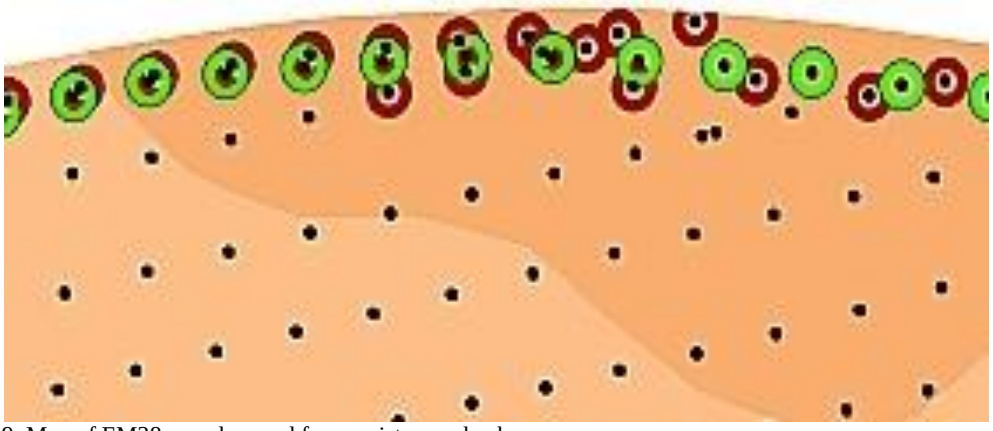

Figure 3-9: Map of EM38 samples used for consistency checks
Edge points used for consistency checks circled: green indicates control points (contiguous measurements); red indicates test points.

To illustrate instrument drift, the difference between control point and test point EC_a at the field edge was plotted against the amount of time separating the two measurements[3]). Sensor drift is evident in topsoil measurements in two of the three fields (Figures 3-11 and 3-12). In both cases, the linear trend is not evident with subsoil EC_a measurements. For this comparison, Field M54 had outliers removed (as described above). Field M21 did not show an evident linear trend (Figure 3-10). EC_a data from fields B207 and M21, while not supported by speed and heading measurements, did not contain apparent outliers as did M54, presumably indicating post-processing QC removed data that would have been flagged in this procedure. Scatter of differences between control and test points was less in M21 and B207 (±25%) than in M54 (-25% to +50%).

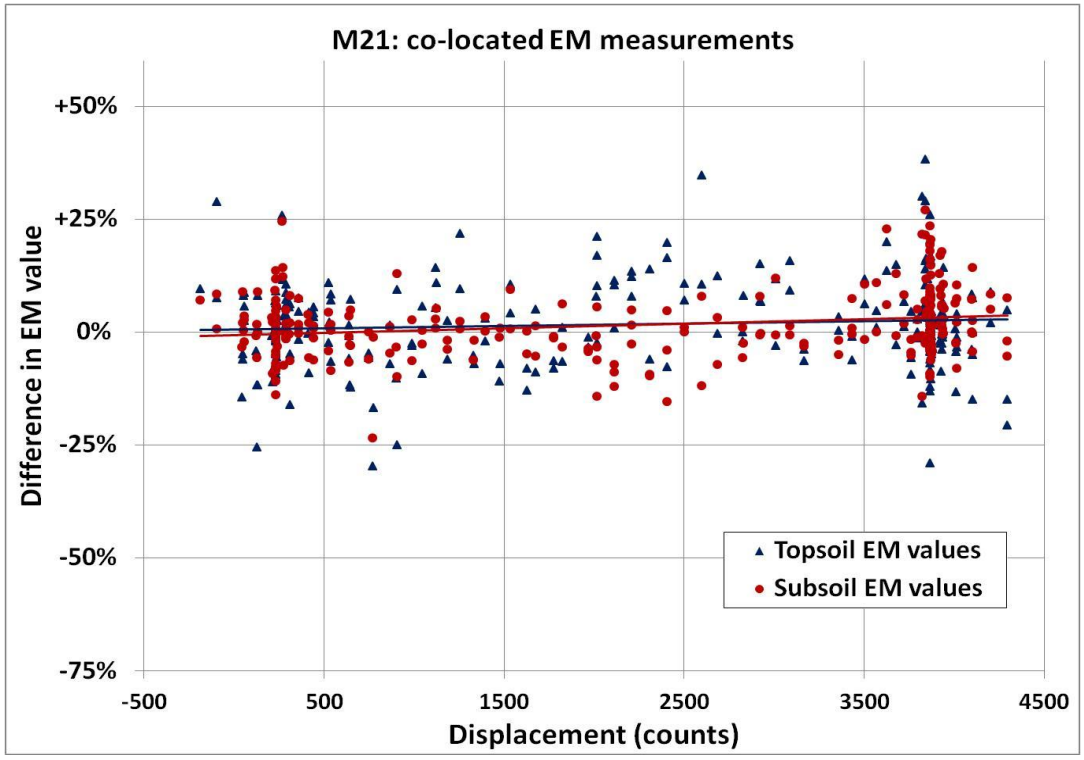

Figure 3-10: Consistency check results, Field M21
Linear trend (indicating instrument drift) is not evident in data from M21

[3] Time stamps were not provided with the raw data. For this analysis, time displacement is in counts which were used as a surrogate for measurement time. The data was collected continuously, so it was assumed that no major differences from actual time would occur.

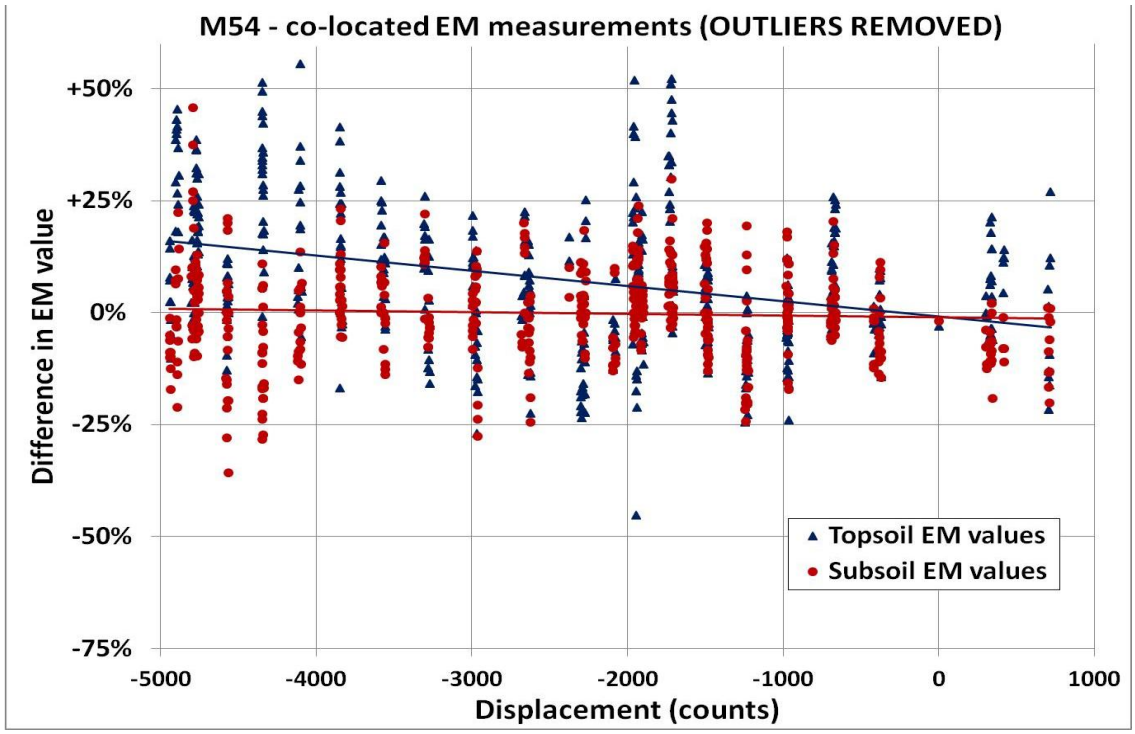

Figure 3-11: Consistency check with outliers removed (Field M54).

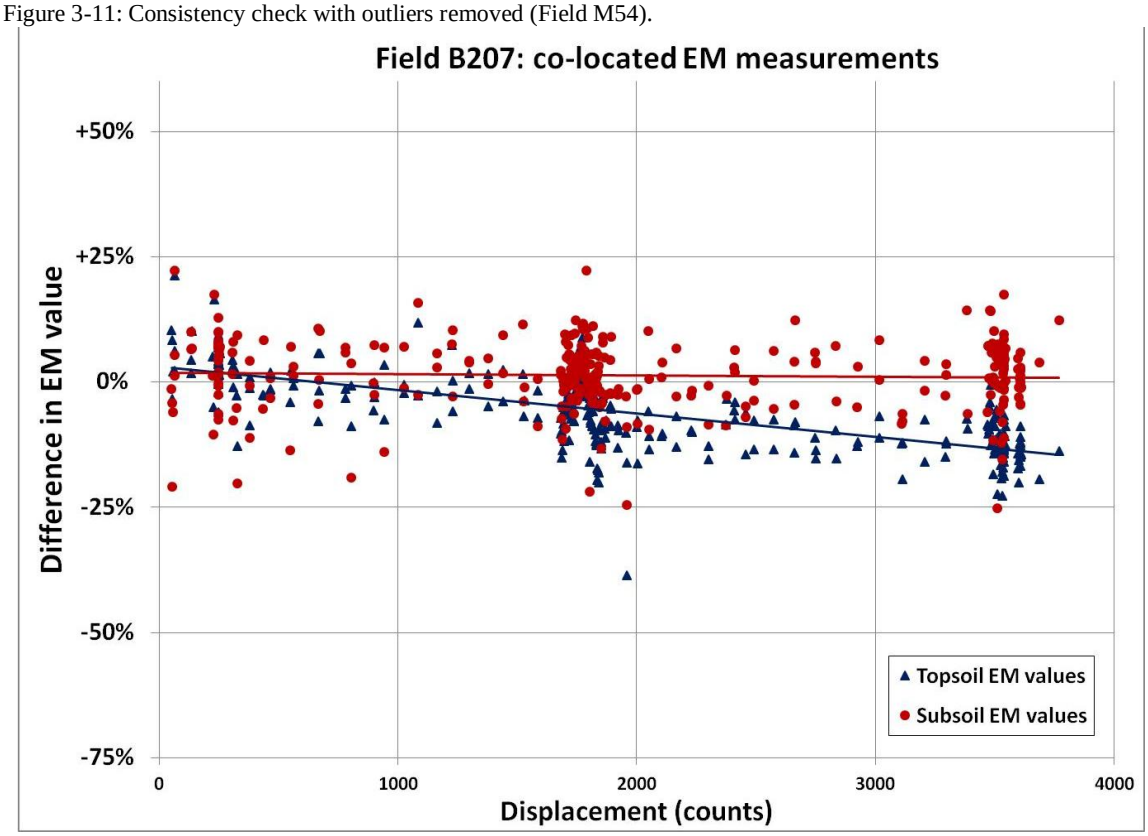

Figure 3-12: Consistency check for (Field B207)

Difference between test and control points in field B207. Linear trend is also evident indicating instrument drift over time.

The raw data from M54 included a "final cross check swath, which is usually a diagonal swath across the field when finishing the data collection to double check that readings haven't significantly changed from earlier readings, due to temperature or some other factor." (EM38 operator, personal correspondence). A map of "cross check" points are shown in figure 3-13- the same process of tabulating co-located points was repeated with these points. This field comparison improved scatter significantly over field edge comparison for M54 (±25%) (Figure 3-14). Presumably, this improvement reflects measurement error at the field edge reflecting complications from instrument operation, intra-field variability, or some other effect at the field edge. It is also possible that actual soil conditions at the field edge may be different due to irrigation or cultivation, although this cannot be determined from the data due to the sampling method and the measurement error indicated above (Section 3.3.1).

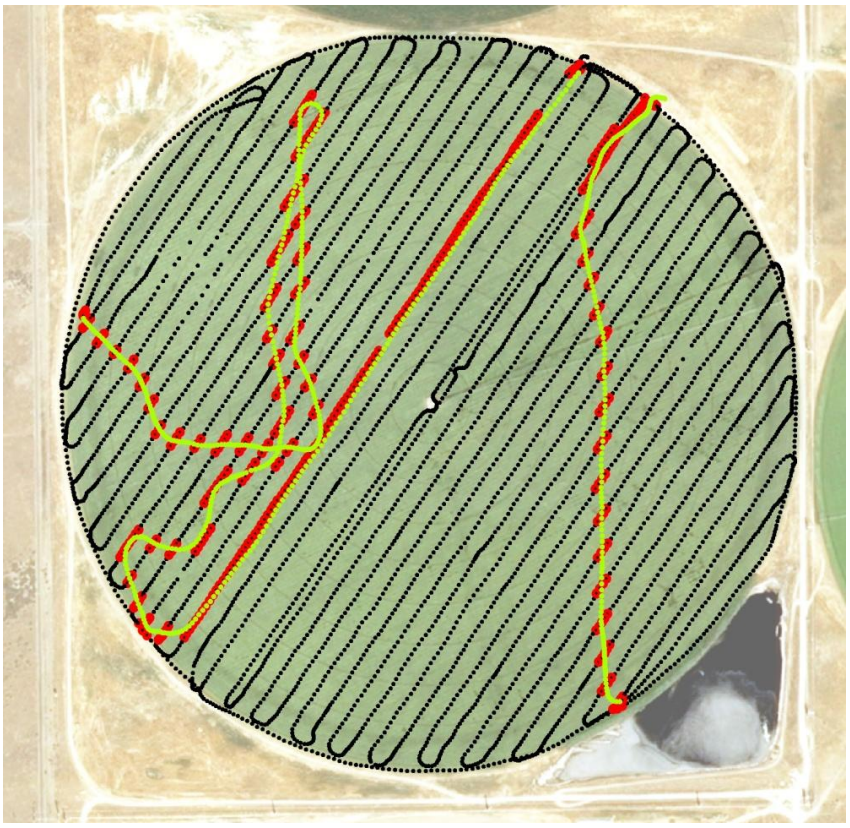

Figure 3-13: EM38 "cross check" measurement locations in field M54.
"Cross check" points are indicated in green and were used as controls. Adjacent test points are indicated in red.

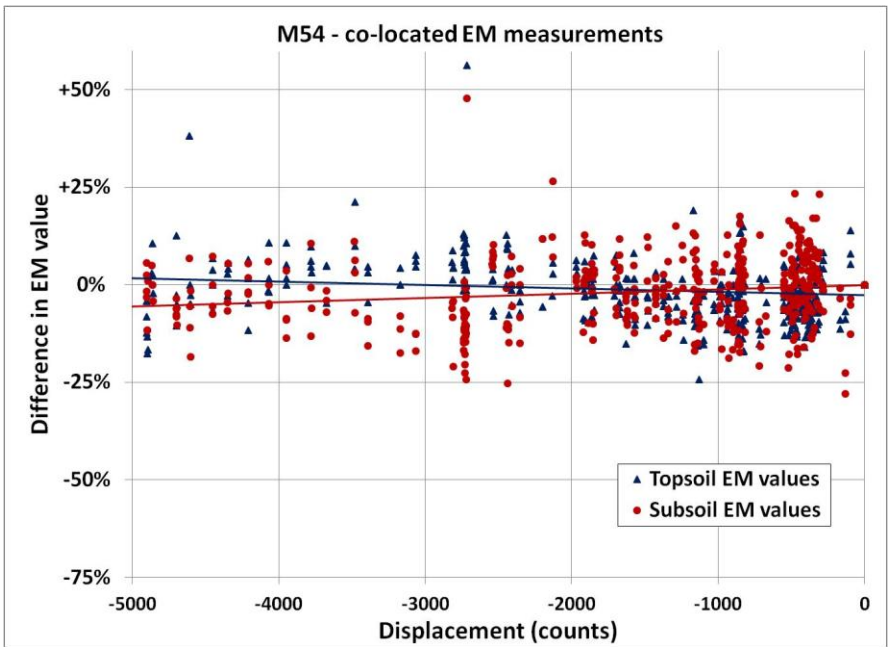

Figure 3-14: In field "cross check" comparison.
Control and test points improved considerably from the edge checks performed for field M54. Both linear trend and scatter are considerable reduced (compared to figure 3-11).

3.3 Spatial Analysis Method and Results: Using PCA To Interpret Correlation

The application of EC_a data to map soil characteristics relies on establishing correlative relationships between physical and chemical soil characteristics and EC_a readings. Typically, these relationships are determined from a limited number of physical samples (~ 30), which are collected with a stratified design. Stratified sample areas are determined from initial EC_a mapping. Once EC_a measurements are taken, areas within field with high, intermediate, and low EC_a values are mapped, and samples are taken from each area. Linear correlation between the EC_a and samples was determined in Matlab (using function *corrcoef.m*) to evaluate the reliability of EC_a for spatial maps of soil texture.

In this study, no a priori assumptions were made about spatial distributions or relationships between EC_a and soil properties. The following analysis is conducted in the parameter space of soil characteristics, and does not rely on unknown spatial distributions and correlations. This approach requires that all permutations of correlation be checked, and the distribution and range

of each parameter described. First, cross correlation was computed for all soil sample measurements and the EC_a values. Even with a large number of samples, coefficient of correlation between soil characteristics and EC_a were generally less than 0.5 (see Figure 3-16 and Appendix B). In fields M21 and B207, correlation with soil texture was not significantly better than correlation with other soil properties, except in the case of field M54. Cross correlation additionally provides a quality check on soil sampling and lab measurements, confirming expected relationships among soil textural properties and soluble ion chemistry in general.

Because all soil properties are spatially variable, do not necessarily co-vary, and may combine to have non-linear effects on EC_a, further analysis is required. To explore how EC_a correlations vary within each parameter space, a second step was employed. Principle component analysis was used to quantify the contributions of each soil characteristic to the overall spatial variability. This parameterized description identified soil parameters that are most likely contributing to or detracting from ability of correlation to evaluate spatial variability. Cross correlations between all variables were then conditionally sampled within sub-classes of each variable. For each important soil characteristic (identified by significant cross correlation or by PCA), samples were binned (by Base Saturation, Potassium, et cetera), and then correlations were found within each bin. Where PCA identified those variables that explained the largest percentage of variability within each field, cross correlation was used to identify the physical and chemical soil characteristics that were globally related to EC_a measurements. The combination of PCA and cross correlations provides a framework for evaluating within field variability of the relationship between EC_a and physical soil properties, and to quantify the effect of soil characteristics on correlation between EC_a and useful soil characteristics.

To collate EC_a measurements and soil physical properties, ArcMap was used to generate kriged interpolations of EC_a values at the locations of the soil samples. Using the geostatistical toolbox in ArcMap (ESRI 2011.), an ordinary kriging method was constrained to an

exponential/Gaussian model, but allowed to optimize the sill and range for the semi-variogram (Figure 3-15). Due to the large number of EC_a measurements, and generally smooth transitions between points, the interpolated model conformed reasonably well to measured values, with an average standard error of less than 10%- less than the average error observed in the self-consistency checks. Interpolated EC_a values were then joined to the table of sample variables in the geodatabase, and exported to Matlab for further analysis.

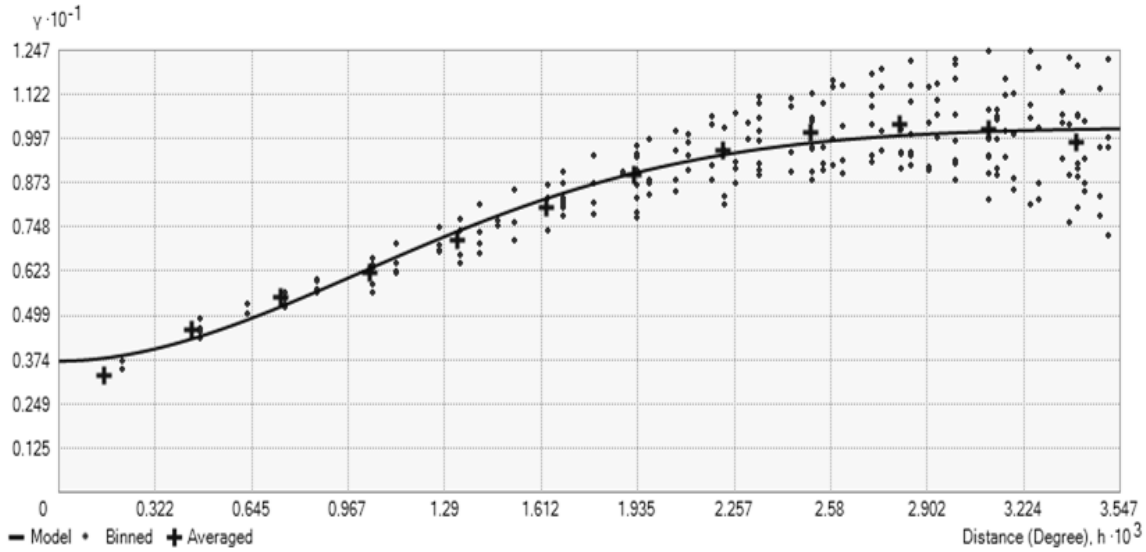

Figure 3-15: Semivariogram of sub-soil EC_a (Field M21)
The horizontal scale represents spatial distances, and the vertical scale represents variance. The model described by the line is used to generate kriged interpolations of EC_a values for sample locations.

3.3.1 Cross-correlation between sampled soil characteristics

Cross correlations were calculated in Matlab (MATLAB, Release 2012b, The MathWorks, Inc., Natick, Massachusetts, United States.) using the *corrcoef* function with pairwise comparisons (ignoring missing and excluded values). The function returns a normalized correlation coefficient and p value. The p value corresponds to the likelihood of finding "correlation as large as the observed value by random chance, when the true correlation is zero" (MATLAB, 2012b). Correlations and p values for field M21 are shown in Figure 3-16 (B207 and M54 in Appendix B). In the upper right side of Figure 3-16, large positive and negative

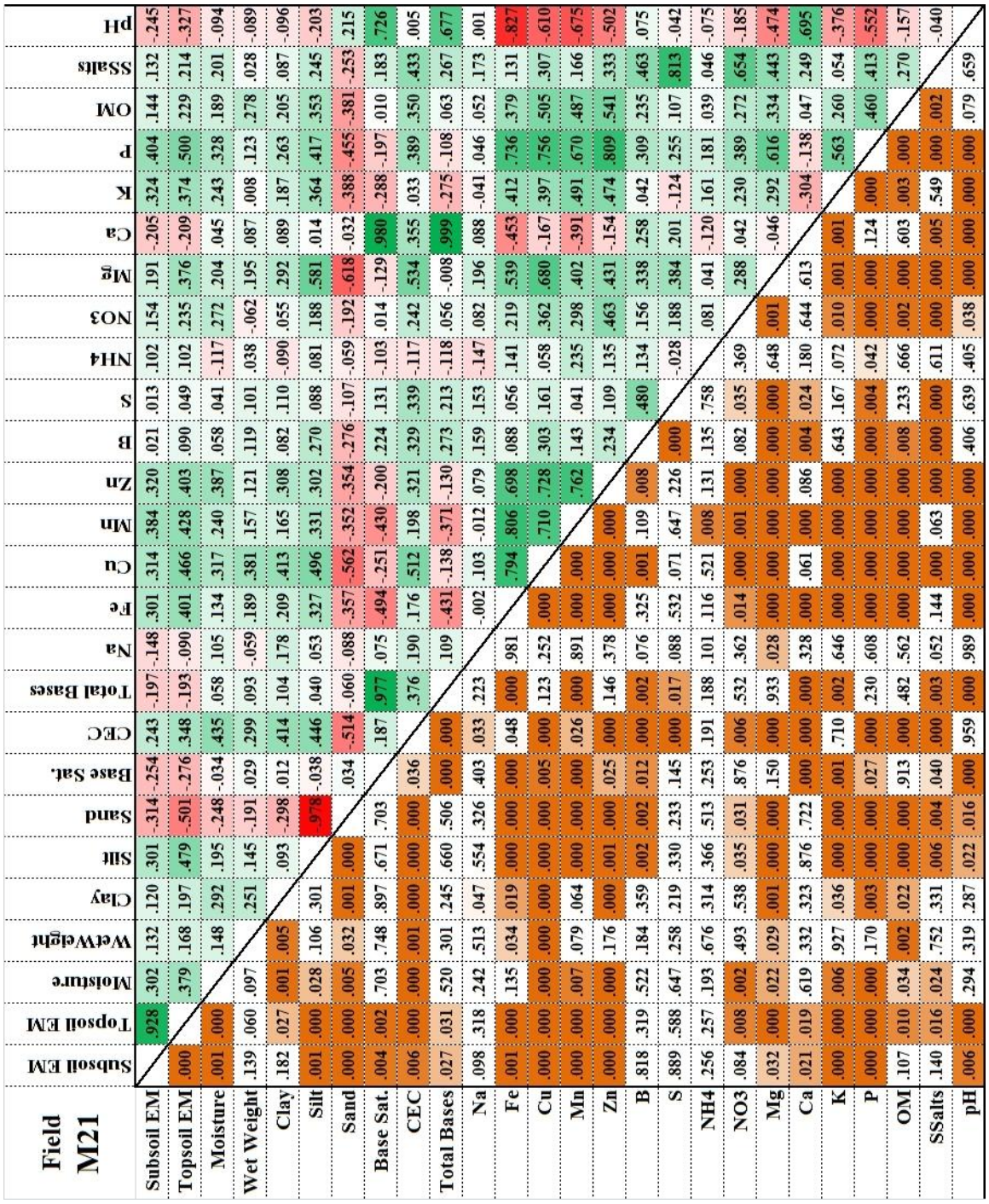

Figure 3-16: Correlation coefficients and p values for one field.

Greater negative and positive correlation is indicated by darker red and green, respectively. Darker orange indicates significant (low) p- values. Cross correlation tables for M54 and B207 are in Appendix 1. Full size reproduction for all 3 fields in Appendix B

Field M21	Residual Variance (%) →																								
	52.21	28.83	11.76	5.563	0.659	0.412	0.242	0.155	0.062	0.04	0.029	0.014	0.012	0.01	0.001	0.001	8E-04	4E-04	2E-04	1E-04	8E-05	6E-05	2E-06	1E-06	7E-09
pH	.005	.002	-.003	.000	-.002	-.012	-.029	-.005	-.020	.049	-.027	-.006	.015	-.013	.026	-.096	.152	.164	-.455	.377	-.088	-.181	.022	-.024	.011
SSalts	.000	.000	.001	.001	.001	.000	.000	.000	.000	.001	.000	.000	.000	-.001	-.003	-.004	.014	.005	-.023	.018	-.001	.003	-.006	.973	-.228
OM	.000	.001	.001	.000	.000	.006	.006	-.001	.001	-.006	.000	.002	.023	-.021	.021	-.013	.084	.053	.060	.082	.890	.410	.068	-.008	-.007
P	-.038	.047	.048	.020	.063	.209	.692	.227	.306	.222	-.455	-.234	.036	-.055	.054	.005	-.028	-.051	.012	-.017	-.006	.004	-.003	.000	.000
K	-.596	.758	-.201	-.095	.123	-.030	-.058	-.003	.000	-.006	.007	.010	-.008	-.002	-.005	.000	.000	.001	.000	.000	-.001	.000	.000	.000	.000	.001
Ca	.079	.057	.000	.003	.013	.059	.052	-.076	-.021	.188	-.093	.492	-.211	-.233	-.088	.126	-.277	.158	.166	-.127	-.422	.037	-.010	.036	.119	.479
Mg	-.001	.001	.001	.002	.002	.007	.014	-.008	-.007	-.007	-.007	.007	-.024	.005	-.013	.032	.063	-.120	-.176	.204	.420	.294	-.586	-.229	.113	.485
NO3	-.064	.236	.918	-.027	-.308	.003	-.052	-.006	.000	-.009	.000	-.004	-.008	.000	.002	-.001	-.003	-.002	.002	.000	.000	.000	-.001	-.001	.000	.000
NH4	-.009	.006	.002	.026	-.013	.027	.045	.749	.645	.076	.002	.078	-.026	.073	-.031	-.009	.007	.002	-.013	-.001	.003	.004	.004	.000	.000	.000
S	.059	.013	.306	.309	.893	-.070	-.063	.001	-.012	-.015	.025	-.006	.007	.010	-.002	-.001	.001	.002	-.001	-.004	-.001	.000	.001	-.002	.000	.000
B	.001	.001	.001	.003	.004	.003	.007	.004	-.006	-.004	-.011	-.004	.021	-.024	.011	-.033	.211	.022	.541	.784	.171	.037	.063	-.101	.012	-.001
Zn	-.004	.004	.006	-.001	.002	.023	.059	.018	.029	-.006	.005	.038	.127	.000	.107	.024	.269	.909	-.239	.069	.016	-.034	-.057	-.034	-.004	.003
Mn	-.017	.006	.013	-.001	.007	.080	.164	.075	.014	-.127	.334	.214	.644	-.483	.327	.085	-.025	-.145	.018	-.029	.011	-.024	-.015	-.015	.001	.000
Cu	-.001	.001	.002	.001	.001	.015	.019	-.004	.004	-.013	.005	.020	-.003	.004	.019	-.002	.086	-.023	-.017	.129	-.003	.065	-.275	.945	.008	-.002
Fe	-.033	.002	.021	.003	.019	.190	.425	.113	.180	-.532	.477	.203	-.273	.239	-.210	.055	-.002	.028	.063	-.027	.013	-.003	.007	-.015	-.002	.001
Na	.000	.000	.000	.000	.000	-.001	.001	-.004	.001	-.004	-.007	.008	.005	.008	.012	-.015	.060	-.023	-.068	.119	.459	-.316	.609	.177	.111	.501
Total Bases	.077	.059	.001	.005	.016	.065	.067	-.087	-.026	.175	-.108	.507	-.228	-.220	-.091	.151	-.145	.017	-.074	.200	.480	-.012	.024	-.014	-.115	-.481
CEC	.002	.004	.007	.007	.009	.049	.054	-.077	-.027	.121	-.061	.300	-.099	-.151	-.049	-.505	.688	-.221	-.169	-.119	-.137	-.051	.009	-.055	-.010	.002
Base Sat.	.787	.589	-.101	-.055	-.010	-.007	.010	.027	.011	-.043	.039	-.093	.041	.045	.015	-.025	.039	-.018	-.011	-.006	-.006	-.002	-.001	-.002	.000	.000
Sand	.017	-.036	-.007	-.089	.001	-.206	-.366	.581	.662	.063	.020	.166	-.052	-.028	.018	.019	.050	-.021	-.004	.001	.006	.004	-.006	.000	.000	.000
Silt	-.033	.108	-.103	.939	-.292	-.028	-.035	.031	.075	-.024	-.013	.015	.000	-.006	.007	-.002	.000	.000	-.001	-.001	.000	.000	-.001	.000	.000	.000
Clay	-.001	.004	.000	.000	.007	.041	.027	.054	.005	.041	.040	.254	.151	.463	.826	.008	.027	.076	.013	.001	.019	.004	.001	.024	.003	.002
Wet Weight	.002	.003	-.010	.019	.044	.919	.374	.050	.058	.017	.048	.067	.009	.012	.003	.001	.002	.001	.000	.001	.002	.004	.001	.005	.000	.000
Moisture	-.003	.006	.007	.004	.002	.035	.022	.062	.058	.212	.076	.346	.583	.589	.356	.048	.054	.033	.019	.011	.003	.014	.002	.002	.000	.000
Topsoil EM	-.009	.005	.006	.021	-.003	.050	.073	.038	.010	.360	.312	.074	.095	.099	.053	.715	.441	.123	.004	.093	.063	.033	.026	.016	.003	.005
Subsoil EM	-.011	.006	.004	.023	.004	.056	.075	.005	.061	.615	.565	.176	.091	.005	.029	.411	.252	.086	.011	.079	.047	.027	.009	.014	.002	.003

Figure 3-17: Variance table (PCA analysis) for one field.

Each columns represents a vector of linear weighting coefficients of soil variables, listed on left. Colors indicate higher coefficients, red and green indicating negative and positive weighting respectively. Residual variance for each column is the percent of remaining variance. PCA tables for all field are in Appendix B.

correlations are shown in green and red, respectively; significant (<0.1) p values are shaded orange in the lower left. The top two rows and left two columns correspond to correlations with EC_a (deep and shallow measurements). Correlation across all samples were generally low, although patterns do emerge when all three fields are considered. Correlation with texture (the characteristic useful for managing irrigation) is highest for field M54, and lowest for B207. Other properties show correlation with EC_a in one or all fields, including those that correspond to previously cited contributing factors (CEC, dissolved salts, moisture content), as well as unanticipated properties (magnesium, iron, copper, sodium). These unanticipated correlations are not consistent between fields, and with low correlation values (>0.3) it is unclear if these are spurious relationships, or some non-linear combination of factors.

3.3.2 Principal Component Analysis

Principle Component Analysis (PCA) was used to describe variability of soil parameters, and to identify the most significant properties that might influence measured EC_a values. PCA was selected as it requires no assumptions about underlying co-distributions of characteristics, and instead finds linear combinations ("components") of all soil parameters that minimize global variability. PCA was performed with sample data from each field and with data from all fields together, and was implemented in Matlab Results for B207 are tabulated in figure 3-17 (Fields M21 and M54 are shown in Appendix B). Each column (component vector) contains a linear combination of weighted coefficients for each soil parameter, with larger magnitude coefficients indicated in red (negative) and green (positive). Proceeding from left to right, successive components account for smaller residual variability in the data the percent of total remaining variance is shown at the top of each column.

The greatest part of variance (~99%) is explained within the first 4-5 principle components (columns) in all three fields. In all three fields, potassium content was a significant contributor to variability in the first few components. Base saturation was a major contributor to variability in

field B207, less so in field M21, and did not contribute to variability in M54 until the fourth principal component (represent about 1% of the residual variance). Nitrate, iron, phosphate and sulfate all appear significant in the PCA for some fields.

3.3.3 Conditional Correlation Analysis

To map the variability of water holding capacity within the field, the EC_a method must correlate to textural characteristics. This requires that confounding effects from other soil properties (CEC, organic matter, salts, water content) do not overshadow this correlation, especially if these other properties do not co-vary with texture. To visualize these confounding effects, we plotted correlation of texture and subsoil EC_a measurements for subsets within each field. Each subset was defined by binning the independent (potentially confounding) parameter (such as base saturation, CEC, organic matter…), and then conditionally sampling the corresponding EC_a and texture. Independent variables was selected in one of three ways: first, the variable was identified by PCA as a source of significant variance within one or all fields; second, that correlation of the entire field showed a significant relationship with EC_a measurements; third, that previous studies have shown the variable to have significant correlation with EC_a measurements. No variable fulfilled all three definitions for all three fields. Following the regional soil characteristics (well drained, cultivated sandy soils, very high Calcium content, arid climate, long history of irrigation) characteristics related to soluble ions were predominantly selected. A broad range of other variables fulfilled one of the above criteria, including pH, nitrate, phosphorus, copper, iron, and sulfate. When the data was binned by these other variables, no significant trends were apparent (not shown). In some cases, there was not a sufficient range of the variable to differentiate different classes of correlation.

The confounding effects of characteristics are also related to soluble ions: base saturation, cation exchange capacity and total bases. Also shown below are analyses of specific soluble ions: potassium, calcium, and magnesium. The principle component analysis indicated that potassium

could explain a large percentage of the variability that was observed in the entire constellation of measured quantities. The histogram of the potassium values and the correlation between silt and EC_a show that EC_a measurement is influenced by potassium concentration (Figure 3-18). From the histogram it is clear that the fields are substantially different in their distribution of potassium concentrations, with a wide range of variability spanned in the data. The conditional analysis indicates that the EC_a measurement behaved differently in each field (3-19). There is increased correlation between EC_a and texture at potassium concentrations between 400 and 600 ppm, but this may be spurious and the overall effect of potassium on the resulting soil map is unclear and inconsistent within the available data.

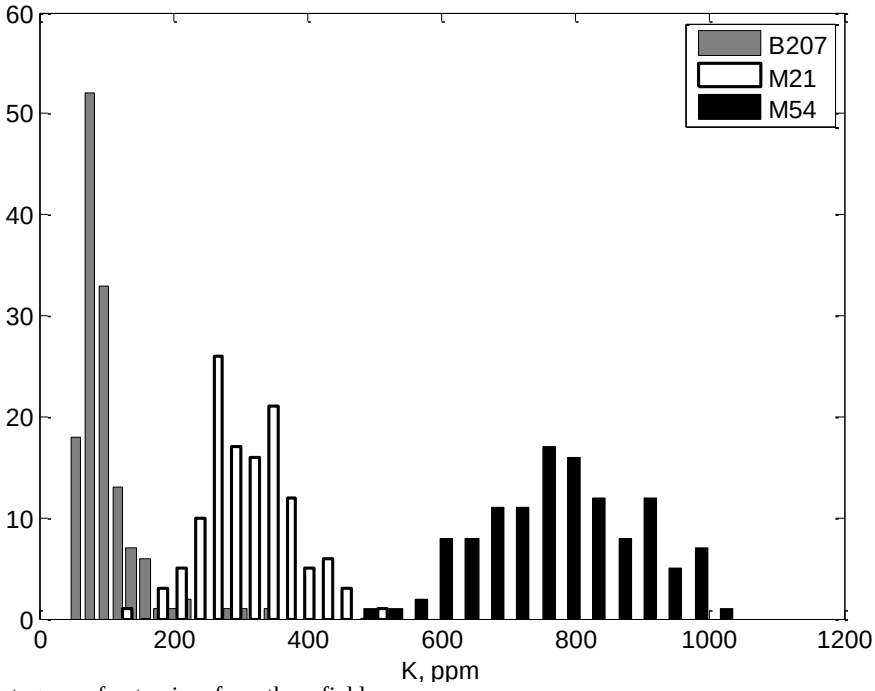

Figure 3-18: Histogram of potassium from three fields.
Each field has a normally distributed range of K measurements, and each field has a significantly different mean value. PCA also indicated that K could potential be a confounding factor in EC_a-texture correlation.

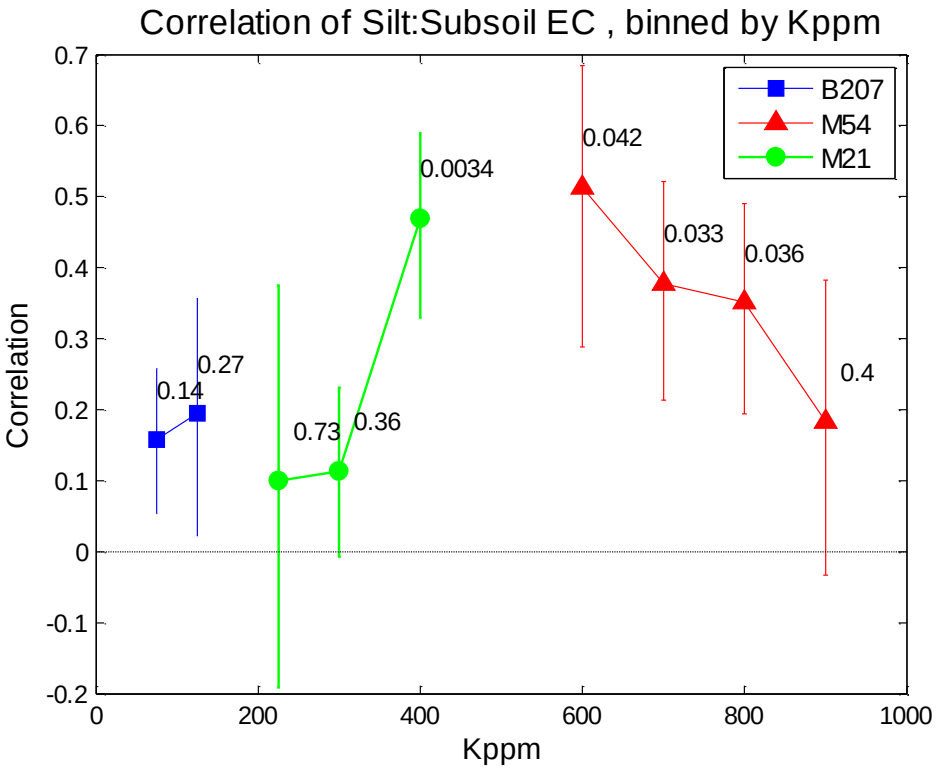

Figure 3-19: Conditional analysis, binned by potassium of soil samples.
The vertical axis is the correlation coefficient of Silt:EC_a for the conditionally sampled subset. p values are indicated for each point, plotted with confidence intervals for 1 standard deviation. Each point represents a set of 5-100 points, based on K at each point. Despite a wide range of K in each field, potassium has no clear effect on EC mapping.

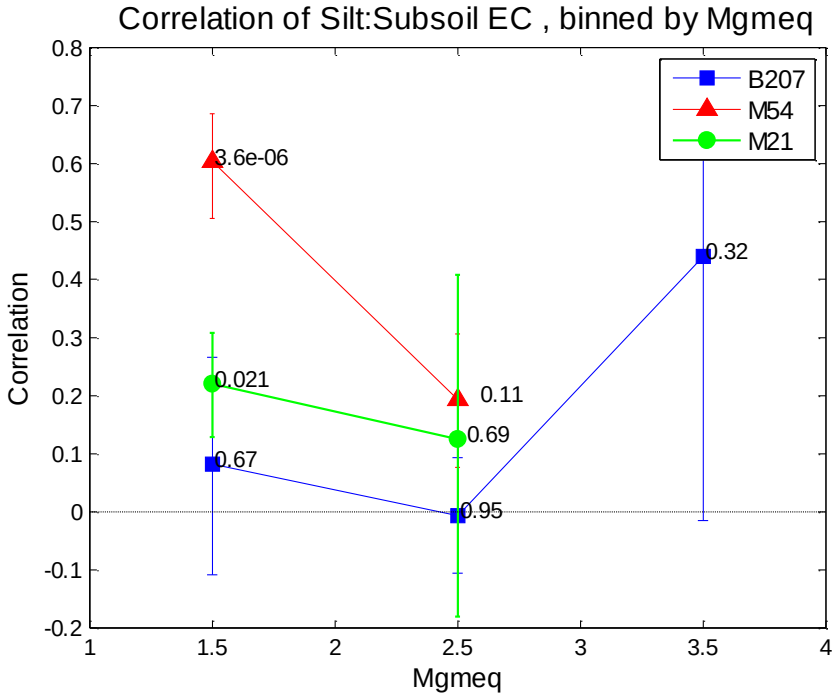

Figure 3-20: Correlations conditionally sampled by magnesium.

The global correlation analysis indicated that magnesium was a substantial contributor to the EC_a readings. The correlation between silt and EC_a, may be slightly conditional on magnesium (Figure 3-20). Correlations between the texture and EC_a at 1m depth have a slight increase with decreasing Mg concentrations. This is consistent with Mg being a transportable ion that has the potential to obscure the correlative relationship between the texture and EC_a.

The scientific literature indicated that calcium could influence the readings from the EM30. Furthermore, calcium was the dominant base ion that was measured in the collected samples. The correlation between silt and EC_a conditioned on calcium concentration is shown in Figure 3-21. Similarly to conditional analysis of potassium, no clear trend emerges which indicates that calcium concentrations alone are not responsible for poor mapping correlation in these fields.

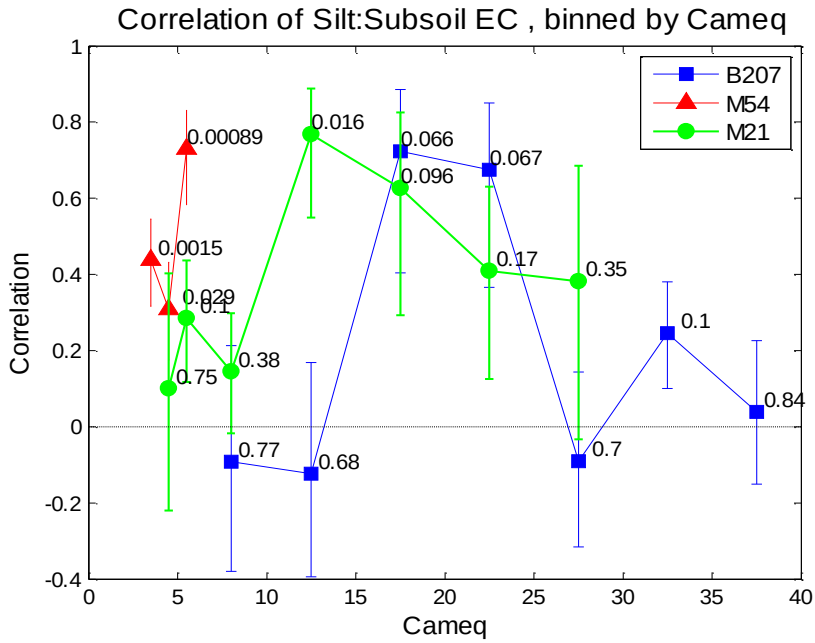

Figure 3-21: Correlations conditionally sampled by calcium.

Global correlation analysis confirms previous findings of (Doolittle and Brevik, 2014; Triantafilis et al., 2009), indicating that the cation exchange capacity (CEC) should be related to the EC_a readings. Weak, but statistically significant correlations between EC_a and the CEC can be observed, but the correlation between silt and the EC_a measurements was not strongly

conditional on CEC values (Figure 3-22). Although there is a statistically significant relationship between the EC_a and CEC, the CEC is not responsible for a lack of observed correlation between EC_a and soil texture in some fields.

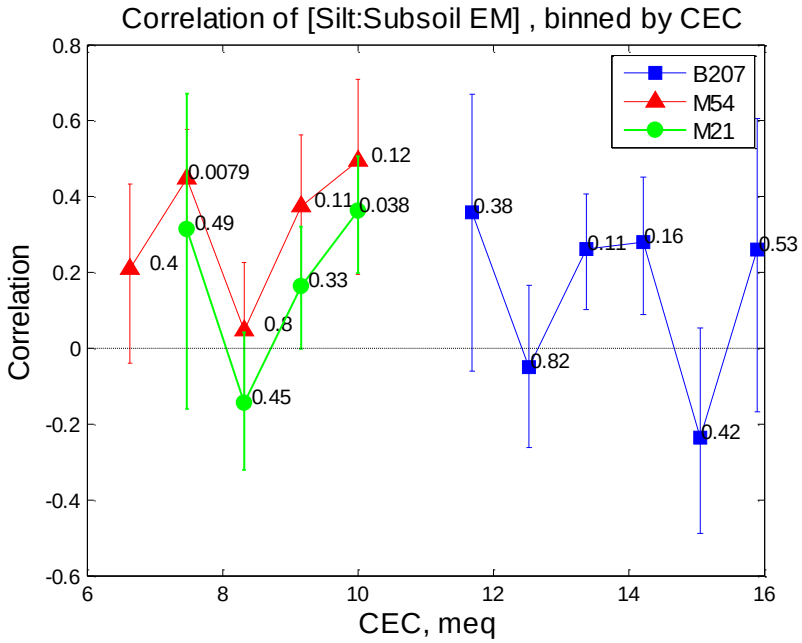

Figure 3-22: Correlations conditionally sampled by CEC.

The principle component analysis indicated that base saturation was the most important variable in fields B207 and M21 where the overall correlation between the EC_a and soil texture was weakest. Further, The PCA did not indicate base saturation was an important variable in M54 where the correlation between EC_a and the texture was the highest observed in among the three field. The correlation between EC_a and the silt content of the soil, is conditional on the base saturation (Figure 3-23). It appears that as base saturation decreases, there is a substantial and statistically significant increase in the correlation between EC_a and soil texture. This relationship was the most significant of all variables tested and likely indicates that the base saturation is the variable within these soils that is confounding the desired correlation between soil textural properties and the EM38 readings. One hypothesis is that in cases where base saturation is 100% and positive ions are sorbed to all available surfaces of clay particles responsible for the CEC,

free ions obfuscate the measureable cation properties of the soil, thereby reducing correlation between electrical conductivity and soil texture.

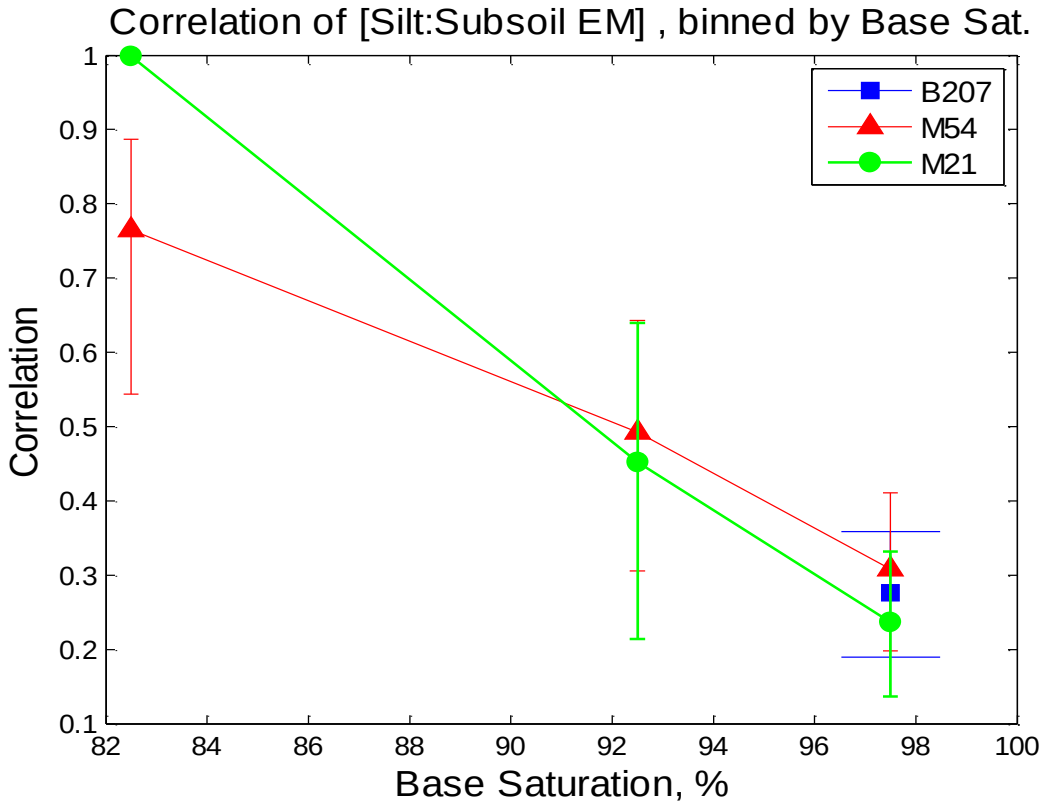

Figure 3-23: Correlations conditionally sampled by Base Saturation.

3.4 Discussion and Conclusions

The self-consistency checks quantified the scatter and drift associated with the EM38 instrument over the duration of the mapping time interval. Over the course of this time period, instrument drift is consistent with the soil temperature increasing (due to incident solar heating). Drift occurred only in the shallow measurements where soil temperature responds more rapidly to radiant solar heating at the surface. The temperature hypothesis is also consistent with the fact that M21 has the lowest amount of drift. This field was mapped near solar noon where the soil temperature experiences little change. However, these suppositions could not be verified with the existing data set. Soil temperature was not measured, and some other effect could be the source of drift.

More importantly, if instrument drift is observed, no matter the cause, it is an indication that the accuracy of the map could be improved. Soil properties are unlikely to change in a matter of hours, and large persistent changes in that time are likely due to transient effects that reduce the resolution and accuracy of the final mapping product. Since some drift occurred in two out of three soil maps, this drift is likely a common phenomenon. Steps should be introduced into a data processing protocol to quantify and eliminate the effect of drift from the finished mapping product. Following the recommendations of Sudduth et al. (2001), it is important that EC_a measurements are corrected for systematic instrument drift. The EM38 be operated in a stationary position for several minutes within the field before the mapping process begins to provide an accurate calibration. At the end of the mapping exercise, the EM38 is returned to the same location and allowed to collect data for several minutes. The difference between readings at the beginning and end of the measurement period, in addition to the existing self-consistency checks, can be used to de-trend the data and improve map accuracy. Further, the mapping procedure should be performed at times of the day when there is less expected temperature change (when radiative solar heating is constant), such as mid-day, and not during periods of rapid temperature change in the soil.

Correlative analysis and principle component analysis were used to reduce a broad array of measured soil characteristics to a small suite of variables that may be responsible for the apparent weak correlations between EC_a readings and soil texture. These potential confounding characteristics were related to soluble ions: base saturation and cation exchange capacity, and soluble ions: potassium, calcium, and magnesium. Conditional sampling, based on these variables was then used to isolate the variable(s) that are responsible for the apparent low correlation between texture and EC_a. The analysis demonstrated that the base saturation was the most influential soil property on mapping success. One interpretation of this finding is that as the positive base ions are bound to the negatively charges sites on clay and organic soil particles, and

the total electromagnetic field detected by the EM38 is reduced. In this way, the saturated CEC become less apparent, and the signal to noise ratio associated with CEC is reduced. EC_a correlations with texture of zero when base saturation approached 100% and these correlations generally increased as the base saturation decreased, approaching near 100% as base saturations decreased below 80%. Preliminary soil testing can be performed prior to mapping to determine base saturation. In field where base saturation is high, it is likely that the EM38 is not an appropriate instrument for mapping soil texture, and an alternative method is recommended.

Mapping soil texture via EC_a can provide highly resolved maps of water holding capacity with some degree of confidence in many places. While this method may be precluded from use in some field conditions, EC_a provides insights into the spatial variability of other soil properties at low cost and high resolution. It may be especially valuable to be able to map other soil parameters such as salinity and fertility, as techniques such as fertigation and deep leaching can be implemented with precision irigayion systems as well as can simple irrigation (to meet crop water demand). The low cost of the method is particularly important for fields that are cultivated annually, as this both makes the fields bare (allowing measurement to happen) and because cultivation may affect long term stability of soil properties such as organic matter content and texture. Open question remain as to the ability to predict crop water demand from soil properties, particularly at the spatial scales relevant to precision irrigation systems (~30 m, or 0.1 hectares). Even assuming that knowledge of the soil texture (at one time during the season) can provide a map of the soil's water holding capacity, other factors mediate the rate at which crops transpire. Consequently, knowing soil water storage is only part of the required information- to have a complete picture of crop water demand, crop evapotranspiration must also be measured.

4. Measuring Evapotranspiration for Agriculture

Efficient irrigation planning depends on reliable and site-specific information to anticipate crop water demand, to assure that irrigation is adequate to prevent drought stress, and to maximize yields from the available resources. Irrigation facilitates more than 40% of global food production on less than 20% of agricultural land, and requires more than 80% of global consumptive water use (Siebert and Döll, 2010). Growers and irrigation specialists can access many sources of water use information including historical irrigation records, regional weather networks, and remotely-sensed estimates of weather and water demand (Perry et al., 2009). For this information to be useful to producers, it must be affordable, readily accessible, and updated regularly (Clary, 2015). Uncertainty about crop water requirements and water availability add additional risks to farming systems that depend on irrigation (Evans and King, 2012). Climate change, drought, and water allocation rights also add to uncertainty about water availability, and affect seasonal decisions about the extent and timing of planting, irrigation, and harvesting of crops (Knox et al., 2012).

Irrigation research and weather monitoring networks have facilitated improved irrigation by providing detailed and specific information about the actual crop water demand (Smith, 2015). Advances in precision irrigation can incrementally reduce water use while maintaining yields, but these systems are constrained by a lack of local, real-time data at the field scale (Daccache et al., 2015; Evans and King, 2012; Evans and Sadler, 2008). In the case of incremental water use reductions, the risks of under-watering often outweigh the costs of over-watering; consequently, irrigators are averse to risk and do not optimize water allocation (English and Raja, 1996). Irrigators make daily and hourly decisions based on a suite of information, but many default personal experience and professional knowledge of crops, field conditions, and local climate. Within the framework of an irrigation district or a single farm, readily available estimates of crop

water demand are not local or frequent enough to make specific incremental water allocation decisions at the scale of field irrigation (Sadler et al., 2005). For regional water managers, basin scale water demand estimates are similarly limited in resolution and immediacy (Sorooshian et al., 2012; Wisser et al., 2008).

While there are many methods to determine crop water demand, each method is constrained or inaccurate under some specific field conditions. Under some conditions (such as over mixed crop canopies, or during seasons with many of days light rainfall) accurate estimates of water demand are challenging with any existing method. Irrigators increasingly use irrigation software and web based resources to predict crop water demand when scheduling irrigation (Hillyer, 2011). However, a lack of confidence in these estimates discourages implementing efficient irrigation practices, which can increase the risk . To avoid risks of catastrophic crop loss, irrigators default to historical practices and site-based experience, limiting the potential efficiency gains of scientifically based methods (Knox et al., 2012; Molden et al., 2010). To implement more efficient precision irrigation methods, detailed crop water demand information is required to support rigorous irrigation prescriptions (Laurenson et al., 2002; Perry et al., 2009). This data gap must be overcome to facilitate greater irrigation efficiency while avoiding increasing the burden of additional risk and retaining cost effectiveness of existing systems.

4.1 Meeting the Data Requirements for Precision Irrigation

Large scale precision irrigation systems are now capable of controlling water application to areas smaller than 0.1 hectare (Daccache et al., 2015; O'Shaughnessy et al., 2013). Knowing crop demand on daily or shorter timeframes is required to coordinate complex irrigation systems with limited water supplies. For example, large farms in the arid western United States can operate dozens of large irrigation systems, each irrigating more than 100 hectares, that depend on a single source of water. Even when multiple sources of water supply (groundwater wells,

surface diversions) are available, the rate and timing of deliver may be limited by water rights or actual availability. In real world terms, managing crop demand within the context of these constraints requires real time data; site-specific information can reduce risk of crop loss as well as improve allocation strategies (Evans et al., 2013; Liu et al., 2011).

Accurate, local, and timely estimates of ET require a significant investment of resources and highly skilled and informed professionals (Allen et al., 2011a). To be directly useful to irrigators and water management professionals, ET estimates need to be resolved to the spatial scale and delivered on timeframes at which irrigation decisions are made. A straightforward way to determine the amount of required irrigation is to track the amount of water stored in the soil (plant available water, PAW), and apply irrigation as PAW is depleted. The biggest challenge of this approach is in extrapolating soil moisture measurements over the large extent of farm fields, while still capturing heterogeneous characteristics at sub-field scales. Techniques measuring water potential (pressure), volumetric content, and soil electrical properties have attempted to develop consistent methods that are applicable for the diversity of characteristics found in agricultural soils (Cuenca et al., 2013b; Topp, 2003). Despite ongoing challenges in the development of low cost sensors, soil moisture management remains a common method used in scheduling irrigation, often in conjunction with monitoring of ET (Evett, 2007).

Complementary to the measurement of water stored, another approach to measure crop water demand is to measure evapotranspiration of water from the surface to the atmosphere. Evapotranspiration is the combination of surface evaporation and active transpiration from vegetation. Evapotranspiration (ET) accounts for huge volumes of water and energy in global cycles; terrestrial ET returns between 60-65% of precipitation to the atmosphere, and accounts for half of all energy received at the land surface via latent heat (Brutsaert, 1982). Despite the magnitude of water and energy flux, there are fundamental and practical challenges to obtaining

real-time, local estimates of ET, hampering the ability of water managers to make informed decision at field scales. While the partitioning of ET into evaporation and transpiration is a current area of research (Burt et al., 2005; Wang and Dickinson, 2012), monitoring ET has become a predominant concern for both research and monitoring of water resources (Baldocchi, 2014). ET estimates are an important piece of information in modern farming, helping predict actual consumptive water use and facilitate irrigation scheduling. Because of atmospheric mixing, ET estimates provide a spatially integrated measure of crop water demand. Disentangling the measured ET is required to resolve underlying spatial heterogeneity.

Many regional networks provide reference or potential ET estimates, but these are not local in the sense that they may only resolve ET estimates at the scale of square kilometers, county boundaries, or for entire regions, and are often based on either remotely sensed data (Anderson et al., 2012; Kalma et al., 2008) or using sparse networks of meteorological stations (Gowda et al., 2008). On site weather measurements and soil moisture can be used to estimate crop water demand, but affordable equipment can be unreliable and imprecise, and also time-consuming to operate (Elliott et al., 2000; Reges et al., 2016). More involved methods for measuring ET used by researchers can be very accurate, but by definition, these experiments have been executed in controlled field conditions that are impractical within the context of farm operations. Regardless, the labor and expertise constraints leave irrigators without feasible methods to accurately measure ET directly on site (Allen et al., 2011a; Evans et al., 2013).

4.2 Physical Mechanisms Underlying ET Measurement

To better utilize ET estimates that are currently available, it is essential to understand the underlying physical principles driving ET, and the uncertainty associated with measuring these drivers. Solar radiation is the primary driver and limiting energy source. Other important factors that mediate the rate of crop ET include soil texture and water content; biophysical controls such

as stomatal resistance and drought adaptation; meteorological conditions including air temperature, precipitation, microclimate, and large scale transport processes. Advances in measurement have systematically addressed these factors according to the relative influence each phenomena exerts on the rate of evaporation. Advances in technology have allowed measurement of phenomena that are inherently more difficult to measure quantitatively, such as solar radiation, sap flow, or rapid fluctuations in air humidity (Shuttleworth, 2007). Refinements to instrumentation can now make accurate and rapid measurements of radiation, temperature, humidity, soil moisture, and wind speed; these measurements are now customary (Allen et al., 2011a). There are excellent technical reviews of applied ET measurement (Table 1).

Bastiaanssen et al., 2000	Remote sensing in agriculture - research and applied methods
Jones, 2004	Plant Based Methods for Irrigation Scheduling
Shuttleworth and Gash, 2005	Survey of large scale field experiments studying ET
Farahani, et al., 2007	ET Measurement and Modeling in Agriculture
Gowda, et al., 2007	ET mapping for agriculture - present status and challenges
Shuttleworth, 2007	Direct ET measurement and parameterization methods
Kalma, et al., 2008	Temperature based remote sensing methods
Verstraeten et al., 2008	ET and Soil Moisture across Scales of Observation
Li et al. , 2009	Review of remote sensing methods to measure ET
Allen et al., 2011	Measurement accuracy for ET methods (2 parts)
Anderson, et al., 2012	Remote sensing methods for water mgmt and ET monitoring
Cuenca, et al. 2013	Progress in Monitoring Soils and soil hydraulic properties
Morton, et al., 2013	Uncertainty in remotely sensed agricultural ET estimates
Evett et al., 2013	Soil Moisture Sensing for ET and WUE
Baldocchi, 2014	State and Future of Eddy Covariance
Vereecken, et al., 2014	Spatio-temporal dynamics of soil moisture
Gago, et al., 2015	Use of UAVs to assess water stress in agriculture

Table 1: Reviews describing recent developments and current status of ET measurement in agriculture

Methods to determine ET directly from field measurements were developed beginning in the 1930's. Most notably, I.S.Bowen and H.L.Penman provided a framework to measure evaporation derived from the principles of thermodynamics (Bowen, 1926; Penman, 1948). This framework was developed and validated over the remainder of the twentieth century (Jensen and Allen, 2000), culminating in the adoption of standard measurement methods. Examples of these standards include ASCE-EWRI's Reference Manual 70 "*Standardized Reference Evapotranspiration"* (Allen and Jensen, 2015) and the FAO Irrigation and Drainage Paper No. 56 "*Crop Evapotranspiration- Guidelines for computing crop requirements*" (Allen et al., 1998). These standards are used in the operation of regional ET monitoring networks, which have been integral to modern water allocation and irrigation practices (Elliott et al., 2000). Regional authorities, recognizing the dramatic economic and conservation benefits of monitoring and reporting ET, have established state and regional monitoring networks, often as a direct extension of weather forecasting services (Farahani et al., 2007; Snyder et al., 2009). The methods employed at regional weather stations forecast and record long term ET estimates, usually relying on simple and robust instrumentation. A network of monitoring stations allow ET data from a few locations to generate forecasts for a large geographic area (Horel et al., 2002). However, because the methods employed to determine ET (such as Penman-Monteith equation) depend on a controlled reference site, these estimates do not translate directly and robustly to all field conditions. Web based forecasts and crop specific guidance provide valuable information to improve irrigation practices, but in many cases interpolated ET estimates fall short of the providing detailed information required for precision irrigation applications (Daccache et al., 2015; Evans et al., 2013).

In the last 25 years, a number of developments in instrumentation have dramatically extended the range of conditions under which ET determinations can be made (Ortega-Farias et al., 2009). As with many types of technology, decreasing cost of sensors, computers, and telemetry have

expanded the capacity to measure ET. More extensive deployments of cheaper sensors, rapid computation and massive data storage, and immediate global communication have all factored into an improved understanding of the variability of ET across the landscape. Fast response sensors (sonic anemometers and infrared gas analyzers) have replaced slow response instruments, allowing direct measurement of turbulent fluxes in the surface layers of the atmosphere, and these approaches have become ubiquitous in studies describing ET at field to regional scales (Baldocchi, 2014). In particular, the eddy covariance method allows measurements over tens of minutes, allowing experiments to resolve fluxes for both smaller areal footprints and to explore variability in ET at daily and shorter time periods (Foken et al., 2012). Implementation of large scale field experiments have led to improved understanding of field scale processes; flux estimates from these large scale experiments have been used to validate regional and global scale models of ET (Shuttleworth and Gash, 2006). Development of continental scale sensor networks (Jung et al., 2011; Lawford et al., 2011) and the advent of aerial and satellite instruments (Anderson et al., 2012; Li et al., 2009) have improved mapping of ET on global and regional scales.

Ongoing refinements in ET theory and instrumentation have allowed scientists to estimate evaporation rates under a greater range of complex and practical conditions. By measuring different properties and principles, long term ET estimates from different methods vary significantly (Mauder et al., 2013; Wang and Dickinson, 2012). By combining measurement techniques, limitations of any single method may be overcome and facilitate measurement in difficult or complex conditions. In large field campaigns, ET has been estimated across wide spatial scales with heterogeneous vegetation cover (Chehbouni et al., 2000; Evett et al., 2012). Combining methods can also improve long term estimates with poor quality data and when data are missing (Droogers and Allen, 2002). Results from multiple methods can reveal shortcomings of field methods and instrumentation, and guide experimenters to improve site specific

measurements (Higgins, 2012).

Significant progress has been made in validating remotely sensed ET estimates with ground based measurements (Kalma et al., 2008; Lewis et al., 2014), and integrating these ET maps into irrigation management (Cuenca et al., 2013b; Melton et al., 2012). For regional scale fluxes, a large number of studies have compared fluxes from eddy covariance tower networks with ET estimates based on multispectral satellite imagery (Chasmer et al., 2009; Gowda et al., 2015). In those conditions where remote sensing works well, spatial maps of ET can be produced, ostensibly generating site-specific information over a much larger extent than would be feasible by ground based measurement (Allen et al., 2011a). Ongoing research continues to validate remote measurements with ground based ones (Cammalleri et al., 2014a), to interpolate between intermittent ET estimates that are captured by satellite imagery and aerial photography (Ha et al., 2013), and to standardize spatial aggradation and interpolation methods (Ershadi et al., 2013; Karimi and Bastiaanssen, 2014).

This review focuses on the theoretical underpinnings of ET measurement, concluding with the current state of efforts by the research community. Following the structure of previous reviews (Allen et al., 2011a; Farahani et al., 2007; Rana and Katerji, 1998), representative methods are used to illustrate four fundamental approaches to measuring ET: water budgets, energy balance, atmospheric phenomena, and biophysical phenomena. These four approaches are complementary, yet common assumptions and experimental limitations mean that there remain places and conditions under which ET cannot be measured readily and reliably. Scaling limitations and practical constraints need to be overcome to provide more detailed ET information to inform irrigation planning. The review concludes by outlining ongoing research areas in irrigation and ET measurement, and giving a few examples of new methods that may expand the our ability to estimate ET.

4.3 Methods to Measure Evapotranspiration

This survey emphasizes measurement methods that are commonly used to monitor and forecast crop water demand, divided into four classes of ET measurement techniques. The first class includes methods that measure changes in water storage, in the soil, plants, or some combined control volume. The second class of techniques calculate ET as a part of the surface energy balance, composed of solar radiation, sensible and latent heat exchange.

The other two groups of methods refine and extend mass and energy balance methods, by parameterization of biophysical and atmospheric phenomena. The third class of techniques measure evaporation via transport of water vapor in the atmosphere. Biophysical methods measure physiological qualities (such as leaf color, canopy temperature, or sap flow rates) and parameterize growth, photosynthesis, or rates of active transpiration. These two groups of phenomenological methods make use of direct measurements of physical phenomena, but rely on a empirical relationships to equate measured variables with estimates of ET.

4.3.1 Conservation of Mass - Water balance methods

The first group of methods are based on measurements of soil moisture, with ET indirectly estimated from changes in water storage. Soil moisture measurement can be obtained at relatively low cost to determine the irrigation requirement. More generally, lysimeters, neutron probes, and other soil moisture measurements are used as the basis for quantitative determinations of crop water demand and ET rates from specific crops (Jensen and Allen, 2000). In general, these methods employ measurements of soil water content via weight, electromagnetic properties, or other physical proxy.

Soil water availability strongly controls the crop transpiration. Generally, irrigators attempt to keep crops adequately watered at all times, as even short term water stress can cause irrecoverable growth reduction and yield losses. This is especially true if crops are stressed

during early season growth (Lambers et al., 1998). Accounting for changes in soil water content (SWC) is one way to anticipate crop water demand and schedule irrigation. The simplest method to determine SWC is to collect a sample, weigh it at field moisture, dry it and determine the change in mass. However, collecting soil samples is an impractical method to determine irrigation decisions for large fields. In general, *in situ* measurements of SWC are used to track the uptake rate and forecast irrigation requirement, using various techniques including lysimetry, neutron scattering, measuring water potential (pressure), and measuring electrical properties of soil.

The earliest rigorous studies of crop water demand were lysimeter experiments conducted in the 17th century (Howell et al., 1991). Weighing lysimeters are large vessels enclosing soil and vegetation, buried flush with the surface. The lysimeter is constructed to replicate surrounding field conditions, both at the surface and throughout the soil profile. Inflow and drainage are controlled, and by recording changes in the weight of the lysimeter, changes in SWC are due to ET from the vegetated surface. Lysimeter studies are often conducted to establish crop coefficients (which are used with reference ET, section 2.4). Lysimeters continue to serve as control measurements of ET rates in the validation of new methods (Alfieri et al., 2012; Castellví and Snyder, 2010; Chavez et al., 2009). As a result, lysimeter operation and uncertainty have been researched extensively (Allen et al., 1991). The primary challenge in operating lysimeters is maintaining a surface that is representative of more general field conditions (Allen et al., 2011a); additional technical issues have been identified that originate from the physical construction and operation of the lysimeter enclosure (Grebet and Cuenca, 1991). Because of the high cost of constructing and maintaining lysimeters, and difficulties in extrapolating to larger scale field conditions, lysimetry is primarily a research technique rather than being used directly for irrigation monitoring.

To monitor field conditions and to forecast irrigation demand, several other techniques are employed to take direct measurements of SWC, including neutron scattering, time domain reflectometry, and capacitance probes. In contrast to weighing lysimeters, these methods use sensors that are relatively small and therefore movable, so that these methods can used to collect repeated SWC measurements in many locations. By using a sampling protocol which captures significant spatial heterogeneity (both by landscape area and by depth/profile), soil probes are used both in water management and in research to monitor spatial variability in SWC as it changes over time (Evett, 2007). By extension, similar electromagnetic properties that are measured by capacitance probes are applied in ground penetrating radar and microwave measuring systems to make remotely sensed SWC measurements.

The neutron scattering method has been a standard for determining soil moisture in the field since the 1950's. The neutron probe consists of high energy neutron source (usually americium-beryllium) and a low energy neutron detector. The probe is typically used in hollow access tubes which allow measurements at depth. Counts of slow neutron returns are negatively correlated with SWC. Regression analysis is used to develop calibration curves for different soil types (Bell, 1987). Field calibration is typically required to account for electronic drift (Schmugge et al., 1980). Regulation and safety of neutron sources limit the use of neutron probes to trained professionals, and this method requires manual measurement, so that labor costs can limit the number of repeat measurements that can be obtained. Nonetheless, because neutron scattering is non-destructive, repeatable, and is not affected by water phase (frozen), it continues to be used regularly for tracking SWC (Cuenca et al., 2013a; Evett et al., 2009).

Starting in the 1970's, methods were developed to determine SWC by measuring electromagnetic properties of the soil (Topp, 2003). These methods offered significant advantages over earlier methods by increasing the robustness of soil moisture measurements,

reducing the cost of implementation and instrumentation, and led to the development of remote measurement. Time domain reflectometry (TDR) uses pulsed current across two electrical contacts to determine electrical conductivity via travel time of the pulse wave. TDR returns a spatial average of the water content of the soil volume contained by an open conducting path between the probes, with typical separation distance of 20-150cm (Dalton and Van Genuchten, 1986). TDR has come to be regarded as a standard measurement method alongside neutron moderation (Topp, 2003), although its use is more common in research applications rather than applied monitoring for irrigation management.

Electrical capacitance is dependent on SWC, and the development of reliable methods to determine soil moisture from capacitance measurements has resulted in widely available capacitance probes suited to use in agriculture. Although there are a variety of configurations in commercial capacitance probes, the measurement principle is the same for all. A soil volume between electrodes of the probe acts as a capacitor, and by measuring capacitance of the circuit and knowing the instrument's capacitance, the soil moisture can be determined. Soil capacitance is also sensitive to soil texture, ion concentration (conductivity) of pore water, and temperature. Regression analysis is typically used to calibrate for sensor response across the expected range of field conditions, but these confounding factors can limit the reliability of these instruments (Baumhardt et al., 2000). While some authors report that calibration may be sufficient to overcome any environmental sensitivity (Kizito et al., 2008), other studies indicate that soil properties may lead to capacitance measurements that are poorly correlated to actual water content (Evett et al., 2009). Nonetheless, capacitance probes and other electromagnetic sensors continue to be at the forefront of applied monitoring as they are relatively robust, easy to deploy, yield simple determinations of SWC, and are very affordable compared to other instruments.

Regardless of the physical measurement used to determine SWC, probe type methods all

measure a relatively small control volume. While sampling strategies can address spatial heterogeneity, capturing adequate spatial and temporal resolution with point measurements is ultimately limited by practical considerations of cost and time. To overcome the sampling limits of point measurements, dielectric properties can also be measured remotely using ground based, airborne, and satellite sensors. At microwave frequencies, the radiative emissivity of soil is a function of the dielectric constant, and the induced magnetic field can be measured using either an active or passive mobile sensor (Huisman et al., 2002). Maps of water holding capacity and actual water content now allow assessment of soil water budgets at field scales (Minet et al., 2012; Vereecken et al., 2014; Verstraeten et al., 2008). A phased development of mobile and remote sensing systems began with ground based methods and proceeded to the development of aerial and satellite platforms. Ground penetrating radar (GPR) allows the mapping of soil moisture by a variety of methods measuring soil water distributions down to the scale of square meters (Huisman et al., 2003).

Terrestrial, active radar systems laid the foundations for remote sensing methods which use passive radar to measure water content from planes and satellites. While the resolution of measurements taken above the surface is proportionally reduced, these methods allow soil moisture mapping to occur over the extent of basins, regions, and even globally (Petropoulos et al., 2015). Programs such as AirMOSS (Chapin et al., 2012), SMOS (Kerr et al., 2012), and SMAP (Brown et al., 2013) currently produce repeat images and soil moisture data products using L and P band radar at spatial resolutions from 40km down to 3km. While these are not directly applicable to irrigation decisions at the field scale, this information has been used directly in determining risk of crop losses (Champagne et al., 2015), and has been validated for long term forecasting of regional water distribution (Gumuzzio et al., 2016).

Because physical properties of soil can vary greatly over short distances, the main challenge

of using soil moisture to determine the irrigation demand lies in capturing representative measurements, and accurately extrapolating to field conditions over large areas. This process is confounded by the fact that soil properties (such as water holding capacity) can vary greatly even over short distances, and mineral and electrical properties are confounding factors in the determination of water content and holding capacity. The actual water content of the soil is not the only factor in determining crop water demand: PAW can vary in response to soil texture or other environmental influences. Knowing the status of PAW and water holding capacity in the soil is complemented by knowing the actual rate of water use. With limited water resources, irrigation scheduling requires rigorous methods to predict actual crop water demand as well as soil water availability. Direct measurement of ET can be done by measuring the energy that drives evaporation and plant metabolism.

4.3.2 Conservation of Energy - the Surface Energy Balance

Solar radiation is the source of energy for ET, both through photosynthesis and direct evaporation. Incoming radiation from the sun is partitioned between sensible heating (of the air) at the surface, heating of the ground, and latent heat exchange (ET). The use of thermodynamics to determine ET represented a significant advance in the study of crop water use. A simplified the surface energy budget (SEB) is composed of four terms: net solar radiation received at the surface (R_n); the sensible heating (H) and latent heat exchange (LE) occurring in the air at the surface; changes in stored heat, the largest part of which is ground heat flux (G). These are only the largest terms in the energy balance of at the surface; a small part of the available energy is used in photosynthesis and biochemical processes. By assuming a balanced energy budget, $R_n - G = H+LE$ (the convention of the positive sense of H and LE being upward from the surface), allowing ET to be approximated from a few basic measurements- air temperature, incoming solar radiation, wind speed. Sensible heat flux can measured directly by thermometry. The standard instrument to measure solar radiation is with radiometers, which use thermopiles. Heating of the

ground heat is either approximated as a fraction of incoming radiation, or can be measured via thermopile. ET (latent heat) is calculated as a residual term in the energy budget.

Significant advances were made with the advent of energy based methods to determine crop water use. Bowen (1926) proposed the first important energy based estimate of evaporation over land surfaces (Lewis, 1995). The Bowen ratio is concisely described as the ratio of sensible and latent heat fluxes ($\beta o = H/\lambda E$). Bowen derived a thermodynamic relationship from the SEB, using the concepts of Fickian diffusion and similarity in the transport of heat and water vapor. Under homogenous surface conditions, lateral transport is negligible (when time averaged), the Bowen ratio is combined with the SEB to allow ET to be determined from gradients of temperature and vapor pressure (described as the Bowen Ratio Energy Balance method or BREB) For any given surface and over short (daily) time periods, it is expected that the ratio of sensible and latent heat flux remains constant (Brutsaert and Sugita, 1992). For general conditions, it is possible to make valid estimates of net radiation and ground heat flux based on time of year, latitude, and weather (Irmak et al., 2003; Jensen and Haise, 1963), although radiation and ground flux can also be measured directly. The Bowen ratio has been used extensively in agricultural settings to estimate ET, particularly since it is possible to measure humidity and temperature at two heights with robust and low cost instrumentation, and because hourly and daily estimates of ET were adequate for planning conventional irrigation planning (Cellier and Olioso, 1993; Fritschen, 1965; Perez et al., 1999). The BREB method continues to be used as a standard comparator for hourly and daily ET (Ortega-Farias et al., 1995; Prueger et al., 1997). While some authors have noted that the BREB is less affected by in homogeneous field conditions than other meteorological methods (Heilman et al., 1989), other studies have found that the BREB approach is sensitive to advection under many conditions (Gavilán and Berengena, 2007; Perez et al., 1999; Todd et al., 2000).

The second major theoretical contribution was Penman's (1948) paper on "evaporation from natural surfaces". One significant novel contribution of Penman's original equation is the inclusion of the vapor pressure deficit (VPD) and the slope of the saturation curve, incorporating the concept of aridity driven evaporation. Other formulation of the energy balance equation preceded and followed Penman's equation, notably by (Budyko, 1958), (Thornthwaite, 1948), Makkink (Rijtema, 1958), (Blaney and Criddle, 1962), (Priestley and Taylor, 1972) and (Hargreaves and Samani, 1985). The Penman equation combines the surface energy budget with an unknown "wind effect", using earlier work by Dalton as a basis to describe wind driven evaporation as a function of the vapor pressure deficit and wind speed. Subsequently, many authors have described ET equations including a wind effect (Allen, 1986). Various equations have expanded the original equation to quantify the contribution of wind and atmospheric effects on ET rates. Most notably, the Penman-Monteith equation has received the most use in the preceding decades (Jensen and Allen, 2000). Comparisons between different equations for potential ET are a perennial source of research projects (Amatya et al., 1995; Itenfisu et al., 2003; Ventura et al., 1999), and selection of a single equation for reference ET has coalesced with the development of standard methods (Allen et al., 2000; Hargreaves, 1994). One criteria in selecting a particular equation is to obtain the greatest accuracy under a specific range of conditions, such as over well watered crops in arid conditions (Droogers and Allen, 2002; Walter et al., 2000). Alternately, a reference ET equation may be selected for robustness under a broad array of field conditions (such as when applying to a regional network), especially when data sources are limited or unreliable. Some methods rely solely on single factors such as daily radiation (Samani, 2000) or air temperature (Tabari et al., 2013). Such methods are especially useful in regions lacking long term weather records or when data quality is poor.

In addition to instrumentation at the surface, surface heat flux can be estimated remotely from radiant temperature measurements, which are used to calculate surface temperature gradients, and

by extension, the surface energy budget. Theoretical models such as SEBAL (Bastiaanssen et al., 2005) use algorithms to calculate surface parameters (roughness, reflectance, transmissivity, etc.) and radiation measurements at each pixel are used with a reference ET to calculate a spatial map of relative ET rates (Allen et al., 2001). This approach requires continuous data for weather and reference ET, and requires validation for assumptions about the relationships between remote observations and surface parameters (Chávez et al., 2008; Field et al., 1992). Closure of the surface energy budget is assumed for these methods to work; variability (such as advective redistribution and missed energy pathways) is generally addressed by time averaging (Allen et al., 2011a). The use of remote thermal imaging to map ET at the field to basin scale has become common practice in water resource research (Anderson et al., 2012; Kalma et al., 2008) and in direct application to mapping irrigation (Cuenca et al., 2013a) and to map water productivity in irrigated crops (Zwart and Bastiaanssen, 2007). Validation (Behnke et al., 2016; Gowda et al., 2015) and accuracy assessment (Karimi and Bastiaanssen, 2014; Morton et al., 2013) of spatially explicit ET estimates are ongoing areas of research.

4.3.3 Atmospheric phenomenology

From the earliest observations of evaporation, it was recognized that wind and atmospheric conditions affect the rate of flux (Brutsaert, 1982). Methods to determine ET from measurements of turbulent air flow and boundary layers are based on the concept that atmospheric transport of momentum, heat, and water vapor are similar. By measuring gradients or profiles of temperature and humidity, vertical flux from the surface is treated as a diffusive process. However, turbulent mixing in the atmosphere is orders of magnitude more effective than diffusion in transporting scalars. By assuming that turbulence is geometrically homogenous at small scales, and that scalar fluxes are driven by gradients, turbulent driven flux is treated as an enhanced diffusive process, albeit with a much higher rate of transport (Brutsaert, 1965). Based on theories of turbulent behavior, scaling relationships and statistics of wind speed, humidity, and temperature are used to

determine surface flux rates. Important parameterizations of atmospheric measurements include: decomposition of flows into mean rate and fluctuations (Reynolds, 1894); dimensionless scaling parameters such as mixing length, stability, and friction velocity (Prandtl, 1925; Sutton, 1949); spectral distribution of energy between transport scales and mixing scales (Kaimal and Finnigan, 1994; Yaglom, 1957); and the distribution of scalars in the vertical wind profile (Hill, 1989). Monin and Obukhov similarity theory (MOST) uses these scaling parameters to describe the relationship between flux and atmospheric profiles under various stability conditions (Monin and Obukhov, 1954; Yeh and Brutsaert, 1971). By fitting empirically measured data relationships to experimental data, universal functions for flux profiles have been experimentally validated for both unstable (Brutsaert, 1982) and stable conditions (Andreas, 1988; Pahlow et al., 2001).

Actual measurements of turbulent flow in the atmosphere began with validations of the "log law" of vertical wind profiles (Sutton, 1949) and estimation of ET from those climactic parameters which could be feasible measured (Priestley and Taylor, 1972). Flux-profile relationships (Businger et al., 1971; Dyer, 1974) led directly to estimations of latent heat flux from temperature and water vapor measurements. To determine fluxes from gradient profiles, an assumption of homogenous surface conditions is required, which assures that turbulent flow is fully developed and well mixed at the measurement height (Lettau, 1969). Effects of advection and inhomogeneity, are assumed to be averaged out by selecting a site fin which upwind field conditions are as homogeneous as possible, and approximating aerodynami effects of the surface with linear functions of measureable factors such as vegetation height (Penman, 1948). The validation of these calibration factors for a wide range of field conditions has resulted in widespread applicability of the Penman-Monteith equations (Farahani et al., 2007).

The practical application of the statistical descriptions from turbulence theory for determining scalar fluxes became feasible in the 1980's with the advent of fast response sensors for

temperature and humidity, and with improvements to sonic anemometers and data loggers. In the eddy covariance (EC) method, the flux of water vapor is determined from the covariance of fluctuations of water vapor and vertical wind – i.e. flux away from the surface occurs when wind speed fluctuations and changes in water content vary together, and flux towards the surface when fluctuations are opposite in sign (Schotanus et al., 1983). Early experiments established the validity of eddy covariance as a method of determining scalar fluxes over crop and forests (Desjardins et al., 1984; Verma et al., 1986). Flux measurements are averaged every 10 to 30 minutes during periods which have reasonably stationary wind conditions (Businger, 1986; Yeh and Brutsaert, 1971). A number of mechanical and statistical considerations are important to assure that covariance measurements are valid (Baldocchi, 2014; Foken et al., 2012). EC is a predominant method for measuring ET, with the worldwide networks of EC towers such as FLUXNET (Wilson et al., 2002). Conceptual footprint models are used to extrapolate areal estimates of ET from point measurements; various footprint models are based on stochastic Lagrangian dispersion, Large Eddy Simulation (LES), and analytic solutions for contributing area (Rannik et al., 2012; Vesala et al., 2008). The use of footprint models are validated by experiments in heterogeneous land cover (Schmid and Lloyd, 1999), and useful to understanding the cumulative contribution to flux from heterogeneous vegetation (Sutherland et al., 2014). Additional assumptions of statistical validity are required for simplification of time averaged measurements (Higgins et al., 2013; Katul et al., 2006) and to address extrapolation of short measurement periods to ET of daily or longer periods (Massman and Lee, 2002).

To measure areal estimates of ET directly, turbulence theory can also be applied to relate fluxes with the scintillations in the atmosphere, integrated over the path of a laser at distances of from hundreds of meters to several kilometers. Scintillations in the transmitted light are due to variation in the refractive index, which is a function of air density, temperature, and water vapor. Scintillations in the transmitted light correspond to turbulent eddies which are responsible for the

major part of flux. By directing multiple beams of infrared or microwave light, the rate of scintillation can be used to determine the contribution from different scalar fluxes (water vapor, temperature, etc.). The measurement is a path averaged intensity between of the transmitted beam and the sensor (Leijnse et al., 2007; Priestley and Hill, 1985). Refraction is different for each wavelength of transmitted energy, and by using multiple wavelengths of light, determinations of water vapor, heat, and momentum flux can be measured (Andreas, 1989; Hill, 1997). Alternately, non-linear effects to determine scalar fluxes can be simplified using assumptions from similarity theory (Hill, 1992). Additionally, scintillometry depends on measurement of mean temperature, pressure, and humidity; so that defining an appropriate averaging period can be a difficult (Andreas et al., 2003). While this method gives an integrated, path averaged measurement, the homogeneous surface assumption from M-O similarity theory require that special care must be taken to interpret measurements over heterogeneous surfaces, where behaviors such as boundary layer development may not be uniform (Beyrich et al., 2012).

4.3.4 Biophysical phenomenology

Plants cover the majority of the terrestrial surface, and consequently the rate of ET is controlled by plant metabolism and ecology in addition to soil water availability, net solar energy, and atmospheric transport. Plants have complex mechanisms adapted to conserve water while maximizing carbon and energy exchange for photosynthesis and respiration. Complex biological pathways, drought adaptation, and physical characteristics such as rooting depth, vegetation height, and leaf area can all significantly affect ET rates on daily and seasonal time scales. In some cases, these effects can be measured directly, or modelled effectively with empirically calibrated relationships.

The most ubiquitous method used to estimate daily ET is the Penman-Monteith (PM) equation, expanding on the Penman equation by incorporating biophysical properties of crop

canopies (FAO 56). The PM equation is used to determine a reference evapotranspiration ET_0, which is employed with crop-specific coefficients to estimate actual crop ET_a (Allen et al., 1998; Hargreaves, 1994). The reference ET_0 can be determined daily or instantaneously: daily calculations use averaged meteorologic and radiation data, while instantaneous calculations also require continuous wind speed inputs (Allen, 2005). Crop coefficients are used to adjust reference ET to a specific crop ET; these coefficients account for differences in crop water use and aerodynamic properties of the crop canopy (Allen et al., 1998). Crop coefficients are determined experimentally, typically from lysimeter studies, although methods to approximate unknown coefficients have been proposed using both field measurements (Allen and Pereira, 2009) and remotely sensed data (Hunsaker et al., 2003). Crop coefficients (K_C) adjust reference ET for seasonal variability, drought adaptation, and other non-linear effects to a specific crop's rate of water use. The PM equation relies on measurements taken under reference conditions, so that in most cases, reference ET estimates are derived from measurements taken at long term monitoring sites. Maintaining a monitoring site requires reference surfaces (12 cm grass turf or 50 cm alfalfa) that are well-watered to minimize drought stress. Crop coefficients are available for most commercial crops, but are more limited in predicting ET rates for new crop varieties (Fisher, 2012), or under deficit irrigation and other conservation strategies (English and Raja, 1996). Also, reference ET alone is not sufficient to address the information requirements of precision irrigation systems (Daccache et al., 2015). Networks of these monitoring sites have become ubiquitous in the continental United States, and ET forecasting is increasingly integrated into the cooperative networks of weather forecasting including the National Weather Service's web delivered products[d]. Despite limitations on the representativeness of reference ET, network monitoring and ET reporting are now widely accepted as a standard data source in estimating basin scale ET (Mateos et al., 2013) and for irrigation scheduling (Allen and Jensen, 2015).

[d] *http://www.emc.ncep.noaa.gov/mmb/nldas/drought/Evap/*

Modernization and systemization of ground-based weather networks has been a national priority since the 1990's (National Research Council, 2012). Critical end uses of weather data include refining understanding of hydrologic processes, and specifically crop ET information (NRCS, 2015)[e]. Consequently, states and regional water authorities have increasingly allocated resources to developing networks specifically to measure and report ET, primarily in agriculturally productive areas (Elliott et al., 2000; Horel et al., 2002). Automation, improving instrumentation reliability, and quality control of data are areas of ongoing research (Allen et al., 2011b; Fiebrich and Crawford, 2009). Several ET specific networks (and those with ET reporting as a primary purpose) have now been fully automated for over two decades: a few examples include OKMesonet (Oklahoma); Agrimet (Pacific Northwest); CIMIS (California); TexasET network; AgWeatherNet (Washington State); FAWN (Florida). Most of these networks also offer information on irrigation efficiency, integrated irrigation scheduling apps, and other agriculture specific resources. A more comprehensive list can be found at the Agricultural Water Conservation Clearinghouse, part of the Colorado Water Institute[f]. The National Weather Service (NWS-NOAA) has begun to include reference ET product in the web based forecast interface as of 2015[g], and ET maps are already implemented on an experimental basis in some regions (Snyder et al., 2009) . The extent of these efforts reflects the extensive list of benefits including water use efficiency gains, reduced direct costs, improved pest and disease management, and irrigation savings in non-ag sectors (Parker et al., 2000). Reduced risk of crop loss provides a direct benefit and also can reduce insurance costs (Barnett and Mahul, 2007). The direct benefits in resource conservation greatly outweigh the cost of building capacity to deliver ET forecasts (Parker et al., 2000), and federal state and regional authorities increasingly prioritize the development and maintenance of these services. The value of these network to state and regional

[e] *http://www.nrcs.usda.gov/wps/PA_NRCSConsumption/download/?cid=stelprdb1269279&ext=pdf*
[f] *http://www.agwaterconservation.colostate.edu/ToolsWeather.aspx*
[g] *http://products.weather.gov/PDD/FRET_PDD.pdf, Accessed 10Mar2016*

authorities is evident in ongoing work to improve the reliability and utility of these estimates (Liu et al., 2011).

In forested areas and on other non-irrigated land, ET is constrained by plant-mediated stress response to water limitation (Manzoni et al., 2011). To address biological control mechanisms, sap flow can be measured through individual plants (Wullschleger et al., 1998). The most often employed methods determine sap flow from measuring the dissipation of heat: heat flux (between two probes, or in terms of power loss from a single probe) is correlated to volumetric sap flow (Marshall, 1958; Smith and Allen, 1996). This method directly measures active water transport in the plant, but has a large labor cost to obtain sufficient samples for representative measurements (Oren et al., 1998; Schaeffer et al., 2000). The sampling method also requires experimental design that accounts for temporal (especially diurnal) variability, homogeneity of canopy cover, and storage of heat and water within the canopy itself (Hatton and Wu, 1995). Increasingly, sap flow studies also measure use isotope analysis to determine fractional contributions of evaporation and transpiration, providing new insights on the contribution of biological controls on the ET rate (Good et al., 2015; Wang and Dickinson, 2012).

Finally, multispectral imagery can be used to parameterize vegetation characteristics, and these vegetation characteristics, corroborated with ground measurements, can be used to generate maps of ET for entire basin and regions. These methods differ from temperature based remote sensing methods (described above) by using correlation between vegetation properties and ET, rather than calculating ET as a direct residual in the surface energy balance. As with SEB methods, these ET models require ground validation or use input parameters from field measurements. Heterogeneity in land cover and vegetation may be derived from high resolution photography (Detto et al., 2006) or multispectral imagery (Hashimoto et al., 2008) and used to drive parameterized vegetation response models. Lidar scanning has also been used to determine

leaf area index (LAI) and calculate fluxes using the Penman-Monteith equation (Farid et al., 2008). The determination of vegetation characteristics from remote imaging relies on indices that relate spectral reflectance to vegetation structure, the simplest example being the Normalized Differenced Vegetation Index (NDVI). Vegetation reflects light at near infrared (NIR) wavelengths and absorbs red wavelengths preferentially, so the ratio of NIR and red reflectance is used to calculate vegetation density.

Vegetation maps are used to estimate landscape scale ET even with surface heterogeneous conditions, but remotely sensed data is limited in temporal resolution because while satellite and aerial images are captured instantaneously, they are also collected intermittently (Cammalleri et al., 2014a; Li et al., 2009). Furthermore, different algorithms may be preferred under different soil, vegetation, and atmospheric conditions, limiting and complicating the automation of surface models (Chávez et al., 2008). In addition to estimating ET between images, issues with spatial scaling of imaging data increases uncertainty in correlations with point measurements taken at the surface; some estimates of biological and atmospheric parameters are scale dependent and mismatched to remote measurements (McCabe and Wood, 2006). Several excellent and comprehensive reviews of the remote sensing ET methods exist (Anderson et al., 2012; Kalma et al., 2008; Li et al., 2009).

4.4 ET Measurement - Progress and Challenges

To make ET estimates useful to water managers, substantial progress has been made to improve the spatial resolution and extent of ET measurements, to make on-demand estimates readily available, and to improve the reliability of reference ET methods. Nonetheless, ET measurement remains challenging under some conditions, such as during light rain and fog (R. Moratiel et al., 2013), for under-irrigated crops (Barker et al., 2015), or when advection strongly affects the transport rate (Lee et al., 2004b). Real-world conditions often don't conform to theoretical simplifications: soils characteristics aren't homogenous; crops control respiration in

response to water shortage; advection and overland flow redistributes irrigation water; the wind does not conform to theoretical profiles. While corresponding adjustments (such as provided in the Penman-Monteith equation) can correct for some degree of uncertainty, ET estimates are tied to the specific sites, spatial scales, and the time that physical measurements were taken.

Estimating ET is more complicated in areas with heterogeneous vegetation or with variable soil characteristics (Anderson et al., 2009; Raupach and Finnigan, 1995). The daily cycle of the surface energy budget, synoptic scale weather variability, and extreme events such as drought all limit the periods at which valid flux measurements can be obtained (Katul et al., 2005; Massman and Lee, 2002). Biophysical controls on ET such as drought adaptation and growth rates vary between species and individuals, so that plant response varies with environmental conditions (Katul et al., 2012). The development of ET measurement methods has been marked by advances to overcome these specific limitations (Droogers and Allen, 2002).

4.4.1 Spatial and temporal scales of measurements

Evapotranspiration is variable over time and across the land surface. For decades, a general experimental guideline was to maintain a ratio of 1:100 (height to fetch) of homogenous conditions upwind of a measurement (Horst and Weil, 1994). This was meant to ensure that advection and non-uniform field conditions could be neglected in flux calculations that treat ET as a one dimensional (surface to atmosphere) diffusion-like process. A more nuanced concept of footprints has emerged that allows researchers to evaluate fluxes calculated from surface measurements within more challenging, non-uniform conditions (Schmid, 2002; Vesala et al., 2008). Localized measurements (lysimeters, eddy covariance, surface renewal, sap flow, et cetera) can be highly resolved in time, but must be sited carefully to capture representative measurements of spatial patterns; site selection can present a significant challenge (Allen et al., 1991; Lee et al., 2004b). ET measurements can be averaged over periods long enough to minimize the relative influence of advection, but this can also mask spatial differentiation of ET rates (Allen et al., 2011a; Mauder et al., 2013). It is easier to measure ET at sites with

homogeneous surface conditions, determination of ET with complex vegetation and topography remains an important area of applied research.

Spatially explicit determinations are possible from satellite and aerial imaging, from path measurements obtained with scintillometers, and from interpolating dense networks of local ET estimates. Remotely sensed imaging methods flatten surface irregularities to the scale (pixel size) of the measurement (Kalma et al., 2008). Spatial maps provide new insights into ET from complex landscapes, but these methods still require corroboration from ground measurements (Cooper et al., 2000; Gowda et al., 2007). Images obtained from satellite and aerial platforms also require interpolation between intermittent images. The return time of remote sensing varies from 8 day intervals (such as Landsat), to annual overflights (National Agricultural Imagery Program). Interpolation requires validation using continuous surface measurements (Anderson et al., 2011).

Daily and seasonal variability of surface and atmosphere conditions also complicate the estimation of ET. Ground based methods (eddy covariance, Bowen ratio, Penman Monteith, et cetera) can measure ET continuously. These methods assume stationarity over an averaging period, and consequently miss some portion of the flux that occurs over time scales longer than the averaging period, as shown by long term records (Malhi et al., 2004; Mauder et al., 2006). Similarly, the sampling frequency for any method determines the limit for detecting high frequency fluxes. The development of fast response sensors has allowed the exploration of spectral attenuation at high frequencies in flux measurements (Biltoft and Pardyjak, 2009; Vickers and Mahrt, 2003). Converting field measurements to ET is aided by uniform protocols and quality control criteria, which are still being established for eddy covariance (Allen et al., 2011b; Mauder et al., 2013). Non-uniform field conditions require extra consideration during experimental design and processing of data (Gu et al., 2012; Moncrieff et al., 2005).

4.4.2 Practical considerations

Some of the techniques to determine ET measurements can be implemented directly by farmers and water managers. Other methods require instrumentation, labor, or expertise that practically limits their use to professional researchers or specialized contractors. Substantial research and technological development have greatly expanded the types of affordable and robust instrumentation available directly to irrigators and water managers (Burt et al., 2005). Miniaturization and telemetry systems have made it possible to maintain on-farm and in-field weather monitoring at low cost (Ruiz-Garcia et al., 2009). Capacitance probes have made monitoring continuous soil feasible at low cost, allowing relatively widespread deployment (Kizito et al., 2008), as well as real time integration of this data into irrigation scheduling (Buhrig and Shock, 2015). Over the last 50 years, farming has become a highly technical profession, require expertise not only with tractors, implements and water delivery systems, but also knowledge of sensors, computers, navigation systems, and telemetry. The available data often outpaces farmers, who struggle to find time to incorporate this information into existing farm systems (Perry, 2007; Weiss et al., 2000); integration and decision support systems are an area of rapid expansion (Barker et al., 2015; Hillyer, 2011).

Additionally, many sources of ET data are available through web-based interfaces, decision support software, and direct technical support for irrigation systems (Elliott et al., 2000). Integration of technology and IT infrastructure facilitates the availability of these systems, but downscaling regional estimates and applying the information to site-specific irrigation still requires substantial adaptation (Evans et al., 2013). By improving the resolution and increasing the frequency of remotely sensed imaging, and by expanding the number of ground based observations, these services have been vastly improved in the last two decades (Gowda et al., 2015; Karimi and Bastiaanssen, 2014). However, this information is still not resolved to scales matching that of site-specific irrigation technology. Site based measurements will continue to be important into the foreseeable future, and developing cost-effective and robust methods to

measure ET on-site will be a priority for sustainable and efficient water use planning.

4.4.3 New directions in ET measurement

There has been substantial improvements to the reliability, accessibility, and resolution of ET estimates. Yet significant work remains to address the need for site-specific, on-demand, high resolution ET information required for precision irrigation and water management strategies. Standardized procedures for methods such as the Penman Monteith equation and eddy covariance are being actively updated to include the latest advances in sensors, theory, and quality control. There are a number of new ways to that ET estimates are disseminated to irrigators and water managers in real time including web based ET mapping products, the surface renewal method, UAVs as measurement platforms.

Standardized method has been particularly developed for eddy covariance and the Penman-Monteith equation, as these have become the most common control estimates in research and monitoring, respectively. As of the time of this review, the second edition of ASCE's Manual 70, "Evaporation, Evapotranspiration, and Irrigation Requirements" is in press. Jensen and Allen (2015) described extensive updates to the Manual, expanding coverage of standard reference ET and crop coefficient methods, direct ET measurement, data quality, the role of modern computing, and methods to deal with inaccurate or incomplete data. Similarly, eddy covariance research had addressed corrections for factors including energy balance closure (Foken, 2008; Irmak et al., 2014), advection and footprint models (Lee et al., 2004b; Vesala et al., 2008), instrumentation error (Kochendorfer et al., 2012; Rubén Moratiel et al., 2013), and data quality control (Kim et al., 2011; Mauder et al., 2006). A number of texts cover implementation of eddy covariance (Burba, 2013; Lee et al., 2004a); standardization of eddy covariance measurements have been developed for continental networks (Baldocchi et al., 2001; Papale et al., 2006). However the data processing requirements for eddy covariance measurements have limited the transition of eddy covariance from research to monitoring applications (Lawford et al., 2011). Mauder et al. (2013) proposed an overall framework for quality control of long term eddy

covariance measurements. (Baldocchi, 2014) outlined several areas where eddy covariance continues to provide insight: paired studies in complex environments; long term measurement sites and networks that study climate variability; validation and calibration of other methods, particularly remote sensing; providing baseline data for models and machine learning algorithms.

By standardization of methods and establishment of monitoring networks, the extent of ET estimates has been expanded to cover most agricultural production areas of the US. With remote sensing, operational estimates of ET are available globally. However, increasing the resolution and robustness of these estimates continues to depend on ground based measurements. A huge volume of data is available via internet resources generated and maintained by public agencies (increasingly for no cost) and from private companies targeting the agricultural sector. In addition to regional weather networks, many states and regional water authorities provide irrigation scheduling software and daily ET estimates. The ability to provide continuous maps of reference ET is possible due to the combined progress on reference ET equations, remote sensing technology, and biophysical models. Recent work validates RS estimates from ground measurement (Cammalleri et al., 2014a; Mateos et al., 2013); check spatially interpolation (Ershadi et al., 2013; Ha et al., 2013; Tang et al., 2013a); and temporal interpolation, i.e. between satellite images (Cammalleri et al., 2014b; Tang et al., 2013b); and to check the robustness of automation and user skill limitations (Allen et al., 2015; Morton et al., 2013). Many providers are including reference ET in more generalized weather data, calculating ET maps using a combination of gridded weather information and Landsat images, and calculating ET from the P-M equation (Liu et al., 2011). Most recently, the National Weather Service has begun to produce experimental forecast maps of reference ET for the entire contiguous U.S.[h]. The accessibility of these ET map products make them directly transferable to an integrated water management system, but generally, their spatial resolution is on the order of kilometers or greater, resulting in pixel areas of 100 hectares. Precision irrigation equipment is capable of delivering water to areas

[h] *http://digital.weather.gov/, Accessed March 11, 2016*

on the order of 0.1 hectare or better, requiring ET and water use estimates matched to this finer resolution.

The surface renewal (SR) approach estimates air exchange rates from fast response measurements of air properties like temperature and humidity. In particular, fast response thermometry can be conducted cheaply and easily, so that surface renewal theory creates a low cost method of determining sensible heat flux with no additional instrumentation (Snyder et al., 2008). Conceptually, SR is based on the observation that rapid temperature changes are associated with surface air parcels that are displaced and "renewed" from upper air (Paw U et al., 2005). Under turbulent conditions, the rate of temperature renewal is the majority portion of the sensible heat flux. With this estimate of sensible heat exchange, surface renewal can be used with measured net radiation and ground flux to calculate the latent heat flux as a residual (Castellvi et al., 2006). Alternately, the latent exchange can be deduced directly from high frequency measurements of humidity, where a sharp change in humidity is associated with a displacement of moisture enriched parcels with drier air from above, or vice versa (Castellvi et al., 2008; Katul et al., 2006). SR has been shown to be reliable and low cost method to measure ET for both high value crops (Spano et al., 2000) and pasture (Castellvi et al., 2008), but challenges remain in establishing robust and low cost instrumentation for direct estimates of latent exchange, as there is no low cost fast response humidity probe available.

Applications of unmanned aerial vehicles (UAVs) to rapidly and cheaply collect imagery that has many applications in agriculture: UAVs are increasingly used to detect drought stress (Gago et al., 2015). Multispectral imagery has been used to index plant water stress in vineyards (Bellvert et al., 2014), citrus (Gonzalez-Dugo et al., 2013), and field crops (Rossini et al., 2013). The utility of UAVs in collection agricultural information relate directly to the needs identified above- they provide a platform for real-time, on demand, and highly resolved imaging of field conditions . The majority of sensors utilized in UAVs are high resolution cameras and multispectral imaging devices (Herwitz et al., 2004; Zhang and Kovacs, 2012), but also to

calculate surface fluxes using energy balance models (Hoffmann et al., 2016) and to measure atmospheric profiles directly in combination with fiber optic[i] and other sensor technologies (Lampert et al., 2016). Although UAVs are not inherently a measurement technology, they will become increasingly prominent as a platform for ET measurement for agriculture generally and precision irrigation specifically (DeBell et al., 2015; Vivoni et al., 2014).

4.5 Conclusions

Researchers and extension agencies have made substantial progress in addressing the need for real-time, site specific ET data. Methods to map the spatial variability of ET include both direct field measurement and remote sensing technology. Daily, gridded ET maps are readily available in most agricultural regions of the US, and can be validated from continuously measuring regional ET networks. On farm weather stations can potentially provide site-specific ET estimates that, given sufficient refinement and maintenance have nearly the and reliability of regional network weather systems. Water managers and irrigators have at their disposal a number of commercially produced measurement methods that can be combined to produce sophisticated and robust ET estimates.

Yet challenges remain to coordinate the myriad sources of ET information into a reliable and affordable system for determining crop water demand, particularly for precision irrigation systems. Precision irrigation in some cases requires ET estimates resolved spatially to 10's of meters (10^{-2} hectares). Furthermore, irrigators scheduling large complex delivery systems (often with limited power and water resources) need this information to be updated as rapidly possible, and available on demand. With increasing farm sizes, tracking crop demand is complicated by heterogeneous soil types, microclimates, and the various types of crops grown. In the arid west, increasing regulation and renegotiation of water withdrawals, coupled with seasonal uncertainty and climate change, will require irrigators and water managers to have increasingly sophisticated information and understanding to optimize water distribution.

---

[i] *https://eos.org/project-updates/drone-squadron-to-take-earth-monitoring-to-new-heights*

Incorporating new technology and information into planning farm operation can be costly and risky, and overcoming reluctance of farmers requires that new methods are easy to understand, provide relevant information, and are reliable. On-farm sensing of ET will be critical to making site-specific ET measurements in precision irrigation applications. For this to be feasible, the marginal benefits of optimizing water use must outweigh the costs of implementing and maintaining sensors. Growing crops requires huge amounts of water, so that efficiency gained through precision irrigation can be a significnat source of resource conservation and cost savings. But for these savings to be realized, precision irrigation requires highly resolved maps of crop water demand.

5. Surface Renewal in Motion for Mapping Evapotranspiration

Mapping the spatial variability of evapotranspiration to determine actual crop water use is a critical step in using precision irrigation to increase efficiency. These maps need to fulfill three criteria to be useful in planning irrigation. First, ET must be measured often enough to detect when crops when require irrigation. This means ET estimates should be updated weekly, daily, or even more often, depending on crop drought sensitivity, soil water holding capacity, and type of irrigation system. Second, ET maps need a spatial resolution matching the best possible irrigation precision. As shown in Chapter 2, the determination of the spatial resolution of a center pivot system is on the order of 30 m (~0.1 hectare area). Third, the ET information needs to be readily available and obtained at low cost to be broadly useful to irrigators. At present, precision irrigation scheduling relies on a combination of information sources, including ET forecasts from regional weather networks (Snyder et al., 2009), crop water demand models (Hillyer, 2011), soil texture maps (Hedley and Yule, 2009), on-site weather stations (Elliott et al., 2000). No single method fulfills the three requirements of precision irrigation: local specificity, regular updating, and affordability. It is theoretically possible to combine the strengths of several methods by combining information from different sources: for instance, continuous ground based measurements can be used to validate extensive, intermittent satellite images. However, combining different information sources is problematic when they do not agree, and no there is no established method to decide which is the most reliable estimate (Allen et al., 2011b). Because farmers lack the time and resources to reconcile discrepancies and choose the most reliable source for themselves, there is a tendency to default to a conservative strategy of overwatering to reduce risk of crop loss; this is a major impediment to maximizing water efficiency (Molden et al., 2010). Yet farmers readily acknowledge a desire for more accurate and reliable information on crop water demand (Weiss et al., 2000), and seek to justify the use of

precision systems with demonstrable cost savings and water conservation (Sadler et al., 2005).

From a review of methods available to measure ET (Chapter 4), the surface renewal (SR) technique emerged as potentially capable of meeting three requirements needed to map ET using direct field measurements (as opposed to using remotely sensed ET estimates). Previous studies have shown that flux measurements can be captured very near the surface or near the top of the plant canopy using SR (Katul et al., 1996; Paw U et al., 1992). By taking measurements very close to the surface, the measurement fetch is effectively reduced and consequently the area from which the flux can be attributed is smaller. Several authors have found that the method can measure fluxes during periods of stable conditions (Paw U et al., 1992; Snyder et al., 2008). Because of a reduced dependence on flux-gradient theory, it has been noted that SR may be less affected by fetch requirements (Paw U et al., 2005). Following on this concept of reduced spatial requirements, it was further postulated for this study that the detection of rapid events (ramp-like coherent structures) may allow flux estimates over shorter periods possible with EC (Figure 5-1). Finally, the SR method can obtain heat flux using only high frequency measurements of air temperature, depending on the calculation method. Low cost equipment thermocouples allow sensible flux to be measured in more locations than could be accomplished with expensive equipment such as EC systems, and future sensor developments could allow direct measurement of latent fluxes as well. Flux can be also measured in situations where deploying more expensive equipment would be infeasible (such as under moving irrigation systems).

EC is not more widely used for agricultural monitoring precisely for reasons of equipment cost and fragility, and the need for skilled maintenance and data analysis (Allen et al., 2011a). As with many methods that have been adapted to tractors and vehicles for agricultural monitoring (Gago et al., 2015; Peters and Evett, 2007; Steinberger et al., 2009), it would be useful to be able to measure a flux from unmanned aerial vehicles (UAVs) to obtain maps of ET and water demand

in actively growing crops. The low weight of fine wire thermocouples suggested the possibility of deploying a SR sensor on small UAVs or on other machinery employed in farm operations such as center pivots, ATVs, or tractors. This study specifically addresses the feasibility of moving SR flux measurements. Field validations were conducted to establish the robustness of SR to measure flux from a moving measurement platform. The long established eddy covariance (EC) method was used as a control measurement. To accomplish this, co-located instrumentation was used to obtain simultaneous EC and SR fluxes, both in stationary trials and trials conducted on a moving vehicle. With the rapid expansion of aerial sensor platforms into the agricultural sector, surface renewal offers a feasible method to map variable ET at scales relevant to precision irrigation. A mobile SR method has the potential to be more cost effective than eddy covariance, Bowen ratio determinations, or Penman-Monteith methods to resolve crop water demand spatially at sub-field scales.

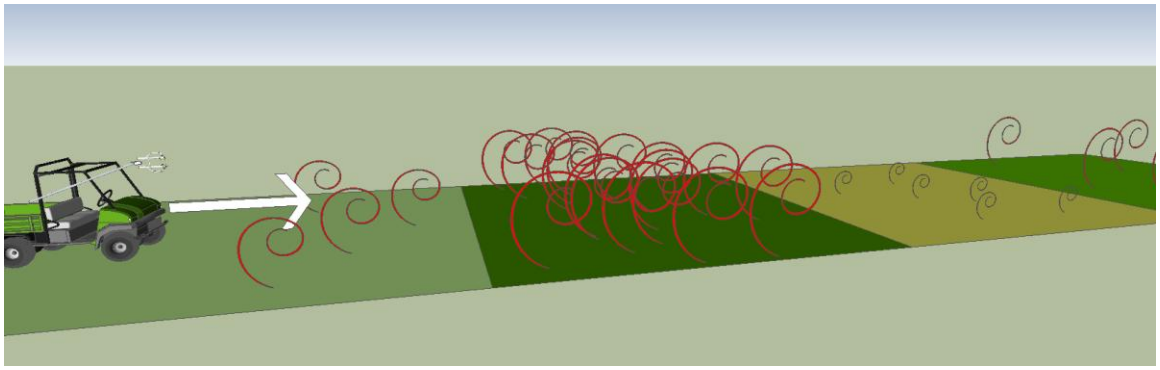

Figure 5-1: Conceptual Moving SR Method, Mapping ET

If ET near the surface can be measured rapidly **while moving**, high resolution maps of ET can be generated. Here, landscape variability is visualized as different colored surfaces, with variable flux rates from these surfaces imagined as eddies (red), indicating the role of turbulence as the primary driver of transport.

5.1 Surface Renewal Theory and Review of Previous Studies

5.1.1 Physical Model of Coherent Structures and Method Assumptions

The surface renewal (SR) method estimates air exchange rates from fast response measurements of temperature, humidity, and other transported scalars. The concept of surface renewal is based on the idea that rapid temperature changes are associated with surface air parcels

that are displaced and "renewed" from upper air (Castellví et al., 2002; Katul et al., 1997). These parcels can be also be described as intermittent, coherent structures visible in a time trace of the measured scalar (Figure 5-2). In the physical model of eddy covariance (EC), turbulence is the primary agent mixing and transporting scalars from the surface. When sampling over some reasonable averaging period, flux equals the covariance of vertical wind speed and the scalar concentration. This is notated as $\langle w'T' \rangle$, where w' indicates wind speed, the prime (e.g. T') indicates fluctuations from the mean temperature, and < > brackets indicate a time average. For periods of 10-60 minutes, this averaging procedure allows the determination of the sensible heat flux by multiplying air density [$kg \cdot m^{-3}$] times the heat capacity of the air [$J \cdot kg^{-1}K^{-1}$] and $\langle w'T' \rangle$ [$m \cdot K \cdot s^{-1}$] to obtain the heat flux in watts per square meter. SR theory extends this by attributing the majority of flux to episodic, turbulent ejections from the surface layer into the upper air. Calculating fluxes using EC, the vertical flux can be thought of as the transport of a scalar property (such as heat content, water vapor, etc.) via the vertical component of intermittent wind gusts. When measuring the scalar over time, the intermittent transporting gusts can be considered coherent structures, with a definite duration and marked by a rapid change in the scalar (temperature). The magnitude of these rapid changes, also called ramps, and the ramp duration are used to determine the flux.

Experimental evidence shows that these coherent structures are responsible for the majority portion of the flux (Gao et al., 1989). The physical basis of these periodic changes are based on air "parcels" residing temporarily at the surface, where the parcel is enriched (or depleted) by the scalar property. The enrichment that occurs during connection with the surface is driven by diffusion. The rate of diffusion is controlled by the temperature difference between upper air (where the parcel originated), and the surface temperature. During the time of contact, the parcel changes temperature as it absorbs (or loses) heat, and the surface is the source (or sink) of heat

exchange. The **magnitude** of the temperature change, and the **duration** over which warming (or cooling) occurs are used to calculate the flux rate (equal to $\langle w'T' \rangle$). Such a process is equally valid for any other scalar exchange; ET is the flux that occurs when the parcels are exchanging water vapor.. Figure 5-2 portrays a parcel model of sensible heat flux, in which the measured scalar is temperature. In the figure, a parcel of cold air descends to the surface, where it is gradually warmed over a period of 2 seconds. This warmed air is then ejected back into the upper, and cooler air from above again replaces the ejected parcel.

In the SR method, the total derivative (the flux) is equated with the time derivative (the measured scalar trace). In other words, the cycling rate of these parcels at a stationary location (in an Eulerian reference frame) is considered to be statistically equivalent to the transport velocity of the Lagrangian parcel (Katul et al., 2006). As with EC, measurement over some reasonable time period is assumed, reducing the dependence of the flux on variable concentration within the parcel. Any inhomogeneity could be due to uneven heating, advection, or vertical pressure variations. Experimental validation has shown that a semi-empirical linear calibration can be used to correct the difference between the ramp geometry and flux, and that this calibration depends on measurement height, surface roughness, and on atmospheric turbulence and stability (Castellvi, 2004; Chen et al., 1997a).

Eddy covariance measures flux directly by determining $\langle w'T' \rangle$ from measurements of w and T. By using the vertical component of wind velocity and assuming that over a reasonably long averaging period that there is no mean vertical wind flow, EC flux estimates are not restricted to a stationary measurement[10]. In contrast, SR flux estimates depend directly on empirical calibration coefficients that are in turn derived from flow characteristics, surface roughness, and

[10] *Strictly speaking, coordinate rotations applied in the EC method violate this independence. The effect of these corrections on short term fluxes is minimal. See* (Rebmann et al., 2005; Wilczak et al., 2001).

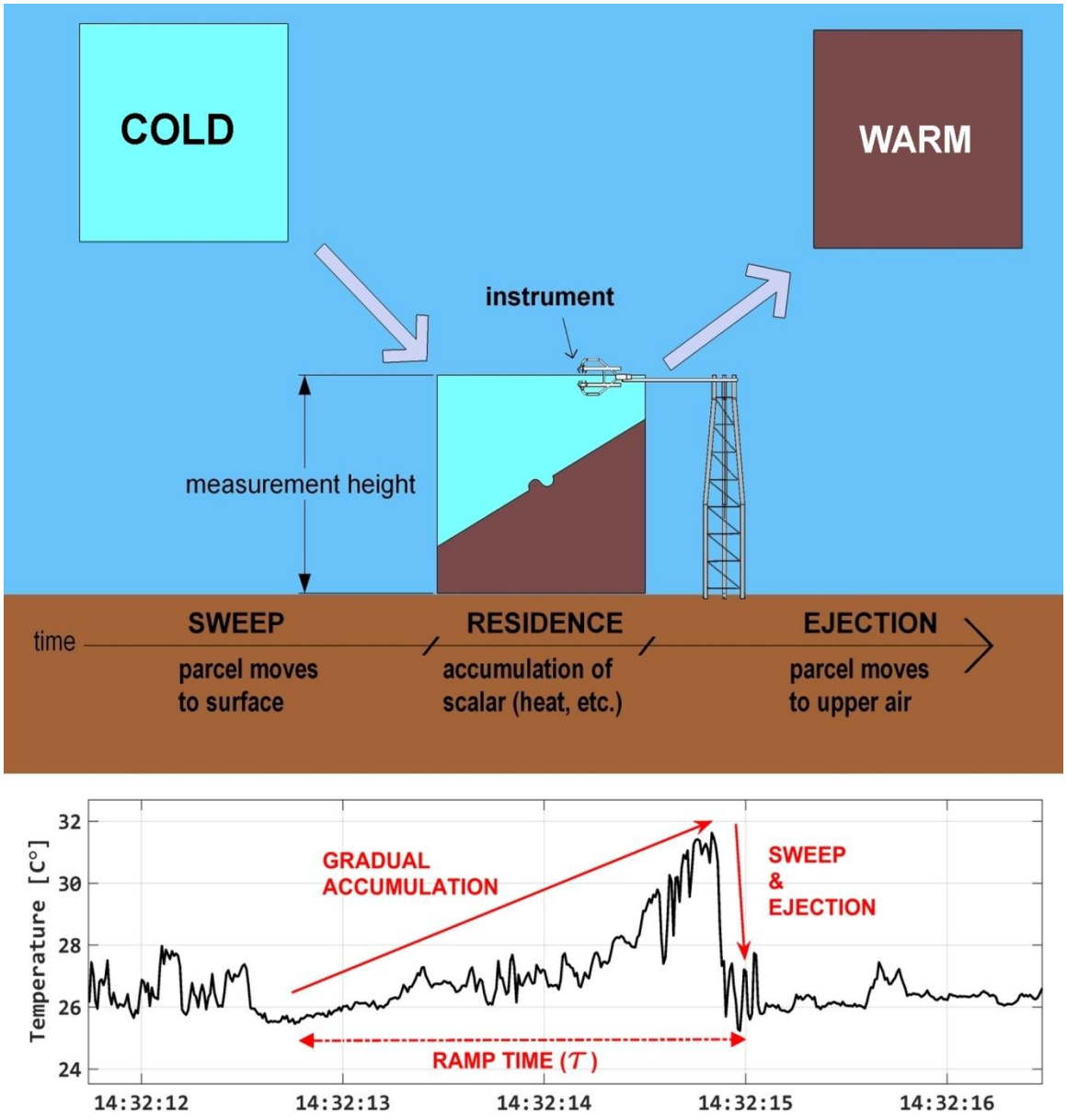

Figure 5-2: Diagrammatic representation of parcel displacement model of flux.
The diagram shows the evolution of the surface renewal model in time. The temperature trace shown is selected from sonic temperature data collected September 12, 2015 over a dry field of hay stubble.

measurement height. When measurements are taken from a moving position within the flow, it is unknown if this dependence will confound the SR flux. These experiments were conducted to test the robustness of the SR method to determine flux from moving measurements, using co-located EC flux determinations as a control basis.

For a given set of surface conditions over a short time period, the ramp structure has been

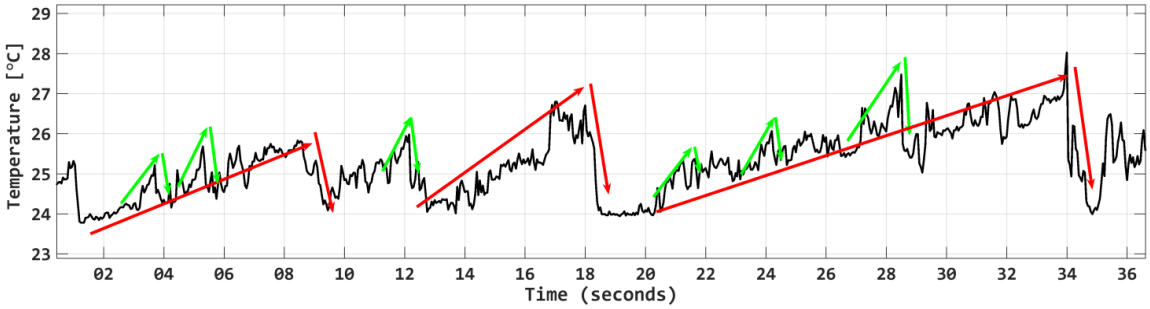

Figure 5-3: Heterogeneity in actual ramp geometry
Pictured is a typical temperature trace randomly selected from June data. Note that multiple ramp scales coexist (marked in red and green), and that ramp geometry from a single scale varies in duration and magnitude. Nonetheless, a single scale can be described statistically using structure functions and estimate flux using SR.

shown to be effectively constant (Castellvi et al., 2008; Chen et al., 1997a). The flux determination is based on calculating a single representative amplitude and ramp time; however examining a representative sample of the temperature trace demonstrates that multiple ramp scales co-exist in (Figure 5-3). Shapland et al., (2012a, 2012b) considered cases where multiple ramp frequencies contribute to flux, but for the purposes of this study, the calibration coefficients and time scales associated with flux were assumed to be mono-modal, so that only one frequency of ramps is used to calculate flux. For the control EC measurement, the mean vertical velocity should be zero and the mean scalar measurement (temperature, humidity) should be stationary over a block averaging period for which flux is calculated. Typically, EC flux estimates are based on averaging periods of 15-30 minutes (Aubinet et al., 2012). The length of the averaging period is critical to the validity of the EC calculation for two reasons. The averaging period must be long enough to obtain a statistically significant number of samples, and so that low frequency fluxes are captured. But the period must be short enough so that the mean wind speed and scalar values are stationary (Sakai et al., 2001).

Operating under an assumption that SR fluxes were only due to one ramp amplitude and duration, the analyses below derive the minimum averaging period required by the SR method, analyzing a range from 1-60 minutes. These are compared against simultaneous EC fluxes averaged over 12-60 minute periods. The motivation for this experiment was to determine if SR

could measure flux over a sufficiently short measurement period so that it can be used while moving. This seemed possible as the SR method detects rapid, coherent features in the time trace, and because the method had been shown to work within the roughness sublayer (Paw U et al., 2005). Without depending on low frequency contributions that are accumulated in the EC method, rapid SR flux measurements could yield a higher resolution map of sensible fluxes (and ET) by measuring flux rapidly while moving over a crop canopy (Figure 5-1).

5.1.2 Mathematical description of coherent structures and flux determination

The physical model of transport occurring via coherent structures can be described by two divergent models, with corresponding equations that express the rate of heat transport. First, the Langrangian model of flux (a moving parcel control volume) can be defined by total and partial derivatives:

$$S_L = \frac{dT}{dt} = \frac{\partial T}{\partial t} + u_i \frac{\partial T}{\partial x_i} \qquad \text{Eq. 5-1}$$

where S refers to the source (the surface heat), T is the parcel temperature, t is time, u is the wind speed, x the position vector, and i indicates vector notation for the three directional components of wind velocity (i.e. u,v, and w) and location vector (x, y, and z).

The second way to define the flux is the Eulerian derivative, in which the temperature is defined or measured at a stationary location. In this definition, the equation gains an additional term when the vector terms are multiplied. Following (Paw U et al., 2005) the mass balance equation is simplified here to 2 dimensions (vertical and mean horizontal flow):

$$S_E = \frac{dT}{dt} + \frac{\partial u_i T}{\partial x_i} = \frac{\partial T}{\partial t} + u_i \frac{\partial T}{\partial x_i} + T\left(\frac{\partial u}{\partial x} + \frac{\partial w}{\partial z}\right) \qquad \text{Eq. 5-2}$$

This equation includes additional terms w and z, the vertical wind speed and position vectors.

The final term on the right side of Equation 5-2 is addressed by previous work on compressibility effects, known as the WPL correction (Webb et al., 1980). For small scale measurements taken over short periods, the flow can generally be considered incompressible, and the WPL correction is negligible. These effects are most significant during period of density stratification (due to advection or strong stability). Compressibility was neglected here, as this study is primary focused on daytime fluxes, which are the greatest cumulative source of crop water use. As such, the Eulerian and Lagrangian source terms are considered equal without additional corrections.

During the "gradual rise period" in which the parcel resides at the surface, the air is relatively stationary and the advective component of the total derivative is negligible. Heat diffuses into the parcel during this period, driven by the temperature difference between the surface air and the parcel. To define the parcel's physical control volume, the horizontal dimensions has some nominal source area (origin of S_E) and a vertical extent which is defined as the height of the sensor above the surface. The temperature of the entire parcel is thought to relate to the measured temperature (at one point) in some predictable manner. A gradual rise in the measured parcel temperature marks the diffusion of heat from the near surface air, which is the heat source (or sink). Dividing the volume of the parcel (V) by the source area (A), and multiplying by the air density (ρ) and heat capacity (C_p) gives the surface flux rate,

$$H = \alpha \frac{V_{parcel}}{A_{source}} \rho C_p \frac{dT}{dt} \qquad \text{Eq. 5-3}$$

which gives the sensible heat flux (H) in units of Wm^{-2}. By dividing V by A, the parcel is now described by the measurement height z (m). The calibration coefficient α was originally proposed to have a value of 0.5, which assumes a linear rate of heating from the surface to the parcel top (Paw U et al., 1995). However, α has been shown to vary widely from 0.5, and relate

to both inhomogeneity in the parcel temperature (Chen et al., 1997a), and sensor response (Shapland et al., 2014).

Finally, it should be noted again that this argument can be generalized to any scalar constituent of a turbulent fluid. In particular, latent heat (ET) can be calculated from the direct measurement of ramps in the humidity trace (Katul et al., 1996; Suvočarev et al., 2014). Other studies have shown the application of coherent structures to measure carbon flux (Castellvi et al., 2008) and methane flux (Suvočarev, forthcoming). Finally, development of the SR method has been in part motivated by the advantage of reduced implementation cost (as compared to methods such as EC). To measure ET with the SR method without expensive IRGAs, latent heat flux can be derived as a residual of the surface energy budget from the measured sensible heat flux, net radiation and ground heat flux (Paw U et al., 2005).

5.1.3 Algebraic determination of ramp geometry from structure function

Equation 5-3 describes the calculation of heat flux from the dimensions of intermittent ramps (the dT/dt term) in the temperature trace. Ramps are an identifiable feature in the measured temperature trace above any natural surface (Figure 5-2), yet calculating the amplitude of characteristic ramps from high frequency data requires an efficient, robust, and preferably automated procedure. There are several methods to determine ramp geometry, including visual detection (Shaw and Gao, 1989), low pass filtering (Katul et al., 1996; Paw U et al., 1995) wavelet analysis (Gao and Li, 1993), and structure functions (Spano et al., 1997). Structure functions in particular provide both objective criteria to detect ramps and an efficient method to tabulate ramp geometry. The general form for structure functions is:

$$S^n(r) = \frac{1}{N-r} \sum_{1}^{i=N-r} \left[T(i+r) - T(i) \right]^n \qquad \text{Eq. 5-4}$$

in which the structure function of order n for a given time lag r is obtained by finding differences

between each sample i and sample i+r (lagged in time by r samples), raised to the nth power, summed and normalized by the total number of samples minus r. The time series of signal ΔT in a turbulent flow can be shown to be a combination of random fluctuations and coherent structures (Van Atta and Park, 1972). The random (incoherent) part is produced by isotropic turbulent processes, and thus has no particular sense. By contrast, coherent structures are by definition anisotropic, with gradual rise period and sharp transitions during sweeps and ejections . Considering the total variance is composed of additive random and coherent components, the structures functions can be used to decompose the measured variance into random and coherent components, and detect the geometry of ramps in a time trace of a measured scalar (Van Atta, 1977).

For the EC method, the flux for some averaging period is defined by the covariance of fluctuations in wind speed and temperature ($<w'T'>$). The covariance gives the magnitude and direction of the material flow rate. The temperature trace is decomposed into a mean and a fluctuating part, i.e. $T = <T> + T'$. In contrast, SR treats the temperature time trace as composed of a coherent and a random component, i.e. $T = T_c + T_r$, in which the random noise can be described as a symmetric, pseudo-random distribution. The coherent part, on the other hand, is asymmetric and represents the intermittent coherent structures evident in the trace. Recognizing this symmetry as a mathematically distinct feature, (Van Atta, 1977) showed that atmospheric measurements do not conform to an isotropic turbulence model; a model of the coherent features using 2nd, 3rd, and 5th order structure functions is sufficient to detect coherent structures ("microthermals"). Until the 2000's, computational power and sensor logging frequency could prevent accurate detection of rapid events, so that the ramp model was used subjectively by visually detecting ramps and summing the calculated ramp geometry by hand (Spano et al., 1997). Advances in computational power and logger sampling rates now allow automated, rapid

calculation of structure functions of high frequency data, facilitating the detection of events much shorter than 1s with long (hourly or daily) records.

Van Atta's model defines the simplest geometrical definition of ramp amplitude and duration, and assumes that the coherent and random components are statistically independent. By expansion of even and odd ordered terms, (Van Atta, 1977) showed that the coherent part can be reduced to the form:

$$\left\langle (\Delta T_C)^n \right\rangle = \frac{(-1)^n A^n r}{\tau} \qquad \text{Eq. 5-5}$$

Where A and τ are the ramp amplitude and duration, respectively. By expanding and combining terms to the fifth order structure function $S^5(r)$, and defining the structure function probability distribution in terms of the ramp geometry, an equation for the ramp amplitude can be derived:

$$A^3 + \left(10S^2(r) - \frac{S^5(r)}{S^3(r)} \right) A + 10S^3(r) = 0 \qquad \text{Eq. 5-6}$$

Equation 5-6 is in the form of a depressed cubic polynomial. Solving for the roots of this function yields a single, predominant ramp amplitude from a given temperature trace (with units of °C or K). Furthermore, Van Atta (1977) suggested that ramp time τ should be related linearly to amplitude and proposed:

$$\tau = \frac{-A^3 r}{S^3(r)} \qquad \text{Eq. 5-7}$$

In practice, determination of ramp τ from A using this equation requires empirical calibration (see discussion of γ, below); this calibration has been shown to be related to surface conditions and instrumentation (Chen et al., 1997a). Ongoing work using replicate measurements at multiple heights (Castellvi, 2004) and frequency response calibration (Shapland et al., 2014) promise to

resolve this unexplained parameter. Regardless, it was found in this study that this calibration remains constant at a single site, allowing for a site based determination that is valid over a reasonable range of conditions.

Efforts to define efficient and accurate methods to derive the ramp geometry are ongoing. Following successful demonstrations of SR to measure flux, several authors developed efficient and automated methods to derive the ramp geometry. Successful application of Equation 5-6 depends on selecting a specific lag which captures the dominant ramp scale which contributes to flux. By comparing temperature traces measured over three different surfaces, (Chen et al., 1997b) established that this lag can be found by plotting the third order structure function, normalized by the lag, for a range of lag sizes (Figure 5-4). The lag which maximizes this ratio is the lag used to determine ramp geometry in equations 5-6 and 5-7.

5.1.4 Calibration of SR flux calculation

While SR allows <w′T′> to be determined from temperature variance alone, the dependence on calibration parameters requires that the method be calibrated for each specific deployment. Several approaches have been attempted to reduce this dependence and evaluate the physical rationale of SR theory. The relationship between structure functions and ramp geometry is not exact as originally proposed in Van Atta, and requires empirical calibration specific to site conditions and sensor response. Consequently, Equation 5-7 is reorganized:

$$\tau = -\frac{1}{\gamma^3}\frac{A^3}{S^3(r)/r} \qquad \text{Eq. 5-8}$$

In Equation 5-8, γ is the ratio between the lag-normalized 3rd order structure function and the ramp amplitude divided by ramp duration (Chen et al., 1997b). Ideally, this ratio is near unity, and in field trials, calibrated values for γ vary between 0.9 and 1.2 (Castellvi et al., 2008). Chen et al. (Chen et al., 1997b) note that these values appear to be related to surface roughness

conditions, but not in a linear way- γ generally increases with surface roughness, but the highest values reported have been found over open ocean. By algebraic reordering of terms in Equation 5-8, the lag r is selected in the structure function calculation (*strfnc.m*) by maximizing the value of $S^3(r)/r$ (Figure 5-4).

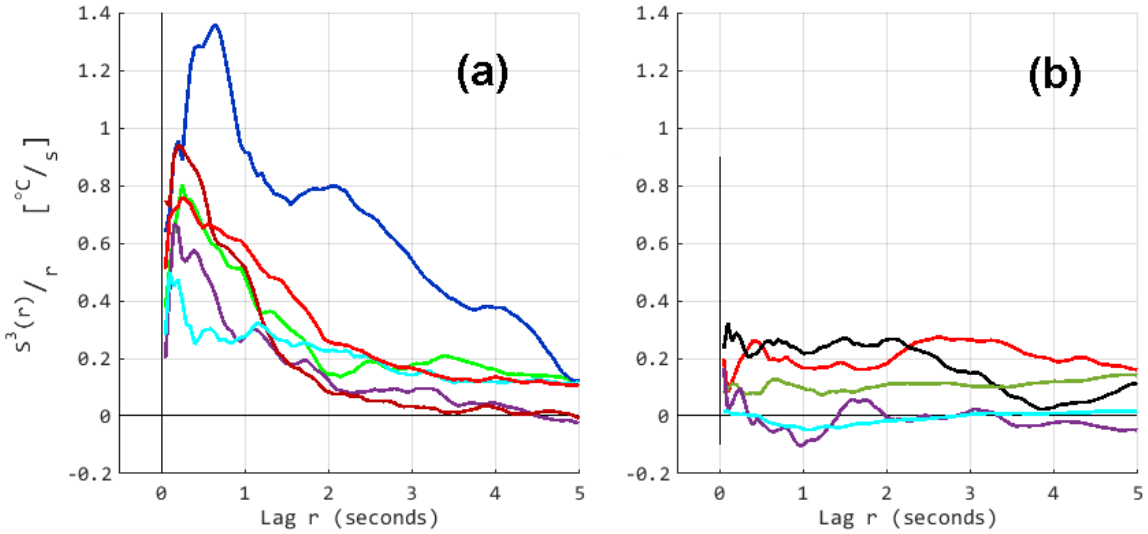

Figure 5-4: Plot of $S_3(r)/r$: method to optimize lag used in structure functions.
In both figures, each colored line represents the normalized 3rd order structure function of the temperature trace of a 3 minute averaging period. In some 3 min. averaging periods (a), a well defined maximum is found over a range of different ramp durations (x-axis) and ramp magnitudes (y-axis). For other 3 minute periods (b), no well defined maximum is evident- this results in poor flux estimate or complete failure to estimate flux. As indicated by the total magnitude on the y axis, variance is low and consequently this usually occurs during quiescent periods, when flux is minimal. In terms of cumulative flux, this impact is minimal.

For this study, values of γ ranging from 0.7 to 1.4 were initially used to identify reasonable limits for this relationship, but for final results, γ was constrained to the range 0.9-1.2, and corresponded closely to values reported by others for corresponding surface roughness (Castellvi et al., 2006; Snyder et al., 2008). The evaluation of γ was complicated by the cubic terms and the detection of negative ramp durations in the calculation method (see discussion in 5.3.5 below). Additionally, the selection of a single lag time (r) only reflects the flux contribution from ramps with one geometry. Consideration of more complex flow geometries (Finnigan et al., 2009; Shapland et al., 2012a, 2012b) was neglected in this study; poorly defined maximum $S^3(r)/r$ is

hypothesized to be a source of erroneous flux estimates (see discussion of method error, section 5.3.2).

The second parameter α is applied in Eq. 5-3 to adjust <w′T′> according to the effects of advection on the temperature trace, and frequency dependent sensor response (Paw U et al., 1995; Shapland et al., 2014). Progress in defining and validating values for α has included: investigation into the effect of surface roughness and the ramp geometry (Chen et al., 1997a); use of the wind and stability measurements via similarity theory to set α (Castellvi, 2004); use temperature gradients for automated calibration (Castellví, 2013); sensor frequency compensation (Shapland et al., 2014); and evaluating contributions using the multiple ramp model (Suvočarev et al., 2014). For this study, calculation of α followed the method outlined in (Castellvi et al., 2008; Snyder et al., 2008), using sonic anemometer data (rather than iteration) to determine the stability parameter (ζ) and friction velocity (u_*):

$$\alpha = \begin{cases} \left[\frac{\kappa}{\pi} \frac{(z-d)}{z^2} \tau u_* \phi_h^{-1}(\zeta) \right]^{0.5} & (z-d) > z_* \\ \left[\frac{\kappa}{\pi} \frac{z^*}{z^2} \tau u_* \phi_h^{-1}(\zeta) \right]^{0.5} & h \le (z-d) \le z_* \end{cases} \qquad \text{Eq. 5-9}$$

where κ is the von Kármán constant (=0.4), d is the displacement height (due to surface roughness), and z_* is the height of the roughness sublayer (where flow distortion due to surface roughness predominates). The coefficients used in the phi function for heat transfer $\phi_h(\zeta)$ are those given by (Högström, 1988):

$$\phi_h^{-1}(\zeta) \begin{cases} 0.95 + 7.8\zeta & 0 \le \zeta \le 1 \\ 0.95(1-11.6\zeta)^{-0.5} & -2 \le \zeta \le 0 \end{cases} \qquad \text{Eq. 5-10}$$

It was found that applying this definition more broadly ($-5 < \zeta < 2$) yielded acceptable results and included some flux calculations that would otherwise return no value. The needed inputs for the

above equations are integrated into the EC code (*ECflux.m*). The equation for stability is $\zeta = z/L_O$, where z is the measurement height and the Obukhov length is given by:

$$L_O = \frac{-u_*^3}{\kappa_v \frac{g}{\bar{T}} \overline{w'T'}} \qquad \text{Eq. 5-11}$$

in which g is the force of gravity. The equation for friction velocity from anemometer measurements is:

$$u_* = \left[(\overline{u'w'})^2 + (\overline{v'w'})^2 \right]^{1/4} \qquad \text{Eq. 5-12}$$

For this analysis, L_O and u_* were calculated directly from anemometer measurements, using the eddy covariance software. Lacking this instrumentation, these parameters can be resolved from mean wind speed measurements by iteration (Castellvi et al., 2008; Paw U et al., 1995).

5.1.5 Flux Footprints and Moving Measurements

Flux divergence, a difference in the vertical flux measured at two heights, is largely caused by horizontal advection and flow distortion over rough surfaces. Divergence is source of error when calculating surface with eddy covariance, necessitating that measurements be obtained with adequate fetch and above the roughness sublayer (Allen et al., 2011a). The general requirement for homogenous upwind fetch requires that flux-gradient methods and eddy covariance measurements be conducted in homogenous field conditions (Brutsaert, 1982). As normal field conditions often do not meet this ideal description, one concept to investigate the role of heterogeneity is the concept of flux footprints. Footprint models[11] use measured wind speed, scalar concentrations, and approximations of turbulent diffusivity to define an areal footprint,

[11] Footprint areas described by these models are defined by the statistical likelihood that the measured flux can be attributed to a particular source area. This area is defined by an definite integral (Horst and Weil, 1994), evaluated at bounds associated with specific distances (e.g. likely to contain 90% of the measured flux).

defined as a source area from which the vertical flux is attributed (Rannik et al., 2012). By equating eddy covariance footprint models and the height dependence of the surface renewal method, flux footprint models have been shown to be directly applicable for attributing SR fluxes to a source area (Castellví, 2012). Likewise, SR has been shown to be as reliable as EC for estimating fluxes from heterogeneous canopies (Suvočarev et al., 2014). The role of advection is modified when measuring flux from a moving platform (Vickers and Mahrt, 1997), and while a formal footprint model was beyond the scope of this analysis, the ability to map heterogeneous fluxes depends on valid footprint models. For this analysis, the induced wind speed during moving trials was roughly equal to the actual wind speed, so that footprints were considered secondary to evaluating the validity of the SR method while moving. EC flux estimates, being independent of the horizontal movement vector, can be regarded as valid when measured during motion. For example, EC fluxes have been implemented and validated from aircraft based measurements (Gioli et al., 2004; Vickers and Mahrt, 1997). To the author's best knowledge, no work has been published showing the implementation of SR from a moving vehicle (Kyaw Tha Paw U, personal correspondence).

Based on the potential for the SR method to be implemented over shorter time periods and from measurements taken closer to the surface, it was hypothesized that SR measurements taken from a platform moving over the surface (within ~2m of the top of vegetation) could successfully approximate surface fluxes at higher resolution than would typically be possible with the EC method. The desired increase in resolution would be to estimate flux from areas at least as small as 0.1 hectares (related to the ~30m length scales from Chapter 2). Neglecting advective transport, a flux footprint of a moving measurement is largely dependent on vehicle velocity, so that the best resolution of the flux determination is determined by the shortest valid averaging period. For example, on a vehicle moving at 1 m/s, the smallest possible flux footprint, assuming no advection, determined over a 1 minute averaging period would be 60 meters in

length, or 0.36 hectares. Consequently, a feasible aerial SR system for the precision irrigation system described in Chapter 2 would be able to resolve fluxes faster, or requires a system moving more slowly than 1 m/s. Conversely, if 5 minutes averaging periods were used, the measurement would need to move slower than 0.1 m/s. Based on this logic and practical considerations of vehicle velocities, the experiments were conducted at velocities ranging from 0.5-3 m/s and the focus of the study was to determine the shortest possible flux averaging period.

5.2 Site Descriptions and Field Methods

Field experiments were conducted during three seasons (early spring, mid-summer, and early fall) to establish a robust protocol for the determination of SR fluxes. An integrated sonic anemometer and open path gas analyzer (Campbell Scientific IRGASON) with a co-located 76μm (0.003") constantan-chromel Type E fine wire thermocouple (Campbell Sci. Model FWT03) were used for all experiments. These were supported with slow response temperature/humidity probes (Vaisala H2S3 HMPs), and during moving trials, a GPS receiver was also used, all mounted on an all-terrain vehicle (Figure 5-7).

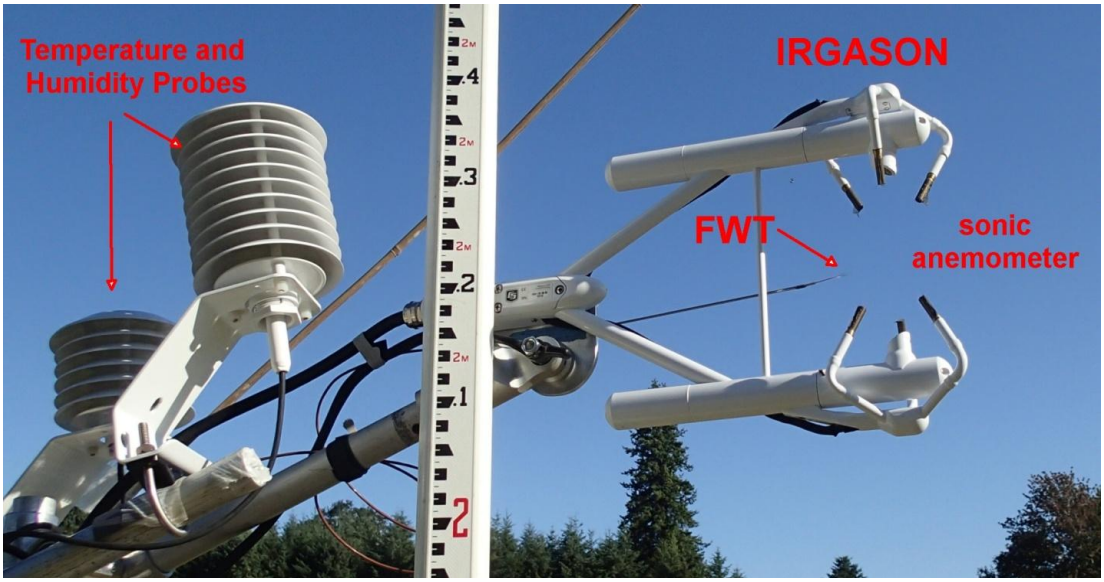

Figure 5-5: Mounting arrangement of instruments used in moving trials.

In each field trial, flux was measured across a range of stability conditions, surface roughness, and wind speeds. The separate trials were timed to capture a range of field conditions such as surface wetness, vegetation growth cycle, and an expanded range of temperature and humidity.

The fine-wire thermocouple (FWT) was mounted adjacent to the sonic anemometer/gas analyzer (IRGASON). This IRGASON was the primary source of data used to determine temperature fluctuations, as it was common to all field experiments. For calculation of true air temperature, air density, and heat capacity, calibrated slow response humidity/temperature probes (HMPs) were used. Air pressure was measured by the IRGA EC100 unit. Water vapor content was calculated with the IRGA and checked against HMPs. SR and EC flux estimates primarily utilized sonic temperature (T_S) in the analyses below, and SR heat flux estimates were also performed using the FWT temperature trace (T_{FWT}). The FWT was mounted adjacent to the spherical 10cm control volume of the sonic anemometer in such a way that it did not block the sonic anemometer and IRGA paths (Fig5-6).

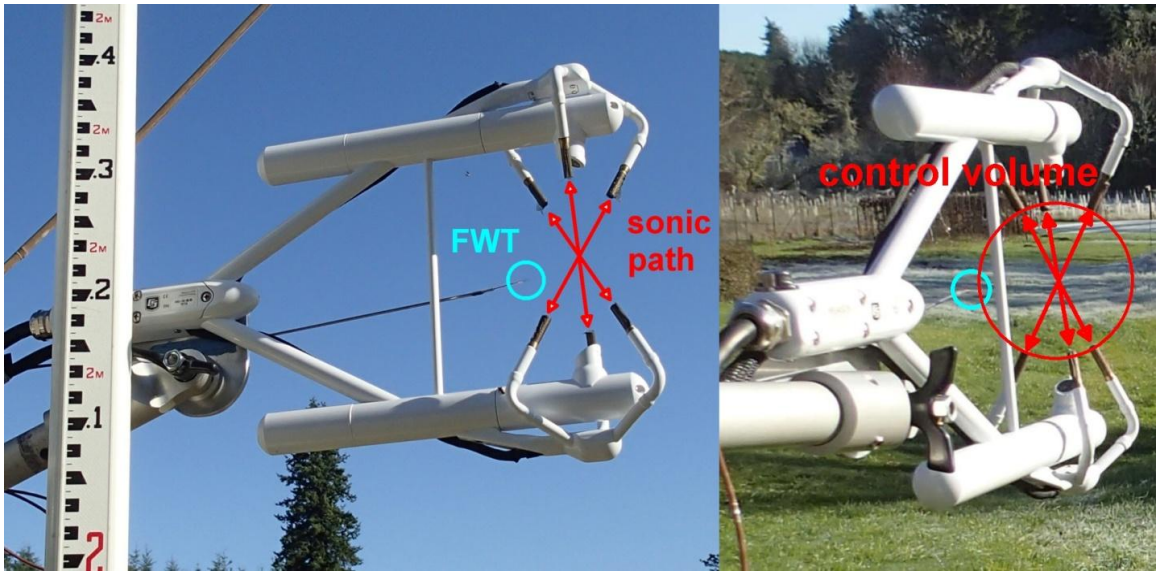

Figure 5-6: Alignment of FWT with respect to IRGASON.
FWT is located within a 10 cm spherical "sampling volume" of the anemometer (and gas analyzer), but does not actually interfere with measurement path of the two instruments.

Additional data used in the SR analysis were collected at a different site during August 2014, and three times in March, June and September 2015 (site 2). These experiments employed two IRGASON systems and two HMPs; and consequently SR flux was only determined from sonic temperature and IRGA humidity measurements. Earlier, preliminary attempts were made to determine SR fluxes from data collected at a third site in March 2014. These first trials showed that over a short crop surface, 10Hz measurements (with sonic anemometer only) taken near the surface were not fast enough to resolve coherent structures and flux, despite being collected over a broad range of wind speeds and stability conditions. Anticipating that detection of ramps during moving trials would require even more rapid measurements, fine wire thermocouples (FWTs) were obtained and programmed to collect temperature data at 100Hz. Data from all sensors were recorded using a Campbell Scientific CR1000 data logger, and written to CF cards. The logger frequency was the maximum rate that the CR1000 supports (without burst mode), and the logger program was validated in previous field trials to establish that all measurements could be completed within the logger scan rate. The moving systems was powered by a 12v battery, which was charged rotated and charged between trials.

A mounted GPS unit (Garmin Oregon 450) was used to record timestamps and locations continuously during moving trials at 1m distance intervals, as calculated by the GPS unit. The Garmin unit reports, but does not record, GPS solution uncertainty in absolute distance (as opposed to dilution of precision- DOP- or running least squares error). During moving trials this accuracy ranged from 3-7m, which was comparable to stationary periods. For some trials, a survey grade, real time kinematic GPS unit (Topcon Hiper II antennae) was also mounted on the vehicle, and a separate Bluetooth connected datalogger continuously recorded time stamped location measurements at a one second rate. The RTK base station was located at a position that

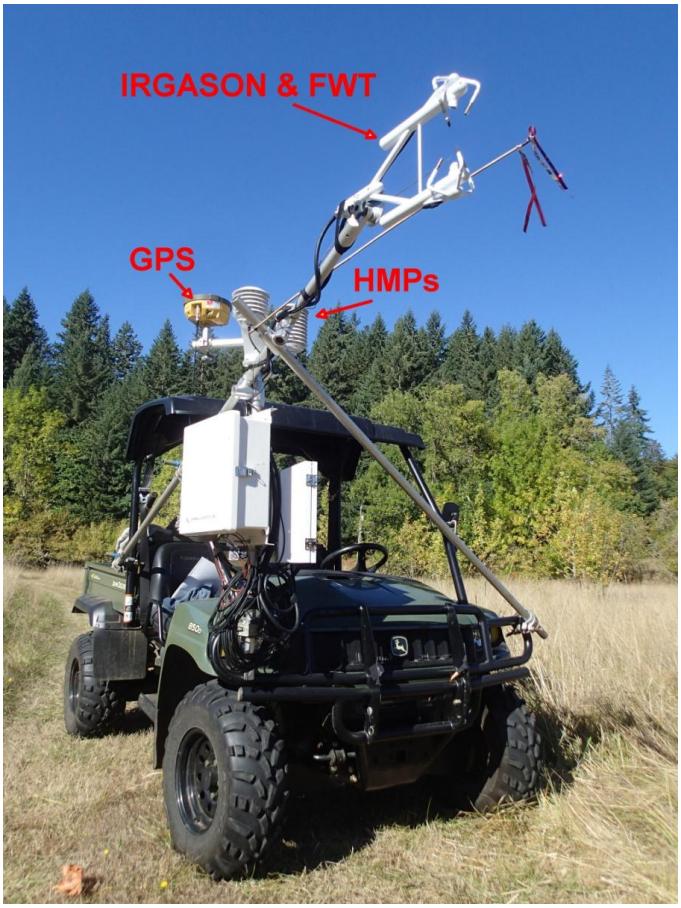

Figure 5-7: All terrain vehicle and instruments used for moving trials.

was previously established by 2+ hour static determination via the UGS OPUS system[12]. The Topcon unit also records horizontal and time DOP and calculates the horizontal uncertainty, which varied from 2cm 10cm, although occasionally to 100cm. GPS measurements were also used to determine vehicle orientation and velocity, to coordinate timestamps with the datalogger, and to classify moving and stationary trials. While absolute location varied by 2-10 m between the two GPS systems at any particular moment, GPS calculated position, velocity, and orientation was generally within 5% when averaged over 1 minute intervals. Because the processed data from both GPS units generally agreed, and because each unit intermittently failed to resolve a solution, GPS data was combined from both methods to determine the time, speed, location, and bearing of moving trials.

[12] *http://www.ngs.noaa.gov/OPUS/*

5.2.1 August 2014 field trials

This study was conducted at the edge of an irrigated field of (established) annual clover, with data used from 11 days 2-12AUG. The purpose of the study was to determine the edge effect- areas immediately adjacent to the field edge were not irrigated. A range of distances to the field edge (as a function of wind direction) represented a range of advective effect as determined from the vertical flux divergence. To measure flux divergence, two IRGASONs were mounted at 1.2 and 1.9 meters height (above the ground). Vegetation height in the field was approximately 0.5 meters (Figure 5-8, 5-9)

This data was re-processed for use in SR analysis, adding field conditions that were not otherwise represented in the analysis. First, these fields are the only well-watered crops during the active growing season, with daytime Bowen ratios varying from 0.1-0.5 and a range of surface wetness conditions. The two instrument heights were near the boundary between the roughness and inertial sublayers (2 and 5 times the vegetation height), which allowed checking of the alpha parameter's dependence on this height.

Figure 5-8: IRGASON instruments at two heights, August 2014

Weather over the 11 day measurement period was generally hot and dry, with light precipitation event on 12AUG. Irrigation was applied twice during the experiment (midday on 04AUG and 11AUG), which is evident in a sharp drop to negative sensible and near zero latent heat flux during the time at which irrigation was applied, also evident on 12AUG during rain. Data from nearby meteorological stations[13] indicate that incoming solar radiation peaked at 950-980 Wm^{-2} for 10 days until 12AUG (Figure 5-8), when solar radiation only reached ~400-500 W m^{-2} (Figure 5-9).

Figure 5-9: Field conditions of the August 2014 trials
Instruments are located at center of the photo, which looks in the upwind direction. Photo taken on August 12, during the only day of clouds/ light rain. Center pivot is visible at sides (panoramic photo, approximately 180° field of view)

5.2.2 March 2015 field trials

This was the first experiment implementing the SR method from the moving platform. The trials were conducted over the course of one day in two different fields. This site was used for the remainder of the trials (June and September 2015). For all studies, trials were conducted at one or both of two fields, near to each other but with different crops and surface conditions. The north field is managed in cover crop rotations, with a small part managed as turf. The south field is managed as hay/pasture, but was not hayed or grazed during 2014 or 2015. In March, the north field was covered by ~15cm grass/cover crops, with some areas in mowed (5 cm) turf (Figure 5-10). The south field was covered by patchy dead grass 10-30cm in height, with scattered areas of

[13] Station data from CRVO and FNWO3 obtained via the MesoWest archives: http://mesowest.utah.edu/

bare soil and standing water at the surface. Trials were conducted in the field at speeds 1-2m/s, in repeated patterns around the cover crop (north field) and on grasses access roads (south field); see maps in Figures 5-13 and 5-14. 15 minutes of data was also collected on a paved road to allow fast vehicle speeds (to 10 m/s); this data was not treated separately but was included in the analysis. Weather conditions were clear sky throughout the day, with mean wind speed 1-2 m/s in the morning and 0.5-1 m/s in the afternoon, gusting up to 2.5 m/s. Temperatures began at 8°C at 0800 and rose to 20°C by 1600, dropping rapidly to 12°C after 1430 (local sunset at 1530). Relative humidity was 85% in the morning, dropped to 55% during the day, and returned to 75% at sunset; and pressure varied 101-101.5 kPa over the course of the day.

Figure 5-10: Sites of moving trials (March 2015).
North field (top) in semi-dormant cover crops, and some areas turf (left side of image). In the top image, the ATV is located at the approximate location of the tower during the September trial.
South field (bottom) is unmanaged pasture / hay, with intermittent standing water. In the bottom image, the ATV is parked at the approximate location of the tower for September trials-
These are the primary locations for stationary measurements for repeated trials.

5.2.3 June 2015

The trials were conducted over the course of one day, only in the north field (as described above). The largest part of north field was in over-mature cover crop 1.8m tall, with the remainder mowed to 5 cm turf (Figure 5-11, top). Moving trials were conducted both on the turf area, as well as in course on a mowed path around the perimeter of the 1.8m grass(Figure 5-11, bottom). Weather conditions were clear throughout the day, with mean wind 1-2 m/s in the morning, gusting up to 4 m/s, and 1.5-3 m/s in the afternoon, gusting upwards of 8 m/s. After 1800, wind speed and temperature dropped steadily to calm conditions. Temperatures began at 12°C at 0700 (local sunrise 0545) and rose to 28°C by 1430, falling to 18°C after 1900 (local sunset at 2100). Relative humidity was nearly 90% in sunrise, falling steadily to 40% during the day, and returned to 55% by sunset; pressure was 100.2-100.45 kPa over the course of the day. During stationary periods, the instruments were located either at the downwind edge of the tall vegetation or at the center of the mowed turf, approximately 30 meters downwind of taller vegetation.

Figure 5-11: Field conditions during June 2015 trials.
Turf in near field of view, cover crop is approximately 1.8 m in height. ATV was positioned so that IRGASON array was located above tall canopy during some stationary trial periods.

5.2.4 September 2015

Trials were conducted as in March, with additional stationary instrumentation mounted on 7m towers in both fields. The vehicle based instruments ran continuously from 12SEP 0900 until 13SEP 2000, during both stationary and moving trials. Instrumentation in this trial was expanded with two stationary arrays of four 3-d sonic anemometers (RM Young 8100 VRE) and four temperature/humidity probes (Vaisala HMP155) in each array. All stationary equipment (at towers) ran continuously during this period. The cover cropped portion of the north field had been mowed but not plowed, so that substantial straw mulch remained on the surface (Figure 5-12, top), with the smaller turf area managed as normal (5cm height). The south field continued as marginal pasture (not grazed), with patchy, lodged (blown over) vegetation 0.7-1.5m in height (Figure 5-12, bottom).

Figure 5-12: Field conditions during September 2015 trials.
North field (top), with mowed cover crop. South field (bottom) with unmowed hay/pasture.

Weather conditions were clear, warm, and dry on both days. On 12SEP, wind speed steadily increased from 0.5m/s at dawn to 3m/s at 1700, with gusts up to 7 m/s. Air temperature was 15°C at 0800, rising to 32°C by 1600, decreasing to 25°C at sunset (1745), with overnight temperatures falling to 8°C. Relative humidity was 85% in the morning, dropped to 40% during the day, and returned to 85% at sunset. Overnight water vapor and RH measurements were not captured due to instrument malfunction. On 13SEP, wind speed remained consistently between 1m/s and 2m/s all day, with gusts up to 6 m/s. Following a cool night, air temperature was 10°C at 0800, only rising to 25°C by 1500, falling to 18°C at 2000. Relative humidity was 85% in the morning, dropped to 40% during the day, and returned to 85% at sunset. Pressure varied from 99.9-100.5 kPa over the course of the two days..

Eight moving trials between 13 and 40 minutes in duration were conducted on 12SEP. On 13SEP, eight additional moving trials of 10-35 minutes were conducted. Moving trials were conducted throughout the day to capture the broadest possible range of atmospheric stability and turbulent flow conditions: near sunrise before the break up of the night time stable layer; during the middle of the day when strong convection was dominant; and near and after sunset as the katabatic wind had begun draining from the upper valley above the study site. In between trials, the vehicle based system was placed in proximity to the stationary towers, with the IRGASON oriented into the direction of the predominant wind

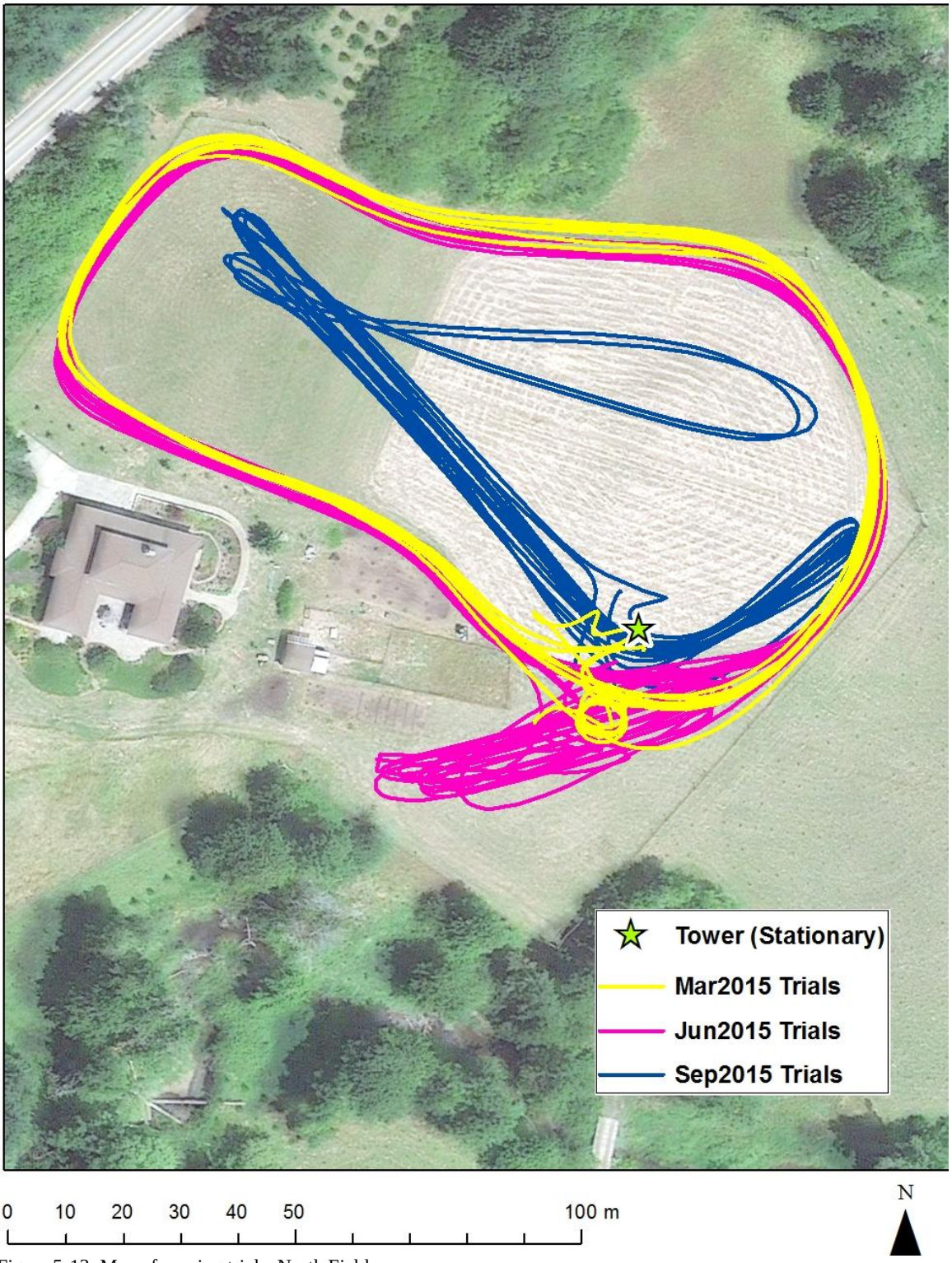

Figure 5-13: Map of moving trials: North Field

Hayed area (visible as rows) and area west-northwest of hayed area were in cover crop 2015. Note that imagery is from prior year: Aerial imagery composite of Google Earth Image and NAIP, both dated 2014.

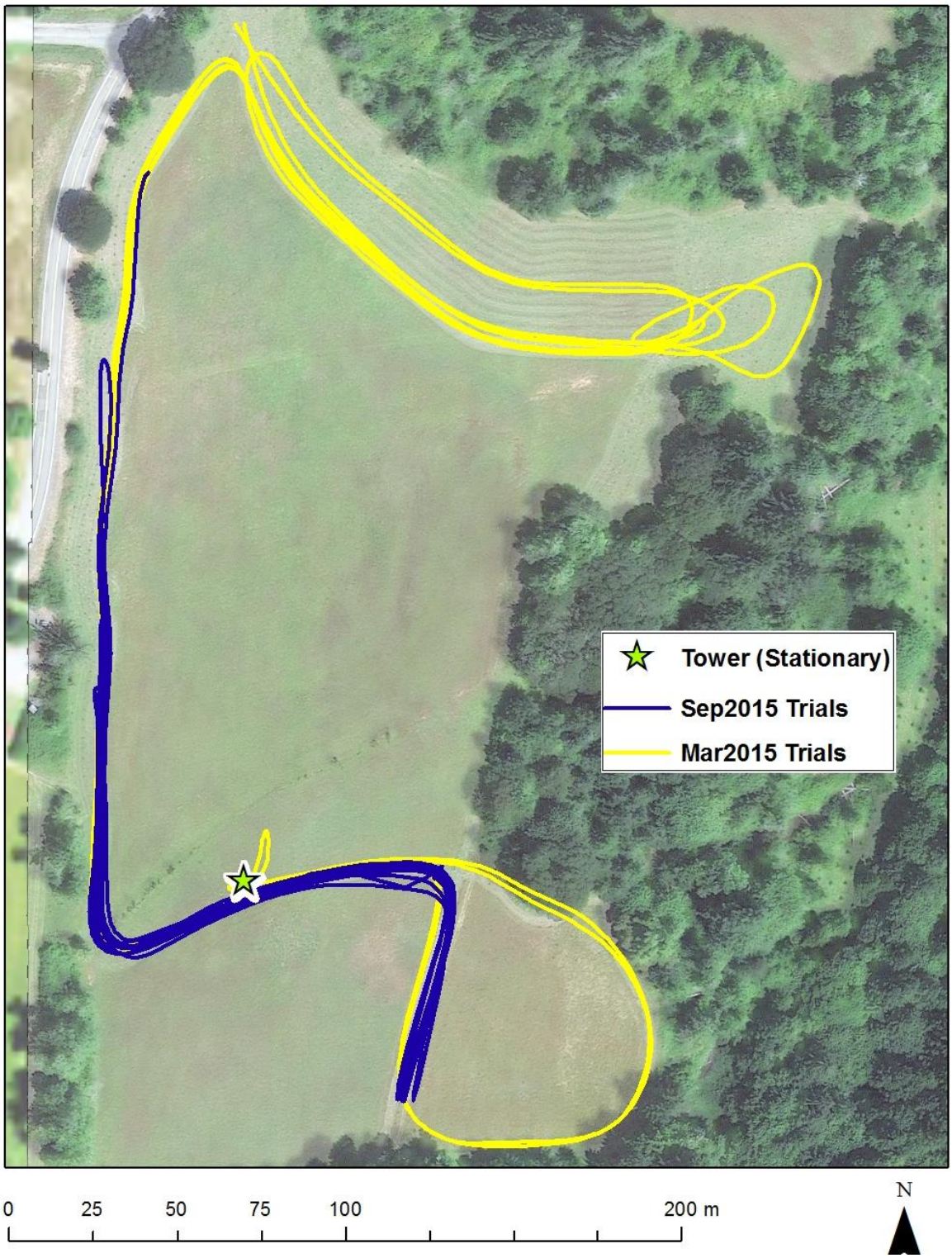

Figure 5-14: Map of moving trials, South Field
Aerial imagery composite of Google Earth Image and NAIP, both dated 2014.

5.3 Results and Error analysis

The experiment successfully showed that it is possible to compute a flux using SR from measurements taken while in motion. Nonetheless, it was determined that the minimum time over which SR could reliably estimate flux was between two and three minutes. Consequently, the method used in this study cannot feasibly be applied to map heterogeneous fluxes at the spatial resolution matched to precision irrigation systems. At the outset of the project, it was unknown if translation of the thermocouple would interfere with the determination of the ramp durations used to calculate flux. To address this, the study design proposed five sequential analyses:

1. Determine amplitude and time scale of coherent structures. Develop a dimensionally reduced statistic for amplitude and time scale of coherent structures.
2. Identify time scales of averaging periods that maximize the 3rd order structure function (SR) and optimize agreement between EC and SR flux estimates. Identify possible time scales/velocities at which aliasing might occur in moving trials. Determine scale of variability of "alpha" corrections for z0-height dependence. Evaluate influence of changing measurement height of moving platform compared to variable vegetation/displacement height of surface.
3. Compare SR fluxes with independently derived, co-located EC measurements while moving.
4. Use GPS data to determine the velocity and position of measurements. Separate wind velocity in the moving and stationary reference frame via 3d anemometry.
5. Compare flux estimates with observations of vegetation height. Map flux & surface condition.

For each proposed analysis, objective and programmable validations were used to additively construct a surface renewal program (*SR_v7c.m*) that was used for the final results presented here. Some analyses were replaced as the moving flux calculation method was developed. For instance, separating the vehicle/instrument velocity from the wind speed did not appreciably improve agreement between EC flux and SR flux. This was taken as indicating similarity between horizontal wind and vehicle speed (both 0.5-2 m/s) did not significantly affect the SR flux calculation by aliasing or alteration of the calculated friction velocity and stability parameter.

This may be important for further refinement of SR methods, especially development of SR footprint models (see discussion 5.4). Expanding on the proposed analyses, the development of the SR program required additional attention to the consistency and automation of the calibration parameters. Ultimately, the ability to map ET was shown to be theoretically possible, although not feasible at the desired resolution using this methodology. Alternate applications of this approach are proposed in the discussion.

5.3.1 Surface Renewal Calibration

The most significant challenge in developing a consistent SR flux program was the automated determination of calibration coefficients. These calibration coefficients have been approximated via surface roughness, measurement height, wind shear, boundary layer stability, and similarity theory. The study design maximized the range of the parameters represented in the study, so as to test the robustness of the moving SR method. The three parameters addressed in this calibration process were: alpha (α), the correction for the parcel homogeneity (Eq. 5-3); gamma (γ), the ratio between the structure functions and the ramp geometry (applied with Eq. 5-8 to determine ramp duration τ); and the mean displacement height (d).

Estimating the displacement height is complicated during moving trials as vegetation height and roughness, although uniform in a normal sense, varies significantly within the field. The sensitivity of the calculated SR flux to roughness led to uncertainty in the initial flux calculation as it was treated as independent of γ. As a simplifying assumption, d was calculated as 0.67*h, where h is the measured vegetation height (Stull, 1988). Satisfactory results were obtained when attempts to vary these parameters independently were dropped, and one set of values (h, d, and γ) was used for each different ground cover (tall grass, turf, bare earth, etc.). In each case, a mean vegetation height was used for h, confirming that that a more complex description of vegetation roughness was not needed.

5.3.2 Stationary Flux estimates

Comparison of SR and EC flux estimates for all measurement periods (mostly stationary) were used to address the first two proposed analyses. First was to establish an automated method to derive the ramp amplitude and duration; second, to objectively describe the reliability of SR over different averaging periods; and finally to determine a baseline variability of calibration parameters, including the dependence of calibration on measurement height and surface roughness (based on vegetation height). Initial attempts were hindered by varying the calibration parameters independently. Least squares regression to calibrate the flux was not successful when calibration parameters were allowed to vary independently. Each parameter (γ , h, and α) would vary widely between days without regard to realistic values. When γ was restricted to single decimal place (0.9, 1.0,1.1, etc) and linked to the measured vegetation height, the determination of ramp amplitude (A) and duration (τ) stabilized to reasonable values for most periods, with good agreement between SR and EC flux estimates (H_{SR} & H_{EC}). A flow chart is included with the SR code (Appendix E), which shows the parameters which are manually set by the user. The method employed here was checked against all four measurement periods, with data from the FWT, and with some data from the IRGA water vapor trace (calculating ET directly). After setting the measured vegetation height and minimal calibration of γ, flux estimates were in good agreement for all time periods, with minor exceptions during instrument malfunctions.

Figure 5-15 shows the time series of H_{EC} and calibrated H_{SR} fluxes during 12-13SEP. While the 3 minute H_{SR} is widely scattered, it reproduces the general trend of H_{EC}. For both flux estimates, 30 minute running average is plotted as dotted lines; 30 minutes is more typical of the averaging period for the EC method (Fratini and Mauder, 2014). The individual points (15min. H_{EC} or 3min. H_{SR} flux estimates) vary from the 30 minute running averages for two possible reasons. The first source of variance could be measurement error. Sources of error include: no flux estimate due to no solution (such as no real root found to Eq. 5-6); temperature outliers can

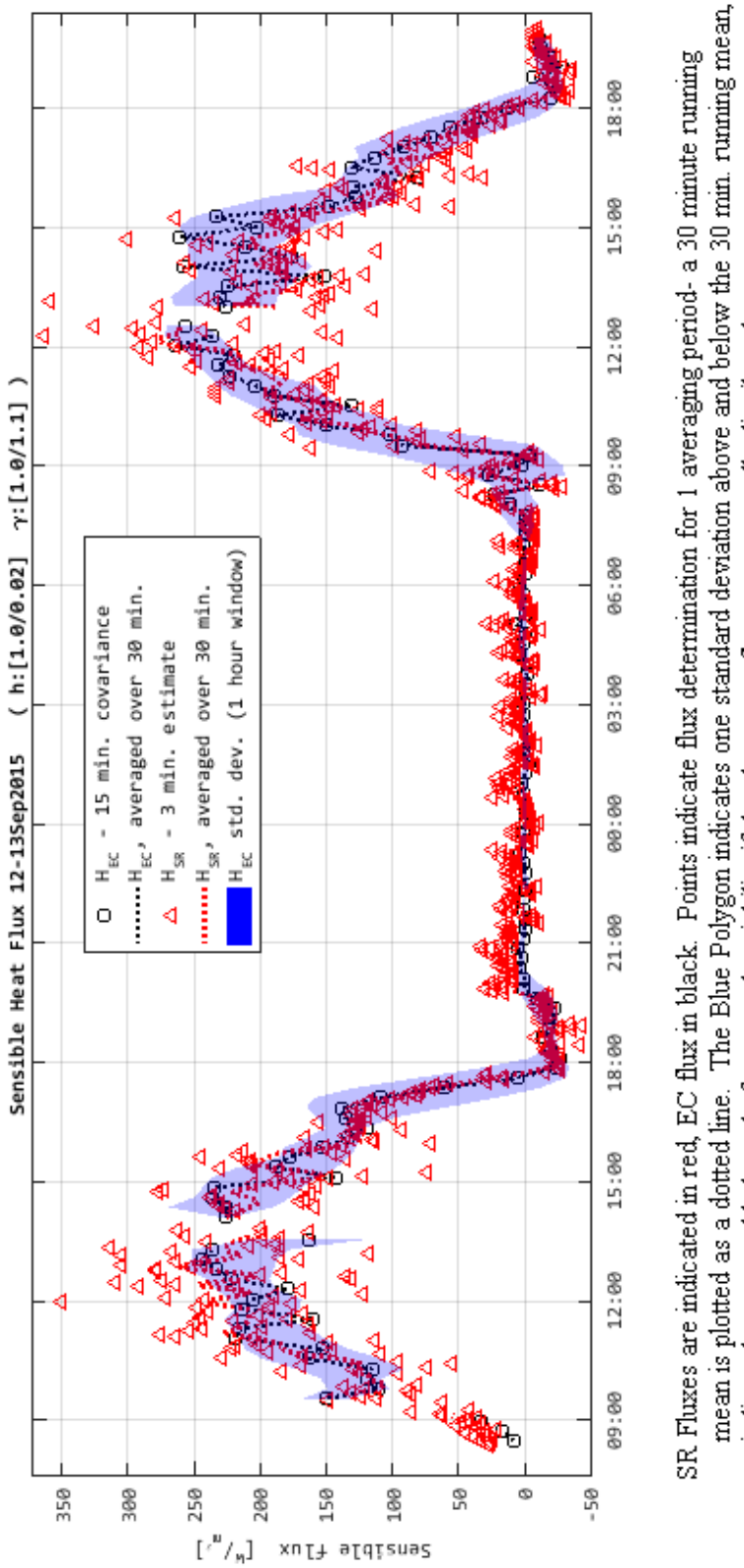

SR Fluxes are indicated in red, EC flux in black. Points indicate flux determination for 1 averaging period- a 30 minute running mean is plotted as a dotted line. The Blue Polygon indicates one standard deviation above and below the 30 min. running mean, indicated a reasonable bound of expected variability if the short term fluxes are normally distributed.
Complete times series are reproduced in Appendix C.

Figure 5-15: Example time series of calculated flux

offset structure functions and give erroneous ramp estimates; flux direction can be assigned incorrectly, particularly at periods of low magnitude flux. Error also occurs in the EC measurement, especially over short measurement periods. These types of errors often correspond to periods when assumptions in the basic method, such as homogenous parcel or no horizontal advection, are violated. Error in H_{EC} was disregarded in this analysis. An independent estimate of the error can be obtained by measuring net radiation and ground flux, and determining if the calculated fluxes close the surface energy budget (Castellvi et al., 2008; Snyder et al., 1996).

The second reason for this variability (from the 30 minute mean) is that the method is detecting flux varying over short periods,. When SR flux is calculated over shorter averaging periods than EC, it may be possible that SR is able to detect rapid variations in sensible flux that are not detected by the EC method. This seems plausible both because of the good agreement of the two methods when averaged over 30 minute periods, and also because of the close agreement between the two methods at rapid and identifiable features (Figure 5-16).

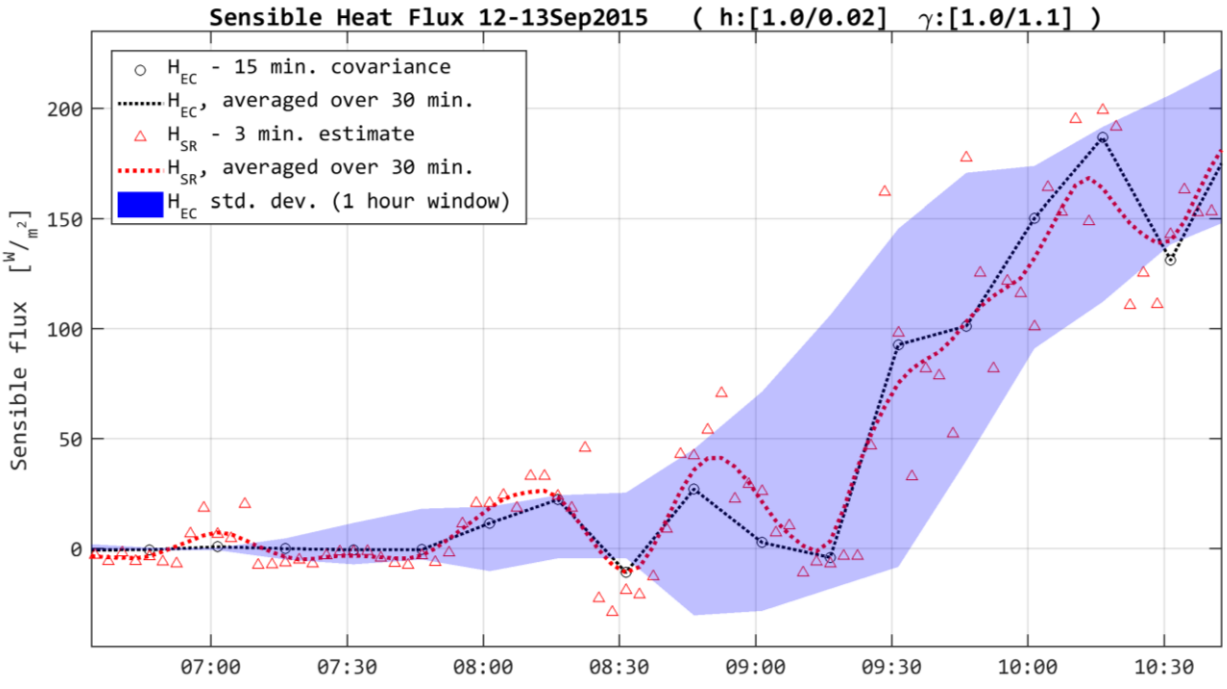

Figure 5-16: Identifiable feature in time series of H_{SR} H_{EC}
The two methods independently reproduce similar features when averaged over 30 minutes, although 3 minute SR fluxes and 15 minute EC fluxes diverge significantly.

Figure 5-17 plots SR flux against simultaneous EC flux as a reference measurement. Proximity to the 1:1 line shows agreement between the two methods. Figure 5-18 is the style of presentation used in the remainder of this analysis, which plot the 15 minute average H_{SR} against each corresponding H_{EC}. Averaging of H_{SR} reduces scatter and may consequently obscure error and measurement noise. Time series and multivariate (2-d and 3-d) plots were used to reference and identify scatter and method agreement to specific sources of error (analyses not shown). More importantly, averaged H_{SR} plotted against H_{EC} allows a comparison over simultaneous time periods, even if the two methods use different

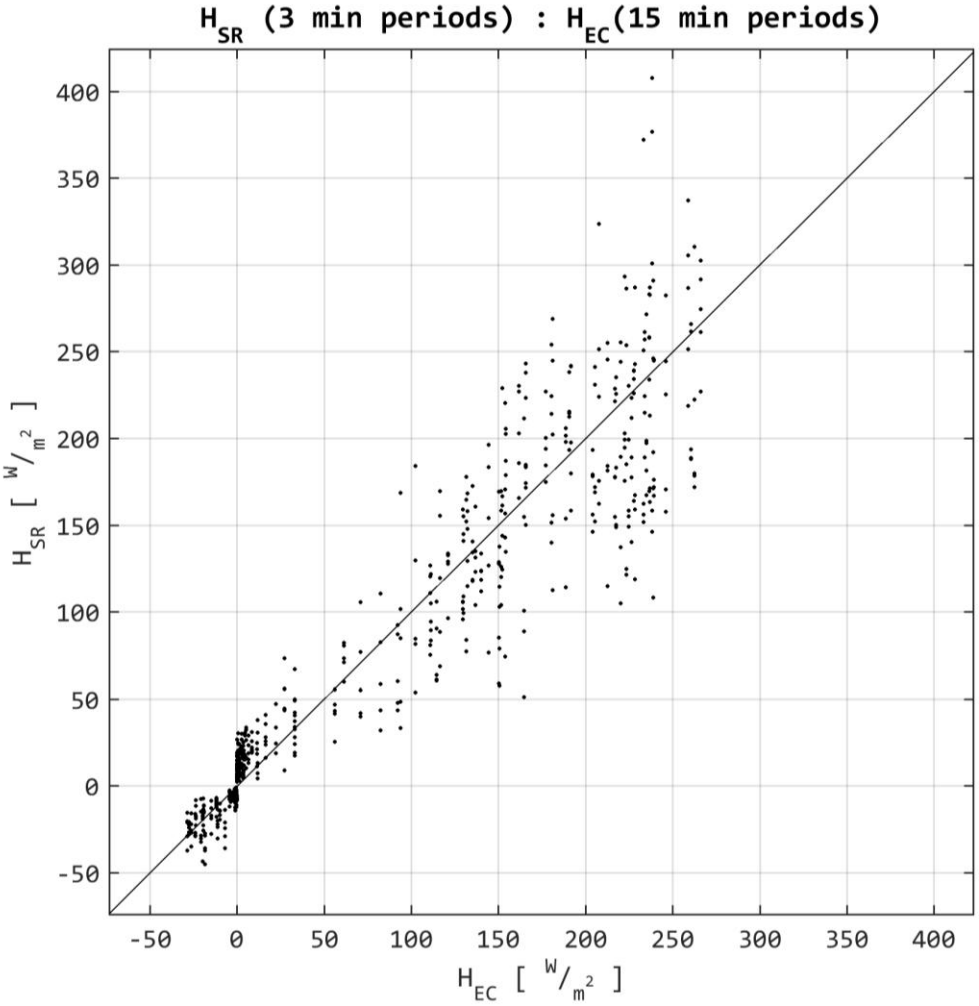

Figure 5-17: Comparison of H_{EC} and H_{SR}

averaging periods. As the intent of this study is to determine the minimum averaging time possible with SR, and because no assumption is made about the ability of SR to resolve fluxes of shorter duration, this averaging represents a more accurate, if less resolved comparison of SR against the control method EC. A table of the calibration parameters, vegetation heights, averaging periods, and statistical measures is tabulated in Table 5-1. Complete time series of fluxes and plots of H_{SR}:H_{EC} for all trials can be found in Appendix C.

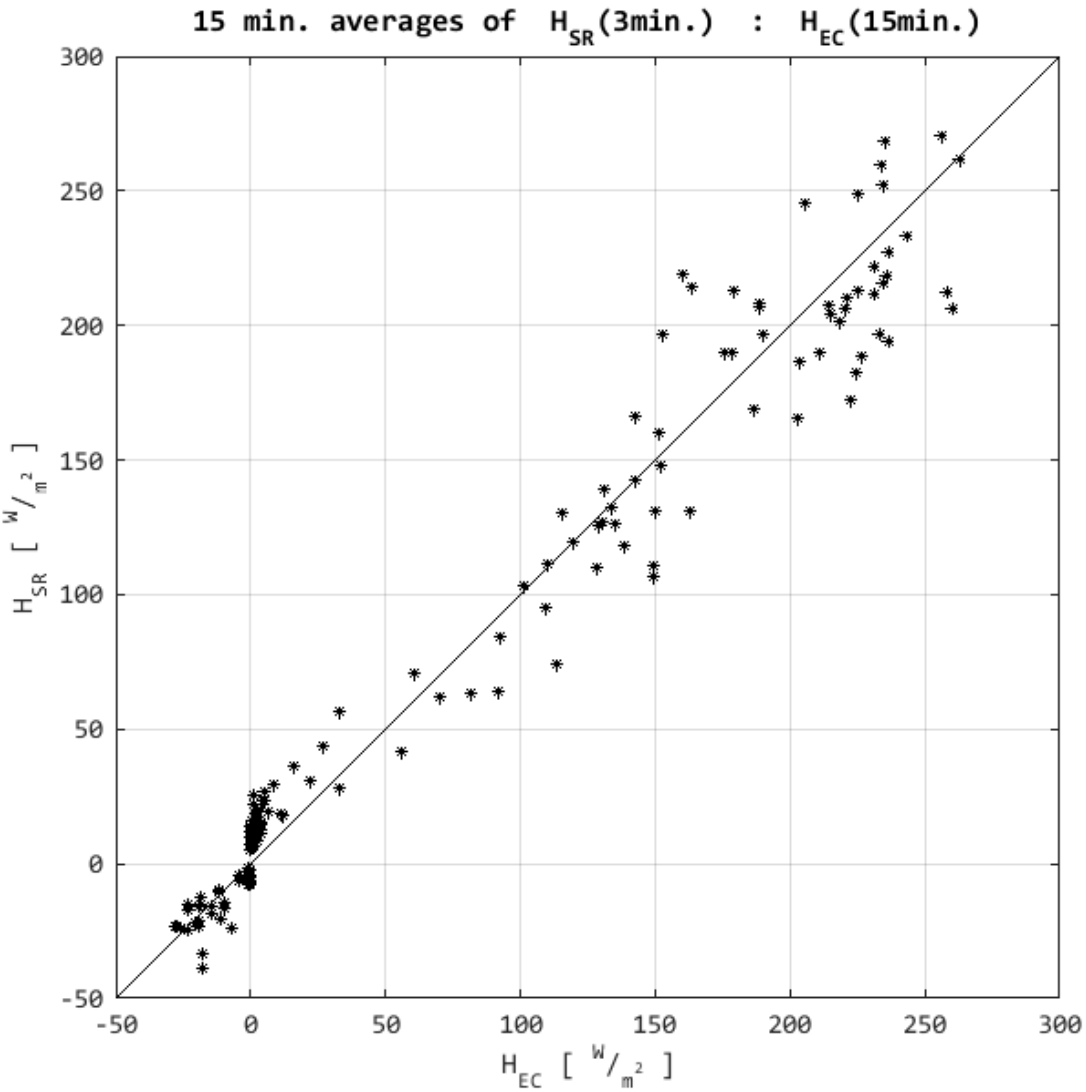

Figure 5-18: Comparison of simultaneous H_{EC} and H_{SR} (same averaging period)

	02-11 AUG14 (z=1.2m)	(z=1.9m)	07 MAR 2015	18JUN15 (tall veg.)	(short veg)	12-13SEP15 (straw)	(short veg)
γ	0.9	0.9	1.0	1.1	1.2	1.1	1.1
h (m)	0.5	0.5	0.05	1.8	0.05	1.0	0.02
R^2	0.97	0.96	0.80	0.96		0.92	
RMSE [W/m^2]	7.66	11	18.9	20		24	
Slope of regr. line	1.00	1.06	0.95	0.94		0.94	
Intercept of regr. [W/m^2]	-1.5	-2.1	13.8	3.0		4.4	

Table 5-1: Final statistical agreement with final calibration parameters used in analysis
All regressions compare EC flux calculated over 15 minutes and 15 minute averages of 3 minute SR flux. Flux during June and September trials were computed continuously: R^2 and other statistics represent regression for all data in these trials.

5.3.3 Moving Trials

Moving trials did not appear to cause the two methods to diverge in the respective flux estimates H_{EC} (15min.) or H_{SR} (3min.), particularly after averaging. (Figure 5-19 to 5-22). In some moving trials, the SR did not converge on a solution for flux, although at least for some of these failed executions, the problem was in the estimate of the stability parameter (from the anemometer) falling temporarily and artificially outside the range of ζ within Högström's function $\phi_h(\zeta)$, which was expanded in this analysis to range $-5 < \zeta < 2$. Some additional technical problems occurred during moving trials. In particular the IRGA (gas analyzer) data was very noisy during moving trials, making flux determinations of latent heat flux (and carbon dioxide) infeasible. Despiking and low pass filtering was attempted to try to utilize these measurements without success. Figures 5-20 reproduces the above figure with the addition of moving trials being marked as noted. In all three trials (March, June and September) the fluxes measured while moving do not differ from H_{EC} significantly more than stationary measurements; in contrary, they appear to conform to the control H_{EC} measurement better than the general scatter (Figures 5-20 and 5-22).

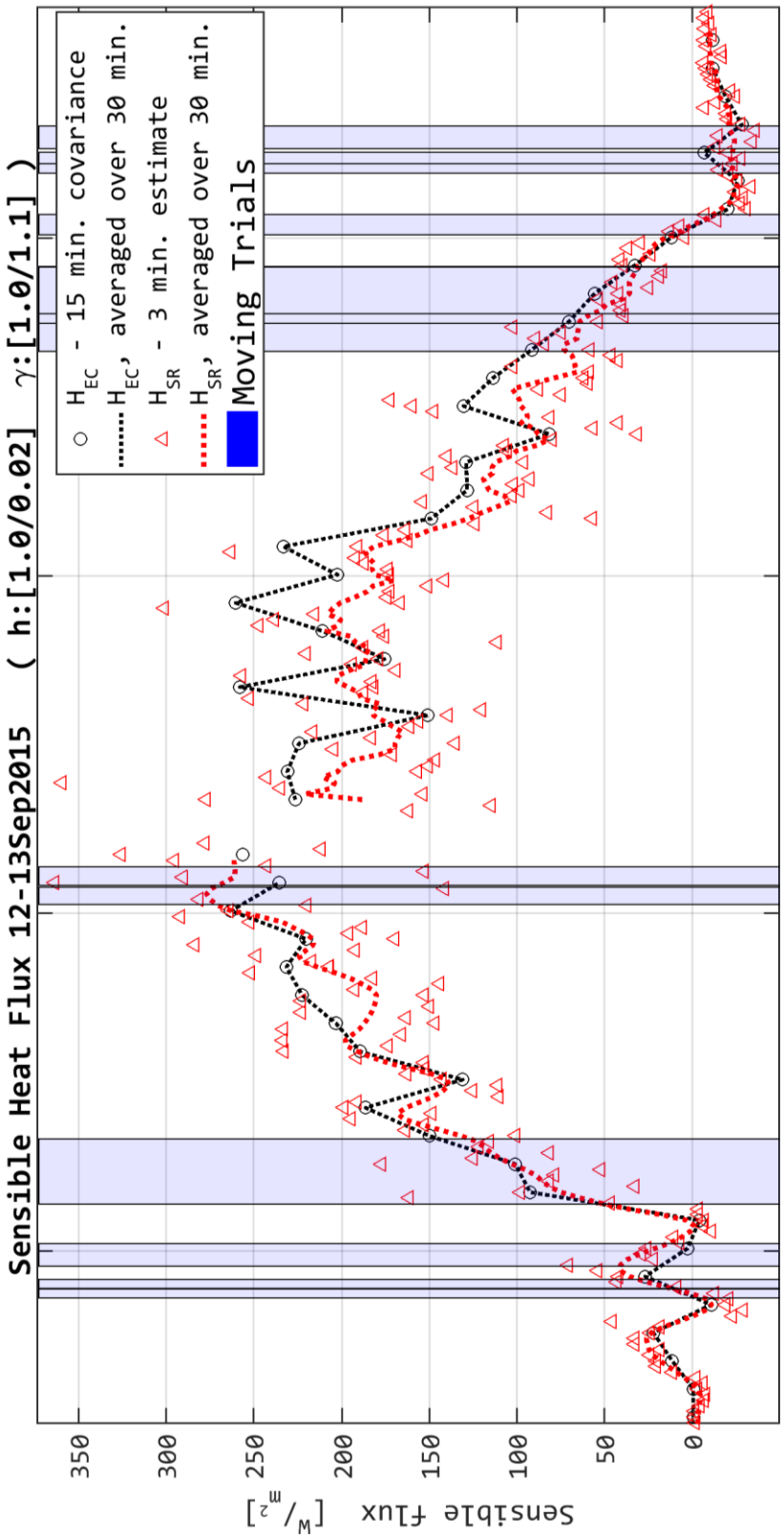

The time series of the flux is reproduced with the time periods of the moving trials indicated by blue vertical bars.

Figure 5-19: Time series of flux on September 13th indicating moving trials.

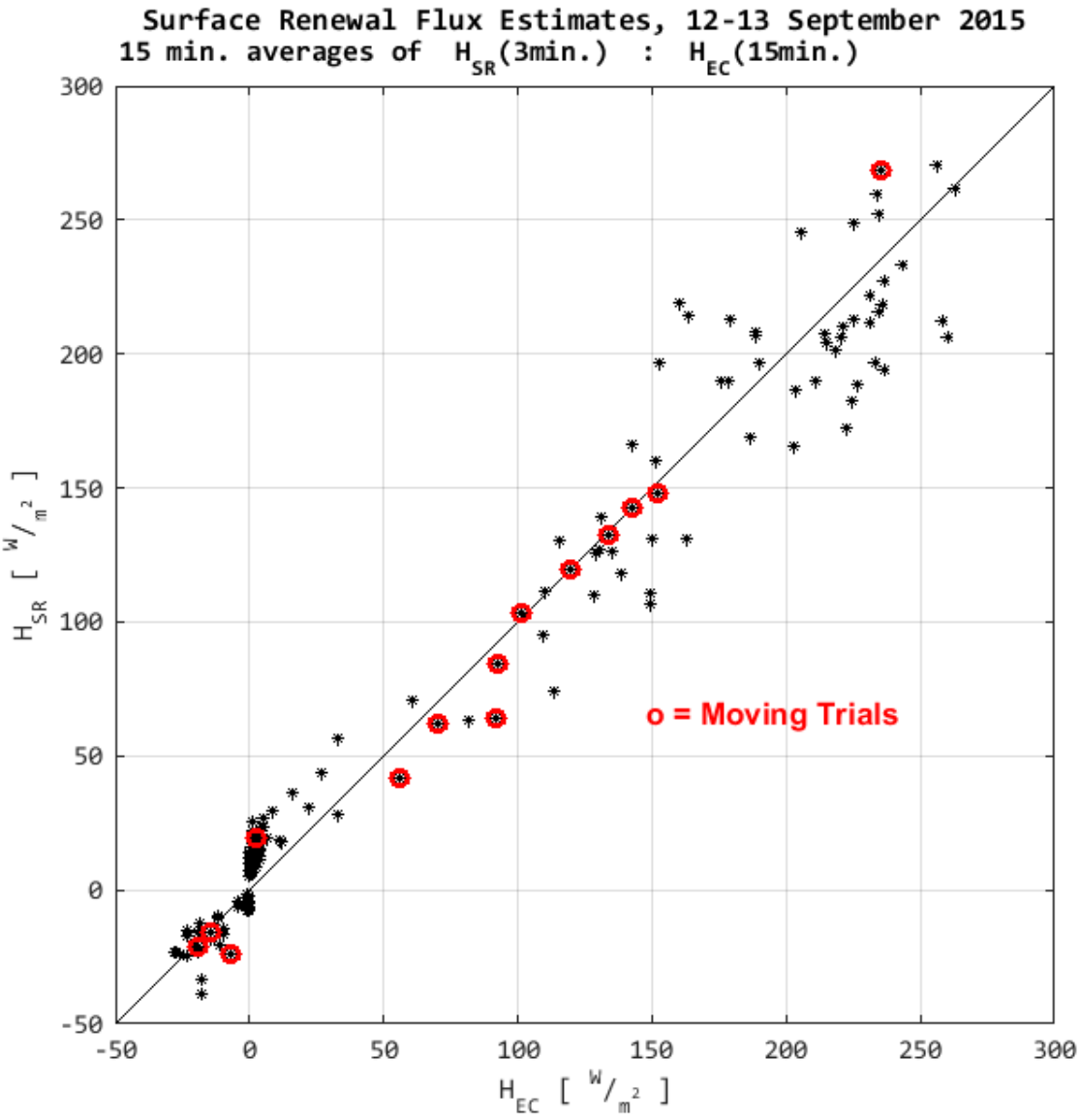

Figure 5-20: Comparing H_{SR} and H_{EC}, moving trials indicated. (September 2015)

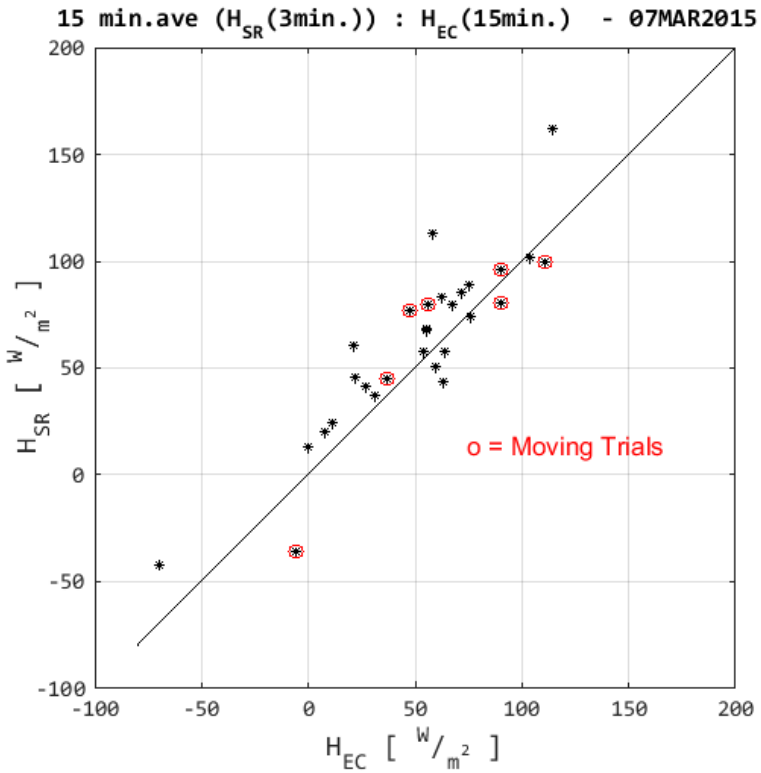

Figure 5-21: Comparing H_{SR} and H_{EC}, moving trials indicated. (March 2015)

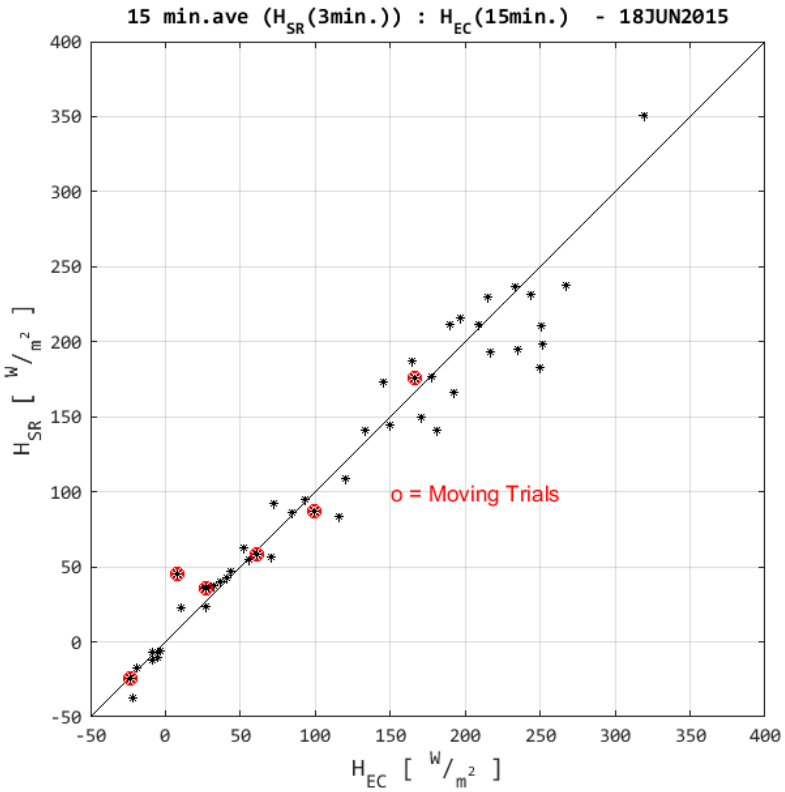

Figure 5-22: Comparing H_{SR} and H_{EC}, moving trials indicated. (June 2015)

5.3.4 Error analysis/Determination of appropriate averaging time

Although the original planned analyses proposed developing a new statistic through dimensional analysis, anticipating that a dimensionless temperature or a higher order statistic such as kurtosis would be useful in determining a minimum averaging period for the SR method. However, it was found that linear regression between H_{EC} and H_{SR}, combined with the efficiency of the automated SR program, allowed for a simple and comprehensive examination of the effect of the averaging period. To accomplish this, the EC and SR programs were automated to calculate flux for a range of periods, from 1-60 minutes with SR, and from 10-60 minutes for EC. SR averaging periods were restricted to not exceed the EC averaging periods. It was found that for some trials, if the SR period was not an even multiple of the EC period, that the two fluxes would diverge widely (an aliasing problem), so that this additional constraint was employed.

As fluxes were calculated for each set of averaging periods, a linear regression was performed between H_{SR} (without averaging) and H_{EC}. The slope and intercept of the regression line, the coefficient of determination (R^2), and the root mean square error (RMSE) was recorded in each case. For each set of time series data, each statistical parameter was plotted against the SR averaging time (with separate series for each EC averaging period). Figures 5-23 to5-35 show a representative series of these plots. (Plots of all results in Appendix C) In general, the agreement between SR and EC degrades significantly for SR averaging periods less than five minutes (Figure 5-23), resulting from the increased scatter of flux estimates when H_{SR} is calculated over very short time periods. More importantly, the slope of the regression line (Figure 5-24) departed from unity rapidly for averaging periods *longer* than five minutes. For some trials, the slope started greater than unity and crossed the line of agreement at times shorter than three minutes. Other general observations to note from these plots are that agreement (slope) is generally poor for longer time periods (both EC and SR), and scatter (R^2) decreases. Without attributing the variability in the flux estimates to either error or true, short duration flux events, it

is nonetheless necessary to compromise between scatter and agreement. Even neglecting measurement error, short term (< 3min) fluctuations that scatter widely are not useful to determine longer term fluxes that contribute to the average transport rate. For these reasons, 15 minute average periods for EC and 3 minute average periods for SR were used for the above analyses.

The summary result of this analysis is that while SR may be able to detect coherent fluctuations and calculate flux over very short time periods, the **shortest reliable measurement time that can be expected with SR is on the order of three minutes**. Furthermore, without some comparator that can independently detect shorter duration fluxes, these three minute averages should be treated as samples to be averaged over a comparable time period (15 minutes) to be considered robust.

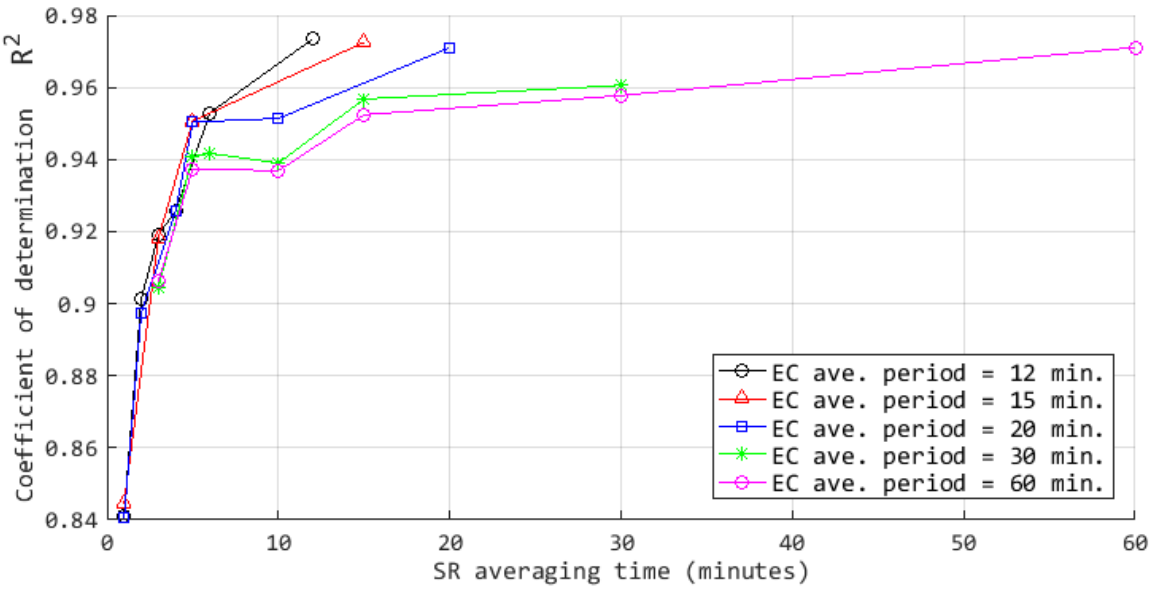

Figure 5-23: Coefficient of determination of regression H_{EC}:H_{SR} for different periods.
While the coefficient of determination is generally high (indicating low scatter about the slope of the linear regression), the resolution of SR at very short averaging period degrades rapidly at times shorter than 3minutes.

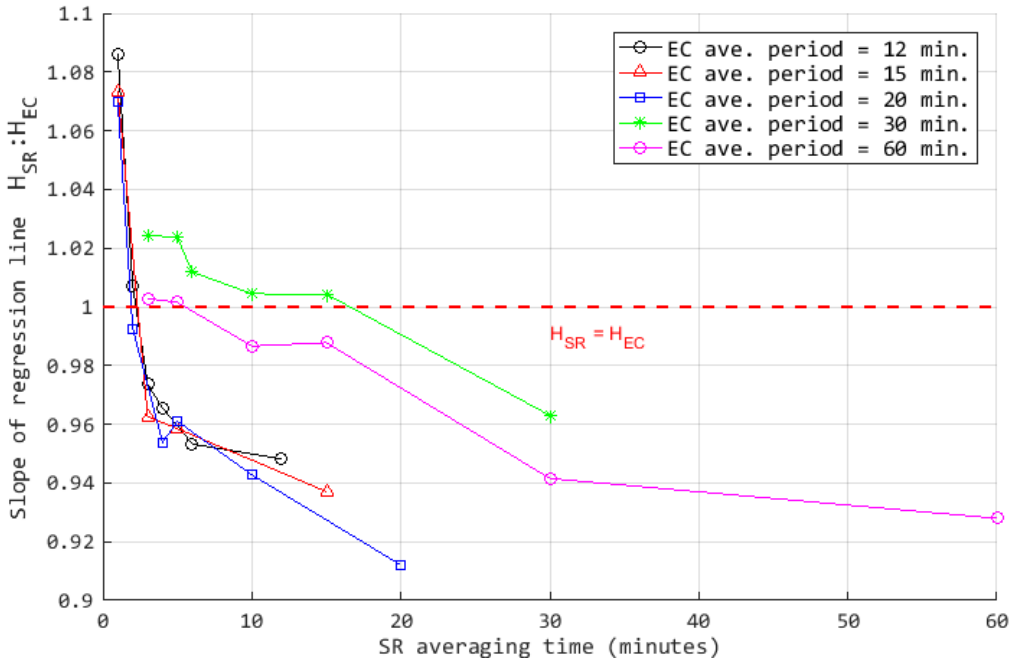

Figure 5-24: Slope of regression H_{EC}:H_{SR} for different periods.

The red line (y = 1) indicates perfect overall agreement between the methods. Typically, slope < 1 indicates that H_{SR} is under reporting flux at higher flux rates, compared to H_{EC} (intercept is typically small, Appendix C)

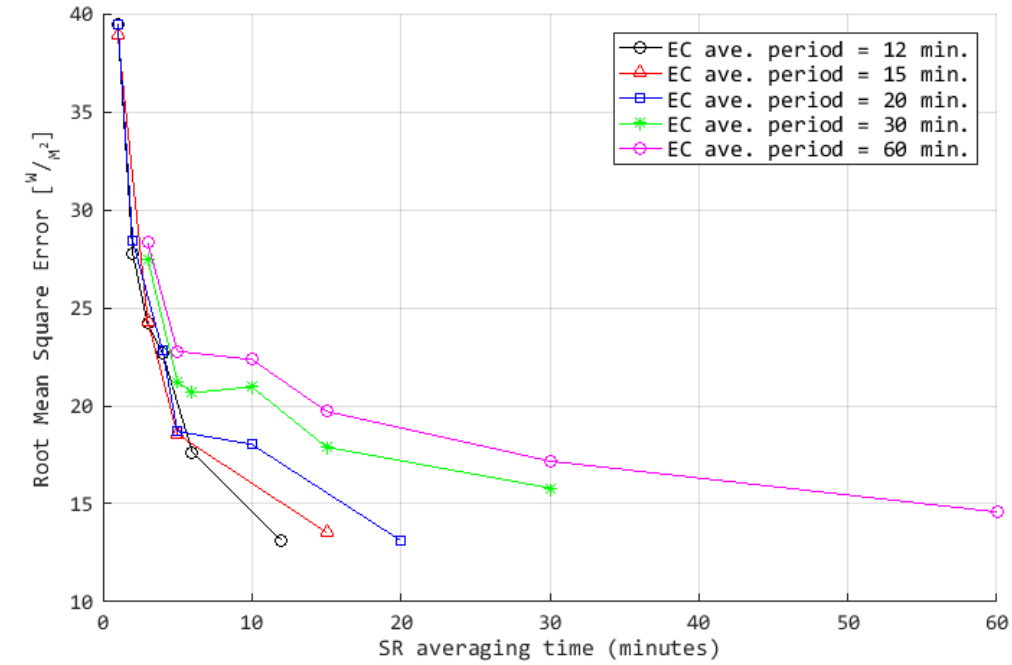

Figure 5-25: RMSE of regression H_{EC}:H_{SR} for different periods.

Given in standard flux unit of W/m^2. Decrease in the absolute difference between SR and EC is likely due to combination of the reduced scatter of SR flux and increased correspondence of sensitivity to actual fluxes during periods of 3-10 minutes.

5.3.5 SR using 100 Hz FWT

Early in the data analysis, it was decided that 100 Hz FWT data was not necessary to detect fluxes while moving- i.e. hypotheses questioning the validity of the method to detect ramps were disqualified on the basis of success using 20 Hz T_{sonic}. This was confirmed by inspecting the spectra of the temperature traces (Figure 5-26); 100Hz was fast enough able to capture variance down to the "noise floor" associated with instrument error (Figure 5-26b). Comparing plots for 20Hz T_{sonic} and 100Hz T_{FWT} , variance drops off rapidly at frequencies faster than 1s, and at frequencies 25-100Hz, turbulence is primarily dissipating energy rather than contributing to vertical flux. At both measurement frequencies, the inertial subrange can be seen in the log-log plots, signified by a -5/3 slope (Kaimal and Finnigan, 1994).

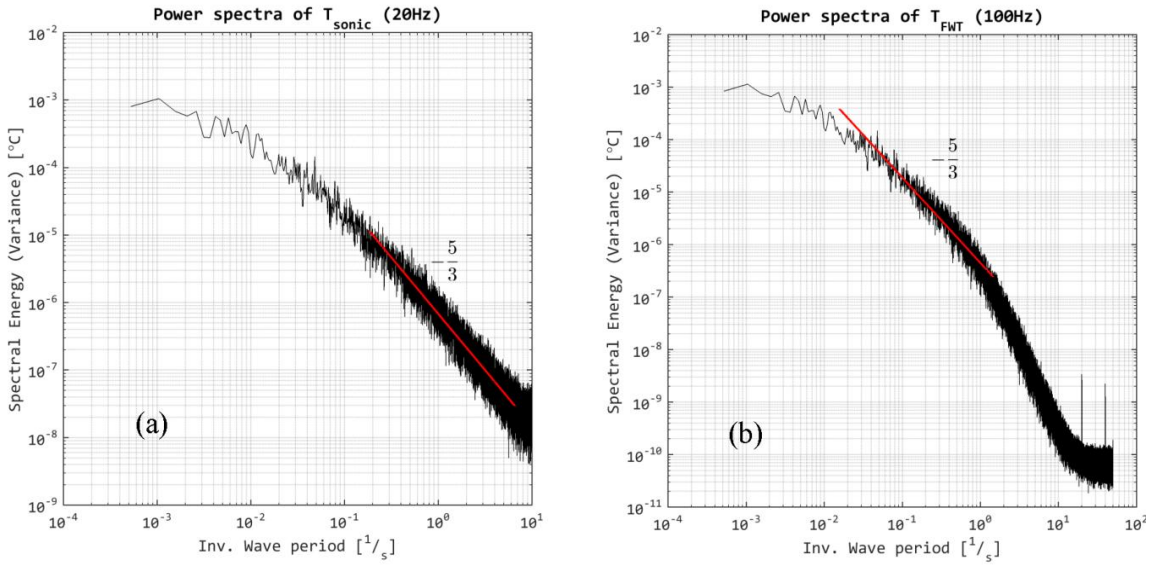

Figure 5-26: Spectra of 20 Hz T_{sonic} (a) and 100Hz T_{FWT} (b)
The -5/3 slope (red) indicates the frequencies at which scales of motion are predominated by inertial transport. Noise floor, the horizontal section at far right in (b) indicates that FWT frequency is only capturing measurement noise above 20Hz.

Flux estimates were successfully calculated for both T_{FWT} and T_{sonic}. although γ values differed between the two instruments after calibration, as reported by other authors (Figure 5-27). Structure function and lag calculation is computational expensive for real time flux measurement. To compare the two physical measurements directly, fluxes were also calculated from every fifth

sample, generating a 20 Hz FWT measurement as well. Restricting the selection of γ to one decimal place (e.g. 0.9, 1.0, 1.1, 1.2), H_{FWT} , at both 100Hz and 20 Hz compared favorably to H_{Ts} (20 Hz). (Figure 5-28a,b,c). There does appear to be some bias among moving trials, indicating that frequency dependent sensor calibration may be appropriate and required for FWT is used for moving measurements.

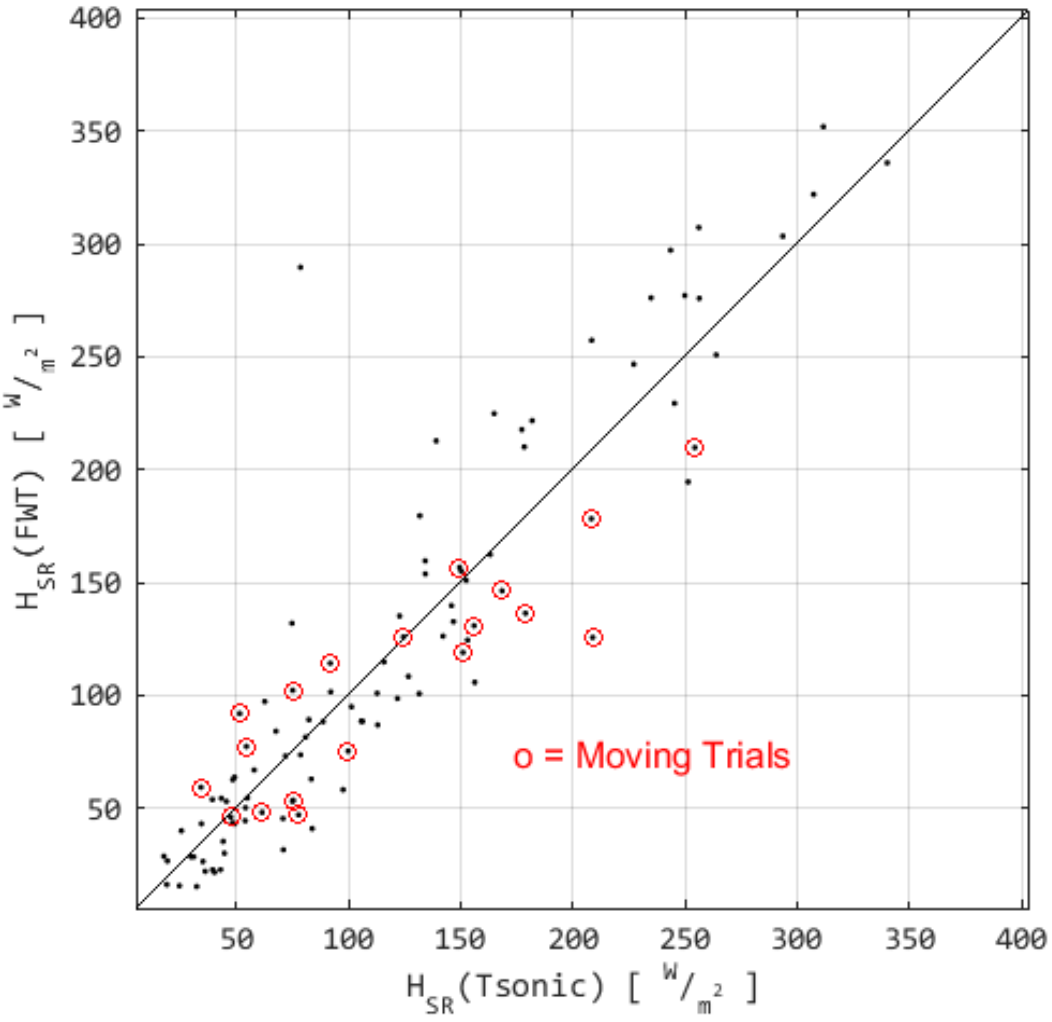

Figure 5-27: Comparison of SR flux calculated by T_{sonic} and by $T_{FWT.}$
The slope of the regression line is nearly one, but less than 1 for moving trials, indicating that the α calibration parameter changes with instrument response during moving trials, see (Shapland et al., 2014). The physical basis for this difference is that frequency response of the sonic temperature measurement is distorted differently than FWT measurement when wind changes in frequency distribution
(June 2015 data used in this figure).

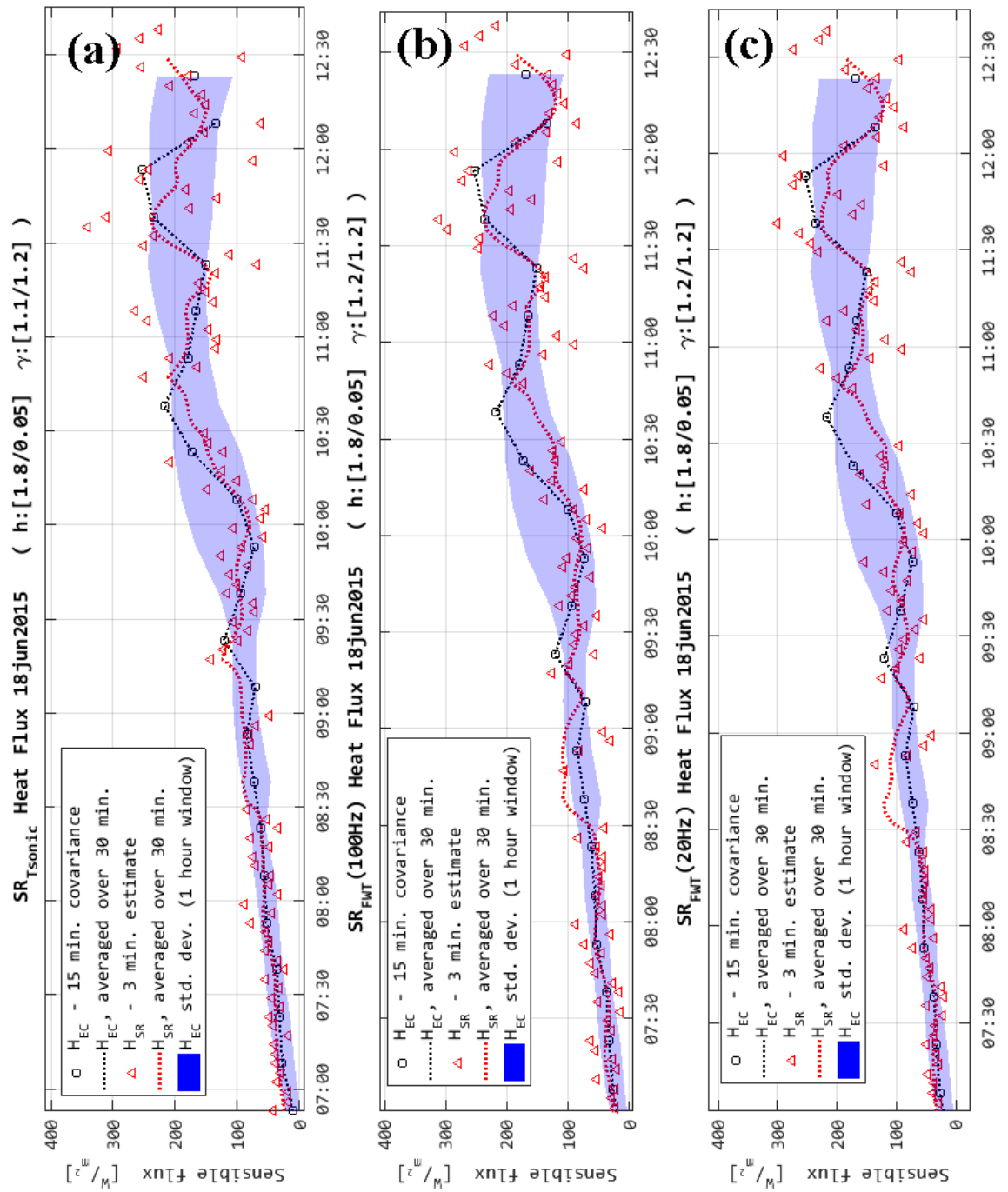

Figure 5-28: Times series of H_{SR} calculated with IRGASON and by Fine Wire Thermocouple

5.3.6 Other methods used with SR

As discussed above, the SR method requires calibration and complementary methods to determine flux, especially latent flux used that is relevant when estimating crop water use. Two complementary flux estimates were utilized to validate the SR method. The first method employed the temperature variance scaling during periods of free convection, which gives an independent estimator of sensible flux. Second, latent flux was computed directly from the high frequency water vapor concentration (measured by the IRGASON) using SR, and this latent heat flux was compared to the EC estimate.

Flux variance methods use scaling relationships during periods of free convection to determine heat and momentum flux. Temperature variance is already calculated for EC and SR, and provides an independent value for sensible flux using only the temperature trace. Following the scaling relationships proposed by Monin-Obukhov similarity theory (Wyngaard et al., 1971), the temperature parameter ($T_* = \langle w'T' \rangle / u_*$) combined with the Obukhov length gives a functional relationship between temperature variance σ_T and stability that under free convection reduces to the form:

$$\sigma_T / T_* = C_1 \left(-\zeta\right)^{-1/3} \qquad \text{Eq. 5-13}$$

in which C_1 is a empirical constant. Above the roughness sublayer, buoyancy is the dominant force during free convection, and (Albertson et al., 1995) derive that sensible heat flux can be estimated as:

$$H = C_1^{-\frac{3}{2}} \left(\rho C_P (\kappa g z)^{\frac{1}{2}} \sigma_T^{\frac{3}{2}} T_{air}^{-\frac{1}{2}} \right) \qquad \text{Eq. 5-14}$$

in which κ is the von Kármán constant, g is the acceleration due to gravity, and z is the measurement height. This flux estimate, termed H_{FCS} below, was calculated using 20Hz sonic

temperature (for variance) and calibrated HMP temperature for the mean (T_{air} in Eq 5-14). As this does not require additional instrumentation, this method can potentially provide an independent estimate against which SR can be calibrated by direct comparison of the flux magnitudes.

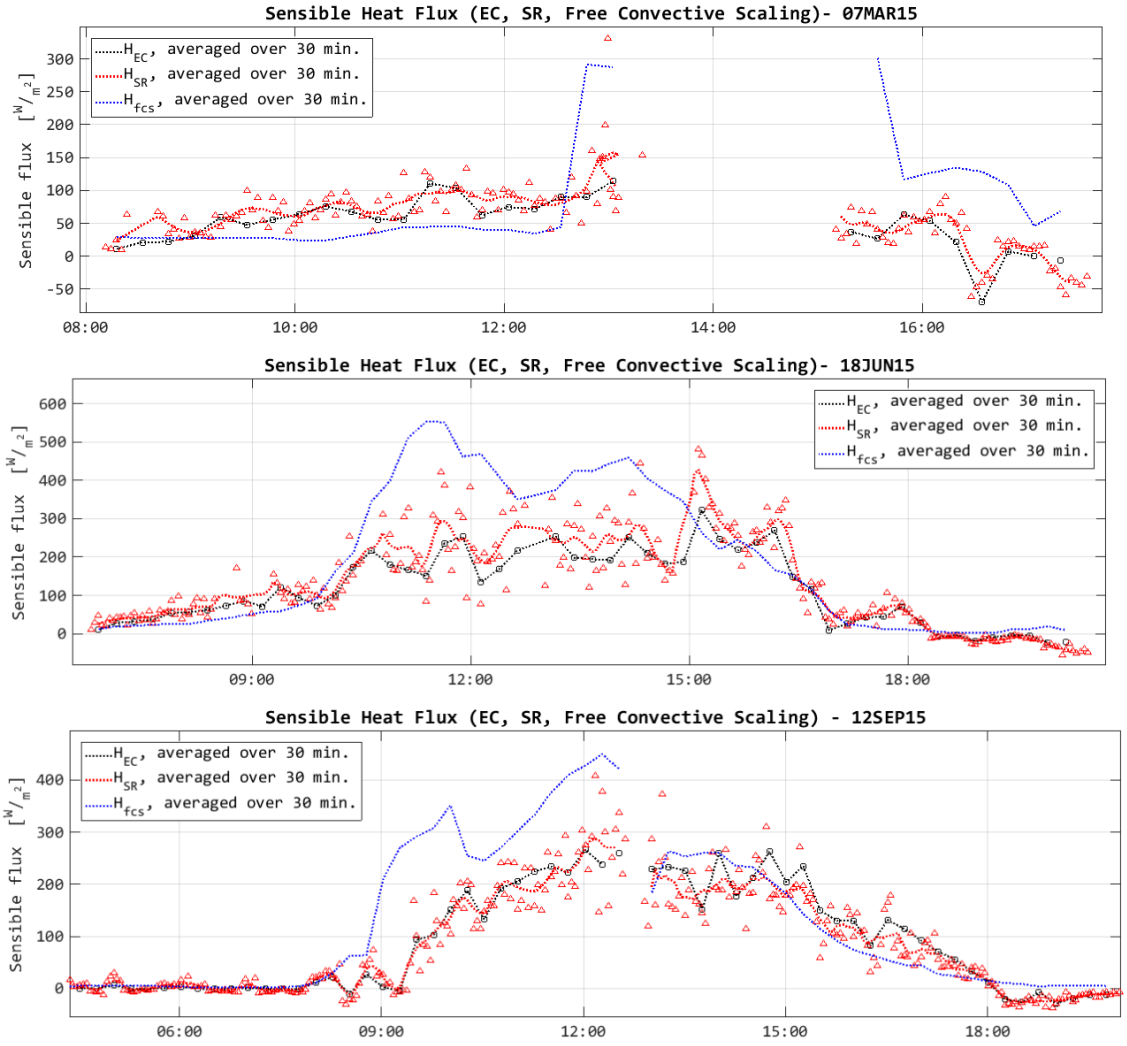

Figure 5-29: Independent flux estimates using free convective scaling.
Red and black represent surface renewal and eddy covariance flux estimates, as above. Blue line indicates 30 minute moving average of sensible flux as estimated from temperature variance using free convective scaling method (Eq. 5-14). 15 minute estimates of H_{FCS} are not shown.

As shown in Figure 5-29, H_{FCS} did not closely follow either H_{EC} or calibrated H_{SR}. Even allowing for A 10-15% error in H_{EC} as a control estimate, temperature variance gave flux estimates that were unreliable. It should be noted that the continuous H_{FCS} (blue lines) are generated for all periods, regardless of atmospheric stability. Since this estimate is only valid during periods of free convection, H_{FCS} was constrained to periods where $\zeta < -2$ and $H_{EC} > 100$ W/m^2, and sorted according to stability (not shown). Although in some period, H_{FCS} corresponded closely to H_{EC}, it was also dissimilar for some periods, with no apparent relationship with ζ, flux magnitude, or σ_T. Because initial efforts to use temperature variance were unsuccessful, this method was not further refined. However, free convective scaling remains an important method- (Castellví, 2013) used this to determine flux when SR was not valid.

Ultimately, this study is intended to shed light on evapotranspiration; to this end it would be more valuable to estimate latent flux directly. Indirect latent flux estimates are possible by assuming a closed surface energy balance, and measuring sensible heat flux, ground flux, and net radiation (Paw U et al., 1995). Direct estimates of latent flux has been demonstrated (Katul et al., 1996; Snyder et al., 1996; Suvočarev et al., 2014), yet as with measuring H_{SR}, no demonstration of a moving SR method has been attempted. During the trials, the IRGASON's infrared gas analyzer measures the water vapor density (g_{vapor}/m^3) at 20 Hz, and the SR estimate of latent flux was calculated using the same code and calibrations used for sensible flux. Water vapor density was converted to specific humidity q ($kg_{water}/kg_{dry\ air}$) and the 20Hz trace of q was substituted for T_{sonic} in the Matlab function (*SR_v7bLE.m*).

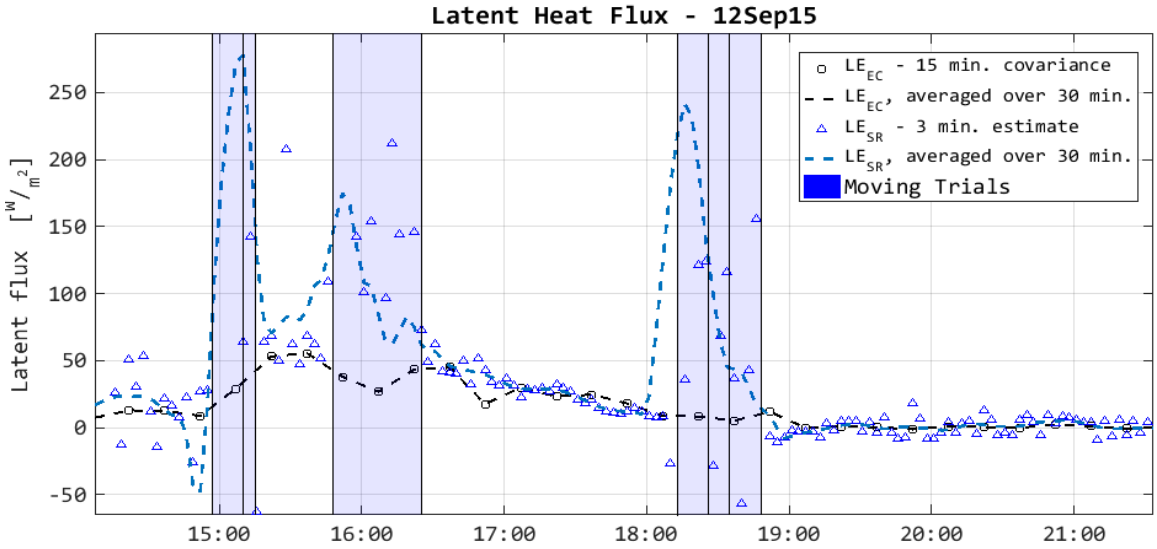

Figure 5-30: Example trace of latent heat flux calculated using SR method.
There is close correspondence between methods during stationary periods, but the SR method does not work during moving trials. Error was due to extreme noise in IRGA data, caused by vehicle bouncing over rough fields causing instrument vibration. Note that some 3 minute LE_{SR} points are excluded from the view as they extended -500-1000 W/m^2.

In general, the SR method worked in estimating latent heat flux LE as well as it did for sensible heat flux. However, the method did not work at all during moving trials (Figure 5-30). Inspecting the humidity trace, it was evident that the gas analyzer was the source of the problem, as the variance in q increased tenfold (not shown). The despiking algorithm was adapted in an attempt to extract useful information from the noisy signal, but was ultimately unsuccessful. The physical limits of the IRGA clearly limit its application on a moving platform without modification to reduce vibration. Nonetheless, the SR method is directly useful in measuring evapotranspiration, given a fast humidity sensor.

5.3.7 Negative ramp time and flux direction

As a final point on implementation of the SR method, the direction of the flux (i.e. upward or downward) is not explicit in the SR equations as it is with the EC method. (Chen et al., 1997b) note that the flux direction can be recovered from the sign of $S^3(r)$, and this was tabulated in the code *strfnc.m* as the variable *fluxdir*. Initially, SR trials were conducted during the day when sensible fluxes were positive (upward) at all times. However, upon conducting trials overnight

and during morning and evening transitions, it was clear that this determination was not reliable, particularly during transitions when flux magnitudes were low and switching sense. Various solutions to determine the cause of this variability were posed, and subsequently revealed several problems in intermediate calculations including: negative ramp durations; only imaginary solutions for ramp amplitudes; contradictory flux magnitudes depending on calculation method. To resolve these differences, different implementations of the SR method were employed (version 3-6). Generally, the problematic time periods were found to be at transitions and when flux magnitude is low, which is similar to EC and other methods, when gradients are near instrument detection levels. As an alternative to determining the flux direction from the sign of the structure function, the sign of the stability parameter ζ was used instead. By definition, stability is inverse related to the sign of the sensible flux (e.g under stable conditions $\zeta > 0$, and cold dense air lies below warm less dense air, inhibiting vertical mixing). It was found that using ζ to determine flux direction prevented the majority of obvious incorrect assignations by *fluxdir*. In either case, the number of cases in which flux direction was unclear was very small, and the majority of these cases occurred when flux magnitude was low, so that the cumulative effect on measuring flux is small.

5.4 Discussion and Conclusions

As noted above the shortest time period that SR can reliably measure a flux is on the order of three minutes. For a measurement taken from moving vehicle, moving at 1 m/s, this gives a spatial resolution, neglecting advection or flux footprints, on the order of 180 m. Even if the conversion from sensible heat flux to evaporation measurement can be accomplished, this spatial resolution is not adequate to address the data needs of precision irrigation systems (Chapter 2). Nonetheless, new applications of the SR method are suggested by these results. This study and other recent published work suggest novel applications and correction methods for SR, and a

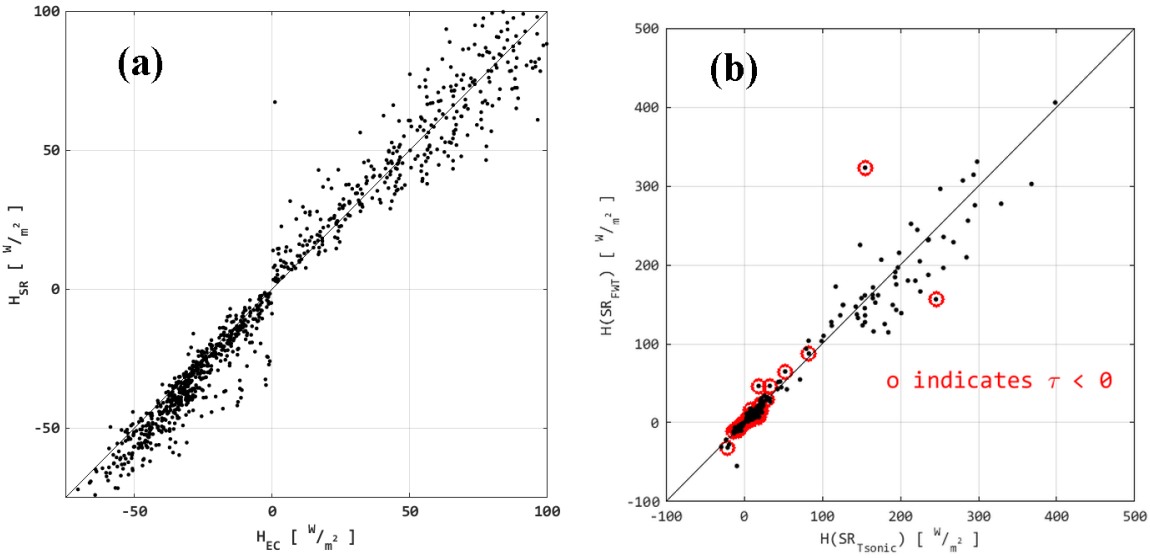

Figure 5-31: Indications of flux direction errors.

Fig.5-31(a) shows the 02-11 August 2014 H_{EC} : H_{SR} comparison (z = 1.9m), including 1074 15 averaging periods. The direction of sensible flux (positive upward, negative downward) was assigned using the (opposite) sign of ζ. This constraint is visible as a discontinuity in scatter when the magnitude of H_{SR} is small (a).

Few or no cases of large magnitudes with misassigned flux direction were observed in any trials. Remaining outliers are often related to problematic calculation of the ramp duration (τ) or ramp amplitude (A). Figure 5-31(b) shows a example in which outliers in the comparison (in this case between H_{SR}@100Hz and H_{EC}@20Hz) are clearly related to negative ramp times. Cases with $\tau < 0$ are indicted in red: note that the vast majority of cases with negative ramp times are during negative flux, which is correctly assigned (the direction of the ramps is opposite in sense as is flux direction).

combination of approaches may be combined to develop new field methods for rapid, high resolution, and low cost ET measurement.

5.4.1 Determination and robustness of calibration terms γ and α

As demonstrated in this study, the need for site specific calibration of the γ parameter is required. Without a clear physical explanation for the value of γ, new approaches are needed to formulate reliable and automated procedures to establish γ for a particular field conditions, and to determine the long term stability of this calibration in relationship to the change in ground cover. Obscured by the generally good agreement between H_{SR} and H_{EC}, the calculated ramp time was occasionally negative, and imaginary components in the solution for the cubic terms in Equation 5-8 could be neglected because of cancelled terms. There is no physical explanation for these

problems. In many cases when flux calculations failed, the calculation breakdown occurred at transitions (sunrise and sunset) when stability was near zero and flux magnitudes were very small. While this can generally be overlooked in a cumulative water budgets, it does not help clarify the flux calculation in those marginal cases where SR has been suggested to offer new insights. For this study, α was calculated automatically using information from the sonic anemometer and using similarity theory to predict boundary layer behavior, following the work of Castellví, Paw U, and others. Explicit determination of the roughness height is also required to solve for α, and this proved to be problematic, especially since the relationship between vegetation height and roughness is only approximate. The parameter α varies according to both site conditions and instrumentation, and this was probably obscured in the FWT analysis above by adjustment of γ. Independent determination of α, using methods suggested by Shapland, Suvočarev and others may be feasible in field applications to decouple these two parameters (Shapland et al., 2014; Suvočarev et al., 2014).

In general, three approaches to further refine the SR calibration can be described. First, calibration against some control measurement of the flux magnitude can be accomplished by a variety of established methods- this is the standard approach used in by researchers. In research applications, comparison against eddy covariance or lysimeters (Castellví and Snyder, 2010) is a reliable and precise method. In field applications such as irrigation monitoring, research methods are not feasible because of cost, operator skill, or simple physical limitation of deploying sensors in working farm fields. Other comparator methods, free convective scaling being one example, can be used with the same FWT/ high frequency measurements of temperature. These methods are only valid under certain conditions (such as neutral stability conditions), for which objective selection criteria are needed in calibration protocol.

A second approach is to calibrate against flux estimates from standard methods such as

Penman-Monteith. This approach requires taking long term estimates and establishing cumulative fluxes, which may be relatively affordable but require periods of data collection to adequately calibrate SR estimates. Another approach has used gradients to characterize the affect of coherent structures on stability, and subsequently calibrate high frequency measurements for SR flux estimates directly (Castellví, 2013). Finally, computational methods may provide efficient ways to leverage existing information without requiring comparison with an expensive method (eddy covariance) or a long term measurement. Neural networks are one example a computation tool that is already employed in determining ET from low cost sensors (Fernando and Pardyjak, 2013; Kumar et al., 2011). Such approaches can be used to control nonlinear calibration, used to generate feedback learning for flux estimates, and to establish site specific flux models (Bowden et al., 2005; Trajkovic et al., 2003).

5.4.2 Feasibility and cost of SR for mapping flux

Surface renewal is often proposed as a cost-effective alternative to eddy covariance because of the very low cost of fine wire thermocouples (~100 USD) compared to sonic anemometers and gas analyzers ($5000-15000 for each instrument). Additionally, the FWT is a very small and light device, and therefore feasible to mount on small, low cost UAVs. However, once it was determined that 20Hz sampling was adequate to detect the coherent ramp structures, data from the sonic anemometer was used almost exclusively in this analysis. The need to calibrate via friction velocity and function $\phi(\zeta)$ was much more robust and efficient using direct measurements rather than iterative methods as proposed by (Snyder et al., 2008). A reasonable range of air speeds for UAVs is 0.5-5m/s, precluding their use to map flux with the SR method. However, it is still possible to implement moving SR estimates at slower speeds; center pivot mounted sensors are demonstrably feasible and effective for mapping variable water stress (Peters and Evett, 2007). Such a SR implementation may be most cost effective for a large system such as a center pivot (irrigating areas greater than 100 hectares). By including a single anemometer could

be justified by feeding calibration parameters to multiple, distributed FWTs, and mapping water demand over entire fields from the pre-existing irrigation infrastructure. Additionally, high frequency wind speeds allow a calibration directly from eddy covariance.

FWTs can be used in other distributed geometries- either as networks or with mobile units - to generate low cost flux maps. Maps combining statistical interpolation (such as kriging) and footprint models would be able to capture heterogeneous fluxes, especially considering the calibration methods demonstrated by (Castellví, 2013, 2012; Shapland et al., 2014). By combining flux-gradient methods (e.g. Bowen ratio), similarity theory (e.g. free convective scaling), and surface renewal, a suite of low cost sensors can theoretically capture flux in almost any surface condition. Scaling the sensor design to match the needs of any specific field condition can make flux measurement cost effective for a range of irrigation systems.

5.4.3 Next steps

The calibration methods and sensor designs indicated above address the utility of SR to capture sensible heat fluxes, yet sensible heat alone does not directly map latent fluxes that are relevant to crop water demand. While sensible heat flux can be used in conjunction with heat flux plates and radoometers to derive ET as a residual term in the surface energy budget, this doesn't help with moving or distributed flux maps- the footprints of the various sensors don't match. Moving latent flux estimates were not possible even with the gas analyzer in this study, due to sensor noise induced by undamped vibration in the mounting assembly during moving trials (and possibly the motor of the ATV itself).

Latent flux was captured during stationary trials, so that in principle, SR can be used to map ET directly. For irrigation management, this will require the development of a low cost, robust fast response humidity sensor. Various technologies have been proposed, including electrically conductive ceramics (Higgins, personal correspondence), fiber Bragg grating (Correia et al.,

2012), and supramolecular nanofibers (Mogera et al., 2014). Generally, the cost of developing these sensors has restricted their application to medical and manufacturing fields, but their development suggest that environmental applications are possible.

More immediately, the combining data from multiple sensors can illuminate linkages in hydrologic processes. By measuring soil water potential, solar and sky radiation, sensible heat fluxes, and other parameters, computation methods can be implemented to understand the non-linear relationships that drive (or at least correlate to) ET rates. Neural networks have been successfully used to estimate surface fluxes from low cost sensors (Jensen et al., 2015) to forecast ET (Trajkovic et al., 2003), and model daily ET (Kişi and Cimen, 2009). Ground estimates of ET can also be used in conjunction with low cost or publicly funded forecast networks (Mancosu et al., 2014; Snyder et al., 2009) and satellite imagery (Allen et al., 2015) to generate site specific ET estimates, although refining this data to the scale required for precision irrigation is not yet feasible.

The SR method provides novel insights into the role of turbulence in driving surface fluxes. New calibration methods that do not require expensive instrumentation show promise, demonstrating that the SR method is ready for broader implementation not just in research, but as a monitoring tool in irrigation. By resolving flux over short periods, SR can be used in conjunction with other methods to map flux over heterogeneous surface conditions, and guide efficient allocation decisions and robust irrigation scheduling.

6. Providing Data to Precision Agriculture- Future Steps

Advances in precision irrigation systems (Chapter 2), soil moisture monitoring (Chapter 3), and flux measurement (Chapters 4 and 5) can allow irrigators to match water delivery to crop demand for areas as small as 0.1 hectare. Implementation of these methods is not only limited by technical feasibility, but also by social, environmental, and economic factors. Every farm venture must manage risks from weather and crop variability. Increasingly, projecting the availability of water for irrigation is also affected by water law, depressed aquifers, and competition for surface water allocations. Uncertainty about water supply adds an additional dimension of risk to irrigated farming (Evans and King, 2012). Climate change, drought, and water rights are all important drivers of water availability, and also affect the decisions that farmers make each season (Knox et al., 2012). Irrigators still need to make daily and hourly decisions on how best to use the available water; irrigation research and weather monitoring networks have facilitated improved irrigation by providing detailed and specific information about the actual crop water demand (Smith, 2015). However, low cost, onsite, and real time data will be increasingly important to adapt regional data to site specific ET estimates and field scale maps of crop water demand. To encourage adoption of new technologies into farming practices, new methods will need to use open source designs, have low implementation and maintenance costs, and implement strategies which can be readily integrated into existing farm systems. Two examples of technology that embody this modality include low cost electronics and neural networks.

The rapid expansion of simple, low cost electronics including smart phones and weather stations are radically changing farmers' access to real time water use information. Increasingly, on-farm sensors systems are capable of collecting the necessary data to estimate ET, and can help translate regional ET network data into site specific demand estimates. In the last decade, there has been an explosion of high quality, consumer grade microcontrollers (such as Arduino) that are readily incorporated into sensor systems (Junior et al., 2013), on-farm weather stations

(Mesas-Carrascosa et al., 2015), and telemetry to control irrigation (Lim et al., 2014). Low cost sensors for humidity, temperature, and light, as well as sensors for wind and soil properties can be purchased directly from web based suppliers or can be assembled from readily available components. Wireless networks allow water use, soil moisture, and operational data to be integrated automatically (Carland et al., 2013; Ruiz-Garcia et al., 2009). While these sensors do not replace research grade instruments for more rigorous experimentation, low cost sensors can facilitate continuous ET monitoring at the field scale. Existing farm labor can maintain such systems without the need for dedicated scientists or contractors. Sensors are already being integrated into normal farm equipment, including water flow meters, GPS, yield measurements, and cameras. Combining these sensors with a system to measure soil moisture and ET can provide the information needed for precision irrigation.

Integrating low cost sensors and more rigorous ET measurement can be accomplished using non-linear approaches such as artificial neural networks (ANNs). Neural networks are used to predict the behavior of non-linear systems, and have been applied in hydrologic modelling to approximate environmental behaviors for which no robust mathematical description has been found (Paliwal and Kumar, 2009). ANNs are used to model hydrologic processes such as rainfall, river behavior, and atmospheric transport (Maier and Dandy, 2000) . ANNs are also used for automated control of complex systems from factory robotics to airplane flight [Schumann and Liu, 2010; Hansen and Salamon, 1990]. For ET estimation, a neural network is used to calculate the contribution and relationship of each defined input parameter (such as air temperature, humidity, soil wetness, net radiation, etc.) to a ANN output by comparing against a control estimate of ET (such as eddy covariance or Penman-Monteith). The unknown nodes are recursively adjusted to minimize error and best approximate the control measurement (Kumar et al., 2011). After collecting data for a learning period and averaging many iterative solutions, a robust site-specific solution can be found without requiring models for the underlying physical

drivers (Jensen et al., 2015). Neural networks have been used to forecast ET from long term weather records (Kişi and Öztürk, 2007; Trajkovic et al., 2003); to predict ET in desert environments from limited data inputs using eddy covariance as a control estimate and Penman-Monteith reference ET as a comparator (Fernando and Pardyjak, 2013); and to evaluate real time irrigation requirement from remotely sensed data (Irmak and Kamble, 2009). ANNs are used interpolate ET measurement networks, and may augment site-specific ET estimation using existing sensors and measurements. Neural networks can also be integrated into a larger integrated farm and water distribution control system.

The near future demands increased agricultural production despite more competition for water resources, and despite increasing risks and long term uncertainty due to climate change. Meeting this challenge will require combining low cost, easily distributed technology, with open source, adaptable techniques. As with other industries, agriculture can become more efficient not just through economies of scale, but through the synergies made possible by collaboration and innovation. Remote sensing and the internet together make possible global scale monitoring and prediction of weather and water data. Mobile instruments such as the EM soil mapping sensor can map with unprecedented detail. New techniques such as surface renewal have been refined in previous decades, and can be disseminated rapidly through both conventional and new media outlets. Low cost sensors can be manufactured and modified by end users following online forums and with technologies such as 3-d printing. Machine learning techniques such as neural networks can bring together seemingly disparate elements and find site specific solutions. The diversity of this list reflects the complexity of the challenges and solution to addressing water management in agriculture. Success in farming always requires adapting and making best use of whatever resources are available, and in this era of shrinking water availability, information technology is the resource at hand. The current era of information and communication technology offer new ways to economize farming production and water resource management.

References

Albertson, J.D., Parlange, M.B., Katul, G.G., Chu, C.-R., Stricker, H., Tyler, S., 1995. Sensible Heat Flux From Arid Regions: A Simple Flux-Variance Method. Water Resources Research 31, 969–973.

Alfieri, J.G., Kustas, W.P., Prueger, J.H., Hipps, L.E., Evett, S.R., Basara, J.B., Neale, C.M., French, A.N., Colaizzi, P., Agam, N., 2012. On the discrepancy between eddy covariance and lysimetry-based surface flux measurements under strongly advective conditions. Advances in Water Resources.

Allen, R., 2005. The ASCE standardized reference evapotranspiration equation. Amer Society of Civil Engineers.

Allen, R., 1986. A Penman for all seasons. Journal of Irrigation and Drainage Engineering 112, 348–368.

Allen, R., Bastiaanssen, W., Tasumi, M., Morse, A., 2001. Evapotranspiration on the watershed scale using the SEBAL model and Landsat images, in: ASAE Meeting Presentation, Paper.

Allen, R., Jensen, M.E., 2015. ASCE Manual 70–Second Edition: Evaporation, Evapotranspiration and Irrigation Requirements, in: 2015 ASABE/IA Irrigation Symposium: Emerging Technologies for Sustainable Irrigation-A Tribute to the Career of Terry Howell, Sr. Conference Proceedings. American Society of Agricultural and Biological Engineers, pp. 1–16.

Allen, R., Morton, C., Kamble, B., Kilic, A., Huntington, J., Thau, D., Gorelick, N., Erickson, T., Moore, R., Trezza, R., 2015. EEFlux: A Landsat-based Evapotranspiration mapping tool on the Google Earth Engine, in: 2015 ASABE/IA Irrigation Symposium: Emerging Technologies for Sustainable Irrigation-A Tribute to the Career of Terry Howell, Sr. Conference Proceedings. American Society of Agricultural and Biological Engineers, pp. 1–11.

Allen, R., Pereira, L.S., Howell, T.A., Jensen, M.E., 2011a. Evapotranspiration information reporting: I. Factors governing measurement accuracy. Agricultural Water Management 98, 899–920.

Allen, R., Pereira, L.S., Howell, T.A., Jensen, M.E., 2011b. Evapotranspiration information reporting: II. Recommended documentation. Agricultural Water Management 98, 921–929.

Allen, R., Pereira, L.S., Raes, D., Smith, M., 1998. Crop evapotranspiration-Guidelines for computing crop water requirements-FAO Irrigation and drainage paper 56. FAO, Rome 300, 6541.

Allen, R., Pruitt, W.O., Jensen, M.E., 1991. Environmental requirements of lysimeters. Lysimeters for evapotranspiration and environmental measurements 23–25.

Allen, R.G., Pereira, L.S., 2009. Estimating crop coefficients from fraction of ground cover and height. Irrigation Science 28, 17–34.

Allen, R.G., Walter, I.A., Elliott, R., Mecham, B., Jensen, M.E., Itenfisu, D., Howell, T.A., Snyder, R., Brown, P., Echings, S., 2000. Issues, requirements and challenges in selecting and specifying a standardized ET equation, in: Proc., 4th National Irrigation Symp. Citeseer, pp. 201–208.

Altman, Y., 2015. Accelerating Matlab Performance. CRC Press.

Amatya, D.M., Skaggs, R.W., Gregory, J.D., 1995. Comparison of methods for estimating REF-ET. Journal of irrigation and drainage engineering 121, 427–435.

Anderson, B.T., Ruane, A.C., Roads, J.O., Kanamitsu, M., 2009. Estimating the influence of evaporation and moisture-flux convergence upon seasonal precipitation rates. Part II: An analysis for North America based upon the NCEP-DOE reanalysis II model. Journal of Hydrometeorology 10, 893–911.

Anderson, M.C., Allen, R.G., Morse, A., Kustas, W.P., 2012. Use of Landsat thermal imagery in monitoring evapotranspiration and managing water resources. Remote Sensing of Environment 122, 50–65.

Anderson, M.C., Kustas, W.P., Norman, J.M., Hain, C.R., Mecikalski, J.R., Schultz, L., Gonzalez-Dugo, M.P., Cammalleri, C., d' Urso, G., Pimstein, A., 2011. Mapping daily evapotranspiration at field to continental scales using geostationary and polar orbiting satellite imagery. Hydrology and Earth System Sciences 15, 223–239.

Anderson-Cook, C.M., Alley, M.M., Roygard, J.K.F., Khosla, R., Noble, R.B., Doolittle, J.A., 2002. Differentiating soil types using electromagnetic conductivity and crop yield maps. Soil Science Society of America Journal 66, 1562–1570.

Andreas, E., 1989. Two-wavelength method of measuring path-averaged turbulent surface heat fluxes. Journal of Atmospheric and Oceanic Technology 6, 280–292.

Andreas, E.L., 1988. Atmospheric stability from scintillation measurements. Applied optics 27, 2241–2246.

Andreas, E.L., Fairall, C.W., Persson, P.O.G., Guest, P.S., 2003. Probability distributions for the inner scale and the refractive index structure parameter and their implications for flux averaging. Journal of Applied Meteorology 42, 1316–1329.

Antonia, R.A., Van Atta, C.W., 1978. Structure functions of temperature fluctuations in turbulent shear flows. Journal of Fluid Mechanics 84, 561–580.

Aubinet, M., Vesala, T., Papale, D., 2012. Eddy covariance: a practical guide to measurement and data analysis. Springer Science & Business Media.

Baldocchi, D., 2014. Measuring fluxes of trace gases and energy between ecosystems and the atmosphere–the state and future of the eddy covariance method. Global change biology 20, 3600–3609.

Baldocchi, D., Falge, E., Gu, L., Olson, R., Hollinger, D., Running, S., Anthoni, P., Bernhofer, C., Davis, K., Evans, R., 2001. FLUXNET: A new tool to study the temporal and spatial variability of ecosystem-scale carbon dioxide, water vapor, and energy flux densities. Bulletin of the American Meteorological Society 82, 2415–2434.

Barker, J.B., Neale, C.M., Heeren, D.M., 2015. Evaluation of a hybrid remote sensing evapotranspiration model for variable rate irrigation management, in: 2015 ASABE/IA Irrigation Symposium: Emerging Technologies for Sustainable Irrigation-A Tribute to the Career of Terry Howell, Sr. Conference Proceedings. American Society of Agricultural and Biological Engineers, pp. 1–9.

Barnett, B.J., Mahul, O., 2007. Weather index insurance for agriculture and rural areas in lower-income countries. American Journal of Agricultural Economics 89, 1241–1247.

Bastiaanssen, W.G.M., Noordman, E.J.M., Pelgrum, H., Davids, G., Thoreson, B.P., Allen, R.G., 2005. SEBAL model with remotely sensed data to improve water-resources management under actual field conditions. Journal of irrigation and drainage engineering 131, 85–93.

Baumhardt, R.L., Lascano, R.J., Evett, S.R., 2000. Soil material, temperature, and salinity effects on calibration of multisensor capacitance probes. Soil Science Society of America Journal 64, 1940–1946.

Behnke, R., Vavrus, S., Allstadt, A., Albright, T., Thogmartin, W.E., Radeloff, V.C., 2016. Evaluation of downscaled, gridded climate data for the conterminous United States. Ecological Applications.

Bell, J.P., 1987. Neutron probe practice.

Bellvert, J., Zarco-Tejada, P.J., Girona, J., Fereres, E., 2014. Mapping crop water stress index in a "Pinot-noir"vineyard: comparing ground measurements with thermal remote sensing imagery from an unmanned aerial vehicle. Precision agriculture 15, 361–376.

Berne, D., Cohen, R., Wickes, G., Whitty, K., 2015. Agricultural Irrigation Initiative: Overview. Northwest Energy Efficiency Alliance. Accessed at: http://neea.org/resource-center/market-research-and-evaluation-reports April 2015

Beyrich, F., Bange, J., Hartogensis, O.K., Raasch, S., Braam, M., van Dinther, D., Graf, D., van Kesteren, B., van den Kroonenberg, A.C., Maronga, B., Martin, S., Moene, A.F., 2012. Towards a validation of scintillometer measurements: the LITFASS-2009 experiment. Boundary-Layer Meteorology 144, 83+.

Biltoft, C.A., Pardyjak, E.R., 2009. Spectral Coherence and the Statistical Significance of Turbulent Flux Computations. Journal of Atmospheric and Oceanic Technology 26, 403–409.

Blaney, H.F., Criddle, W.D., 1962. Determining consumptive use and irrigation water requirements. US Department of Agriculture.

Bowden, G.J., Maier, H.R., Dandy, G.C., 2005. Input determination for neural network models in water resources applications. Part 2. Case study: forecasting salinity in a river. Journal of Hydrology 301, 93–107. doi:10.1016/j.jhydrol.2004.06.020

Bowen, I.S., 1926. The ratio of heat losses by conduction and by evaporation from any water surface. Physical review 27, 779.

Brevik, E.C., Fenton, T.E., 2004. The effect of changes in bulk density on soil electrical conductivity as measured with the Geonics EM-38. Soil Horizons 45, 96–102.

Brevik, E.C., Fenton, T.E., Lazari, A., 2006. Soil electrical conductivity as a function of soil water content and implications for soil mapping. Precision Agriculture 7, 393–404.

Brevik, E.C., Lee, J., Fenton, T.E., Horton, R., 2003. Evaluation of the Influence of Soil Moisture, Calcite Content, and Temperature on Bulk Electrical Conductivity. Evaluation of selected factors that may influence the application of electromagnetic induction technology to soil science investigations in Iowa 58.

Bronson, K.F., Booker, J.D., Bordovsky, J.P., Keeling, J.W., Wheeler, T.A., Boman, R.K., Parajulee, M.N., Segarra, E., Nichols, R.L., 2006. Site-specific irrigation and nitrogen management for cotton production in the Southern High Plains. Agronomy Journal 98, 212–219.

Brutsaert, W., 1982. Evaporation into the atmosphere: theory, history, and applications. Reidel Dordrecht.

Brutsaert, W., 1965. A model for evaporation as a molecular diffusion process into a turbulent atmosphere. Journal of Geophysical Research 70, 5017–5024.

Brutsaert, W., Sugita, M., 1992. Application of self-preservation in the diurnal evolution of the surface energy budget to determine daily evaporation. Journal of Geophysical Research: Atmospheres (1984–2012) 97, 18377–18382.

Budyko, M., 1958. 1. 1956. The heat balance of the earth's surface. Translation by US Dept. of Commerce, Weather Bureau, Washington, DC.

Buhrig, W., Shock, C., 2015. Wireless Sensor Network for “On Farm” Soil Moisture Data Acquisition and Irrigation Scheduling. American Society of Agricultural and Biological Engineers, pp. 1–6. doi:10.13031/irrig.20152146938

Burba, G., 2013. Eddy Covariance Method for Scientific, Industrial, Agricultural and Regulatory Applications: A Field Book on Measuring Ecosystem Gas Exchange and Areal Emission Rates. LI-COR Biosciences.

Burt, C.M., Clemmens, A.J., Strelkoff, T.S., Solomon, K.H., Bliesner, R.D., Hardy, L.A., Howell, T.A., Eisenhauer, D.E., 1997. Irrigation performance measures: efficiency and uniformity. Journal of irrigation and drainage engineering 123, 423–442.

Burt, C.M., Mutziger, A.J., Allen, R.G., Howell, T.A., 2005. Evaporation research: Review and interpretation. Journal of irrigation and drainage engineering 131, 37–58.

Businger, J.A., Wyngaard, J.C., Izumi, Y., Bradley, E.F., 1971. Flux-Profile Relationships in the Atmospheric Surface Layer. Journal of Atmospheric Science 28, 181–189. doi:10.1175/1520-0469(1971)028<0181:FPRITA>2.0.CO;2

Businger, Ja., 1986. Evaluation of the accuracy with which dry deposition can be measured with current micrometeorological techniques. Journal of Climate and Applied Meteorology 25, 1100–1124.

Cammalleri, C., Anderson, M.C., Gao, F., Hain, C.R., Kustas, W.P., 2014a. Mapping daily evapotranspiration at field scales over rainfed and irrigated agricultural areas using remote sensing data fusion. Agricultural and forest meteorology 186, 1–11.

Cammalleri, C., Anderson, M.C., Kustas, W.P., 2014b. Upscaling of evapotranspiration fluxes from instantaneous to daytime scales for thermal remote sensing applications. Hydrology and Earth System Sciences 18, 1885–1894.

Carland, J., Umeda, M., Wilkey, T., Oberbeck, A., Cumming, J., Parks, N., Fripp, M., Kuh, A., Garmire, D., 2013. Self-Sustaining Meteorological Wireless Sensor Networks. Sensors & Transducers 160, 118.

Castellvi, F., 2004. Combining surface renewal analysis and similarity theory: a new approach for estimating sensible heat flux. Water resources research 40.

Castellví, F., 2013. A method for estimating the sensible heat flux in the inertial sub-layer from high-frequency air temperature and averaged gradient measurements. Agricultural and Forest Meteorology 180, 68–75. doi:10.1016/j.agrformet.2013.05.005

Castellví, F., 2012. Fetch requirements using surface renewal analysis for estimating scalar surface fluxes from measurements in the inertial sublayer. Agricultural and Forest Meteorology 152, 233–239. doi:10.1016/j.agrformet.2011.10.004

Castellvi, F., Martínez-Cob, A., Pérez-Coveta, O., 2006. Estimating sensible and latent heat fluxes over rice using surface renewal. Agricultural and forest meteorology 139, 164–169.

Castellví, F., Perez, P.J., Ibañez, M., 2002. A method based on high-frequency temperature measurements to estimate the sensible heat flux avoiding the height dependence. Water Resources Research 38, 20–1–20–9.

Castellví, F., Snyder, R.L., 2010. A comparison between latent heat fluxes over grass using a weighing lysimeter and surface renewal analysis. Journal of Hydrology 381, 213–220.

Castellvi, F., Snyder, R.L., Baldocchi, D.D., 2008. Surface energy-balance closure over rangeland grass using the eddy covariance method and surface renewal analysis. Agricultural and Forest Meteorology 148, 1147–1160.

Cellier, P., Olioso, A., 1993. A simple system for automated long-term Bowen ratio measurement. Agricultural and Forest Meteorology 66, 81–92.

Champagne, C., Davidson, A., Cherneski, P., L'Heureux, J., Hadwen, T., 2015. Monitoring Agricultural Risk in Canada Using L-Band Passive Microwave Soil Moisture from SMOS. Journal of Hydrometeorology 16, 5–18.

Chapin, E., Chau, A., Chen, J., Heavey, B., Hensley, S., Lou, Y., Machuzak, R., Moghaddam, M., 2012. AirMOSS: An Airborne P-band SAR to measure root-zone soil moisture, in: Radar Conference (RADAR), 2012 IEEE. IEEE, pp. 0693–0698.

Chasmer, L., Barr, A., Hopkinson, C., McCaughey, H., Treitz, P., Black, A., Shashkov, A., 2009. Scaling and assessment of GPP from MODIS using a combination of airborne lidar and eddy covariance measurements over jack pine forests. Remote Sensing of Environment 113, 82–93.

Chavez, J.L., Gowda, P.H., Howell, T.A., Copeland, K.S., 2009. Radiometric surface temperature calibration effects on satellite based evapotranspiration estimation. International journal of Remote sensing 30, 2337–2354.

Chávez, J.L., Neale, C.M., Prueger, J.H., Kustas, W.P., 2008. Daily evapotranspiration estimates from extrapolating instantaneous airborne remote sensing ET values. Irrigation Science 27, 67–81.

Chávez, J.L., Pierce, F.J., Elliott, T.V., Evans, R.G., 2010a. A remote irrigation monitoring and control system for continuous move systems. Part A: Description and development. Precision Ag. 11, 1–10.

Chávez, J.L., Pierce, F.J., Elliott, T.V., Evans, R.G., Kim, Y., Iversen, W.M., 2010b. A remote irrigation monitoring and control system (RIMCS) for continuous move systems. Part B: Field testing and results. Precision agriculture 11, 11–26.

Chehbouni, A., Watts, C., Lagouarde, J.-P., Kerr, Y.., Rodriguez, J.-C., Bonnefond, J.-M., Santiago, F., Dedieu, G., Goodrich, D.., Unkrich, C., 2000. Estimation of heat and momentum fluxes over complex terrain using a large aperture scintillometer. Agricultural and Forest Meteorology 105, 215–226. doi:10.1016/S0168-1923(00)00187-8

Chen, W., Novak, M., Black, T.A., Lee, X., 1997a. Coherent eddies and temperature structure functions for three contrasting surfaces. Part II: Renewal model for sensible heat flux. Boundary-Layer Meteorology 84, 125–147. doi:10.1023/A:1000342918158

Chen, W., Novak, M., Black, T.A., Lee, X., 1997b. Coherent eddies and temperature structure functions for three contrasting surfaces. Part I: Ramp model with finite microfront time. Boundary-Layer Meteorology 84, 99–124. doi:10.1023/A:1000338817250

Clary, S., 2015. Boosting Agricultural Production through Water Use Efficiency. USDA Information Sheet. Accessed at http://www.westernsare.org/Learning-Center/Fact-Sheets/ Acc'd April 2015

Cooper, D.I., Eichinger, W.E., Kao, J., Hipps, L., Reisner, J., Smith, S., Schaeffer, S.M., Williams, D.G., 2000. Spatial and temporal properties of water vapor and latent energy flux over a riparian canopy. Agricultural and Forest Meteorology 105, 161–183.

Correia, S.F., Antunes, P., Pecoraro, E., Lima, P.P., Varum, H., Carlos, L.D., Ferreira, R.A., André, P.S., 2012. Optical fiber relative humidity sensor based on a FBG with a di-ureasil coating. Sensors 12, 8847–8860.

Corwin, D.L., Lesch, S.M., 2005. Apparent soil electrical conductivity measurements in agriculture. Computers and electronics in agriculture 46, 11–43.

Cuenca, R.H., Ciotti, S.P., Hagimoto, Y., 2013a. Application of Landsat to evaluate effects of irrigation forbearance. Remote Sensing 5, 3776–3802.

Cuenca, R.H., Hagimoto, Y., Moghaddam, M., 2013b. Three-and-a-half decades of progress in monitoring soils and soil hydraulic properties.

Daccache, A., Knox, J.W., Weatherhead, E.K., Daneshkhah, A., Hess, T.M., 2015. Implementing precision irrigation in a humid climate–Recent experiences and on-going challenges. Agricultural Water Management 147, 135–143.

Dalton, F.N., Van Genuchten, M.T., 1986. The time-domain reflectometry method for measuring soil water content and salinity. Geoderma 38, 237–250.

Davis, J.G., Kitchen, N.R., Sudduth, K.A., Drummond, S.T., 1997. Using electromagnetic induction to characterize soils. Better crops with plant food 4, 108–113.

DeBell, L., Anderson, K., Brazier, R.E., King, N., Jones, L., 2015. Water resource management at catchment scales using lightweight UAVs: current capabilities and future perspectives. Journal of Unmanned Vehicle Systems 3, 1–24.

Desjardins, R.L., Buckley, D.J., Amour, G.S., 1984. Eddy flux measurements of CO< sub> 2</sub> above corn using a microcomputer system. Agricultural and forest meteorology 32, 257–265.

Detto, M., Montaldo, N., Albertson, J.D., Mancini, M., Katul, G., 2006. Soil moisture and vegetation controls on evapotranspiration in a heterogeneous Mediterranean ecosystem on Sardinia, Italy. Water Resources Research 42.

Doolittle, J.A., Brevik, E.C., 2014. The use of electromagnetic induction techniques in soils studies. Geoderma 223, 33–45.

Doolittle, J.A., Windhorn, R.D., Withers, D.L., Zwicker, S.E., Heisner, F.E., McLeese, R.L., 2008. Soil scientists revisit a high-intensity soil survey in northwest Illinois with electromagnetic induction and traditional methods. Soil Horizons 49, 102–108.

Droogers, P., Allen, R.G., 2002. Estimating reference evapotranspiration under inaccurate data conditions. Irrigation and drainage systems 16, 33–45.

Dukes, M.D., Perry, C., 2006. Uniformity testing of variable-rate center pivot irrigation control systems. Precision Agriculture 7, 205–218.

Dunn, B.W., Beecher, H.G., 2007. Using electro-magnetic induction technology to identify sampling sites for soil acidity assessment and to determine spatial variability of soil acidity in rice fields. Animal Production Science 47, 208–214.

Dyer, A.J., 1974. A review of flux-profile relationships. Boundary-Layer Meteorology 7, 363–372.

Edwards, A.C., Beaver, J.M., 2015. Investigating Cardano's Irreducible Case. 2015 NCUR.

Elliott, R.L., Hubbard, K.G., Brusberg, M.D., Hattendorf, M.J., Howell, T.A., Marek, T.H., Snyder, R.L., 2000. The role of automated weather networks in providing evapotranspiration estimates, in: Proc. 4th Decennial National Irrigation Symposium. pp. 243–250.

English, M., Raja, S.N., 1996. Perspectives on deficit irrigation. Agricultural Water Management 32, 1–14.

Ershadi, A., McCabe, M.F., Evans, J.P., Walker, J.P., 2013. Effects of spatial aggregation on the multi-scale estimation of evapotranspiration. Remote Sensing of Environment 131, 51–62.

Evans, R.G., King, B.A., 2012. Site-specific sprinkler irrigation in a water-limited future. Transactions of the ASABE 55, 493–504.

Evans, R.G., LaRue, J., Stone, K.C., King, B.A., 2013. Adoption of site-specific variable rate sprinkler irrigation systems. Irrigation Science 31, 871–887.

Evans, R.G., Sadler, E.J., 2008. Methods and technologies to improve efficiency of water use. Water Resources Research 44.

Evett, S.R., 2007. Soil Water and Monitoring Technology. Irrigation of Agricultural Crops 25–84.

Evett, S.R., Kustas, W.P., Gowda, P.H., Anderson, M.C., Prueger, J.H., Howell, T.A., 2012. Overview of the Bushland Evapotranspiration and Agricultural Remote sensing EXperiment 2008 (BEAREX08): A field experiment evaluating methods for quantifying ET at multiple scales. Advances in Water Resources 50, 4–19. doi:10.1016/j.advwatres.2012.03.010

Evett, S.R., Schwartz, R.C., Tolk, J.A., Howell, T.A., 2009. Soil profile water content determination: Spatiotemporal variability of electromagnetic and neutron probe sensors in access tubes. Vadose Zone Journal 8, 926–941.

Farahani, H.J., Howell, T.A., Shuttleworth, W.J., Bausch, W.C., 2007. Evapotranspiration: progress in measurement and modeling in agriculture. Trans. Asabe 50, 1627–1638.

Farid, A., Goodrich, D.C., Bryant, R., Sorooshian, S., 2008. Using airborne lidar to predict Leaf Area Index in cottonwood trees and refine riparian water-use estimates. Journal of Arid Environments 72, 1–15. doi:10.1016/j.jaridenv.2007.04.010

Feinerman, E., Voet, H., 2000. Site-specific management of agricultural inputs: an illustration for variable-rate irrigation. European review of agricultural economics 27, 17–37.

Fernando, H.J., Pardyjak, E.R., 2013. Field studies delve into the intricacies of mountain weather. Eos, Transactions American Geophysical Union 94, 313–315.

Fiebrich, C.A., Crawford, K.C., 2009. Automation: A Step toward Improving the Quality of Daily Temperature Data Produced by Climate Observing Networks*. Journal of Atmospheric and Oceanic Technology 26, 1246–1260.

Field, C.B., Chapin, F.S., Matson, P.A., Mooney, H.A., 1992. Responses of terrestrial ecosystems to the changing atmosphere: a resource-based approach. Annual Review of Ecology and Systematics 23, 201–235.

Finnigan, J.J., Shaw, R.H., Patton, E.G., 2009. Turbulence structure above a vegetation canopy. J. Fluid Mech 637, 387–424.

Fischer, H.B., List, E.J., Koh, R.C.Y., Imberger, J., Brooks, N.H., 1979. Mixing in coastal and inland waters. Academic, New York.

Fisher, D.K., 2012. Simple weighing lysimeters for measuring evapotranspiration and developing crop coefficients. International Journal of Agricultural and Biological Engineering 5, 35–43.

Foken, T., 2008. The energy balance closure problem: An overview. Ecological Applications 18, 1351–1367.

Foken, T., Leuning, R., Oncley, S.R., Mauder, M., Aubinet, M., 2012. Corrections and data quality control, in: Eddy Covariance. Springer, pp. 85–131.

Fratini, G., Mauder, M., 2014. Towards a consistent eddy-covariance processing: an intercomparison of EddyPro and TK3. Atmospheric Measurement Techniques 7, 2273–2281.

Fritschen, L.J., 1965. Accuracy of evapotranspiration determinations by the Bowen ratio method. Hydrological Sciences Journal 10, 38–48.

Gago, J., Douthe, C., Coopman, R.E., Gallego, P.P., Ribas-Carbo, M., Flexas, J., Escalona, J., Medrano, H., 2015. UAVs challenge to assess water stress for sustainable agriculture. Agricultural Water Management 153, 9–19.

Gao, W., Li, B.L., 1993. Wavelet analysis of coherent structures at the atmosphere-forest interface. Journal of Applied Meteorology 32, 1717–1725.

Gao, W., Shaw, R.H., Paw U, K.T., 1989. Observation of organized structure in turbulent flow within and above a forest canopy. Boundary-Layer Meteorology 47, 349–377.

Gavilán, P., Berengena, J., 2007. Accuracy of the Bowen ratio-energy balance method for measuring latent heat flux in a semiarid advective environment. Irrigation Science 25, 127–140.

Gavlak, R., Horneck, D., Miller, R.O., Kotuby-Amacher, J., 2003. Soil, plant and water reference methods for the western region. WREP-125, 2nd edition. WERA-103 Publication, Colorado State Univ. Ft. Collins.

Gioli, B., Miglietta, F., De Martino, B., Hutjes, R.W., Dolman, H.A., Lindroth, A., Schumacher, M., Sanz, M.J., Manca, G., Peressotti, A., 2004. Comparison between tower and aircraft-based eddy covariance fluxes in five European regions. Agricultural and Forest Meteorology 127, 1–16.

Göckede, M., Rebmann, C., Foken, T., 2004. A combination of quality assessment tools for eddy covariance measurements with footprint modelling for the characterisation of complex sites. Agricultural and Forest Meteorology 127, 175–188.

Gonzalez-Dugo, V., Zarco-Tejada, P., Nicolás, E., Nortes, P.A., Alarcón, J.J., Intrigliolo, D.S., Fereres, E., 2013. Using high resolution UAV thermal imagery to assess the variability in the water status of five fruit tree species within a commercial orchard. Precision Agriculture 14, 660–678.

Good, S.P., Noone, D., Bowen, G., 2015. Hydrologic connectivity constrains partitioning of global terrestrial water fluxes. Science 349, 175–177.

Gossel, A., Thompson, A.L., Sudduth, K.A., Henggeler, J.C., 2013. Performance evaluation of a center pivot variable rate irrigation system, in: 2013 Kansas City, Missouri, July 21-July 24, 2013. American Society of Agricultural and Biological Engineers, p. 1.

Gowda, P.H., Chavez, J.L., Colaizzi, P.D., Evett, S.R., Howell, T.A., Tolk, J.A., 2008. ET mapping for agricultural water management: present status and challenges. Irrigation science 26, 223–237.

Gowda, P.H., Chavez, J.L., Colaizzi, P.D., Evett, S.R., Howell, T.A., Tolk, J.A., 2007. Remote sensing based energy balance algorithms for mapping ET: Current status and future challenges. Transactions of the ASABE 50, 1639–1644.

Gowda, P.H., Howell, T.A., Chávez, J.L., Paul, G., Moorhead, J.E., Holman, D., Marek, T.H., Porter, D.O., Marek, G.H., Colaizzi, P.D., 2015. A decade of remote sensing and evapotranspiration research at USDA-ARS Conservation and Production Research Laboratory, in: 2015 ASABE/IA Irrigation Symposium: Emerging Technologies for Sustainable Irrigation-A Tribute to the Career of Terry Howell, Sr. Conference Proceedings. American Society of Agricultural and Biological Engineers, pp. 1–14.

Grebet, P., Cuenca, R.H., 1991. History of lysimeter design and effects of environmental disturbances, in: Lysimeters for Evapotranspiration and Environmental Measurements. ASCE, pp. 10–18.

Gu, L., Massman, W.J., Leuning, R., Pallardy, S.G., Meyers, T., Hanson, P.J., Riggs, J.S., Hosman, K.P., Yang, B., 2012. The fundamental equation of eddy covariance and its application in flux measurements. Agricultural and Forest Meteorology 152, 135–148.

Gumuzzio, A., Brocca, L., Sánchez, N., González-Zamora, A., Martínez-Fernández, J., 2016. Comparison of SMOS, modelled and in situ long-term soil moisture series in the northwest of Spain. Hydrological Sciences Journal.

Ha, W., Gowda, P.H., Howell, T.A., 2013. A review of downscaling methods for remote sensing-based irrigation management: Part I. Irrigation Science 31, 831–850.

Halvorson, A.D., Rhoades, J.D., 1974. Assessing soil salinity and identifying potential saline-seep areas with field soil resistance measurements. Soil Science Society of America Journal 38, 576–581.

Hamer, P.J.C., 1980. An automatic sprinkler system giving variable irrigation rates matched to measured frost protection needs. Agricultural Meteorology 21, 281–293.

Hargreaves, G., 1994. Defining and Using Reference Evapotranspiration. Journal of Irrigation and Drainage Engineering 120, 1132–1139.

Hargreaves, G.H., Samani, Z.A., 1985. Reference crop evapotranspiration from temperature. Applied engineering in agriculture 1, 96–99.

Hashimoto, H., Dungan, J.L., White, M.A., Yang, F., Michaelis, A.R., Running, S.W., Nemani, R.R., 2008. Satellite-based estimation of surface vapor pressure deficits using MODIS land surface temperature data. Remote Sensing of Environment 112, 142–155. doi:10.1016/j.rse.2007.04.016

Hatton, T.J., Wu, H.-I., 1995. Scaling theory to extrapolate individual tree water use to stand water use. Hydrological Processes 9, 527–540.

Hedley, C.B., Yule, I.J., 2009. Soil water status mapping and two variable-rate irrigation scenarios. Precision Agriculture 10, 342–355.

Heermann, D.F., Hein, P.R., 1968. Performance characteristics of self-propelled center-pivot sprinkler irrigation system. Transactions of the ASAE 11, 11–0015.

Heil, K., Schmidhalter, U., 2012. Characterisation of soil texture variability using the apparent soil electrical conductivity at a highly variable site. Computers & Geosciences 39, 98–110.

Heilman, J.L., Brittin, C.L., Neale, C.M.U., 1989. Fetch requirements for Bowen ratio measurements of latent and sensible heat fluxes. Agricultural and Forest Meteorology 44, 261–273.

Herwitz, S.R., Johnson, L.F., Dunagan, S.E., Higgins, R.G., Sullivan, D.V., Zheng, J., Lobitz, B.M., Leung, J.G., Gallmeyer, B.A., Aoyagi, M., 2004. Imaging from an unmanned aerial vehicle: agricultural surveillance & decision support. Computers and electronics in agriculture 44, 49–61.

Higgins, C.W., 2012. A-posteriori analysis of surface energy budget closure to determine missed energy pathways. Geophysical Research Letters 39.

Higgins, C.W., Katul, G.G., Froidevaux, M., Simeonov, V., Parlange, M.B., 2013. Are atmospheric surface layer flows ergodic? Geophysical Research Letters.

Hill, R.J., 1997. Algorithms for obtaining atmospheric surface-layer fluxes from scintillation measurements. Journal of Atmospheric and Oceanic Technology 14, 456–467.

Hill, R.J., 1992. Review of optical scintillation methods of measuring the refractive-index spectrum, inner scale and surface fluxes. Waves in Random Media 2, 179–201.

Hill, R.J., 1989. Implications of Monin-Obukhov similarity theory for scalar quantities. Journal of the Atmospheric Sciences 46, 2236–2244.

Hillyer, C.C., 2011. Optimal irrigation management: a framework, model, and application for optimizing irrigation when supplies are limited.

Hoffmann, H., Nieto, H., Jensen, R., Guzinski, R., Zarco-Tejada, P., Friborg, T., 2016. Estimating evaporation with thermal UAV data and two-source energy balance models. Hydrology and Earth System Sciences 20, 697–713.

Högström, U.L.F., 1988. Non-dimensional wind and temperature profiles in the atmospheric surface layer: A re-evaluation, in: Topics in Micrometeorology. A Festschrift for Arch Dyer. Springer, pp. 55–78.

Hojstrup, J., 1993. A statistical data screening procedure. Measurement Science and Technology 4, 153.

Horel, J., Splitt, M., Dunn, L., Pechmann, J., White, B., Ciliberti, C., Lazarus, S., Slemmer, J., Zaff, D., Burks, J., 2002. Mesowest: Cooperative mesonets in the western United States. Bulletin of the American Meteorological Society 83, 211–225.

Horst, T.W., Weil, J.C., 1994. How Far is Far Enough?: The Fetch Requirements for Micrometeorological Measurement of Surface Fluxes. J. Atmos. Oceanic Technol. 11, 1018–1025. doi:10.1175/1520-0426(1994)011<1018:HFIFET>2.0.CO;2

Howell, T.A., Schneider, A.D., Jensen, M.E., 1991. History of lysimeter design and use for evapotranspiration measurements, in: Lysimeters for Evapotranspiration and Environmental Measurements. ASCE, pp. 1–9.

Huisman, J.A., Hubbard, S.S., Redman, J.D., Annan, A.P., 2003. Measuring soil water content with ground penetrating radar. Vadose zone journal 2, 476–491.

Huisman, J.A., Snepvangers, J., Bouten, W., Heuvelink, G.B.M., 2002. Mapping spatial variation in surface soil water content: comparison of ground-penetrating radar and time domain reflectometry. Journal of Hydrology 269, 194–207.

Hunsaker, D.J., Pinter Jr, P.J., Barnes, E.M., Kimball, B.A., 2003. Estimating cotton evapotranspiration crop coefficients with a multispectral vegetation index. Irrigation Science 22, 95–104.

Irmak, A., Kamble, B., 2009. Evapotranspiration data assimilation with genetic algorithms and SWAP model for on-demand irrigation. Irrigation science 28, 101–112.

Irmak, S., Irmak, A., Allen, R.G., Jones, J.W., 2003. Solar and net radiation-based equations to estimate reference evapotranspiration in humid climates. Journal of irrigation and drainage engineering 129, 336–347.

Irmak, S., Payero, J.O., Kilic, A., Odhiambo, L.O., Rudnick, D., Sharma, V., Billesbach, D., 2014. On the magnitude and dynamics of eddy covariance system residual energy (energy balance closure error) in subsurface drip-irrigated maize field during growing and non-growing (dormant) seasons. Irrigation Science 32, 471–483.

Itenfisu, D., Elliott, R.L., Allen, R.G., Walter, I.A., 2003. Comparison of reference evapotranspiration calculations as part of the ASCE standardization effort. Journal of Irrigation and Drainage Engineering 129, 440–448.

Jensen, D.D., Nadeau, D.F., Hoch, S.W., Pardyjak, E.R., 2015. Observations of Near-Surface Heat-Flux and Temperature Profiles Through the Early Evening Transition over Contrasting Surfaces. Boundary-Layer Meteorology 1–21.

Jensen, M.E., Allen, R.G., 2000. Evolution of practical ET estimating methods., in: National Irrigation Symposium. Proceedings of the 4th Decennial Symposium, Phoenix, Arizona, USA, November 14-16, 2000. American Society of Agricultural Engineers, pp. 52–65.

Jensen, M.E., Haise, H.R., 1963. Estimating evapotranspiration from solar radiation. Proceedings of the American Society of Civil Engineers, Journal of the Irrigation and Drainage Division 89, 15–41.

Johnson, C.K., Mortensen, D.A., Wienhold, B.J., Shanahan, J.F., Doran, J.W., 2003. Site-specific management zones based on soil electrical conductivity in a semiarid cropping system. Agronomy journal 95, 303–315.

Jung, M., Reichstein, M., Margolis, H.A., Cescatti, A., Richardson, A.D., Arain, M.A., Arneth, A., Bernhofer, C., Bonal, D., Chen, J., 2011. Global patterns of land-atmosphere fluxes of carbon dioxide, latent heat, and sensible heat derived from eddy covariance, satellite, and meteorological observations. Journal of Geophysical Research: Biogeosciences (2005–2012) 116.

Junior, M.M., Nunes, R.O., Celinski, V.G., 2013. Comparison of the responses of low cost eletrical soil sensors, and a arduino microcontroller platform. Iberoamerican Journal of Applied Computing 2.

Kaffka, S.R., Lesch, S.M., Bali, K.M., Corwin, D.L., 2005. Site-specific management in salt-affected sugar beet fields using electromagnetic induction. Computers and electronics in Agriculture 46, 329–350.

Kaimal, J.C., Finnigan, J.J., 1994. Atmospheric boundary layer flows: their structure and measurement.

Kalma, J.D., McVicar, T.R., McCabe, M.F., 2008. Estimating Land Surface Evaporation: A Review of Methods Using Remotely Sensed Surface Temperature Data. Surveys in Geophysics 29, 421–469. doi:10.1007/s10712-008-9037-z

Karimi, P., Bastiaanssen, W.G.M., 2014. Spatial evapotranspiration, rainfall and land use data in water accounting. Part 1: Review of the accuracy of the remote sensing data. Hydrology and Earth System Sciences Discussions, 11, 2014.

Katul, G., Cava, D., Poggi, D., Albertson, J., Mahrt, L., 2005. Stationarity, homogeneity, and ergodicity in canopy turbulence, in: Handbook of Micrometeorology. Springer, pp. 161–180.

Katul, G., Hsieh, C.-I., Kuhn, G., Ellsworth, D., Nie, D., 1997. Turbulent eddy motion at the forest-atmosphere interface. Journal of Geophysical Research: Atmospheres (1984–2012) 102, 13409–13421.

Katul, G., Hsieh, C.-I., Oren, R., Ellsworth, D., Phillips, N., 1996. Latent and sensible heat flux predictions from a uniform pine forest using surface renewal and flux variance methods. Boundary-Layer Meteorology 80, 249–282.

Katul, G., Porporato, A., Cava, D., Siqueira, M., 2006. An analysis of intermittency, scaling, and surface renewal in atmospheric surface layer turbulence. Physica D: Nonlinear Phenomena 215, 117–126.

Katul, G.G., Oren, R., Manzoni, S., Higgins, C., Parlange, M.B., 2012. Evapotranspiration: A process driving mass transport and energy exchange in the soil-plant-atmosphere-climate system. Reviews of Geophysics 50.

Kerr, Y.H., Waldteufel, P., Richaume, P., Wigneron, J.P., Ferrazzoli, P., Mahmoodi, A., Al Bitar, A., Cabot, F., Gruhier, C., Juglea, S.E., 2012. The SMOS soil moisture retrieval algorithm. IEEE Transactions on Geoscience and Remote Sensing 50, 1384–1403.

Kim, W., Cho, J., Komori, D., Aoki, M., Yokozawa, M., Kanae, S., Oki, T., 2011. Tolerance of eddy covariance flux measurement. Hydrological Research Letters 5, 73–77.

Kim, Y., Evans, R.G., 2009. Software design for wireless sensor-based site-specific irrigation. Computers and Electronics in Agriculture 66, 159–165.

Kim, Y., Evans, R.G., Iversen, W.M., 2009. Evaluation of closed-loop site-specific irrigation with wireless sensor network. Journal of Irrigation and Drainage Engineering 135, 25–31.

King, B.A., McCann, I.R., Eberlein, C.V., Stark, J.C., 1999. Computer control system for spatially varied water and chemical application studies with continuous-move irrigation systems. Computers and electronics in agriculture 24, 177–194.

King, B.A., Wall, R.W., Karksy, T.F., 2009. Center-pivot irrigation system for independent site-specific management of water and chemical application. Applied engineering in agriculture 25, 198–198.

King, B.A., Wall, R.W., Kincaid, D.C., Westermann, D.T., 2005. Field testing of a variable rate sprinkler and control system for site-specific water and nutrient application. Applied engineering in agriculture 21, 847–853.

Kişi, O., Cimen, M., 2009. Evapotranspiration modelling using support vector machines/Modélisation de l'évapotranspiration à l'aide de "support vector machines." Hydrological sciences journal 54, 918–928.

Kişi, Ö., Öztürk, Ö., 2007. Adaptive neurofuzzy computing technique for evapotranspiration estimation. Journal of Irrigation and Drainage Engineering 133, 368–379.

Kizito, F., Campbell, C.S., Campbell, G.S., Cobos, D.R., Teare, B.L., Carter, B., Hopmans, J.W., 2008. Frequency, electrical conductivity and temperature analysis of a low-cost capacitance soil moisture sensor. Journal of Hydrology 352, 367–378.

Knox, J.W., Kay, M.G., Weatherhead, E.K., 2012. Water regulation, crop production, and agricultural water management—understanding farmer perspectives on irrigation efficiency. Agricultural Water Management 108, 3–8.

Koch, B., Khosla, R., Frasier, W.M., Westfall, D.G., Inman, D., 2004. Economic feasibility of variable-rate nitrogen application utilizing site-specific management zones. Agronomy Journal 96, 1572–1580.

Kochendorfer, J., Meyers, T.P., Frank, J., Massman, W.J., Heuer, M.W., 2012. How well can we measure the vertical wind speed? Implications for fluxes of energy and mass. Boundary-Layer Meteorology 145, 383–398.

Kruse, E.G., 1978. Describing irrigation efficiency and uniformity. Journal of the Irrigation and Drainage Division 104, 35–41.

Kumar, M., Raghuwanshi, N.S., Singh, R., 2011. Artificial neural networks approach in evapotranspiration modeling: a review. Irrigation science 29, 11–25.

Lambers, H., Chapin III, F.S., Pons, T.L., 1998. Plant water relations. Springer.

Lampert, A., Pätzold, F., Lobitz, L., Martin, S., Lohmann, G., Canut, G., Legain, D., Bange, J., 2016. Observing local turbulence and anisotropy during the afternoon transition with an unmanned aerial system-a case study.

Laurenson, M.R., Kiura, T., Ninomiya, S., 2002. Providing agricultural models with mediated access to heterogeneous weather databases. Applied engineering in agriculture 18, 617.

Lawford, R., Kustas, B., Toll, D., Anderson, M., Doorn, B., Allen, R., Engman, T., Morse, T., 2011. Evapotranspiration as a Regional Climate Priority: Results from a NASA/USDA Workshop.

Lee, X., Massman, W.J., Law, B.E., 2004a. Handbook of micrometeorology: a guide for surface flux measurement and analysis. Springer.

Lee, X., Yu, Q., Sun, X., Liu, J., Min, Q., Liu, Y., Zhang, X., 2004b. Micrometeorological fluxes under the influence of regional and local advection: a revisit. Ag. and Forest meteorology 122, 111–124.

Leijnse, H., Uijlenhoet, R., Stricker, J.N.M., 2007. Hydrometeorological application of a microwave link: 1. Evaporation. Water Resources Research 43, W04416. doi:10.1029/2006WR004988

Lettau, H., 1969. Evapotranspiration Climatonomy (New approach to numerical prediction of monthly evapotranspiration, runoff, and soil moisture storage). Research and Development Technical Report 97, pp 691-699.

Lewis, C.S., Geli, H.M., Neale, C.M., 2014. Comparison of the NLDAS Weather Forcing Model to Agrometeorological Measurements in the western United States. Journal of Hydrology 510, 385–392.

Lewis, J.M., 1995. The story behind the Bowen ratio. Bulletin of the American Meteorological Society 76, 2433–2444.

Li, Z.-L., Tang, R., Wan, Z., Bi, Y., Zhou, C., Tang, B., Yan, G., Zhang, X., 2009. A review of current methodologies for regional evapotranspiration estimation from remotely sensed data. Sensors 9, 3801–3853.

Lim, W., Kaell Torres, H., Oppus, C.M., 2014. An agricultural telemetry system implemented using an Arduino-Android interface, in: Humanoid, Nanotechnology, Information Technology, Communication and Control, Environment and Management (HNICEM), 2014 International Conference on. IEEE, pp. 1–6.

Liu, W., Hong, Y., Khan, S., Huang, M., Grout, T., Adhikari, P., 2011. Evaluation of Global Daily Reference ET Using Oklahoma's Environmental Monitoring Network—MESONET. Water resources management 25, 1601–1613.

Maier, H.R., Dandy, G.C., 2000. Neural networks for the prediction and forecasting of water resources variables: a review of modelling issues and applications. Environmental Modelling & Software 15, 101–124. doi:10.1016/S1364-8152(99)00007-9

Malhi, Y., McNaughton, K., Von Randow, C., 2004. Low frequency atmospheric transport and surface flux measurements, in: Handbook of Micrometeorology. Springer Netherlands, pp. 101–118.

Mancosu, N., Snyder, R.L., Spano, D., 2014. Procedures to develop a standardized reference evapotranspiration zone map. Journal of Irrigation and Drainage Engineering 140, A4014004.

Manzoni, S., Vico, G., Katul, G.G., Palmroth, S., Jackson, R.B., Porporato, A.M., 2011. Hydraulic limits on maximum plant transpiration, in: AGU Fall Meeting Abstracts. p. 03.

Marjang, N., Merkley, G.P., Shaban, M., 2012. Center-pivot uniformity analysis with variable container spacing. Irrigation Science 30, 149–156.

Marshall, D.C., 1958. Measurement of sap flow in conifers by heat transport. Plant physiology 33, 385.

Martinez, G., Vanderlinden, K., Ordóñez, R., Muriel, J.L., 2009. Can apparent electrical conductivity improve the spatial characterization of soil organic carbon? Vadose Zone Journal 8, 586–593.

Massman, W.J., Lee, X., 2002. Eddy covariance flux corrections and uncertainties in long-term studies of carbon and energy exchanges. Agricultural and Forest Meteorology 113, 121–144.

Mateos, L., González-Dugo, M.P., Testi, L., Villalobos, F.J., 2013. Monitoring evapotranspiration of irrigated crops using crop coefficients derived from time series of satellite images. I. Method validation. Agricultural water management 125, 81–91.

Mauder, M., Cuntz, M., Drüe, C., Graf, A., Rebmann, C., Schmid, H.P., Schmidt, M., Steinbrecher, R., 2013. A strategy for quality and uncertainty assessment of long-term eddy-covariance measurements. Agricultural and Forest Meteorology 169, 122–135.

Mauder, M., Liebethal, C., Göckede, M., Leps, J.-P., Beyrich, F., Foken, T., 2006. Processing and quality control of flux data during LITFASS-2003. Boundary-Layer Meteorology 121, 67–88.

McBride, R.A., Shrive, S.C., Gordon, A.M., 1990. Estimating forest soil quality from terrain measurements of apparent electrical conductivity. Soil Science Society of America Journal 54, 290–293.

McCabe, M.F., Wood, E.F., 2006. Scale influences on the remote estimation of evapotranspiration using multiple satellite sensors. Remote Sensing of Environment 105, 271–285.

Melton, F.S., Johnson, L.F., Lund, C.P., Pierce, L.L., Michaelis, A.R., Hiatt, S.H., Guzman, A., Adhikari, D., Purdy, A.J., Rosevelt, C., 2012. Satellite Irrigation Management Support With the Terrestrial Observation and Prediction System: A Framework for Integration of Satellite and Surface Observations to Support Improvements in Agricultural Water Resource Management.

Mesas-Carrascosa, F.J., Santano, D.V., Meroño, J.E., de la Orden, M.S., García-Ferrer, A., 2015. Open source hardware to monitor environmental parameters in precision agriculture. Biosystems Engineering 137, 73–83.

Miller, B.A., 2012. The need to continue improving soil survey maps. Soil Horizons 53, 11–15.

Minet, J., Bogaert, P., Vanclooster, M., Lambot, S., 2012. Validation of ground penetrating radar full-waveform inversion for field scale soil moisture mapping. Journal of Hydrology 424–425, 112–123. doi:10.1016/j.jhydrol.2011.12.034

Mogera, U., Sagade, A.A., George, S.J., Kulkarni, G.U., 2014. Ultrafast response humidity sensor using supramolecular nanofibre and its application in monitoring breath humidity and flow. Scientific Reports 4, 4103.

Molden, D., Oweis, T., Steduto, P., Bindraban, P., Hanjra, M.A., Kijne, J., 2010. Improving agricultural water productivity: between optimism and caution. Agricultural Water Management 97, 528–535.

Moncrieff, J., Clement, R., Finnigan, J., Meyers, T., 2005. Averaging, detrending, and filtering of eddy covariance time series, in: Handbook of Micrometeorology. Springer, pp. 7–31.

Monin, A.S., Obukhov, Am., 1954. Basic laws of turbulent mixing in the surface layer of the atmosphere. Contrib. Geophys. Inst. Acad. Sci. USSR 151, 163–187.

Moratiel, R., Martínez-Cob, A., Latorre Garcés, B., 2013. Variation in the estimations of ETo and crop water use due to the sensor accuracy of the meteorological variables.

Moratiel, R., Spano, D., Nicolosi, P., Snyder, R.L., 2013. Correcting soil water balance calculations for dew, fog, and light rainfall. Irrigation Science 1–7.

Morton, C.G., Huntington, J.L., Pohll, G.M., Allen, R.G., McGwire, K.C., Bassett, S.D., 2013. Assessing calibration uncertainty and automation for estimating evapotranspiration from agricultural areas using METRIC. Journal of the American Water Resources Association 49, 549–562.

National Research Council, 2012. The National Weather Service Modernization and Associated Restructuring: A Retrospective Assessment. National Academies Press, Washington, D.C.

O'Shaughnessy, S.A., Evett, S.R., Colaizzi, P.D., Howell, T.A., 2011. Application Uniformity of a Commercial Center Pivot Variable Rate Irrigation System1, in: International Irrigation Show.

O'Shaughnessy, S.A., Urrego, Y.F., Evett, S.R., Colaizzi, P.D., Howell, T.A., 2013. Assessing application uniformity of a variable rate irrigation system in a windy location. Applied Engineering in Agriculture 29, 497–510.

Oren, R., Phillips, N., Katul, G., Ewers, B.E., Pataki, D.E., 1998. Scaling xylem sap flux and soil water balance and calculating variance: a method for partitioning water flux in forests, in: Annales Des Sciences Forestieres. EDP Sciences, pp. 191–216.

Ortega-Farias, S., Irmak, S., Cuenca, R.H., 2009. Special issue on evapotranspiration measurement and modeling. Irrigation Science 28, 1–3.

Pahlow, M., Parlange, M.B., Porté-Agel, F., 2001. On Monin–Obukhov similarity in the stable atmospheric boundary layer. Boundary-layer meteorology 99, 225–248.

Paliwal, M., Kumar, U.A., 2009. Neural networks and statistical techniques: A review of applications. Expert systems with applications 36, 2–17.

Papale, D., Reichstein, M., Aubinet, M., Canfora, E., Bernhofer, C., Kutsch, W., Longdoz, B., Rambal, S., Valentini, R., Vesala, T., 2006. Towards a standardized processing of Net Ecosystem Exchange measured with eddy covariance technique: algorithms and uncertainty estimation. Biogeosciences 3, 571–583.

Parker, D., Cohen-Vogel, D., Osgood, D., Zilberman, D., 2000. Publicly funded weather database benefits users statewide. California Agriculture 54, 21–25.

Paw U, K.T., Brunet, Y., Collineau, S., Shaw, R.H., Maitani, T., Qiu, J., Hipps, L., 1992. On coherent structures in turbulence above and within agricultural plant canopies. Agricultural and Forest Meteorology 61, 55–68. doi:10.1016/0168-1923(92)90025-Y

Paw U, K.T., Qiu, J., Su, H.-B., Watanabe, T., Brunet, Y., 1995. Surface renewal analysis: a new method to obtain scalar fluxes. Agricultural and Forest Meteorology 74, 119–137.

Paw U, K.T., Snyder, R.L., Spano, D., Su, H.-B., 2005. Surface Renewal Estimates of Scalar Exchange, in: Micrometeorology in Agricultural Systems, Agronomy Monograph. American Society of Agronomy, Crop Science Society of America, and Soil Science Society of America, Madison, WI, pp. 455–483.

Penman, H.L., 1948. Natural Evaporation from Open Water, Bare Soil and Grass. Proceedings of the Royal Society of London. Series A, Mathematical and Physical Sciences 193, 120–145.

Perez, P.J., Castellvi, F., Ibañez, M., Rosell, J.I., 1999. Assessment of reliability of Bowen ratio method for partitioning fluxes. Agricultural and Forest Meteorology 97, 141–150.

Perry, C., 2007. Efficient irrigation; inefficient communication; flawed recommendations. Irrigation and drainage 56, 367–378.

Perry, C., Pocknee, S., Hansen, O., 2003. A variable rate pivot irrigation control system, in: Proceedings of the Fourth European Conference in Presicion Agriculture. pp. 539–544.

Perry, C., Steduto, P., Allen, R.G., Burt, C.M., 2009. Increasing productivity in irrigated agriculture: Agronomic constraints and hydrological realities. Agricultural Water Management 96, 1517–1524.

Perry, C.D., Dukes, M.D., Harrison, K.A., 2004. Effects of variable-rate sprinkler cycling on irrigation uniformity. ASABE Paper.

Peters, R.T., Evett, S.R., 2007. Spatial and temporal analysis of crop conditions using multiple canopy temperature maps created with center-pivot-mounted infrared thermometers. Transactions of the ASABE 50, 919–927.

Petropoulos, G.P., Ireland, G., Barrett, B., 2015. Surface soil moisture retrievals from remote sensing: Current status, products & future trends. Physics and Chemistry of the Earth, Parts A/B/C 83, 36–56.

Plant, R.E., 2001. Site-specific management: the application of information technology to crop production. Computers and Electronics in Agriculture 30, 9–29.

Prandtl, L., 1925. Bericht über Untersuchungen zur ausgebildeten Turbulenz. Z. Angew. Math. Mech 5, 136–139.

Priestley, C.H.B., Taylor, R.J., 1972. On the assessment of surface heat flux and evaporation using large-scale parameters. Monthly weather review 100, 81–92.

Priestley, J.T., Hill, R.J., 1985. Measuring high-frequency humidity, temperature and radio refractive index in the surface layer. Journal of atmospheric and oceanic technology 2, 233–251.

Rana, G., Katerji, N., 1998. A measurement based sensitivity analysis of the Penman-Monteith actual evapotranspiration model for crops of different height and in contrasting water status. Theoretical and Applied Climatology 60, 141–149.

Rannik, Ü., Sogachev, A., Foken, T., Göckede, M., Kljun, N., Leclerc, M.Y., Vesala, T., 2012. Footprint analysis, in: Eddy Covariance. Springer, pp. 211–261.

Raupach, M.R., Finnigan, J.J., 1995. Scale issues in boundary-layer meteorology: Surface energy balances in heterogeneous terrain. Hydrological Processes 9, 589–612.

Rebmann, C., Göckede, M., Foken, T., Aubinet, M., Aurela, M., Berbigier, P., Bernhofer, C., Buchmann, N., Carrara, A., Cescatti, A., 2005. Quality analysis applied on eddy covariance measurements at complex forest sites using footprint models. Theoretical and Applied Climatology 80, 121–141.

Rebmann, C., Kolle, O., Heinesch, B., Queck, R., Ibrom, A., Aubinet, M., 2012. Data acquisition and flux calculations, in: Eddy Covariance. Springer, pp. 59–83.

Reges, H.W., Doesken, N., Turner, J., Newman, N., Bergantino, A., Schwalbe, Z., 2016. COCORAHS: The evolution and accomplishments of a volunteer rain gauge network. Bulletin of the American Meteorological Society.

Reynolds, O., 1894. On the dynamical theory of incompressible viscous fluids and the determination of the criterion. Proceedings of the Royal Society of London 56, 40–45.

Rhoades, J.D., Corwin, D.L., 1981. Determining soil electrical conductivity-depth relations using an inductive electromagnetic soil conductivity meter. Soil Science Society of America Journal 45, 255–260.

Rijtema, P.E., 1958. Maandoverzichten over 1957 van het lysimeterstation. Instituut voor Cultuurtechniek en Waterhuishouding.

Rossini, M., Fava, F., Cogliati, S., Meroni, M., Marchesi, A., Panigada, C., Giardino, C., Busetto, L., Migliavacca, M., Amaducci, S., 2013. Assessing canopy PRI from airborne imagery to map water stress in maize. ISPRS Journal of Photogrammetry and Remote Sensing 86, 168–177.

Ruiz-Garcia, L., Lunadei, L., Barreiro, P., Robla, I., 2009. A review of wireless sensor technologies and applications in agriculture and food industry: state of the art and current trends. sensors 9, 4728–4750.

Sadler, E.J., Camp, C.R., Evans, D.E., Millen, J.A., 2002. Spatial variation of corn response to irrigation. Transactions of the ASAE 45, 1869–1881.

Sadler, E.J., Evans, R.G., Stone, K.C., Camp, C.R., 2005. Opportunities for conservation with precision irrigation. Journal of Soil and Water Conservation 60, 371–378.

Saey, T., De Smedt, P., De Clercq, W., Meerschman, E., Monirul Islam, M., Van Meirvenne, M., 2013. Identifying soil patterns at different spatial scales with a multi-receiver EMI sensor. Soil Science Society of America Journal 77, 382–390.

Sakai, R.K., Fitzjarrald, D.R., Moore, K.E., 2001. Importance of low-frequency contributions to eddy fluxes observed over rough surfaces. Journal of applied meteorology 40, 2178–2192.

Samani, Z., 2000. Estimating solar radiation and evapotranspiration using minimum climatological data. Journal of Irrigation and Drainage Engineering 126, 265–267.

Schaeffer, S.M., Williams, D.G., Goodrich, D.C., 2000. Transpiration of cottonwood/willow forest estimated from sap flux. Agricultural and Forest Meteorology 105, 257–270.

Schmid, H.P., 2002. Footprint modeling for vegetation atmosphere exchange studies: a review and perspective. Agricultural and Forest Meteorology 113, 159–183.

Schmid, H.P., Lloyd, C.R., 1999. Spatial representativeness and the location bias of flux footprints over inhomogeneous areas. Agricultural and Forest Meteorology 93, 195–209.

Schmugge, T.J., Jackson, T.J., McKim, H.L., 1980. Survey of methods for soil moisture determination. Water Resources Research 16, 961–979.

Schotanus, P., Nieuwstadt, Ftm., De Bruin, H.A.R., 1983. Temperature measurement with a sonic anemometer and its application to heat and moisture fluxes. Boundary-Layer Meteorology 26, 81–93.

Shaner, D.L., Khosla, R., Brodahl, M.K., Buchleiter, G.W., Farahani, H.J., 2008. How well does zone sampling based on soil electrical conductivity maps represent soil variability? Agronomy Journal 100, 1472–1480.

Shapland, T.M., McElrone, A.J., Snyder, R.L., Paw U, K.T., 2012a. Structure Function Analysis of Two-Scale Scalar Ramps. Part I: Theory and Modelling. Boundary-Layer Meteorol 145, 5–25.

Shapland, T.M., McElrone, A.J., Snyder, R.L., Paw U, K.T., 2012b. Structure Function Analysis of Two-Scale Scalar Ramps. Part II: Ramp Characteristics and Surface Renewal Flux Estimation. Boundary-Layer Meteorol 145, 27–44. doi:10.1007/s10546-012-9740-7

Shapland, T.M., Snyder, R.L., Paw U, K.T., McElrone, A.J., 2014. Thermocouple frequency response compensation leads to convergence of the surface renewal alpha calibration. Agricultural and Forest Meteorology 189–190, 36–47. doi:10.1016/j.agrformet.2014.01.008

Shaw, R.H., Gao, W., 1989. Detection of temperature ramps and flow structures at a deciduous forest site. Agricultural and forest meteorology 47, 123–138.

Shuttleworth, W.J., 2007. Putting the'vap'into evaporation. Hydrology and Earth System Sciences Discussions 11, 210–244.

Shuttleworth, W.J., Gash, J.H., 2006. The Role of Large-Scale Field Experiments in Water and Energy Balance Studies, in: Anderson, M.G., McDonnell, J.J. (Eds.), Encyclopedia of Hydrological Sciences. John Wiley & Sons, Ltd, Chichester, UK.

Siebert, S., Döll, P., 2010. Quantifying blue and green virtual water contents in global crop production as well as potential production losses without irrigation. Journal of Hydrology 384, 198–217.

Smith, D.M., Allen, S.J., 1996. Measurement of sap flow in plant stems. Journal of Experimental Botany 47, 1833–1844.

Smith, R., 2014. Electromagnetic induction methods in mining geophysics from 2008 to 2012. Surveys in Geophysics 35, 123–156.

Smith, S.W., 2015. Practical Implications of Irrigation Application Efficiency Improvements for Transferable Water in Colorado, in: 2015 ASABE/IA Irrigation Symposium: Emerging Technologies for Sustainable Irrigation-A Tribute to the Career of Terry Howell, Sr. Conference Proceedings. American Society of Agricultural and Biological Engineers, pp. 1–3.

Snyder, R.L., Palmer, C., Orang, M., Anderson, M., 2009. National weather service reference evapotranspiration forecast. Crop Water Use 4, 1–6.

Snyder, R.L., Spano, D., Duce, P., Paw U, K.T., Rivera, M., 2008. Surface renewal estimation of pasture evapotranspiration. Journal of Irrigation and Drainage Engineering 134, 716–721.

Snyder, R.L., Spano, D., Pawu, K.T., 1996. Surface renewal analysis for sensible and latent heat flux density. Boundary-Layer Meteorology 77, 249–266.

Sorooshian, S., Li, J., Hsu, K., Gao, X., 2012. Influence of irrigation schemes used in regional climate models on evapotranspiration estimation: Results and comparative studies from California's Central Valley agricultural regions. Journal of Geophysical Research: Atmospheres 117.

Spano, D., Snyder, R.L., Duce, P., 2000. Estimating sensible and latent heat flux densities from grapevine canopies using surface renewal. Agricultural and Forest Meteorology 104, 171–183.

Spano, D., Snyder, R.L., Duce, P., Paw U, K.T., 1997. Surface renewal analysis for sensible heat flux density using structure functions. Agricultural and Forest Meteorology 86, 259–271.

Steinberger, G., Rothmund, M., Auernhammer, H., 2009. Mobile farm equipment as a data source in an agricultural service architecture. Computers and electronics in agriculture 65, 238–246.

Stull, R.B., 1988. An introduction to boundary layer meteorology. Springer.

Sudduth, K.A., Drummond, S.T., Kitchen, N.R., 2001. Accuracy issues in electromagnetic induction sensing of soil electrical conductivity for precision agriculture. Computers and Electronics in Agriculture 31, 239–264.

Sui, R., Fisher, D.K., 2015. Field test of a center pivot irrigation system. Applied Engineering in Agriculture 31, 83–88.

Sutherland, G., Chasmer, L.E., Petrone, R.M., Kljun, N., Devito, K.J., 2014. Evaluating the use of spatially varying versus bulk average 3D vegetation structural inputs to modelled evapotranspiration within heterogeneous land cover types. Ecohydrology 7, 1545–1559.

Sutton, O.G., 1949. The application to micrometeorology of the theory of turbulent flow over rough surfaces. Quarterly journal of the Royal meteorological society 75, 335–350.

Suvočarev, K., Shapland, T.M., Snyder, R.L., Martínez-Cob, A., 2014. Surface renewal performance to independently estimate sensible and latent heat fluxes in heterogeneous crop surfaces. Journal of Hydrology 509, 83–93. doi:10.1016/j.jhydrol.2013.11.025

Tabari, H., Grismer, M.E., Trajkovic, S., 2013. Comparative analysis of 31 reference evapotranspiration methods under humid conditions. Irrigation Science 31, 107–117.

Tang, R., Li, Z.-L., Chen, K.-S., Jia, Y., Li, C., Sun, X., 2013a. Spatial-scale effect on the SEBAL model for evapotranspiration estimation using remote sensing data. Agricultural and forest meteorology 174, 28–42.

Tang, R., Li, Z.-L., Sun, X., 2013b. Temporal upscaling of instantaneous evapotranspiration: An intercomparison of four methods using eddy covariance measurements and MODIS data. Remote Sensing of Environment 138, 102–118.

Thornthwaite, C.W., 1948. An approach toward a rational classification of climate. Geographical review 38, 55–94.

Tilman, D., Cassman, K.G., Matson, P.A., Naylor, R., Polasky, S., 2002. Agricultural sustainability and intensive production practices. Nature 418, 671–677.

Todd, R.W., Evett, S.R., Howell, T.A., 2000. The Bowen ratio-energy balance method for estimating latent heat flux of irrigated alfalfa evaluated in a semi-arid, advective environment. Agricultural and Forest Meteorology 103, 335–348.

Topp, G.C., 2003. State of the art of measuring soil water content. Hydrological Processes 17, 2993–2996.

Toushmalani, R., 2010. Application of geophysical methods in agriculture. Aust J Basic Appl Sci 4, 6433–6439.

Trajkovic, S., Todorovic, B., Stankovic, M., 2003. Forecasting of reference evapotranspiration by artificial neural networks. Journal of Irrigation and Drainage Engineering 129, 454–457.

Triantafilis, J., Lesch, S.M., La Lau, K., Buchanan, S.M., 2009. Field level digital soil mapping of cation exchange capacity using electromagnetic induction and a hierarchical spatial regression model. Soil Research 47, 651–663.

Van Atta, C.W., 1977. Effect of coherent structures on structure functions of temperature in the atmospheric boundary layer. Archiwum Mechaniki Stosowanej 29, 161–171.

Van Atta, C.W., Park, J., 1972. Statistical self-similarity and inertial subrange turbulence, in: Statistical Models and Turbulence. Springer, pp. 402–426.

Ventura, F., Spano, D., Duce, P., Snyder, R.L., 1999. An evaluation of common evapotranspiration equations. Irrig Sci 18, 163–170. doi:10.1007/s002710050058

Vereecken, H., Huisman, J.A., Pachepsky, Y., Montzka, C., Van Der Kruk, J., Bogena, H., Weihermüller, L., Herbst, M., Martinez, G., Vanderborght, J., 2014. On the spatio-temporal dynamics of soil moisture at the field scale. Journal of Hydrology 516, 76–96.

Verma, S., Baldocchi, D., Anderson, D., Matt, D., Clement, R., 1986. Eddy fluxes of CO2, water vapor, and sensible heat over a deciduous forest. Boundary-Layer Meteorol 36, 71–91. doi:10.1007/BF00117459

Verstraeten, W.W., Veroustraete, F., Feyen, J., 2008. Assessment of Evapotranspiration and Soil Moisture Content Across Different Scales of Observation. Sensors 8, 70–117. doi:10.3390/s8010070

Vesala, T., Kljun, N., Rannik, Ü., Rinne, J., Sogachev, A., Markkanen, T., Sabelfeld, K., Foken, T., Leclerc, M.Y., 2008. Flux and concentration footprint modelling: State of the art. Environmental Pollution 152, 653–666.

Vickers, D., Mahrt, L., 2003. The cospectral gap and turbulent flux calculations. Journal of atmospheric and oceanic technology 20, 660–672.

Vickers, D., Mahrt, L., 1997. Quality control and flux sampling problems for tower and aircraft data. Journal of Atmospheric and Oceanic Technology 14, 512–526.

Vitharana, U.W., Van Meirvenne, M., Simpson, D., Cockx, L., De Baerdemaeker, J., 2008. Key soil and topographic properties to delineate potential management classes for precision agriculture in the European loess area. Geoderma 143, 206–215.

Vivoni, E.R., Rango, A., Anderson, C.A., Pierini, N.A., Schreiner-McGraw, A.P., Saripalli, S., Laliberte, A.S., 2014. Ecohydrology with unmanned aerial vehicles. Ecosphere 5, 1–14.

Walter, I.A., Allen, R.G., Elliott, R., Jensen, M.E., Itenfisu, D., Mecham, B., Howell, T.A., Snyder, R., Brown, P., Echings, S., 2000. ASCE's standardized reference evapotranspiration equation, in: Proc. of the Watershed Management 2000 Conference, June.

Wang, K., Dickinson, R.E., 2012. A review of global terrestrial evapotranspiration: Observation, modeling, climatology, and climatic variability. Reviews of Geophysics 50, RG2005. doi:10.1029/2011RG000373

Webb, E.K., Pearman, G.I., Leuning, R., 1980. Correction of flux measurements for density effects due to heat and water vapour transfer. Quarterly Journal of the Royal Meteorological Society 106, 85–100.

Weiss, A., Van Crowder, L., Bernardi, M., 2000. Communicating agrometeorological information to farming communities. Agricultural and forest Meteorology 103, 185–196.

Wilczak, J.M., Oncley, S.P., Stage, S.A., 2001. Sonic anemometer tilt correction algorithms. Boundary-Layer Meteorology 99, 127–150.

Wilson, K., Goldstein, A., Falge, E., Aubinet, M., Baldocchi, D., Berbigier, P., Bernhofer, C., Ceulemans, R., Dolman, H., Field, C., 2002. Energy balance closure at FLUXNET sites. Agricultural and Forest Meteorology 113, 223–243.

Wisser, D., Frolking, S., Douglas, E.M., Fekete, B.M., Vörösmarty, C.J., Schumann, A.H., 2008. Global irrigation water demand: Variability and uncertainties arising from agricultural and climate data sets. Geophysical Research Letters 35.

Wullschleger, S.D., Meinzer, F.C., Vertessy, R.A., 1998. A review of whole-plant water use studies in tree. Tree physiology 18, 499–512.

Wyngaard, J.C., Coté, O.R., Izumi, Y., 1971. Local free convection, similarity, and the budgets of shear stress and heat flux. Journal of the Atmospheric Sciences 28, 1171–1182.

Yaglom, A., 1957. Some Classes of Random Fields in n-Dimensional Space, Related to Stationary Random Processes. Theory of Probability & Its Applications 2, 273–320.

Yeh, G.-T., Brutsaert, W., 1971. A solution for simultaneous turbulent heat and vapor transfer between a water surface and the atmosphere. Boundary-Layer Meteorology 2, 64–82.

Zhang, C., Kovacs, J.M., 2012. The application of small unmanned aerial systems for precision agriculture: a review. Precision Agriculture 13, 693–712. doi:10.1007/s11119-012-9274-5

Zwart, S.J., Bastiaanssen, W.G., 2007. SEBAL for detecting spatial variation of water productivity and scope for improvement in eight irrigated wheat systems. Agricultural Water Management 89, 287–296.

Appendix A: Determination of characteristic length from the diffusion equation.

Diffusive transport is described by Fick's laws, in which an ideal diffusion process leads to redistribution of mass (or heat) by random movement from areas of high concentration to areas of low concentration. At any given moment, this movement trends towards a Gaussian distribution, and is described by a characteristic length that is a function of diffusivity and time.

From Fick's second law of diffusion, the equation for change of concentration in time:

$$\frac{\partial C}{\partial t} = D\nabla^2 C \qquad \text{Eq. A-1}$$

describes the diffusion of a scalar at concentration C through media without mean flow (no advection). The fundamental solution for the diffusion equation has been solved by various methods for both heat and mass transport problems. Fischer et al. (1979) outline a series of steps that result in a solution that is analogous to the step changes of applied depths across transitions in a VRI prescription.

First, a relationship is determined for the physical parameters, including the diffusion coefficient, by dimensional analysis. With 5 variables (C = concentration, M = mass, t = time, x = location vector, D = diffusion coefficient), the prescribed relationship for concentration at a given location and time is:

$$C = \frac{M}{\sqrt{Dt}} f\left(\frac{x}{\sqrt{Dt}}\right) \qquad \text{Eq. A-2}$$

where D takes the zones of length^{2}time^{-1}.

A replacement of variables $\eta = x/\sqrt{Dt}$ allows Eq. A.2 to be transformed to an ordinary differential equation

$$\frac{df}{d\eta} + 2\eta f = 0\text{, with the solution} \qquad \text{Eq. A-3}$$

$$f = C_0 \exp(-\eta^2)\text{.} \qquad \text{Eq. A-4}$$

One method of solution is accomplished via Green's function, where a particular solution is found with infinite positive and negative boundary conditions (infinite domain) and with an initial condition of a pulse input: at time t=0, mass M is released at the origin. Elsewhere, initial

concentration is 0. (For complete solutions for the infinite solution via Green's function, see Carslaw and Jaeger, 1959, Chapter XIV.)

The initial condition of the pulse input can be approximated by the Dirac delta function

$$\delta(x) = \begin{cases} +\infty, \text{ when } x = 0 \\ 0, \text{ when } x \neq 0 \end{cases}, \text{ with an indefinite sum } \int \delta(x)dx = 1. \quad \text{Eq. A-5}$$

The Dirac delta function can be defined by Cauchy's integral formula as:

$$\delta(x-a) = \frac{1}{2\pi}\int_{-\infty}^{\infty} \exp\left[ip(x-a)\right]dp. \quad \text{Eq. A-6}$$

In the case of the particular solution, it is assumed that total mass is constant and, by substitution, the general equation for concentration at any location x and time t is:

$$\frac{\partial C}{\partial t} = -\frac{1}{2t^{\frac{3}{2}}}\exp\left(\frac{-x^2}{4\kappa t}\right) + \frac{x^2}{4\kappa t^{\frac{3}{2}}}\exp\left(\frac{-x^2}{4\kappa t}\right) \quad \text{Eq. A.7}$$

$$\frac{\partial^2 C}{\partial x^2} = -\frac{1}{2\kappa t^{\frac{3}{2}}}\exp\left(\frac{-x^2}{4\kappa t}\right) + \frac{x^2}{4\kappa^2 t^{\frac{3}{2}}}\exp\left(\frac{-x^2}{4\kappa t}\right) \quad \text{Eq. A-8}$$

and at any given time,

$$C(x,t) = \frac{C_0}{\sqrt{4\pi Dt}}\exp\left(\frac{-x^2}{4Dt}\right). \quad \text{Eq. A-9}$$

The initial condition is defined as

$$C(x,0) = C_0\delta(x-a). \quad \text{Eq. A-10}$$

With the initial pulse of mass located at *a*, the infinite domain solution becomes

$$C(x,t) = \frac{C_0}{\sqrt{4\pi Dt}}\left[\frac{-(x-a)}{4Dt}\right]. \quad \text{Eq. A-11}$$

The irrigation prescription solution requires an initial condition of a step change, rather than a

pulse input at a single location. Fischer et al. (1979) show that a step change can be defined by summing instances of Eq. A.11, centered at every location to the right of the origin (a "superposition integral"), so that (Equation A.12, next page)

$$C(x,t) = \int_0^{\infty} \frac{C_0}{\sqrt{4\pi Dt}} \exp \frac{-(x-a)^2}{4Dt} da \quad \text{Eq. A-12}$$

.

Combined with the error function, defined as

$$erf(z) = \int_0^{z} \frac{2}{\sqrt{\pi}} \exp(-\xi^2 d\xi) \quad \text{Eq. A-13}$$

,

Eq. A.11 is simplified to

$$C(x,t) = \frac{C_0}{2}\left[1 + erf\left(\frac{x}{\sqrt{4Dt}}\right)\right]. \quad \text{Eq. A-14}$$

At any given time, the distribution of the mass is described by the characteristic length σ, with σ^2 being the total variance (2nd moment) of the distribution. At some final time when transport effectively ceases, the characteristic length becomes

$$\sigma^2 = \frac{\int_{-\infty}^{\infty} (x-\mu)^2 C(x,t) dx}{\int_{-\infty}^{\infty} C(x,t) dx} = 2Dt \quad \text{Eq. A-15}$$

with the standard notation of statistical moments in the integrals.

To apply Eq. A.14 to the transition depths, *C(0)* is the difference between depths across the transition, namely $D_{max} - D_{min}$, and *C(x,t)* is the depth at location *D(x)* in excess of D_{min}.

$$\frac{C(x,t)}{C_0} = \frac{1}{2}\left[1 + erf\left(\frac{x}{\sqrt{2\sigma^2}}\right)\right], \text{ and} \quad \text{Eq. A-16}$$

$$\frac{D(x) - D_{\min}}{D_{\max} - D_{\min}} = \frac{1}{2}\left[1 + erf\left(\frac{x-a}{\sqrt{2\sigma^2}}\right)\right]. \quad \text{Eq. A-17}$$

A.17 is the function (Eq. 2 in text) used to approximate depth across step changes.

Field M54	Subsoil EM	Topsoil EM	Moisture	WetWeight	Clay	Silt	Sand	Base Sat.	CEC	Total Bases	Na	Fe	Cu	Mn	Zn	B	S	NH4	NO3	Mg	Ca	K	P	OM	SSalts	pH
Subsoil EM		.593	-.043	-.002	-.091	.360	-.335	-.143	.190	.030	.101	.161	.215	.158	-.058	.001	-.014	-.075	-.131	.053	.043	.052	.110	-.081	-.023	-.107
Topsoil EM	.000		.474	-.040	.061	.480	-.487	-.180	.460	.220	.211	.309	.436	.371	.163	.047	.200	.296	.181	.258	.300	-.094	.259	.195	.186	-.332
Moisture	.643	.000		-.337	.066	.080	-.093	-.108	.178	.047	-.046	.245	.182	.241	.291	-.045	.116	.356	.224	.022	.195	-.187	.269	.267	.174	-.182
Wet Weight	.985	.662	.000		.086	.136	-.154	.057	.152	.167	.048	.008	.027	.040	-.028	.120	.094	.123	.104	.198	-.016	.222	.008	.015	.058	-.054
Clay	.322	.509	.474	.352		-.052	-.175	.145	.304	.337	.126	-.157	-.066	-.110	-.167	-.051	-.130	.031	-.063	.352	.120	.019	-.036	-.088	-.125	.177
Silt	.000	.000	.384	.139	.573		.974	-.126	.722	.471	.306	.349	.564	.619	.396	.317	.447	.420	.377	.477	.475	.056	.406	.480	.497	-.495
Sand	.000	.000	.313	.094	.057	.000		.092	-.780	-.541	-.330	-.308	-.541	-.585	-.352	-.300	-.411	-.420	-.357	-.550	-.495	-.061	-.392	-.452	-.462	.448
Base Sat.	.121	.050	.240	.534	.114	.171	.320		-.132	.612	-.041	-.079	-.111	-.168	-.022	.041	-.044	.000	.026	.210	.364	.310	-.046	-.021	.096	.206
CEC	.037	.000	.051	.098	.001	.000	.000	.151		.697	.398	.440	.547	.623	.643	.425	.605	.626	.640	.553	.611	.133	.587	.713	.650	-.547
Total Bases	.746	.016	.612	.069	.000	.000	.000	.000	.000		.278	.282	.345	.360	.493	.375	.452	.493	.540	.589	.754	.323	.424	.554	.593	-.269
Na	.270	.021	.617	.605	.170	.001	.000	.658	.000	.002		.217	.369	.246	.220	.326	.382	.220	.149	.231	.232	-.116	.223	.244	.248	-.261
Fe	.079	.001	.007	.934	.087	.000	.001	.392	.000	.002	.017		.674	.443	.671	.246	.389	.428	.406	.235	.228	.150	.877	.512	.437	-.697
Cu	.018	.000	.046	.766	.471	.000	.000	.228	.000	.000	.000	.000		.559	.517	.317	.542	.439	.437	.291	.371	.029	.535	.476	.500	-.554
Mn	.084	.000	.008	.665	.233	.000	.000	.067	.000	.000	.007	.000	.000		.642	.497	.730	.645	.617	.206	.445	.123	.462	.683	.707	-.726
Zn	.532	.075	.001	.763	.068	.000	.000	.810	.000	.000	.016	.000	.000	.000		.497	.700	.752	.837	.190	.509	.187	.734	.919	.836	-.682
B	.995	.614	.629	.190	.578	.000	.001	.653	.000	.000	.000	.007	.000	.000	.000		.665	.444	.484	.171	.346	.326	.264	.569	.653	-.318
S	.879	.028	.206	.308	.156	.000	.000	.633	.000	.000	.000	.000	.000	.000	.000	.000		.620	.736	.233	.487	.206	.375	.752	.852	-.608
NH4	.413	.001	.000	.182	.741	.000	.000	.999	.000	.000	.016	.000	.000	.000	.000	.000	.000		.801	.262	.546	.174	.503	.771	.784	-.484
NO3	.153	.048	.014	.260	.492	.000	.000	.782	.000	.000	.105	.000	.000	.000	.000	.000	.000	.000		.203	.596	.184	.493	.884	.893	-.563
Mg	.565	.004	.809	.030	.000	.000	.000	.021	.000	.000	.011	.010	.001	.024	.037	.062	.010	.004	.026		.326	.148	.286	.247	.281	-.167
Ca	.643	.001	.033	.863	.191	.000	.000	.000	.000	.000	.011	.012	.000	.000	.000	.000	.000	.000	.000	.000		-.023	.353	.615	.622	-.313
K	.574	.310	.041	.015	.834	.541	.510	.001	.147	.000	.206	.102	.752	.182	.041	.000	.024	.057	.044	.106	.799		.141	.177	.290	-.073
P	.231	.004	.003	.928	.699	.000	.000	.618	.000	.000	.014	.000	.000	.000	.000	.004	.000	.000	.000	.002	.000	.123		.601	.517	-.677
OM	.378	.033	.003	.867	.340	.000	.000	.820	.000	.000	.007	.000	.000	.000	.000	.000	.000	.000	.000	.007	.000	.054	.000		.884	-.632
SSalts	.800	.042	.058	.527	.174	.000	.000	.295	.000	.000	.006	.000	.000	.000	.000	.000	.000	.000	.000	.002	.000	.001	.000	.000		-.570
pH	.244	.000	.046	.559	.054	.000	.000	.024	.000	.003	.004	.000	.000	.000	.000	.000	.000	.000	.000	.069	.001	.428	.000	.000	.000	

Field M54	Residual Variance (%) →																								
	87.3	7.946	1.86	1.049	0.723	0.413	0.306	0.226	0.076	0.049	0.02	0.014	0.008	0.005	0.002	0.002	0.001	6E-04	2E-04	1E-04	1E-04	6E-05	4E-05	2E-05	1E-06	6E-07
pH	.000	-.006	-.002	.004	-.001	-.004	.007	.005	.002	-.030	.019	-.002	.005	.006	.003	.058	.082	.010	.329	.770	-.403	-.308	.173	.028	.015	-.004
SSalts	.000	.001	.002	.000	.000	.000	-.001	-.001	.001	.003	.003	-.003	.000	.001	.003	.003	-.001	.010	.006	.026	.010	.013	-.022	-.004	-.455	.889
OM	.001	.009	.015	-.001	-.004	-.001	-.005	-.003	.003	.014	.015	-.015	-.040	.112	-.034	.022	-.038	.041	-.141	.348	.815	-.407	-.096	-.014	-.005	-.018
P	.037	.760	-.253	.104	.038	-.547	.198	-.013	.009	.057	.009	-.023	.021	-.034	.007	-.006	-.008	.004	.006	.001	.001	-.001	-.001	.000	.000	.000
K	.997	-.054	-.018	-.036	-.024	-.008	-.001	.007	-.004	-.002	-.001	.000	.000	.000	-.002	.001	-.001	.001	.000	.000	.000	.000	.000	.000	.000	.000
Ca	.000	.011	.027	.030	-.001	-.016	-.042	-.005	.005	.005	.043	.048	.115	.107	-.501	.693	-.351	.327	.010	-.049	-.052	.012	.012	.017	.007	.001
Mg	.001	.004	.002	.007	.010	-.008	-.029	.001	-.005	-.023	.064	.085	-.025	-.008	-.120	-.260	.454	.832	.060	-.047	.023	.022	-.002	.013	.013	.000
NO3	.033	.336	.868	-.016	-.078	.111	.162	-.132	.229	-.093	-.073	.028	.016	-.054	.018	.000	.009	.001	.000	.001	-.004	.003	.004	.002	.001	-.001
NH4	.011	.114	.227	-.017	-.008	-.001	-.111	.281	.876	-.250	.075	-.063	.035	-.046	.010	.004	.018	-.012	-.005	-.009	.005	.001	-.004	-.003	.000	-.001
S	.007	.050	.117	-.033	-.004	.069	-.105	-.067	.064	.615	.728	-.120	.080	-.141	.083	.001	-.030	.002	-.017	-.001	-.020	-.024	-.003	-.008	.002	-.004
B	.000	.001	.003	-.001	.000	.001	-.003	-.003	.006	.017	.020	-.003	-.003	.011	.003	.019	-.019	.013	.014	.434	.248	.843	.143	-.130	.004	-.023
Zn	.004	.057	.058	-.002	-.029	.015	.011	-.014	.046	.073	.059	-.189	-.248	.874	.143	-.155	-.217	.105	.053	-.034	-.107	.031	-.017	.006	.002	-.001
Mn	.005	.062	.089	-.065	-.010	.001	-.231	.008	.202	.686	-.601	.223	-.056	.009	-.044	-.008	.036	.007	.010	.025	-.017	-.008	.002	.006	.001	.000
Cu	.000	.006	.001	-.002	.001	.012	-.019	-.004	-.002	.007	.016	.015	.016	-.024	-.015	.002	-.026	-.077	.928	-.224	.266	.028	-.078	-.041	.004	-.002
Fe	.028	.516	-.291	-.027	.022	.781	-.160	-.035	-.020	-.084	-.008	.044	-.023	-.005	-.009	.017	.011	-.007	-.013	.007	-.004	-.001	.003	.000	.000	.000
Na	.000	.001	.000	.000	.001	.000	-.002	-.002	.004	.004	.015	.005	.005	.004	-.002	-.015	-.002	-.027	.027	.005	.088	.097	.153	.978	.010	.010
Total Bases	.004	.017	.030	.064	.019	-.034	-.067	-.011	-.013	-.014	.138	.224	.067	.236	-.393	-.010	.399	-.306	-.026	.108	-.084	.102	.644	.086	.005	-.012
CEC	.001	.021	.024	-.013	.013	-.040	-.063	-.007	-.008	-.012	.132	.229	.066	.253	-.332	-.026	.344	-.279	-.029	-.157	.092	-.074	.701	-.122	-.015	.019
Base Sat.	.036	-.048	.056	.982	.062	.068	-.109	.010	.005	.039	-.028	-.024	.001	-.015	.040	-.022	-.014	.000	.000	-.008	.009	-.008	.050	-.008	-.001	.001
Sand	-.003	-.067	-.061	.052	-.104	.196	.628	.069	.119	.187	-.105	-.285	.132	.018	-.182	-.015	.122	-.035	.003	-.009	.020	.005	.011	-.010	.512	.263
Silt	.003	.070	.060	-.066	.094	-.154	-.617	-.106	-.129	-.111	-.061	-.429	-.009	-.040	-.085	-.017	.060	-.038	-.011	-.001	.007	.004	.007	-.009	.512	.261
Clay	.000	-.003	.001	.014	.010	-.042	-.011	.038	.010	-.076	.165	.708	-.125	.021	.262	.022	-.190	.050	-.009	.010	-.001	-.005	-.020	-.007	.517	.264
Wet Weight	.020	-.004	.087	-.061	.940	.047	.115	.283	-.075	.052	-.009	-.018	-.005	.022	.002	.008	-.006	.002	.002	.000	.000	.000	.000	.000	.000	.000
Moisture	-.011	.065	.035	-.001	-.288	-.004	-.104	.891	-.306	.064	.027	-.044	-.042	.002	.017	.042	.039	-.006	.000	-.005	.003	.005	-.001	.002	.000	.000
Topsoil EM	.000	.003	-.014	-.013	.005	-.005	-.058	-.015	-.022	-.003	-.077	.001	.689	.246	.507	.336	.280	.049	-.006	-.032	.038	.007	-.022	.004	.006	.000
Subsoil EM	-.001	.011	.002	-.013	-.006	.005	-.078	.064	-.037	-.022	-.020	.102	.626	.034	-.264	-.554	-.447	.045	-.001	.064	-.028	-.020	-.002	-.008	-.004	-.001

Field B207	Subsoil EM	Topsoil EM	Moisture	WetWeight	Clay	Silt	Sand	Base Sat.	CEC	Total Bases	Na	Fe	Cu	Mn	Zn	B	S	NH4	NO3	Mg	Ca	K	P	OM	SSalts	pH
Subsoil EM		.682	.222	.279	.032	.159	-.163	.160	.296	.223	.343	.139	.126	-.034	-.191	.161	.286	.092	.243	.557	.187	-.226	-.204	-.183	.228	.039
Topsoil EM	.000		.141	.270	.123	.133	-.156	.058	.267	.115	.512	.119	.174	.060	-.010	.326	.345	.073	.414	.550	.076	-.127	-.127	-.178	.318	-.065
Moisture	.009	.099		.047	.060	.229	-.239	.324	.342	.429	.166	-.147	-.119	-.282	-.106	.173	.160	.007	.156	.090	.425	-.139	-.103	.257	.110	.402
Wet Weight	.001	.001	.587		.096	.101	-.119	-.279	.189	-.231	.190	.348	.360	.244	.017	-.039	-.006	.014	.001	.261	-.251	.084	.101	-.049	-.029	-.301
Clay	.715	.154	.490	.266		-.058	-.135	.000	.191	.050	.054	.074	.136	-.054	-.062	.121	-.097	-.131	-.121	.048	.048	-.197	-.041	.053	-.079	-.029
Silt	.064	.120	.007	.242	.499		.981	.071	.284	.158	.124	-.027	.096	-.196	-.344	-.066	-.041	-.014	-.044	.242	.146	-.359	-.334	.041	-.085	.077
Sand	.056	.068	.005	.168	.115	.000		-.071	-.319	-.166	-.134	.012	-.122	.205	.354	.042	.059	.039	.067	-.250	-.154	.395	.340	-.051	.099	-.071
Base Sat.	.062	.504	.000	.001	.997	.409	.413		.030	.949	-.019	-.553	-.378	-.557	-.188	.273	.050	.090	.198	.056	.952	-.315	-.293	.129	.197	.820
CEC	.000	.002	.000	.027	.025	.001	.000	.725		.313	.390	-.062	.316	-.146	-.088	.295	.171	.066	.077	.315	.295	-.374	-.196	-.056	.171	.114
Total Bases	.009	.180	.000	.007	.563	.065	.052	.000	.000		.098	-.537	-.275	-.575	-.215	.341	.105	.101	.207	.133	.998	-.399	-.331	.109	.240	.812
Na	.000	.000	.054	.027	.529	.149	.120	.830	.000	.256		-.030	.035	.015	-.075	.446	.479	.052	.289	.658	.047	-.185	-.186	-.403	.427	-.022
Fe	.104	.167	.087	.000	.391	.758	.888	.000	.471	.000	.727		.551	.702	.328	-.141	-.081	-.012	-.192	.087	-.549	.450	.509	-.109	-.187	-.698
Cu	.143	.042	.167	.000	.112	.263	.156	.000	.000	.001	.682	.000		.497	.200	.032	-.187	.011	-.244	-.067	-.272	.027	.199	.070	-.218	-.572
Mn	.690	.483	.001	.004	.529	.022	.016	.000	.088	.000	.859	.000	.000		.634	-.053	.091	.049	.001	.014	-.585	.614	.643	-.159	.008	-.739
Zn	.025	.907	.218	.842	.469	.000	.000	.028	.306	.012	.381	.000	.019	.000		.180	.128	.141	.204	-.254	-.207	.693	.765	-.050	.130	-.222
B	.060	.000	.044	.656	.157	.445	.627	.001	.000	.000	.000	.101	.708	.535	.035		.373	.095	.326	.212	.323	-.028	.006	-.079	.417	.232
S	.001	.000	.063	.949	.261	.638	.494	.564	.046	.224	.000	.347	.028	.290	.135	.000		.037	.564	.426	.072	.027	.045	-.167	.840	-.008
NH4	.285	.398	.932	.871	.128	.875	.654	.297	.446	.241	.549	.890	.894	.566	.100	.268	.665		.124	-.029	.101	.173	.094	.076	.055	.107
NO3	.004	.000	.070	.989	.159	.610	.437	.020	.368	.015	.001	.025	.004	.992	.017	.000	.000	.150		.204	.190	.108	.070	-.130	.734	.130
Mg	.000	.000	.297	.002	.577	.004	.003	.515	.000	.120	.000	.310	.434	.870	.003	.013	.000	.733	.017		.065	-.243	-.274	-.403	.328	-.057
Ca	.029	.376	.000	.003	.574	.089	.072	.000	.000	.000	.585	.000	.001	.000	.015	.000	.404	.242	.027	.449		-.394	-.323	.140	.214	.822
K	.008	.139	.107	.332	.021	.000	.000	.000	.000	.000	.030	.000	.758	.000	.000	.746	.755	.043	.211	.004	.000		.805	-.035	.035	-.323
P	.017	.140	.235	.244	.632	.000	.000	.001	.022	.000	.030	.000	.020	.000	.000	.943	.600	.276	.418	.001	.000	.000		-.004	.025	-.345
OM	.033	.037	.002	.570	.538	.635	.555	.132	.512	.204	.000	.205	.414	.063	.563	.360	.052	.375	.129	.000	.102	.681	.963		-.213	.097
SSalts	.007	.000	.202	.739	.359	.324	.248	.021	.046	.005	.000	.028	.010	.924	.131	.000	.000	.522	.000	.000	.012	.683	.775	.012		.103
pH	.651	.451	.000	.000	.733	.371	.411	.000	.185	.000	.796	.000	.000	.000	.009	.006	.926	.213	.131	.509	.000	.000	.000	.261	.232	

Field B207	Residual Variance (%) →																								
	57.88	21.19	13.82	3.981	1.185	0.786	0.463	0.301	0.165	0.11	0.031	0.028	0.023	0.02	0.006	0.004	0.004	0.002	8E-04	4E-04	2E-04	2E-04	5E-05	1E-05	2E-06	1E-28
pH	.007	.001	-.002	-.001	-.011	-.013	.006	.009	.019	-.004	-.077	-.017	-.008	-.028	-.006	.058	.091	.213	-.532	.649	.407	-.256	-.001	.017	.002	.000
SSalts	.000	.001	.002	.001	.000	.000	.000	.000	.001	-.001	.004	.001	-.007	-.001	.001	.002	-.003	-.010	.004	.018	-.043	.026	.056	.996	.041	.000
OM	.000	.000	-.001	.000	.000	-.002	.000	.004	.002	.003	-.027	-.004	-.005	.033	-.017	-.079	.055	-.129	.093	-.435	.866	-.018	.153	.036	.012	.000
P	-.055	.142	-.062	.033	.109	.222	-.194	.886	-.240	.118	-.069	-.032	.042	-.081	.010	.001	-.051	-.010	.000	.003	.001	.001	.000	.001	.000	.000
K	-.298	.845	-.383	.068	-.021	-.162	.055	-.108	.053	-.044	.002	.016	-.005	-.011	.003	.001	.001	-.007	.002	.000	.000	-.001	-.001	.000	.001	.000
Ca	.125	.014	-.012	.012	.054	-.025	-.006	.204	.581	-.194	.087	-.073	-.115	.002	.023	-.401	.165	-.101	-.139	-.069	-.040	-.024	-.271	-.005	.488	.000
Mg	.001	-.001	.007	.007	.020	.003	.016	-.027	.003	-.004	.038	.054	.100	-.086	.017	.435	-.437	.353	.261	-.019	.141	-.135	-.359	.011	.485	.000
NO3	.089	.392	.660	-.630	.031	.047	-.040	-.011	-.004	-.008	-.003	-.006	-.017	.007	.007	.002	-.002	-.001	.001	.001	.001	-.001	.000	-.001	.000	.000
NH4	.003	.018	-.003	-.008	.010	-.029	.035	-.022	.331	.936	-.077	.029	-.041	.054	-.007	-.001	-.019	.008	.005	-.002	-.008	.001	-.003	.001	-.001	.000
S	.028	.215	.602	.767	.001	-.029	.014	-.015	-.020	.008	-.006	-.001	-.020	.000	-.003	-.007	.007	-.005	-.001	.001	.000	-.002	-.001	-.002	.000	.000
B	.001	.001	.001	.001	.000	.001	.001	.002	.009	-.002	.007	.020	.003	-.004	-.048	.023	.022	.006	.063	.283	.194	.909	-.219	-.008	.004	.000
Zn	-.004	.014	-.003	.001	.000	.017	-.016	.058	.004	.013	.137	.044	.052	.110	-.231	.110	.697	.598	.192	-.113	-.028	-.009	.003	.009	-.002	.000
Mn	-.023	.022	-.003	.013	.065	.074	-.037	.021	-.059	.060	.700	.106	.326	.561	.121	-.053	-.127	-.049	-.144	.024	.029	.002	.001	.001	.001	.000
Cu	-.002	-.002	-.001	-.001	.019	.015	.001	.013	.023	.004	.086	.014	.035	.029	-.070	-.108	.159	-.349	.696	.515	.115	-.246	-.041	-.001	-.001	.000
Fe	-.099	.038	-.055	.055	.686	.562	-.300	-.293	.060	-.014	-.064	-.055	-.092	-.011	-.026	.009	.015	.007	-.014	.000	.002	.000	.002	.000	.000	.000
Na	.000	.000	.001	.001	.001	.000	.002	-.001	.005	.000	.005	.009	.014	-.005	-.023	.041	-.041	.039	.047	.136	-.069	.158	.806	-.077	.537	.000
Total Bases	.125	.015	-.004	.021	.075	-.022	.012	.176	.589	-.199	.133	-.008	-.005	-.089	.018	.074	-.317	.290	.171	.055	.046	.024	.267	.005	-.487	.000
CEC	.002	-.009	.013	.003	.036	-.005	.024	.094	.256	-.066	.100	.050	.059	-.070	-.071	.746	.280	-.476	-.165	-.061	-.030	.008	.009	-.006	-.001	.000
Base Sat.	.925	.239	-.213	.063	.050	.047	.005	-.061	-.153	.045	-.015	.009	.009	.014	-.007	.042	.018	-.027	-.003	-.001	-.003	.001	.001	.000	.000	.000
Sand	-.014	.060	-.022	.023	-.449	.518	.078	-.072	.076	.012	.044	-.389	.128	-.051	-.055	.010	-.010	-.003	-.001	-.004	.002	.004	-.001	.001	-.001	.577
Silt	.013	-.053	.023	-.023	.433	-.548	-.080	.029	-.094	.042	.069	-.364	.111	-.066	-.046	.002	.006	.000	-.002	-.003	.000	.007	.000	.001	.000	.577
Clay	.000	-.007	-.001	.000	.015	.031	.001	.043	.019	-.054	-.112	.753	-.239	.116	.101	-.012	.004	.003	.003	.007	-.002	-.011	.001	-.002	.001	.577
Wet Weight	-.028	-.005	.014	-.022	.320	.153	.921	.109	-.080	-.004	.013	-.038	-.060	.017	-.007	-.021	.004	.011	-.007	-.004	-.003	.003	.000	.000	.000	.000
Moisture	.009	.003	.006	.006	.039	-.027	.022	.047	.152	-.122	-.635	-.061	.427	.600	-.036	.049	-.024	-.007	.037	.004	-.037	.004	-.010	.005	-.002	.000
Topsoil EM	.002	.002	.019	-.005	.047	.025	.031	-.041	.028	.018	.028	.312	.531	-.342	-.652	-.201	-.106	-.072	-.112	-.032	-.019	-.017	-.010	.004	-.001	.000
Subsoil EM	.004	-.001	.014	.004	.054	.038	.035	-.053	.044	.029	-.051	.130	.544	-.377	.689	-.069	.215	.045	.036	-.008	.008	.028	.014	.003	.001	.000

Field M21	Subsoil EM	Topsoil EM	Moisture	WetWeight	Clay	Silt	Sand	Base Sat.	CEC	Total Bases	Na	Fe	Cu	Mn	Zn	B	S	NH4	NO3	Mg	Ca	K	P	OM	SSalts	pH
Subsoil EM		.928	.302	.132	.120	.301	-.314	-.254	.243	-.197	-.148	.301	.314	.384	.320	.021	.013	.102	.154	.191	-.205	.324	.404	.144	.132	-.245
Topsoil EM	.000		.379	.168	.197	.479	-.501	-.276	.348	-.193	-.090	.401	.466	.428	.403	.090	.049	.102	.235	.376	-.209	.374	.500	.229	.214	-.327
Moisture	.001	.000		.148	.292	.195	-.248	-.034	.435	.058	.105	.134	.317	.240	.387	.058	.041	-.117	.272	.204	.045	.243	.328	.189	.201	-.094
Wet Weight	.139	.060	.097		.251	.145	-.191	.029	.299	.093	-.059	.189	.381	.157	.121	.119	.101	.038	-.062	.195	.087	.008	.123	.278	.028	-.089
Clay	.182	.027	.001	.005		.093	-.298	.012	.414	.104	.178	.209	.413	.165	.308	.082	.110	-.090	.055	.292	.089	.187	.263	.205	.087	-.096
Silt	.001	.000	.028	.106	.301		-.978	-.038	.446	.040	.053	.327	.496	.331	.302	.270	.088	.081	.188	.581	.014	.364	.417	.353	.245	-.203
Sand	.000	.000	.005	.032	.001	.000		.034	-.514	-.060	-.088	-.357	-.562	-.352	-.354	-.276	-.107	-.059	-.192	-.618	-.032	-.388	-.455	-.381	-.253	.215
Base Sat.	.004	.002	.703	.748	.897	.671	.703		.187	.977	.075	-.494	-.251	-.430	-.200	.224	.131	-.103	.014	-.129	.980	-.288	-.197	.010	.183	.726
CEC	.006	.000	.000	.001	.000	.000	.000	.036		.376	.190	.176	.512	.198	.321	.329	.339	-.117	.242	.534	.355	.033	.389	.350	.433	.005
Total Bases	.027	.031	.520	.301	.245	.660	.506	.000	.000		.109	-.431	-.138	-.371	-.130	.273	.213	-.118	.056	-.008	.999	-.275	-.108	.063	.267	.677
Na	.098	.318	.242	.513	.047	.554	.326	.403	.033	.223		-.002	.103	-.012	.079	.159	.153	-.147	.082	.196	.088	-.041	.046	.052	.173	.001
Fe	.001	.000	.135	.034	.019	.000	.000	.000	.048	.000	.981		.794	.806	.698	.088	.056	.141	.219	.539	-.453	.412	.736	.379	.131	-.827
Cu	.000	.000	.000	.000	.000	.000	.000	.005	.000	.123	.252	.000		.710	.728	.303	.161	.058	.362	.680	-.167	.397	.756	.505	.307	-.610
Mn	.000	.000	.007	.079	.064	.000	.000	.000	.026	.000	.891	.000	.000		.762	.143	.041	.235	.298	.402	-.391	.491	.670	.487	.166	-.675
Zn	.000	.000	.000	.176	.000	.001	.000	.025	.000	.146	.378	.000	.000	.000		.234	.109	.135	.463	.431	-.154	.474	.809	.541	.333	-.502
B	.818	.319	.522	.184	.359	.002	.002	.012	.000	.002	.076	.325	.001	.109	.008		.480	.134	.156	.338	.258	.042	.309	.235	.463	.075
S	.889	.588	.647	.258	.219	.330	.233	.145	.000	.017	.088	.532	.071	.647	.226	.000		-.028	.188	.384	.201	-.124	.255	.107	.813	-.042
NH4	.256	.257	.193	.676	.314	.366	.513	.253	.191	.188	.101	.116	.521	.008	.131	.135	.758		.081	.041	-.120	.161	.181	.039	.046	-.075
NO3	.084	.008	.002	.493	.538	.035	.031	.876	.006	.532	.362	.014	.000	.001	.000	.082	.035	.369		.288	.042	.230	.389	.272	.654	-.185
Mg	.032	.000	.022	.029	.001	.000	.000	.150	.000	.933	.028	.000	.000	.000	.000	.000	.000	.648	.001		-.046	.292	.616	.334	.443	-.474
Ca	.021	.019	.619	.332	.323	.876	.722	.000	.000	.000	.328	.000	.061	.000	.086	.004	.024	.180	.644	.613		-.304	-.138	.047	.249	.695
K	.000	.000	.006	.927	.036	.000	.000	.001	.710	.002	.646	.000	.000	.000	.000	.643	.167	.072	.010	.001	.001		.563	.260	.054	-.376
P	.000	.000	.000	.170	.003	.000	.000	.027	.000	.230	.608	.000	.000	.000	.000	.000	.004	.042	.000	.000	.124	.000		.460	.413	-.552
OM	.107	.010	.034	.002	.022	.000	.000	.913	.000	.482	.562	.000	.000	.000	.000	.008	.233	.666	.002	.000	.603	.003	.000		.270	-.157
SSalts	.140	.016	.024	.752	.331	.006	.004	.040	.000	.003	.052	.144	.000	.063	.000	.000	.000	.611	.000	.000	.005	.549	.000	.002		-.040
pH	.006	.000	.294	.319	.287	.022	.016	.000	.959	.000	.989	.000	.000	.000	.000	.406	.639	.405	.038	.000	.000	.000	.000	.079	.659	

Field M21	Residual Variance (%) →																								
	52.21	28.83	11.76	5.563	0.659	0.412	0.242	0.155	0.062	0.04	0.029	0.014	0.012	0.01	0.001	0.001	8E-04	4E-04	4E-04	2E-04	1E-04	8E-05	6E-05	2E-06	1E-06	7E-09
pH	.005	.002	-.003	.000	-.002	-.012	-.029	-.005	-.020	.049	-.027	-.006	.015	-.013	.026	-.096	.152	.164	.737	-.455	.377	-.088	-.181	.022	-.024	.011
SSalts	.000	.000	.001	.001	.001	.000	.000	.000	.000	.001	.000	.000	.000	-.001	-.003	-.004	.014	.005	.009	-.023	.018	-.001	.003	-.006	.973	-.228
OM	.000	.001	.001	.000	.000	.006	.006	-.001	.001	-.006	.000	.002	.023	-.021	.021	-.013	.084	.053	.060	-.115	.082	.890	.410	.068	-.008	-.007
P	-.038	.047	.048	.020	.063	.209	.692	.227	.306	.222	-.455	-.234	.036	-.055	.054	.005	-.028	-.051	.012	-.017	-.002	-.006	.004	-.003	.000	.000
K	-.596	.758	-.201	-.095	.123	-.030	-.058	-.003	.000	-.006	.007	.010	-.008	-.002	-.005	.000	.000	.001	.000	.000	-.001	.000	.000	.000	.000	.001
Ca	.079	.057	.000	.003	.013	.059	.052	-.076	-.021	.188	-.093	.492	-.211	-.233	-.088	.126	-.277	.158	.166	-.127	-.422	.037	-.010	.036	.119	.479
Mg	-.001	.001	.001	.002	.002	.007	.014	-.008	-.007	-.007	-.007	.007	-.024	.005	-.013	.032	.063	-.120	-.176	.204	.420	.294	-.586	-.229	.113	.485
NO3	-.064	.236	.918	-.027	-.308	.003	-.052	-.006	.000	-.009	.000	-.004	-.008	.000	.002	-.001	-.003	-.002	.002	.000	.000	.000	.000	-.001	-.001	.000
NH4	-.009	.006	.002	.026	-.013	.027	.045	.749	-.645	.076	.002	.078	-.026	.073	-.031	-.009	.007	.002	-.013	.001	-.001	.003	.004	.004	.000	.000
S	.059	.013	.306	.309	.893	-.070	-.063	.001	-.012	-.015	.025	-.006	.007	.010	-.002	-.001	.001	.002	-.001	-.004	-.001	.000	.000	.001	-.002	.000
B	.001	.001	.001	.003	.004	.003	.007	.004	-.006	-.004	-.011	-.004	.021	-.024	.011	-.033	.211	.022	.541	.784	-.171	.037	.063	-.101	.012	-.001
Zn	-.004	.004	.006	-.001	.002	.023	.059	.018	.029	-.006	.005	.038	.127	.000	.107	.024	.269	.909	-.239	.069	.016	-.034	-.057	-.034	-.004	.003
Mn	-.017	.006	.013	-.001	.007	.080	.164	.075	.014	-.127	.334	.214	.644	-.483	.327	.085	-.025	-.145	.018	-.029	.011	-.024	-.015	-.015	.001	.000
Cu	-.001	.001	.002	.001	.001	.015	.019	-.004	.004	-.013	.005	.020	-.003	.004	.019	-.002	.086	-.023	-.017	.129	-.003	.065	-.275	.945	.008	-.002
Fe	-.033	.002	.021	.003	.019	.190	.425	.113	.180	-.532	.477	.203	-.273	.239	-.210	-.055	-.002	.028	.063	-.027	.013	-.003	.007	-.015	-.002	.001
Na	.000	.000	.000	.000	.000	-.001	.001	-.004	.001	-.004	-.007	.008	.005	.008	.012	-.015	.060	-.023	-.068	.119	.459	-.316	.609	.177	.111	.501
Total Bases	.077	.059	.001	.005	.016	.065	.067	-.087	-.026	.175	-.108	.507	-.228	-.220	-.091	.151	-.145	.017	-.074	.200	.480	-.012	.024	-.014	-.115	-.481
CEC	.002	.004	.007	.007	.009	.049	.054	-.077	-.027	.121	-.061	.300	-.099	-.151	-.049	-.505	.688	-.221	-.169	-.119	-.137	-.051	.009	-.055	-.010	.002
Base Sat.	.787	.589	-.101	-.055	-.010	-.007	.010	.027	.011	-.043	.039	-.093	.041	.045	.015	-.025	.039	-.018	-.011	-.006	-.006	-.002	-.001	-.002	.000	.000
Sand	.017	-.036	-.007	-.089	.001	-.206	-.366	.581	.662	.063	.020	.166	-.052	-.028	.018	.019	.050	-.021	-.004	.001	.006	.004	-.006	.000	.000	.000
Silt	-.033	.108	-.103	.939	-.292	-.028	-.035	.031	.075	-.024	-.013	.015	.000	-.006	.007	-.002	.000	.000	-.001	-.001	.000	.000	-.001	.000	.000	.000
Clay	-.001	.004	.000	.000	.007	.041	.027	-.054	-.005	.041	-.040	.254	-.151	.463	.826	-.008	-.027	-.076	.013	-.001	-.019	.004	.001	-.024	.003	-.002
Wet Weight	.002	.003	-.010	.019	.044	.919	-.374	.050	.058	-.017	-.048	-.067	.009	-.012	-.003	.001	-.002	.001	.000	-.001	.002	-.004	.001	-.005	.000	.000
Moisture	-.003	.006	.007	.004	-.002	.035	.022	-.062	.058	.212	-.076	.346	.583	.589	-.356	-.048	-.054	-.033	.019	.011	.003	.014	-.002	.002	.000	.000
Topsoil EM	-.009	.005	.006	.021	-.003	.050	.073	-.038	.010	.360	.312	-.074	-.095	.099	-.053	.715	.441	-.123	.004	-.093	-.063	-.033	.026	-.016	-.003	.005
Subsoil EM	-.011	.006	.004	.023	-.004	.056	.075	-.005	.061	.615	.565	-.176	-.091	-.005	.029	-.411	-.252	.086	-.011	.079	.047	.027	-.009	.014	.002	-.003

Appendix C: Time series and computed flux for SR trials

Fluxes computed at two different heights on 03 August 2014. Site conditions were clear, and clover crop was well watered.

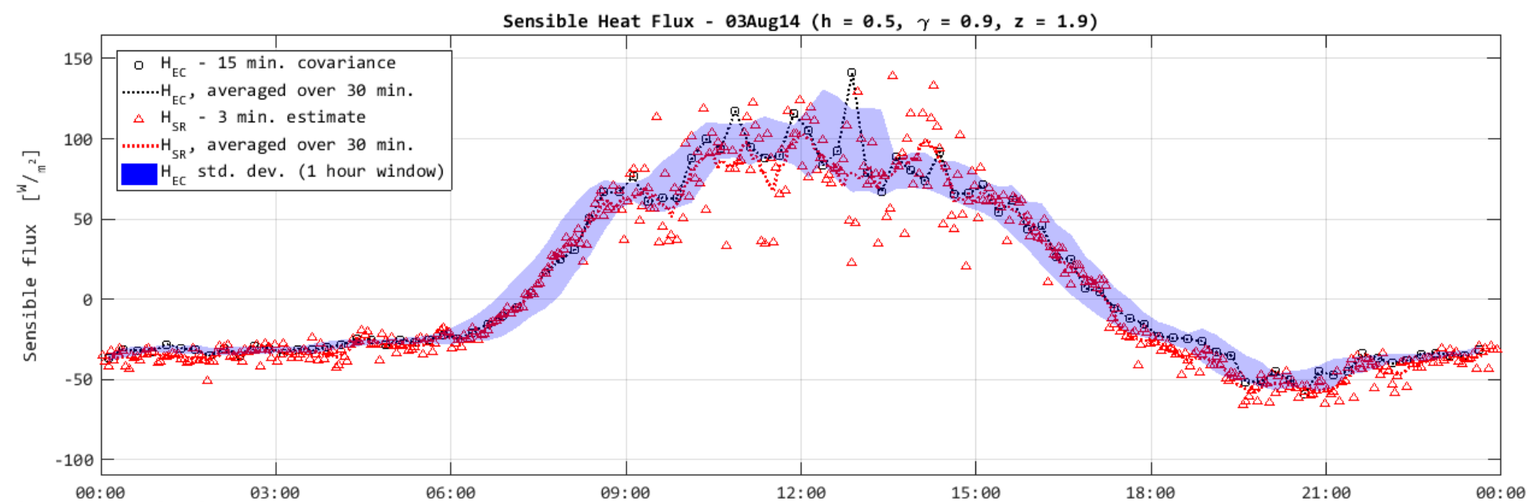

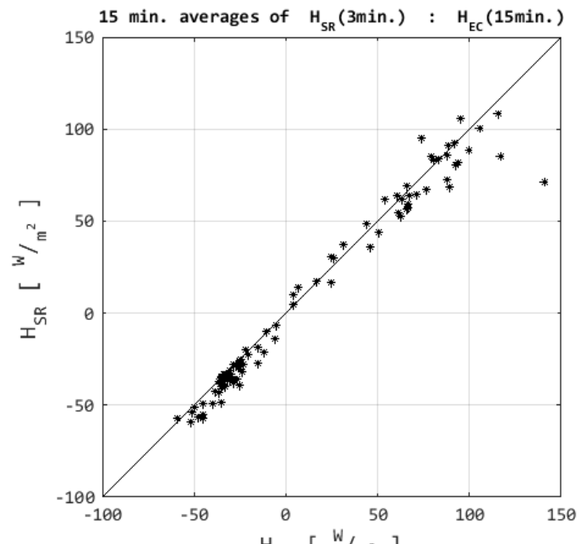

Fluxes computed with IRGASON at 1.9 m

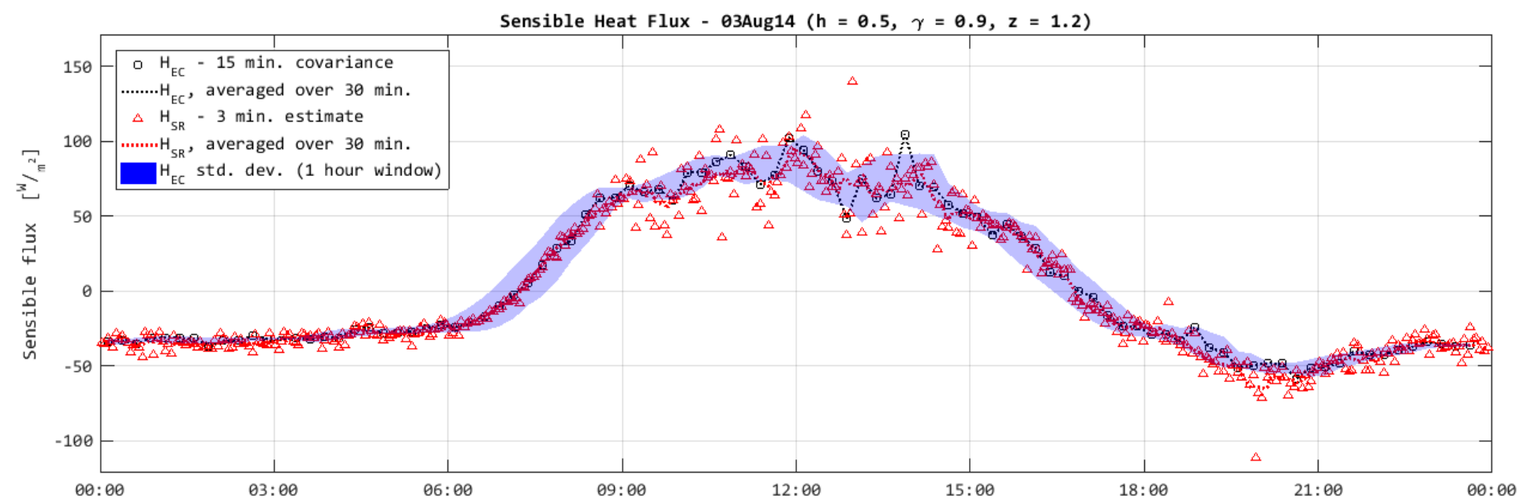

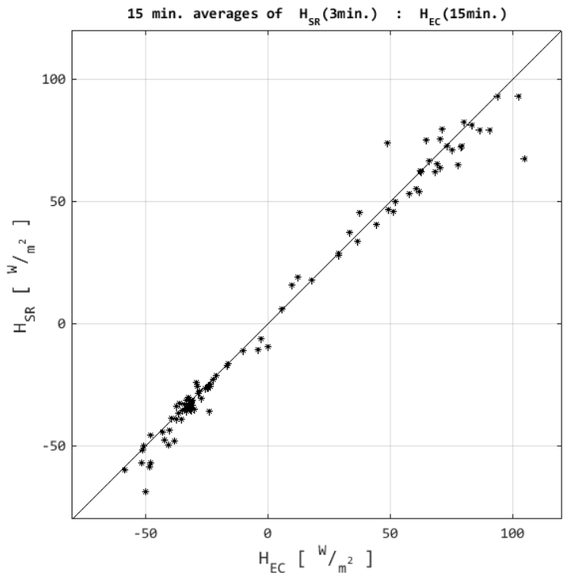

Fluxes computed with IRGASON at 1.2 m

Fluxes computed at two different heights on 04 August 2014. Site conditions were clear, and clover crop was well watered. Irrigation was applied at the instrument location midday, as can be seen by the sharp drop in sensible heat flux centered at 15:00.

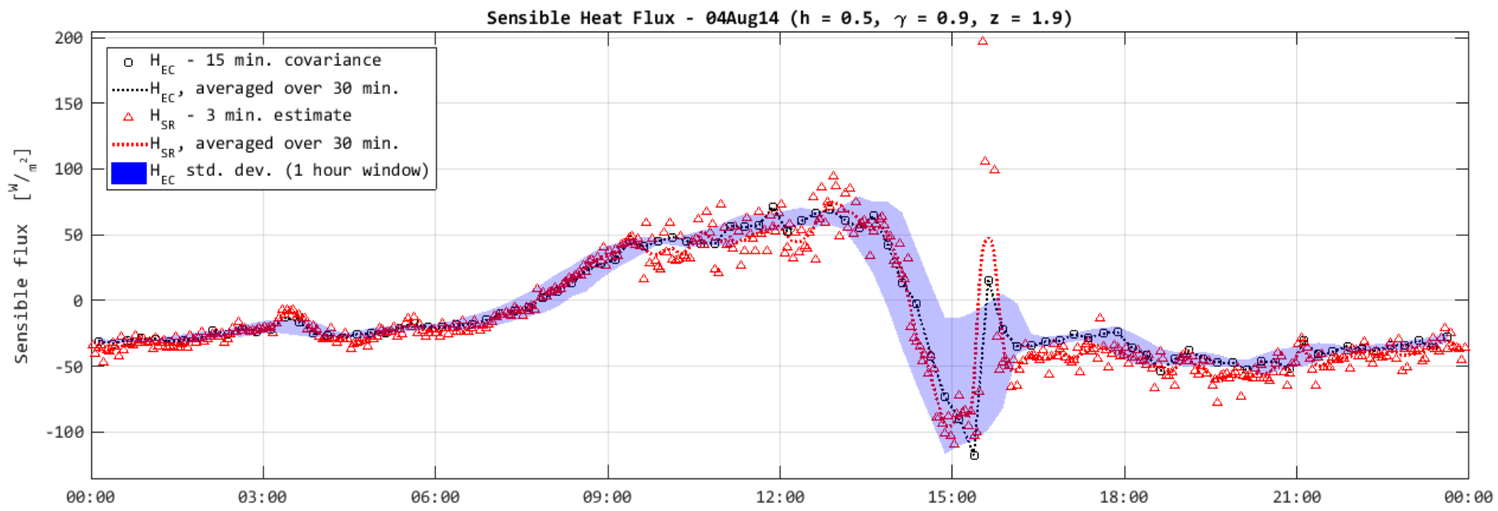

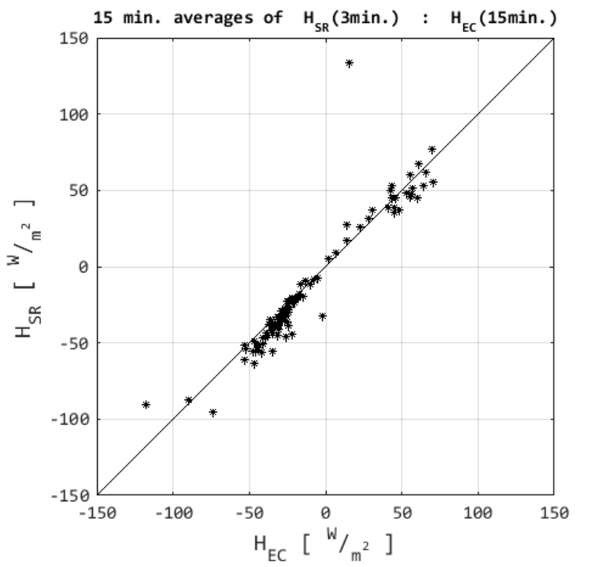

Fluxes computed with IRGASON at 1.9 m

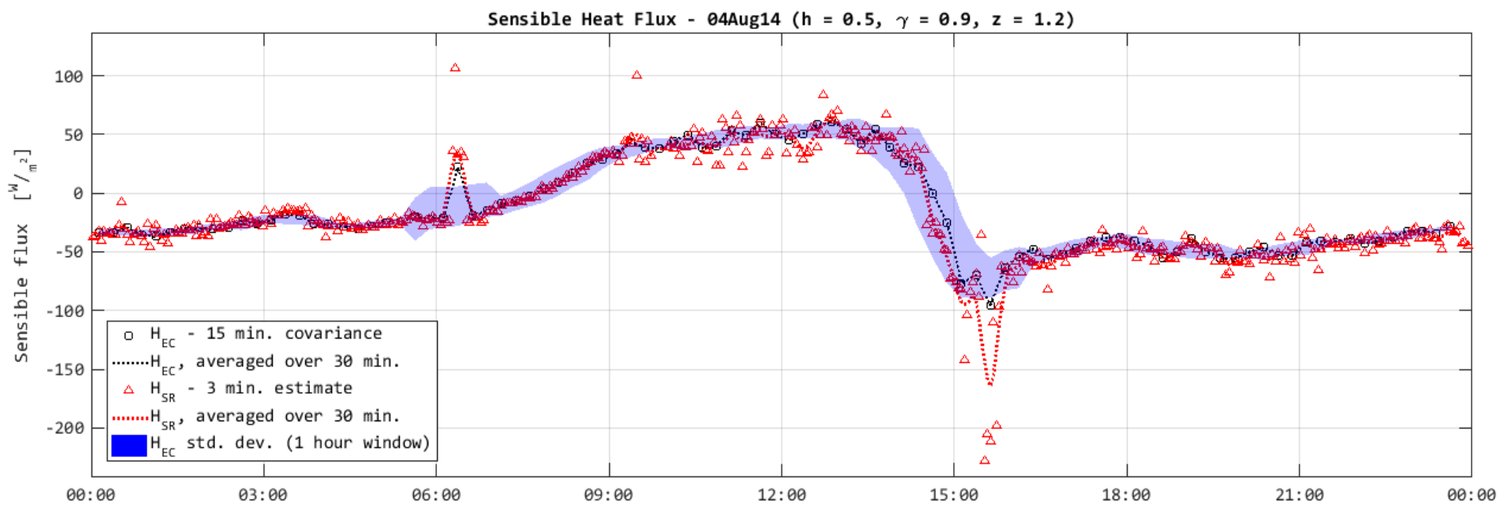

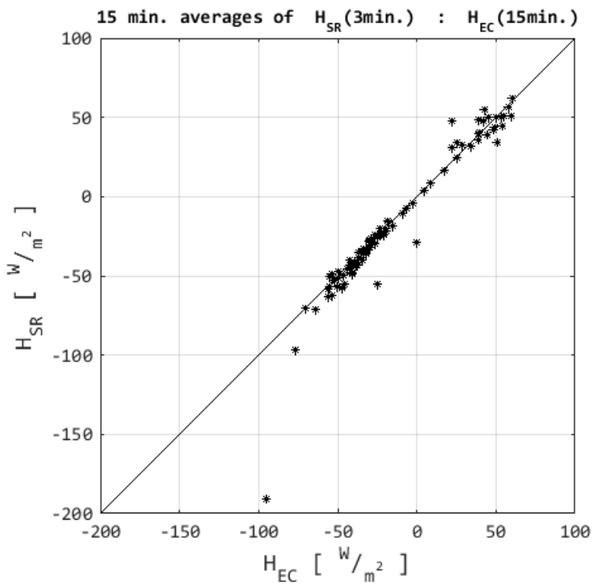

Fluxes computed with IRGASON at 1.2 m

Fluxes computed at two different heights for all days 02-11 August 2014. Site conditions were clear, except for August 11, when conditions were overcast and light rain may have fallen. Irrigation was applied on two days 04August and 10August.

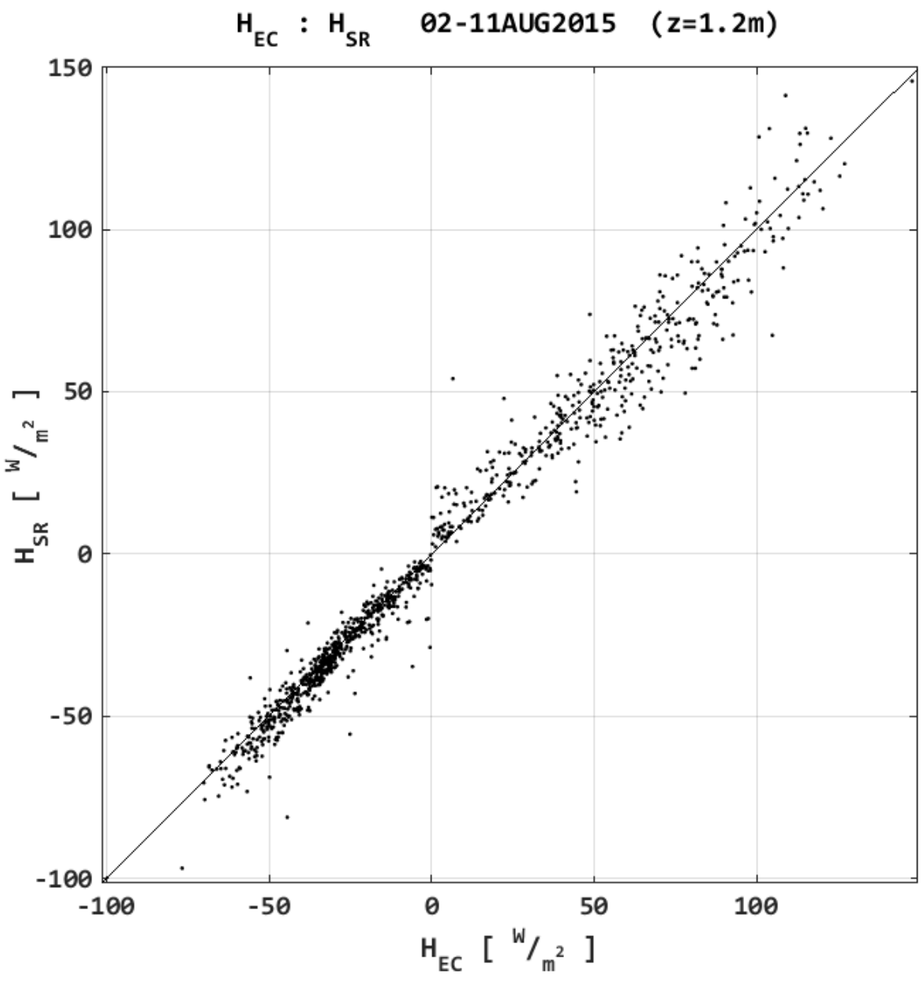

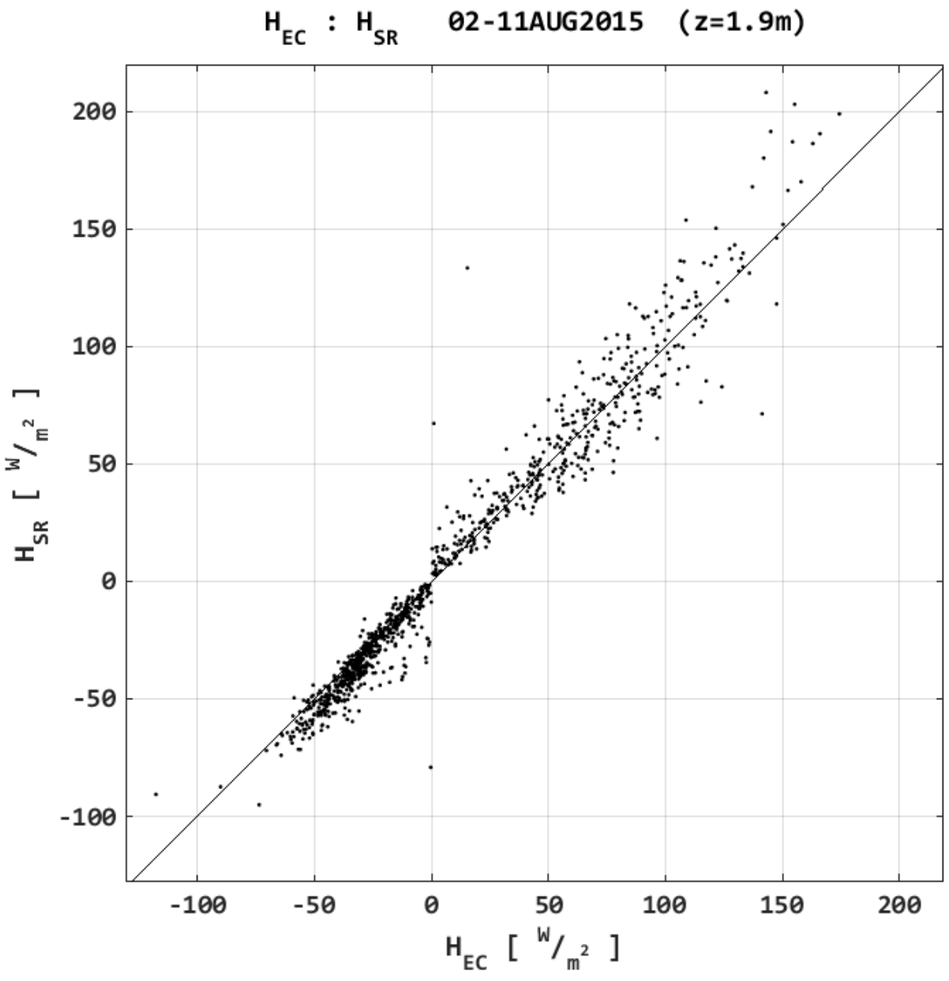

Fluxes computed on 07 March 2015. Trial conducted on two fields with low cover crop (h<15cm) and patchy dead grass (h 10-30cm). Mean vegetation height and γ parameter were treated as equal for both (h = 0.15, γ = 1.0)

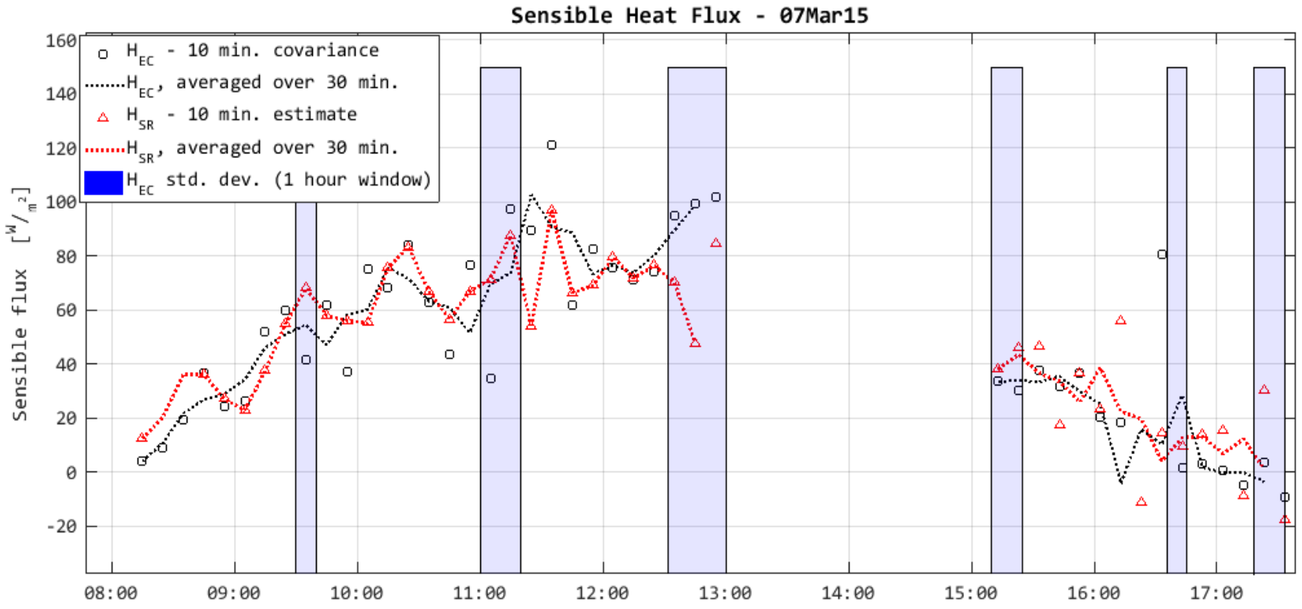

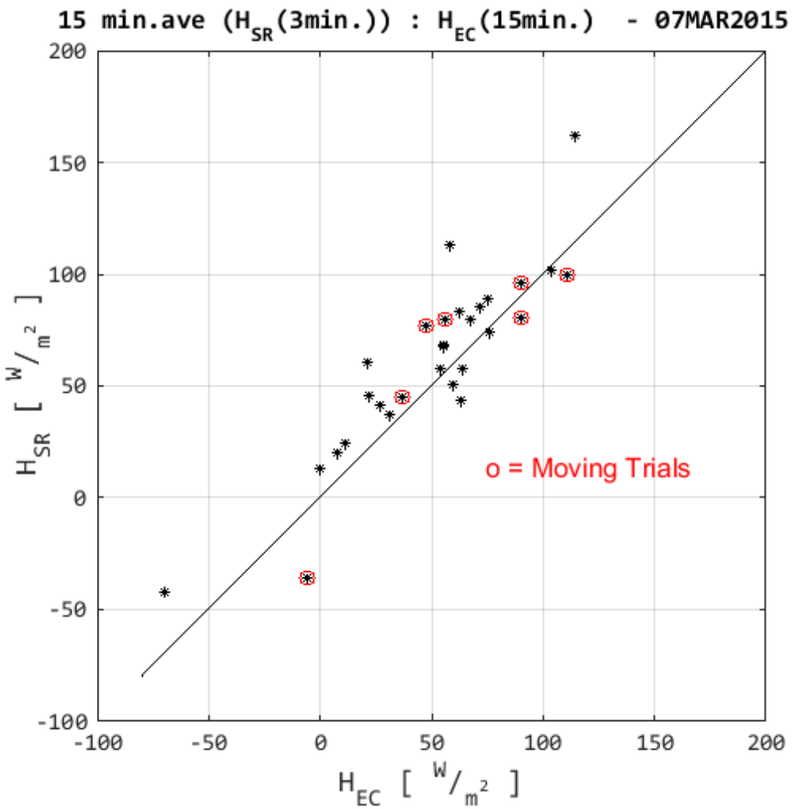

Fluxes computed on 18 June 2015. Trials were conducted on one field only, mostly covered by tall cover crop (h = 1.8m), but some sections maintained as mowed turf (h = 5 cm).

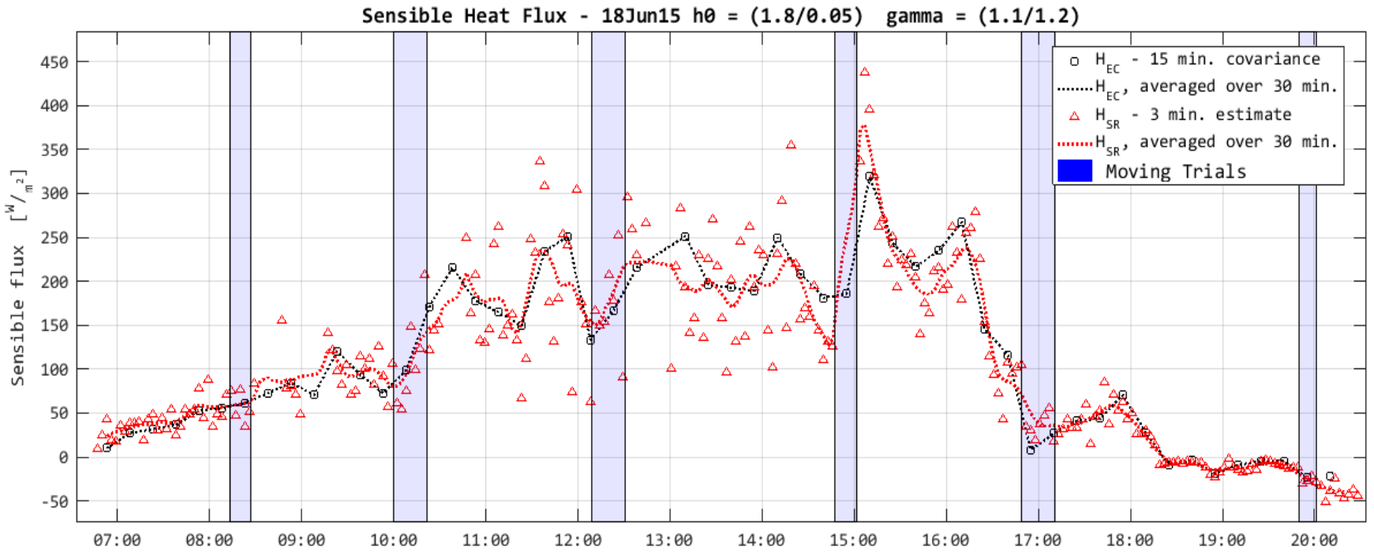

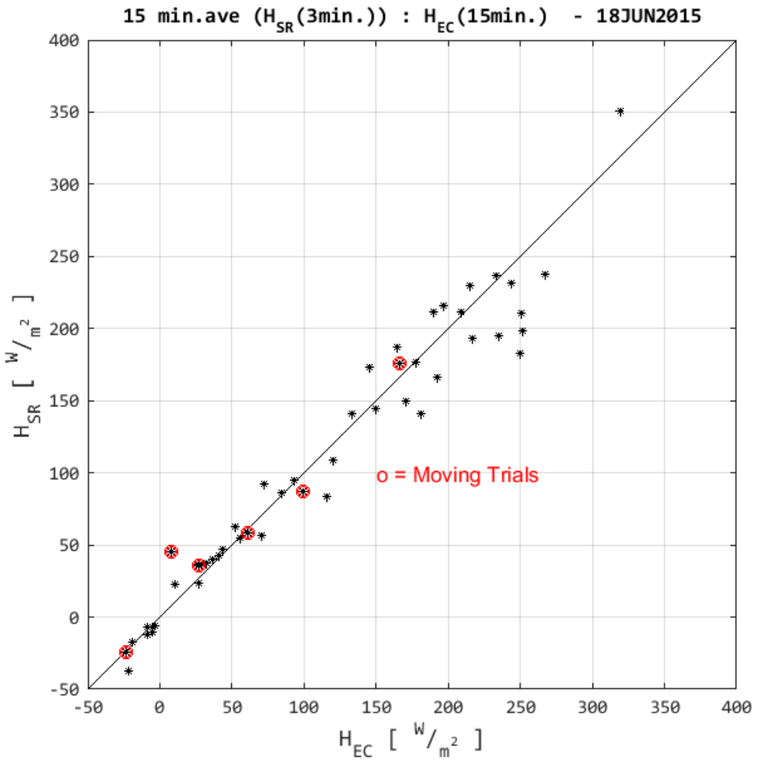

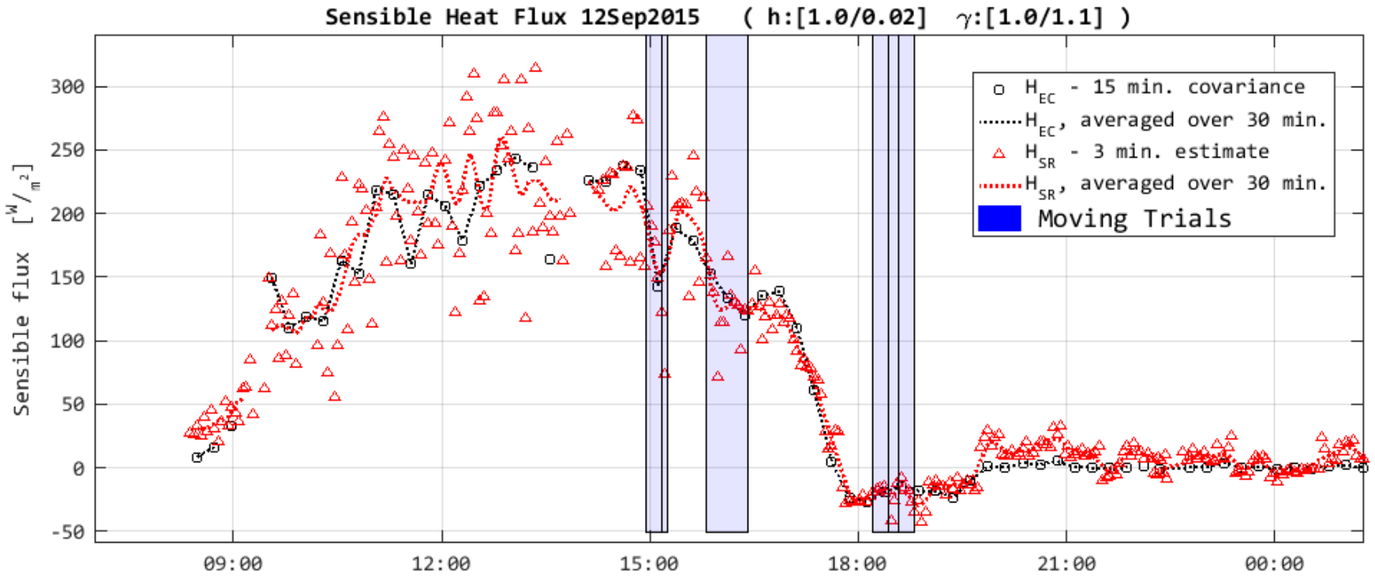

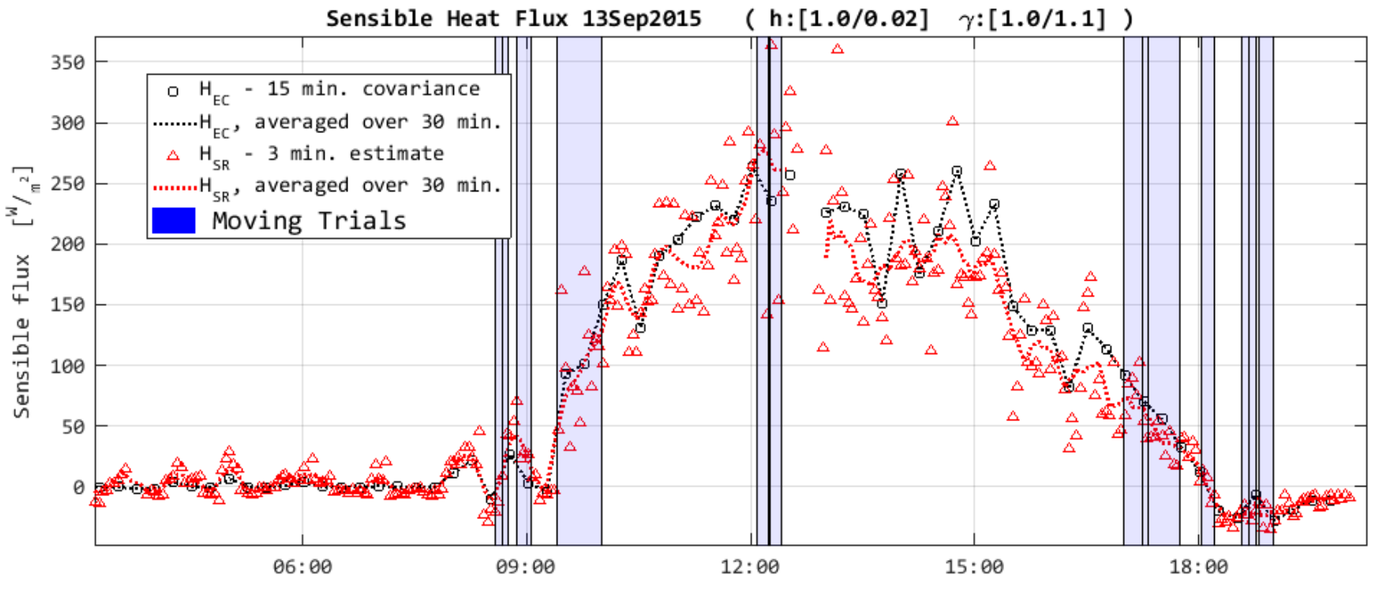

Fluxes computed on 12 and 13 September 2015. Trials conducted on two fields with straw mulch (h = 2cm) and patchy dry hay/grass (h = 1.0m).

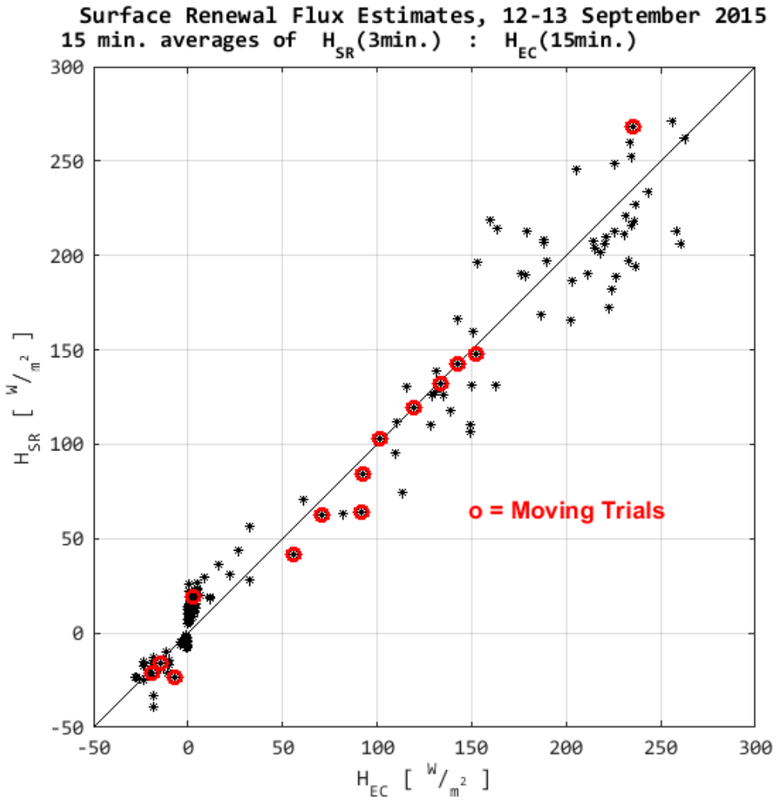

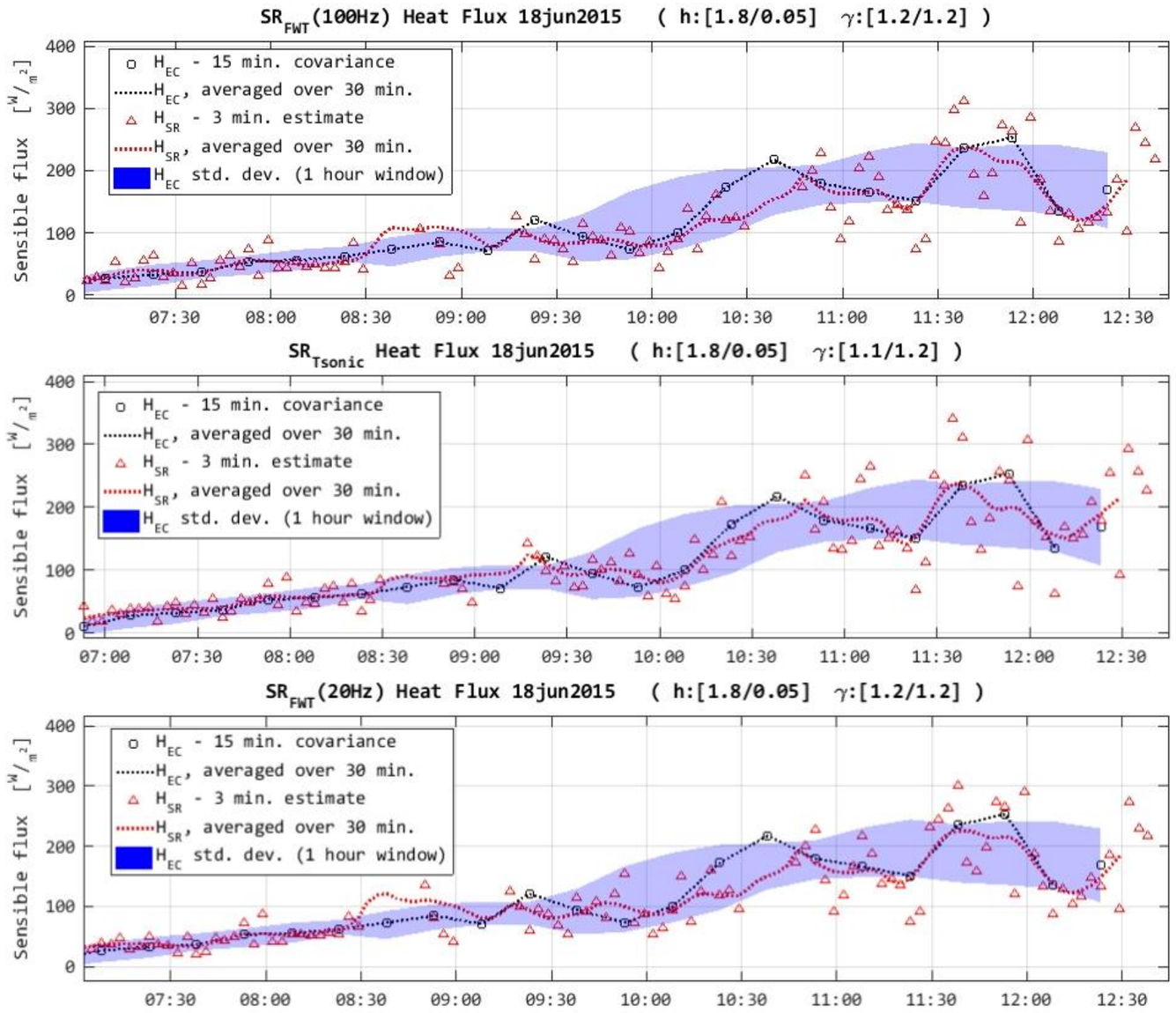

Comparison of surface renewal fluxes computed using FWT and 20 Hz sonic temperature. The 20Hz FWT data (time series at bottom left) is downsampled by selecting every fifth temperature measurement (after despiking). Data used from18 June 2015 same as shown on page C4. Comparison plot (below, right) based on 100Hz FWT and T_{sonic}. The 3 min. averaging periods were used for all flux calculations.

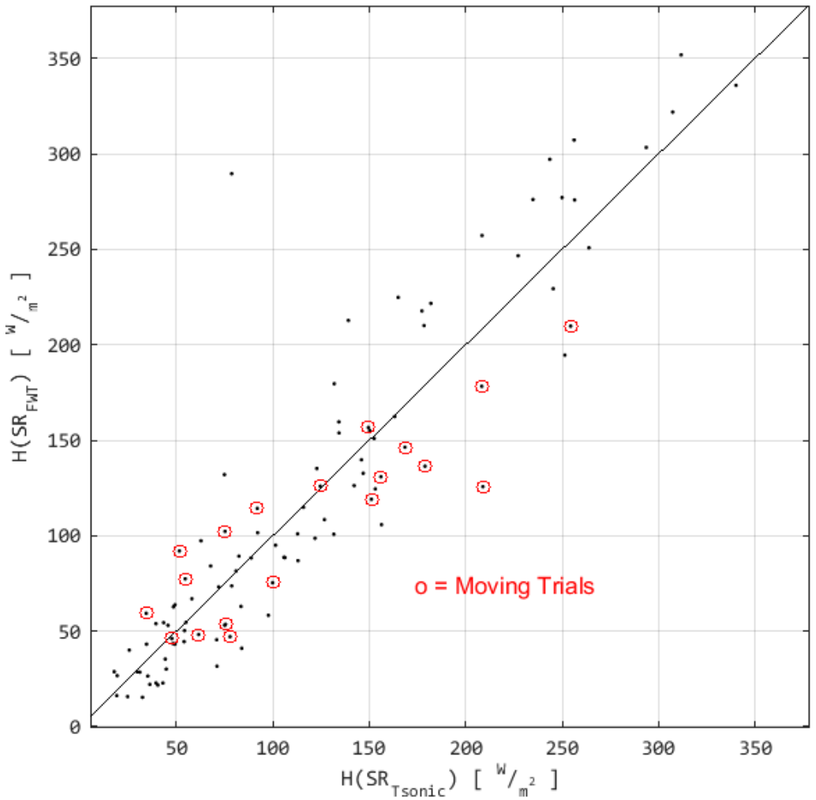

Appendix D: Computational Methods for Surface Renewal Flux

In the course of computing flux using the surface renewal method, an extensive set of program functions were written to compare EC and SR over a wide range of averaging periods and lags (in the structure functions). More efficient calculation methods were required to efficiently perform these calculations iteratively. Many iterations were required to compare the two methods without making *a priori* assumptions about the minimum time resolution of the SR method. All calculation was done in the Matlab language (Versions 8.0 - 9.0 Mathworks), installed with the Statistics, Curve Fitting, and Signal Analysis Toolboxes. Software was developed for the following aspects of this analysis: data import (from Campbell Scientific data loggers); raw data quality control; despiking of time series; coordinate rotations for EC method; eddy covariance flux calculations; GPS import and velocity calculations; surface renewal flux calculations; spectral and co-spectral analysis and plotting; basic meteorological and thermodynamics calculations and unit conversions. Much of this code was adapted from methods found at Mathworks user forum[14]; many direct citations can be found within comments of the code. Original code is appended in part in Appendix E.

D.1: Computational efficiency and vectorized code

Several computational methods were adapted from methods described by previous authors, including despiking of scalar traces (Vickers and Mahrt, 1997), calculation of structure functions (Antonia and Van Atta, 1978), and Fourier analysis of signals i.e. spectral analysis (Stull, 1988). In each of these cases, computation could be dramatically improved in (faster) execution time and (lower) memory usage via programming improvements. This was equally true for root finding for arrays of values (calculation of amplitude), and calculation of moving window statistics (especially standard deviations used in despiking). In the majority of cases, the process of

[14] https://www.mathworks.com/matlabcentral/fileexchange/

vectorizing code was responsible for the majority of improvement. Vectorization of Matlab code entails removing inefficient loops and taking advantage of implicit parallel methods in Matlab's pre-compiled library (Altman, 2015); i.e. calculating using vectors and matrices, which is more efficient using Matlab's memory allocation methods. Most significantly, application of convolution rather than array calculations takes advantage of Matlab's efficient FFT algorithm. In the case of root finding for the ramp amplitude, application of Girolamo Cardano's solution for depressed cubic polynomials (published in 1545) reduces an iterative numerical approximation for the polynomial to an algebraic vector calculation. While some of these programming methods are unique in some aspects to the Matlab language, the general mathematical concepts are universal. In cases where computational power is limited (such as data loggers) or memory constraints are prohibitive (such as long term field deployments), not only are these methods potentially cost saving, but also make SR feasible for monitoring in agricultural context. A few examples of the logic and application of these methods are detailed below.

D.2: Despiking via convolution

Despiking is the removal of erroneous, extreme data points from a time series of sampled values. It is a common procedure when using some types of environmental sensors including those measuring wind speed, temperature, and trace gases (Göckede et al., 2004). The origin of spikes in a time series can be either physical (sensor malfunction or actual physical non-errors) or electronic in nature; regardless, these can be recorded as either abnormally large or small values, or as some pre-defined error flag (9999 is a carryover from earlier systems) which are recognized by Matlab as explicit errors[15]. Spikes interfere with normal statistical calculation, requiring some deliberate and objective method to identify, remove, and interpolate where they exist. Previous authors have described a variety of methods including autocorrelation (Hojstrup, 1993) and

[15] Explicit missing values are denoted as NaN ("not a number") in the Matlab language. Clearly distinguishing between these explicit errors and implied errors (like "9999") is facilitated by objective criteria as described.

statistics of “moving window” sub-samples (Vickers and Mahrt, 1997). Because normal data contains a range of noise, (Rebmann et al., 2012) differentiate between hard spikes characterized as having unreasonable value (such as a temperature of 9999 K) and soft spikes which exceed an arbitrary but objective limit defined as appropriate for the signal to noise ratio of any particular data.

Because despiking is essentially a problem of low pass filtering, this procedure can be efficiently performed using convolution. Mathematically, convolution can be understood as a multiplicative function that combines a data signal with a filter signal. The filter defines the size of moving window and weighting with which data points are multiplied as the window “slides” along the data. Computationally, convolution is very efficient by use of the fast-Fourier transform, which is able to take advantage of memory allocation by a process known as bit switching. To demonstrate the efficiency gains of convolution, two programs were used to despike 8.5 hours of 20 Hz sonic temperature data (609139 samples). One program (*despikeVM.m*) executed a sliding window in a loop, following the objective criteria described in (Vickers and Mahrt, 1997). The second program (*despike.m*) which was used for the analyses below, used convolution to determine a running mean and standard deviation used in the identification of spikes (same criteria as above). After multiple runs with different input parameters, the first program average run time was 27 seconds. Using convolution, the second program average run time was 0.2 seconds, approximately a 99% decrease in run time. While this may be somewhat exaggerated by the difference in slow compile times of loops in Matlab, it nonetheless demonstrates the value of convolution in speeding calculations, and facilitated the abandonment of time saving strategies used by previous authors such as skipping samples.

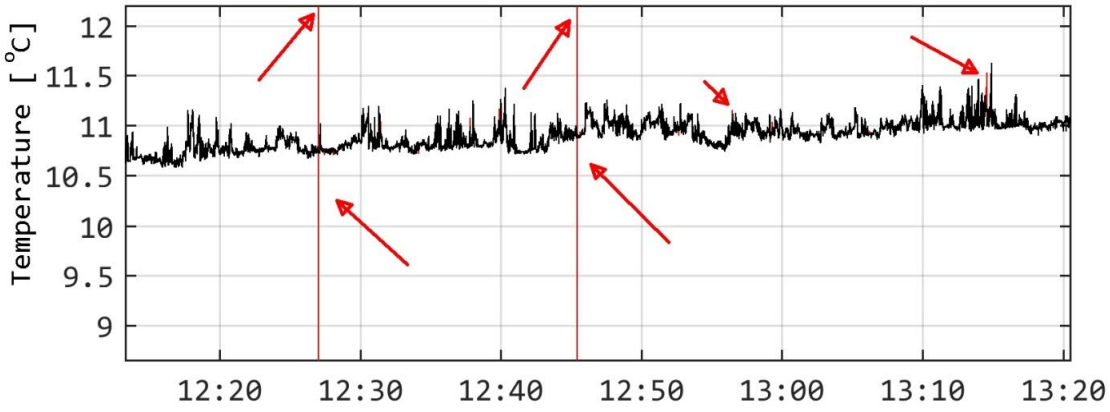

Figure D-1: Example despiking output. Red trace (and arrows) indicate data removed by despiking method.

D.3: Structure function calculation

Another memory intensive process that challenged early implementation of SR was the determination of the 2nd, 3rd, and 5th order structure functions. In deriving a method to find ramp geometry, (Van Atta, 1977) calculated structure functions for eight different lags. Increased processor power and memory size allowed (Snyder et al., 1996) to calculate structure functions on 8 Hz data for lags from 0.25-1.0 seconds, but were unable to resolve fluxes accurately at some measurement heights and surface roughness conditions. Later it was realized that determining the contributions from "imperfect ramp geometry" would require more thorough examination of ramp durations (Chen et al., 1997b; Paw U et al., 2005).

This analysis used sampling frequencies up to 100Hz and relatively long measurement periods (8-24 hours). Calculating the structure functions was inefficient by methods in the literature, and vectorization was required for the number of iterations used in section 5.3.4. Using the same data as described in section D.2, , computation of the structure functions for 3 minute periods with lags up to 10 seconds, required 39 seconds on average with a series of nested loops. In contrast, using 2-d convolution (*strfnc.m*) accomplishes this same calculation in 7.6 seconds (~80% improvement). The function also time stamps the averaging period, finds the sign of $S^3(r)$ (used to find flux direction), and indexes the maximized value of $S^3(r)/r$, preparing the data for

the following step of finding ramp geometry. Using 100 Hz FWT data increases the processing time using the convolution method to 38.4 seconds, indicating that the loop based method would be infeasible for processing 100 Hz data. Early attempts to process FWT data longer than 10 minutes overflowed memory, motivating an approach using convolution.

Two dimensional convolution is accomplished with a filter matrix, with a column for each time lag. Memory savings are not accrued directly from convolution, but by changing the implementation of multiplication which occurs when raising lagged differences to 2,3,and 5th power. This was affected through matrix multiplication rather than iterative scalar multiplication, which is only possible once the data was reshaped by 2-d convolution. Additional steps are required for transforms and data allocation, but otherwise this method reduces the programming complexity and improved data compactness.

D.4: Cardano's method for depressed cubic polynomials

The calculated structure functions are used as coefficients in a polynomial function to find the ramp amplitude (A). The form of the polynomial is referred to as a depressed cubic, restated from 5.1.3:

$$A^3 + \left(10S^2(r) - \frac{S^5(r)}{S^3(r)}\right)A + 10S^3(r) = 0 \qquad \text{Eq. D-1}$$

The magnitude of the real root (of 3 possible roots) can be regarded as the corresponding solution (Spano et al., 1997). The Matlab root finding algorithm computes eigenvalues of a companion matrix to approximate the solution to a n^{th} order polynomial, regarding the input function as a vector with n+1 elements (*roots.m* documentation[16]). Consequently, this function cannot be executed on an array, and motivated the development of a vectorized solution. The solution method proposed by Gerolamo Cardano in the 1545 *Ars Magna* (Edwards and Beaver, 2015) can

[16] *http://www.mathworks.com/help/matlab/ref/roots.html*, Accessed 9AUG2016

be applied to vectors. The important quality of the depressed cubic is that, by lacking a A^2 term, it can be solved algebraically. This is accomplished by substitution $A = (m^{1/3} + n^{1/3})$, into the abbreviated equation $A^3+pA+q=0$. Expanding terms and using the quadratic equation yields an exact (complex) solution:

$$A = \left(-\frac{q}{2} + \sqrt{\left(\frac{q}{2}\right)^2 + \left(\frac{p}{3}\right)^3} \right)^{\frac{1}{3}} + \left(-\frac{q}{2} - \sqrt{\left(\frac{q}{2}\right)^2 + \left(\frac{p}{3}\right)^3} \right)^{\frac{1}{3}} \qquad \text{Eq. D-2}$$

where p and q are the coefficients of the depressed cubic and derived from the structure functions. The function *cardanos.m* was customized specifically for the SR method, adapted from a function by Bruno Luong found at Matlabcentral[17]. The function output was verified against Matlab built-in function for polynomials with real and imaginary, positive and negative solutions. Solution for the real roots of Equation 5-8 in this manner expedited rapid SR flux calculations, and also facilitated analysis of the negative ramp time and the determination of flux direction (section 5.4.5).

[17] *https://www.mathworks.com/matlabcentral/newsreader/view_thread/165013*, Accessed 10MAY2016

Appendix E: Matlab Code used in SR Analysis

Flow Chart of surface renewal calculations (*SRv7c.m*) including functions described in Chapter 5 and Appendix D

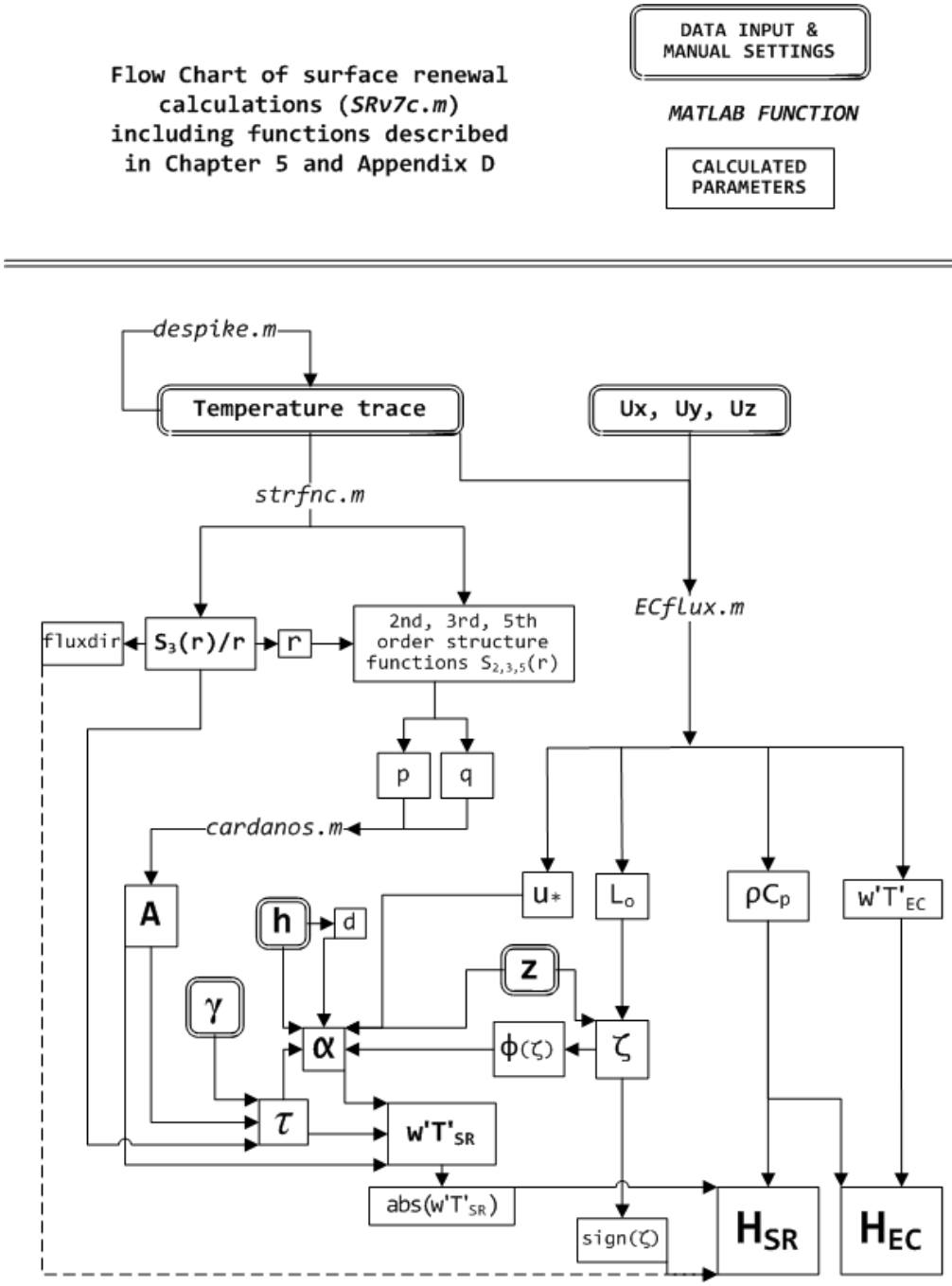

Surface Renewal Calculation (*SRv7c.m*)

```
% SR v7c
% Jason Kelley NEWAg Lab OSU
% Written 29 FEB 2016
% Last modified 11 july 2016

1. Load and pre-process data

DATA = load(file);
DATA.wind = [DATA.Ux, DATA.Uy, DATA.Uz];
fprintf('\n  1. Data loaded from %s\n',file)

% 1b. Despike scalar trace of temperature and humidity
fprintf('  Despiking DATA.H2O...')
DATA.rhov = despike(DATA.H2O,200,4,30,'interp',DATA.TIMESTAMP);
fprintf('  Despiking DATA.Ts....')
DATA.Tsds = despike(DATA.Ts,150,4,10,'interp',DATA.TIMESTAMP);
display('  1b. Despiking completed.')

% 1c. Calculate density of air and heat capacity (to convert units of fluxes)
Tc = [DATA.cell_tmpr];
TK = Tc +273.15;
P = [DATA.cell_press];
Ts = [DATA.Tsds]; %[DATA.Ts];
rhov = [DATA.rhov];
ea = (rhov./1000).*0.287.*TK./0.622;            % [kPa] partial pressure water
rhod = (P-ea)./0.287./TK;                       % [kg/m^3] density of dry air
rho = rhov./1000+rhod;                          % [kg/m^3] density of moist air
DATA.q = rhov./1000./rho;                       % [kg/kg] specific humidity
esat = 0.6112.*(exp(17.27.*Tc./TK));
DATA.RH  = ea./esat.*100;
DATA.RCP = rho_cp(Tc, P, rhov);
clear Ts Tc TK P rhov ea rhod rho esat
display('  1c. Air density and heat capacity calculated')

% 1d. Load time data from data
TIME.t_smp = 0.05;                              % sample time spacing (s)
TIME.freq  = 1/TIME.t_smp;                      % sampling frequency (Hz)
TIME.n     = size(DATA.Ts,1);
TIME.ttot  = TIME.n*TIME.t_smp/60;              % length of record (minutes)
display('  1d. Time stamps loaded')
TIME.start = datevec(DATA.TIMESTAMP(1));
TIME.fin   = datevec(DATA.TIMESTAMP(end));
fprintf('<strong> 1. Data load complete.</strong>\n')

2. Assign averaging periods
if ~exist('ERR','var')
    clearvars -EXCEPT GAR RTK DATA TIME file
else
    clear EC FCS IRGA WIND rcp SR z h gamma
end

TIME.tavEC = 15;                                % EC averaging period (minutes)
```

```
TIME.tavSR = 3;                                         % SR period (minutes)
TIME.tavFCS = 15;                                       % free convective scaling
display('<strong> 2a. Averaging periods assigned.</strong>')
2b. Allocate h0 and γ
    z = 2.05; %2.2
    h = 0.02;                                           % h: vegetation ht. [m]
    h = h.*ones(TIME.n,1);
gamma = 0.9.*ones(TIME.n,1);

display('<strong> 2b. Uniform vegetation height h and gamma allocated.</strong>')
2c. During moving trials, allocate variable h0 and γ via indexing (not shown)
clear h gamma
h1ii = genind(dh,DATA.TIMESTAMP);                       % this is the index
h2ii = ~h1ii;
h1 = 1.0; h2 = 0.2;
h(h1ii) = h1; h(h2ii) = h2; h = h';

gamma1 = 1.0; gamma2 = 1.1;
gamma = gamma1.*(h1ii); gamma(h2ii) = gamma2;

clear h1* h2* gamma1 gamma2 dh
display('<strong> 2b. Veg height h and gamma allocated.</strong>')

3. Eddy covariance calculation
clear EC WIND IRGA                                  % clears arrays- shorter ave. time =
more elements

TIME.npEC = floor(TIME.ttot/TIME.tavEC);            % number of averaging periods
TIME.nEC = floor(60/TIME.t_smp*TIME.tavEC);         % samples per period

for i = 1:TIME.npEC

    ii = (i-1)*TIME.nEC+1:i*TIME.nEC;

    [EC(i), IRGA(i), WIND(i)] = ECflux( DATA.TIMESTAMP(ii), DATA.wind(ii,:),
DATA.Tsds(ii), ...
        DATA.rhov(ii), DATA.cell_tmpr(ii), DATA.cell_press(ii));
end

clear i ii
display(' <strong>3. Completed eddy covariance calculations</strong>')

4. Surface Renewal calculation
% 4a. Structure function and polynomial roots
clear SF SR H* alpha tau rts p q

    maxlag = 10;                                        % range of lags (seconds)
   TIME.nn = TIME.freq*60*TIME.tavSR;
 TIME.npSR = floor(TIME.ttot/TIME.tavSR);

for i = 1:TIME.npSR
ii = (i-1)*TIME.nn+1:((i)*TIME.nn);
        % collect timestamps and field variables (h and gamma)
           time = DATA.TIMESTAMP(ii);
```

```
    SR(i).start = time(1);
      SR(i).ctr = time(floor(TIME.nn/2));
      SR(i).end = time(end);
      SR(i).h   = nanmean(h(ii));
    SR(i).gamma = nanmean(gamma(ii));
      % data and structure functions
          trace = DATA.Tsds(ii);                % the trace to analyze e.g.
                                                    [DATA.Ts(ii)];
    [S,imax,fd] = strfnc(trace,TIME.freq,maxlag); % fd = direction of flux
       SR(i).SF = S(imax,:);
       SR(i).fd = fd;
end

     nn = nnz([SR.ctr]);                        % in case missing time periods
     SF = reshape([SR.SF],5,nn)';
      p = 10.*SF(:,2)-SF(:,5)./SF(:,3);
      q = 10.*SF(:,3);
[~,rts] = cardanos(p,q);                        % Cardanos' soln

clear i ii S imax trace time maxlag nn p q
clear h gamma fd
display('4a. Calculated structure functions and found roots')

% 4b. Coherent structures - ramp time and amplitude
SR = deal2SA(rts(:,1),SR,'Amp');

tau = ([SR.Amp]'./(-[SR.gamma]')./((-SF(:,4)).^(1/3))).^3;
    if any(abs(imag(tau))>(1e-10))
        display('Some values contain a significant imaginary component')
    end
tau = (real(tau));

SR = deal2SA(tau,SR,'tau');

clear tau SF rts
display('4b. Completed ramp geometry calculations')

% 4c. Stability parameter and universal function for heat transfer --start here to
change h--

d = 0.67.*[SR.h]';                                  % d: displacement height [m]
zeta = z./[EC.ObuL];
ust = [EC.ustar];
Hec = [EC.H];

% if tavSR ~= tavEC, distribute eddy covariance calculated values to SR averaging
periods
if numel(SR)<numel(EC);
    error('EC averaging period must be longer than SR period for this calculation');
end
if numel(SR) ~= numel(EC)                           % if tavEC ~= tavSR, distribute
                                                    ustar and zeta
    repn = floor(numel(SR)./numel(EC));
    zeta = reshape(repmat(zeta,repn,1),1,repn*numel(EC));
```

```
    zeta(end+1:numel(SR)) = zeta(end);
    ust = reshape(repmat(ust,repn,1),1,repn*numel(EC));
    ust(end+1:numel(SR)) = ust(end);
    Hec = reshape(repmat(Hec,repn,1),1,repn*numel(EC));
    Hec(end+1:numel(SR)) = Hec(end);
end; clear repn
SR = deal2SA(zeta,SR,'zeta');
SR = deal2SA(ust,SR,'ustar');
SR = deal2SA(Hec,SR,'H_EC');

zzu = zeta>=-5 & zeta<=0;                          % NOTE: this is the relaxed
                                                   constraint zeta < -5
zzs = zeta>0   & zeta<=1;
zzn = zeta<-5  | zeta>1;
phi = zeros(TIME.npSR,1);
phi(zzu) = 0.95.*(1-11.6.*zeta(zzu)).^-0.5;
phi(zzs) = 0.95 +(7.8.*zeta(zzs));
phi(zzn) = NaN;

alpha = (0.4/pi.*((z-d)./z^2).*[SR.tau]'.*[SR.ustar]'./phi).^0.5;

% 4d. Surface Renewal flux
% distribute rho and Cp to convert units
for r = 1:TIME.npSR;
    ii = (r-1)*TIME.nn+1:((r)*TIME.nn);
    rcp(r) = nanmean(DATA.RCP(ii));
end
H = alpha.*z.*[SR.Amp]'./[SR.tau]';
H = (-1*sign([SR.zeta]')).*abs(H).*rcp';
SR = deal2SA(H,SR,'H');
divp = floor(TIME.npSR./TIME.npEC);
modp = mod(TIME.npSR,TIME.npEC);
Have = nanmean(reshape(H(1:end-modp),divp,TIME.npEC),1);
EC = deal2SA(Have,EC,'H_SR');
clear H* alpha divp modp
display('<strong> 4. Surface renewal flux calculation is complete.</strong>')
%5. Free convective scaling
clear FCS

TIME.npFCS = floor(TIME.ttot/TIME.tavFCS);         % number of averaging periods
TIME.nFCS = floor(60/TIME.t_smp*TIME.tavFCS);      % samples per period

FCS(TIME.npFCS).H = [];                            %initialize struct array

for i = 1:TIME.npFCS

    ii = (i-1)*TIME.nFCS+1:i*TIME.nFCS;

    [ec, irga,~] = ECflux( DATA.TIMESTAMP(ii), DATA.wind(ii,:), DATA.Tsds(ii), ...
        DATA.rhov(ii), DATA.cell_tmpr(ii), DATA.cell_press(ii));
    FCS(i).ctr = ec.ctr; FCS(i).zeta = z/ec.ObuL;
    FCS(i).T_m = irga.T_m; FCS(i).T_var = irga.T_var; FCS(i).rcp = irga.rcp;
end
clear i ii ec irga
```

```
c1 = (ones(1,length([FCS.T_m]))).*0.97;
wT = [FCS.T_var].^1.5 .* ([FCS.T_m]+273.15).^-0.5 .* c1.^-1.5 .* (0.4*9.8*2).^0.5;
Hfcs = wT.*[FCS.rcp];
FCS = deal2SA(smooth(Hfcs,6),FCS,'Hsm');

zcond = -0.2;                                          % set stability limit here
Hlim = 100;                                            % arbitrary minimum flux
FCS = deal2SA(([FCS.zeta] < zcond) & (Hfcs>Hlim),FCS,'valid');
Hfcs(~[FCS.valid]) = NaN;                              % set invalid H values to NaN
FCS = deal2SA(Hfcs,FCS,'H');
```

Published with MATLAB® R2016a

Despiking method using convolution (*despike.m*)

```
function [data_ds, ns, index] = despike(data, nw, sig, buffer, varargin)

% DESPIKE filters out spikes from a data vector using a Gaussian convolution.
%   INPUTS: data: nx1 vector
%           nw: width of window fucntion used in convolution
%           sig: # of standard deviations considered significant (& removed)
%           buff: number of adjacent samples to remove
%           varargin{1}: 'interp' option interpolates over nans (cubic)
%           varargin{2}: timestamps for data
%           varargin{3}: (optional) passes interpolation method ('cubic', etc.)
%                        w/o 3rd varargin, reverts to default 'linear'
%  OUTPUTS:  data_ds: despiked data
%           ns: number of (removed) spikes
%           index: logical vector with TRUE = spike
% REQUIRES: setnan.m (function that sets flagged values to NaN via index and buffer
size)
%
% Jason Kelley NEWAg Lab OSU
% Written 29 FEB 2016
% Last modified 27JUL2016 (Jewell)

% check for nans and interpolate
nn = isnan(data);
xs = 1:length(data);
if nnz(isnan(data))>0
    data = interp1(xs(~nn),data(~nn),xs,'nearest')';
end

w = gausswin(nw,1);
sw = sum(w);                    % total area under window function
w = w./sw;                      % normalize window

filter = conv(data,w,'same');   % filtered data

ii = true(length(data),1);      % don't use section of filter within 1/2 window of
ends
    hw = ceil(length(w)/2);
    ii(1:hw) = false;
    ii(end-hw:end) = false;

mstd = mw_std(data,nw).*sig;    % significance in terms of standard deviation w/in
windows
fluc = zeros(length(data),1);   % normalize fluctuations by absolute value
% fluc(ii) = (data(ii)-filter(ii))./data(ii); % original def for significance
fluc(ii) = data(ii)-filter(ii);

% index = abs(fluc)>sig;
index = abs(fluc)>mstd;         % index significant fluctuations (spikes)

ns = nnz(index);
%data_ds = data;
data_ds = setnan(data,index,buffer);
```

```
if nnz(nn)>0                    % reset NaNs in data vector
    data_ds(nn) = NaN;
    data(nn) = NaN;
end
fprintf('  %i spikes removed ; ',ns)
fprintf('%3.3f%% of data NaN''ed\n',(sum(isnan(data_ds))/length(data))*100)
% optional plotting (not included here)

if nargin > 4 && strcmp(varargin{1},'interp')
      % optional interpolation between nan'd points
    ind = isnan(data_ds);
    switch nargin
        case 5
            time = 1:length(data);
        case 6;
            time = varargin{2};
    end
    if nargin == 7
      data_ds(ind) = interp1(time(~ind),data_ds(~ind),time(ind),varargin{3});
    else
      data_ds(ind) = interp1(time(~ind),data_ds(~ind),time(ind));
    end
end % end interp option
end % end function

    function mstd = mw_std(signal,w)
        % adapted from http://matlabtricks.com/post-20/
        % "calculate-standard-deviation-case-of-sliding-window"

        N = length(signal);
        n = conv(ones(N,1),ones(w,1),'same'); % counts no. elements in each window
        s = conv(signal, ones(1, w), 'same'); % s vector
        q = signal .^ 2;
        q = conv(q, ones(1, w), 'same');      % q vector
        mstd = (q - s.^2./n)./(n-1);                % variance of moving window
        mstd = mstd.^0.5;                     % standard deviation

    end % moving window stddev sub-function
```

Published with MATLAB® R2016a

Structure function calculation using convolution (*strfnc.m*)

```
function [S, max_i, fluxdir, S3tr] = strfnc( trace, freq, maxlag )
%STRFNC Structure function calculation (following Van Atta, 1977)
%   Last modified 09mar16
% INPUTS 'trace'    data to analyze (Nx1 vector array)
%        'freq'     sampling frequency (Hz)
%        'maxlag'   maximum lag time, (seconds)
% OUTPUTS 'S'   structure functions S(r)^n and lag r (in seconds) for rows
%               only calculates 2 3 5 order to save memory,
%               column order corresponds to SFs, also calculated -S^3(r)/r
%               format: [r S^2(r) S^3(r) -S^3(r)/r S^5(r)]
%        'S3tr' sinusoidal trace of 3rd structure function
    m = length(trace);
 lags = 1:maxlag*freq;
   rn = length(lags);
    S = zeros(rn,5);
% old method by nested iterative loops
for j = lags
    r = lags(j); early  = trace(1:end-r);     later  = trace(r+1:end);
    diffs  = later-early;
    for i = [2 3 5]
        S(j,i) = sum((diffs).^i)/(m-r);
    end %structure functions at lag j
end % lags j
S(:,6) = lags./freq;
% lagged differences by convolution
filt = [ones(1,rn); -eye(rn)];  % singleton comparators at 1:rn lags  e.g. [1 0 0 -1]
  cT = conv2(trace,filt);       % conv filter with trace to get all lags
  cT = cT(rn+1:end-rn,:);       % trim edges.  'same' does not work here for conv2
cTp(:,:,1) = power(cT,ones(m-rn,rn).*2);    % for second order SF
cTp(:,:,2) = cTp(:,:,1).*cT;                % third order SF
cTp(:,:,3) = cTp(:,:,1).*cTp(:,:,2);        % fifth order SF
         w = (m-rn-(1:rn))-1;               % unbiased weighting vector 1/(N-1)
    S(:,2) = sum(cTp(:,:,1),1)./w;          % column order corresponds to SF order
    S(:,3) = sum(cTp(:,:,2),1)./w;          % i.e. 3rd order SF is S(:,3)
    S(:,5) = sum(cTp(:,:,3),1)./w;
    S(:,1) = lags./freq;                    % sample N -> dt
    S(:,4) = -S(:,3)./S(:,1);               % ratio used to detect lag max'ing S3r
% identify time lag at which S_3(r)/r is maximized, flux direction by +/- S^3(r)/r
  fluxdir = sign(nanmean(S(:,4),1));
[~,max_i] = max(fluxdir.*(S(:,4)));
% optional output of 3rd order S.F. trace to use in time lag spectra
    if nargout>3
       S3tr = cTp(:,max_i,2);
    end
end %function
```

Cardanos Method for roots of depressed cubic polynomial (*cardanos.m*)

```
function [REALrts, ALLrts] = cardanos(p,q)
% CARDANOS(p,q) root finding algorithm for depressed cubic polynomial with real
valued p and q reduced form of CardanRoots for surface renewal vectors p and q to
determine ramp Amplitudes polynomial should be of form A^3 + p*A + q = 0 with p and q
real valued (no complex values)

% RETURNS only positive real valued solutions, with complex and negative solutions
replaced with NaN
%refs:<ahref="matlab:web('https://en.wikipedia.org/wiki/Cubic_function#Cardano.27s_me
thod','-browser')">Wiki</a>
%<ahref="matlab:web('https://www.mathworks.com/matlabcentral/newsreader/view_thread/1
65013?requestedDomain=www.mathworks.com','-browser')">Source Code</a>
% &prev cardanos(b,c,d)
% SEE ALSO: cardanroots.m

D = q.^2 + (4/27)*p.^3;                                 % the discriminant
 Dneg = D<0;
 Dpos = ~Dneg;                                          %~(deltanull | deltaneg);
        n = size(D,1);
      rts = zeros(n, 3);
        a = -q(Dneg);          b = sqrt(-D(Dneg));
       r2 = a.^2-D(Dneg);
      rho = (4^(1/3))*exp(log(r2)/6);
    theta = atan2(b,a)/3;
        a = rho.*cos(theta);   b = rho.*sin(theta);
       S1 = a;
        x = (-0.5)*a;          y = (sqrt(3)/2)*b;
       S2 = x-y;              S3 = x+y;

rts(Dneg,1:3) = [S1 S2 S3];

        E = sqrt(D(Dpos));
       u3 = (-q(Dpos)+E)/2;
       v3 = (-q(Dpos)-E)/2;
        u = sign(u3).*exp(log(abs(u3))/3);              % Cubic roots of u3 and v3
        v = sign(v3).*exp(log(abs(v3))/3);
       S1 = u+v;
        j = complex(-0.5,sqrt(3)/2);                    % Complex solutions
       j2 = complex(-0.5,-sqrt(3)/2);
       S2 = j*u+j2*v;        S3 = conj(S2);

rts(Dpos,1:3) = [S1 S2 S3];
ALLrts = rts;
rts(imag(rts)~=0) = NaN;
REALrts = rts;
end
```

Published with MATLAB® R2016a

Eddy Covariance calculation (*ECflux.m*)

```
function [ EC, IRGA, WIND] = ECflux( times, wind, Ts, rhov, celT, celP )
% ECFlux IRGASON Eddy covariance calculations and flux conversion
%   Jason Kelley NEWAg Lab OSU
%   Last modified 24 FEB 2016
%
% %%%%%%%%%%%%%%%%%%%%%%%%%%%%%%%%%%%%%%%%%%%%%%%%%%%%%%%%%%%%%%%%%%%%%%%%%%%
% INPUT
% times     data timestamps                          [datenums]  Nx1 vector
% tsmp      measurement sample time                  [seconds]  scalar
% z_meas    measurement height                       [meters]  scalar
% wind      Ux,Uy,Uz wind speed                      [m/s]  Nx3 matrix
% Ts           sonic temperature                     [degrees C]  scalar
% rhov      water vapor density                      [g/m^3]  Nx1 vector
% varargin  various scalars for covariance/flux calcs such as
%      CO2
% REQUIRES
% data       formatted for data from importCS.m, using header names from CS
%            program used in logger (TOA5 format output)
%
% %%%%%%%%%%%%%%%%%%%%%%%%%%%%%%%%%%%%%%%%%%%%%%%%%%%%%%%%%%%%%%%%%%%%%%%%%%%
% See also SETNAN ERRNAN CORR_2D IMPORTCS

N  = length(times);                              % number of samples/ave period

% Collect timestamps
EC.start = times(1);
EC.ctr = times(floor(N/2));
EC.end = times(end);

% rotate wind vectors and calculate directional stats
WIND = corr2d(wind);
% Note on directions: Instrument direction is Ux forward, Uy to RIGHT, so that
positive angles proceed from forward to right (cw). Negative angles proceed from
forward to left (ccw)

% temperature
IRGA.T_m = nanmean(Ts);                      % mean sonic temperature
IRGA.T_p = Ts-IRGA.T_m;                      % fluctuations T'
Tii = ~isnan(IRGA.T_p); NT = nnz(Tii);
IRGA.T_var = sum(IRGA.T_p(Tii).^2)/NT;          % variance

% convert vapor density
Tm = nanmean(celT);                             % mean thermistor temperature (degC)
   TmK = Tm+273.15;
    TK = celT + 273.15;
     P = nanmean(celP);                         % [kPa] mean pressure at data logger
    ea = (rhov./1000).*0.287.*TK./0.622;     % [kPa] partial pressure water
  rhod = (celP-ea)./0.287./TK;               % [kg/m^3] density of dry air
   rho = rhov./1000+rhod;                    % [kg/m^3] density of moist air
     q = rhov./1000./rho;                    % [kg/kg] specific humidity

% water vapor trace
```

```
IRGA.q_m  = nanmean(q);                    % mean humidity
IRGA.q_p  = q-IRGA.q_m;                      % fluctuations q'
qii = ~isnan(IRGA.q_p); Nq = nnz(qii);
IRGA.q_var = sum(IRGA.q_p(qii).^2)/Nq;     % variance
```

Covariance

```
EC.uw = nanmean(WIND.u_p.*WIND.w_p);          % Cov u'*w'   - momentum flux
EC.vw = nanmean(WIND.v_p.*WIND.w_p);          % Cov v'*w'   - Crosswind
EC.wT = nanmean(WIND.w_p.*IRGA.T_p);          % Cov w'*T'   - Sensible flux
EC.wq = nanmean(WIND.w_p.*IRGA.q_p);          % Cov w'*q'   - latent flux
EC.Tq = nanmean(IRGA.T_p.*IRGA.q_p);          % Cov T'*q'   - Temperature and
```

Similarity parameters

```
EC.ustar = (EC.uw^2+EC.vw^2)^0.25;            % Friction velocity
                                              % u* = (u'w'^2+v'w'^2)^0.25
EC.ObuL  = -1*(EC.ustar^3)/(0.4*9.81/(IRGA.T_m+273.15)*EC.wT);
                                              % Obukhov Length
                                              % Lo = -(u*^3)/(k*g/T*Qh/rhoCp), where
```

Flux calculation

```
IRGA.rcp = nanmean(rho_cp(celT, P, rhov)); % unit conversion (not included)
IRGA.Le  = nanmean((2500.8-2.36.*celT+0.0016.*celT.^2-0.000006.*celT.^3).*10^3);
IRGA.rLe = nanmean(rho).*IRGA.Le;

 EC.H  = IRGA.rcp .* EC.wT;                % Sensible heat flux [W/m^2]
 EC.LE = IRGA.rLe .* EC.wq;                % Latent heat flux   [W/m^2]
 EC.Bo = EC.H./EC.LE;                       % Bowen ratio H/LE   [ ]
end
```

Published with MATLAB® R2016a